From cocoon to biomaterial: designing and engineering biocompatible, tunable, and photo-responsive cell growth surfaces with *Bombyx mori* silk

Michael J. Landry

A thesis submitted to McGill University in partial fulfillment of the requirements of the degree of Doctor of Philosophy

Department of Chemistry,
McGill University, Montréal,
Québec, Canada

December 2018

Abstract

The design of materials that support cell and tissue growth is complex, due to the multitude of chemical and physical properties which govern basic biological processes such as adhesion, growth and migration. While synthetic polymers have been demonstrated to be an effective, stable and low-cost platform of materials to cultivate cells, they are often poor mimics of a true tissue environment. Bio-inspired and bio-sourced materials present a well-tolerated and tailorable platform for culturing cells, at the expense of stability and higher cost. Within Chapter 2, we explore this duality and study both naturally-derived and synthetic polyelectrolyte surface coatings for the culturing neurons. We assembled polyelectrolyte multilayer (PEM) surfaces with the aim of creating enhanced alternative surfaces to polylysine – the coating of choice. Oligodendroglial and cortical neural cells were cultured onto the PEM substrates and three newly developed silk-based surfaces were found to significantly outperform PDL after substrate optimization.

Chapter 3 further explores silk as a potential platform for supporting human abdominal aortic endothelial cells (HAAECs). HAAECs are sensitive to the hydrophilicity of the substrate they are cultivated on. Thus, to address this, a family of chemically modified silks were created by transforming their pendant tyrosines into azobenzenes through diazonium coupling chemistry. A family of 16 azosilks were synthesized and assessed for their viability using a standard live/dead assay. A linear trend of HAAEC viability with respect to contact angle was observed and demonstrated that more hydrophobic surfaces exhibited higher cellular survival. A sodium sulfanilate azosilk derivative achieved the highest viability (~90%) and was chosen to be further processed into electrospun mats. The mats had a fiber diameter of 140 ± 15 nm and exhibited both a suitable indentation modulus (16 kPa) and a compliance (230 ± 43 MPa) similar to native vascular tissue. The modulus of our azosilk materials were able to be further refined through photo-softening, decreasing an additional 10x to 0.6 kPa.

In Chapter 4 we explore the photomechanical properties exhibited by azosilk films, as the incorporation of azobenzene into a biomaterial creates an externally addressable, yet biologically supportive, material. A sodium sulfanilate derivative of azosilk was studied using two-photon microscopy (800 nm). Upon exposure to high intensity light (100 $\mu J \mu m^{-2}$), fluorescent blisters rose from the surface which were confined to the area that the laser irradiated. These blisters were found

to be filled with water, and exhibited a dramatic photo-softening effect, with modulus softening from 12 kPa to 0.6 kPa. The extent of this effect was controllable and depended on the depth at which the material was written in.

Chapter 5 expands the knowledge gained in Chapter 4 towards creating surfaces for optical control of cell migration. Raised features and modulus gradients have been known to be key physical guidance cues for cells. A reliable, timely, and cheap solution for the creation of surfaces with such features has not been fully explored. Thus, as a proof of principle, an azosilk surface was inscribed with patterns, and Chinese hamster ovary cells were cultured onto the patterned surface. Cell speed, spread area and number of focal adhesions were quantified and compared to the non-patterned area. Cells which were positioned specifically between patterns of lines and dots were found to migrate significantly faster than cells on non-patterned surfaces. Further refinement of these surfaces is currently under investigation; however, the preliminary results show great promise, and azosilk itself may represent a new platform of highly customizable and photo-responsive cell guidance surfaces for studying the cell migration.

Résumé

La conception des matériaux qui supportent la croissance des cellules et des tissus est complexe en raison de la multitude de propriétés chimiques et physiques qui régissent les processus biologiques de base tels que l'adhésion, la croissance et la migration. Bien que les polymères synthétiques se soient révélés être une plate-forme de matériaux efficace, stable et peu coûteuse pour cultiver les cellules, ils sont souvent de mauvais imitateurs d'un véritable environnement tissulaire. Les matériaux bio-inspirés et biosourcés constituent une plate-forme bien tolérée et adaptée pour la culture de cellules, au détriment de la stabilité et d'un coût plus élevé. Dans le chapitre 2, nous explorons cette dualité, et étudions à la fois les revêtements de surface polyélectrolytes naturels et synthétiques pour les neurones en culture. Nous avons assemblé des surfaces compose des multicouches polyélectrolytiques (MPE) dans le but de créer des surfaces alternatives améliorées à la polylysine – le revêtement de choix. Des cellules neurales corticales et oligodendrogliales ont été cultivées sur des substrats de MPE et trois nouvelles surfaces à base de soie se sont révélées nettement plus performantes que le PDL après optimisation du substrat.

Le chapitre 3 explore plus avant la soie en tant que plate-forme potentielle pour soutenir les cellules endothéliales de l'aorte abdominale humaine (CEAAH). Les CEAAH sont sensibles à l'hydrophilie du substrat sur lequel ils sont cultivés. Ainsi, pour remédier à cela, une famille de soies modifiées chimiquement a été créée en transformant leurs tyrosines pendantes en azobenzènes par chimie de couplage au diazonium. Une famille de 16 azosilks a été synthétisée et sa viabilité a été évaluée en utilisant un test vivant / mort standard. Une tendance linéaire de la viabilité de CEAAH par rapport à l'angle de contact a été observée et a démontré que des surfaces plus hydrophobes présentaient une survie cellulaire supérieure. Un dérivé de sulfanilate de sodium azosilk a atteint la viabilité la plus élevée (~ 90%) et a été choisi pour être ensuite transformé en tapis électrospécifiques. Les mats avaient un diamètre de fibre de 140 ± 15 nm et présentaient à la fois un module d'indentation approprié (16 kPa) et une compliance (230 ± 43 MPa) similaire au tissu vasculaire natif. Le module de nos matériaux en azosilk a pu être affiné grâce au photo-ramollissement, en diminuant de 10 à 0,6 kPa supplémentaires.

Au chapitre 4, nous explorons les propriétés photomécaniques présentées par les films en azosilk, car l'incorporation de l'azobenzène dans un biomatériau crée un matériau externe, mais

biologiquement favorable. Un dérivé de sulfanilate de sodium d'azosilk a été étudié en utilisant la microscopie à deux photons (800 nm). Lors de l'exposition à une lumière de forte intensité (100 μJμm-2), des cloques fluorescentes sont apparues de la surface, confinées à la zone d'irradiation du laser. On a constaté que ces vésicules étaient remplies d'eau et présentaient un effet spectaculaire de photo-ramollissement, avec un module de ramollissement de 12 kPa à 0,6 kPa. L'étendue de cet effet était contrôlable et dépendait de la profondeur à laquelle le matériel était écrit

Le chapitre 5 élargit les connaissances acquises au chapitre 4 en vue de créer des surfaces pour le contrôle optique de la migration cellulaire. Les caractéristiques augmentées et les gradients de module ont été connus pour être des indices clés de guidage physique pour les cellules. Une solution fiable, opportune et peu coûteuse pour la création de surfaces avec de telles fonctionnalités n’a pas été complètement explorée. Ainsi, comme preuve de principe, une surface azosilk a été inscrite avec des motifs, et des cellules ovariennes de hamster chinois ont été cultivées sur la surface à motif. La vitesse de la cellule, la surface de propagation et le nombre d’adhérences focales ont été quantifiés et comparés à la zone sans motif. Les cellules qui étaient positionnées spécifiquement entre les motifs de lignes et les points se sont avérées migrer beaucoup plus rapidement que les cellules sur des surfaces sans motif. D'autres améliorations de ces surfaces sont actuellement à l'étude. Cependant, les résultats préliminaires montrent une grande promesse et azosilk lui-même peut représenter une nouvelle plate-forme de surfaces de guidage cellulaire hautement personnalisables et photo-sensibles pour étudier la migration cellulaire.

Acknowledgements

I would like to thank whole-heartedly Prof. Christopher Barrett who allowed me to journey through his laboratory and explore whatever I wanted. I fondly remember the conversations over coffee, beer, and nachos that helped shape the work done within this thesis and beyond. I will never forget my time in the Barrett Lab. I have never met a man with more enthusiasm and positivity and he often helped to serve as a guiding light through the dark periods. His passion for mentorship will be one thing I will bring forward beyond this degree.

I would love to thank my colleagues and co-workers over the years: Oleksandr (my lab husband), Jan, Frédéric, Matt, Victoria, Violeta (my lab mom), Madhi, Mary, Cristina, Louis, Tristan, Igor, Brenda, Thomas (Q) Singleton, Alexis, Yingshan, Mila, and Zahid. Each of you contributed to a friendly atmosphere conducive to intellectualism and fun.

I would like to thank Prof. Audrey Moores for her mentorship. She was instrumental for introducing me to nanoparticles. I still fondly remember when Prof. Barrett introduced us at my first year review, which was the catalyst for our work with silver nanoparticles. I thank the Moores research group, specifically Alexandra and Alain who both have been there for me and helped me on my projects within the group.

I would like the thank Prof. Mark Cronin-Golomb who, during his sabbatical, introduced me to silk materials. I enjoyed all the conversations over coffee about silk and optics and my time I spent with him in Boston. He acted as a mentor whom I rely on still to this day, years after his departure back to Tufts University.

I would like to thank Prof. Timothy Kennedy for his patience, understanding and will-power to teach me, a chemist, aspects of neurology and microbiology. His knowledge always impressed me as I felt like he always knew what to do. I thank him for welcoming me into his group and making me feel like I was part of it. I would also like to thank the members of the Kennedy group, particularly Maran and Laila, for teaching me how to speak to others outside my field and for teaching me how to cultivate neurons.

I would like to thank Prof. Richard Leask and his research group for teaching me about electrospinning and the mechanical properties of biopolymers. Particularly, Matthew Kok and Lisa

Danielczak, who welcomed me with open arms to explore what I wanted within the Leask Lab. Matthew taught me what I know about electrospinning polymers and the electrospun silk materials we developed would have not been possible without him.

Over the years, I had the opportunity to work with four fantastic undergraduate students: Daniel de Biasio, Karlie Potts, Anaïs Robert and Dean Noutsious. I would like to thank them for their hard work and for the opportunity to teach them about silk materials and chemistry in general.

I would like to thank Chantal Marotte, who has always been there for me and has guided me through the intricates of the McGill system. Without her help, I surely wouldn't have finished this degree.

I would like to thank Eric Gauthier, who has been very patient throughout this process and was always there for me through the thick and thin. The Gauthier family, Rob and Donna, has acted like a second family while I have been in Montréal and their presence in my life has made this degree a whole lot easier.

Finally, I would like to thank my parents and family who have always been there for me. I still fondly remember the day I left Fredericton with my aunt Jean and entered the world at McGill, and I appreciate all of the help she has given me throughout the years. My mother has suffered from Parkinson's disease and the work I have done within this thesis is dedicated to her. Both my father and my mother have helped shape me into who I am today, and I thank them for their support.

Table of contents

List of Figures

List of Tables

List of Abbreviations

1-D	one-dimensional
2-D	two-dimensional
3-D	three-dimensional
AA-DR1A	acrylic acid-dispersed red
AFM	atomic force microscope
BDNF	brain derived neurotrophic factor
BMP-2	bone morphogentic protein 2
CHI	chitosan
CHO	Chinese hamster ovary
CNS	central nervous system
cRGD	cyclic arginylglycylaspartic acid
DMEM	Dulbecco's modified eagle medium
DR1A,	dispersed red 1 A
DR2-co-PAA	disperse red 2 co-polyacrylic acid
DRG	dorsal root ganglion
ECM	extracellular matrix
EDC	1-ethyl-3-(3-dimethylamino propyl)carbodiimide
EDS	energy-dispersive X-ray spectroscopy
EDTA	ethylenediaminetetraacetic acid
EGFP	enhanced green fluorescent protein
FBS	fetal bovine serum
GCMS	gas chromatography mass spectrometry
GDNF	glial cell line-derived neurotrophic factor
GFAP	glial fibrillary acidic protein
GTP	guanosine triphosphate
HA	hyaluronic acid
HAAEC	human aortic artery endothelial cell
HEK293	human embryonic kidney 293
HEPES	4-(2-hydroxyethyl)-1-piperazineethanesulfonic acid
HRP	horse radish peroxidase
ICP-MS	inductively coupled plasmon mass spectrometry
ITO	indium tin oxide
LbL	layer-by-layer

MAP	microtubule-associated protein
MEMS	microelectromechanical systems
N52	neurofilament antibody reacting with the 200 side arm
NCs	nanocubes
NGF	nerve growth factor
NIH 3T3	national institutes of health 3-day-transfer mouse embryonic fibroblast cell line
NPC	neural progenitor cell
NPs	nanoparticles
NSPC	neural stem and progenitor cell
OD	optical density
OLDEM	oligodendrocyte defined medium
PAA	polyacrylic acid
PAH	poly(allylamine hydrochloride)
PBS	phosphate buffered saline
PDAC	poly(diallyldimethyl ammonium chloride)
PDL	poly-D-lysine
PE	polyelectrolyte
PEDOT	poly(3,4-ethyl enedioxythiophene)
PEM	polyelectrolyte multilayer
PEO	polyethylene oxide
PET	polyethylene terephthalate
PFA	paraformaldehyde
PLGA	poly(L-glutamic acid)
PLL	poly-L-lysine
PNS	peripheral nervous system
PSS	poly(styrenesulfonate) or SPS, sulfonated polystyrene
PTFE	polytetrafluoroethylene
PVP	polyvinylpyrrolidone
RGD	arginylglycylaspartic acid
SC	Schwann cells
SEM	scanning electron microscopy
SERS	surface enhanced Raman scattering
SF-PG	silk fibroin-polyglutamic acid
SF-PL	silk fibroin-polylysine
SF	silk fibroin
SPR	surface plasmon resonance
SPRANP	SPR-active nanoparticles

TEM	transmission electron microscopy
TEMPO	(2,2,6,6-tetramethylpiperidin-1-yl)oxyl
TGA	thermogravimetric analysis
TSA	p-toluenesulfonic acid
UV-vis	ultraviolet-visible
XPS	X-ray photoelectron spectroscopy
XRD	X-ray diffraction

Preface & Contributions of Authors

The main body of this thesis consists of a published research literature review (Chapter 1), four paper-based research chapters (Chapters 2-5), and a perspective and conclusion chapter (Chapter 6) all with Michael Landry as first author. No parts of any of these co-authored chapters appears in other Theses at McGill, completed or planned. Chapters that have been submitted, accepted for publication, or published are presented either in the submitted, or finalized format with some adaptations. All other chapters are presented as the most recent prepared manuscript and have been formatted into a unified format to the rest of the thesis. Any supporting information was placed in an appendix after each chapter. Chapter 6 was written and edited by Michael J. Landry. An additional appendix (Appendix 5) is placed after the conclusion and represents an additional project which was orthogonal to the main scope of this thesis, yet published research as first author, and was added to demonstrate and document the breadth of collaborative work that was completed during Ph.D. studies.

Chapter 1. Layers and multilayers: Self-assembled, soft, and wet designer neural cell growth surfaces

Michael J. Landry prepared the first draft of the manuscript, with additional first-writing supplied by a former graduate student Frédéric-Guillaume Rollet (Layer-by-layer section, not used for his thesis), Dr. Barrett (*In situ* measurements section), and Dr. Kennedy (some biological parts of the Introduction section). Section 1.9 ‘Thesis scope and overview’ was written and edited by Michael J. Landry and was an addition to the manuscript. The manuscript was edited by Drs. Kennedy and Barrett. Michael J. Landry is first author.

Chapter 2. Tunable engineered extracellular matrix: Polyelectrolyte multilayers promote improved neural cell growth and survival

Landry, M.J.; Gu, K.; Harris, S.N.; Al Alwan, L.; Gutsin, L.; De Biasio, D.; Jiang, B.; Nakamura, D.S.; Corkery, T.C.; Kennedy, T.E.; Barrett, C.J. *Manuscript submitted for publication to Adv. Healthcare Mat.*

Silk materials and any prepared polymers were synthesized and purified by Michael J. Landry. Cortical cell cultures and imaging was performed by undergraduate student Kaien Gu, and MNI researchers Stephanie Harris and Laila Al Alwan. Oligodendroglial cell culture and imaging was performed by Kaien Gu and Diane Nakamura at the MNI. Undergraduate Laura Gutsin and Dr. Corkery (MNI) performed AFM indentation experiments under the supervision of Dr. Ramkaran, the McGill AFM lab facility manager. pH layering and ellipsometry experiments were conducted by undergraduate Bernie Jiang and Dr. Corkery. Undergraduate student Daniele de Biasio and Michael J. Landry prepared the silk-based multilayers and measured their thickness using ellipsometry, their modulus using AFM indentation and their water content using thermogravimetric analysis experiments. Data and statistical analysis was performed by Kaien Gu and Michael J. Landry. Michael J. Landry prepared the first draft of the manuscript, with additional first-writing supplied by Kaien Gu. All authors edited the manuscript, with the bulk of the editing being performed by Drs. Kennedy and Barrett. The project was supervised by Drs. Kennedy and Barrett. Michael J. Landry is first author.

Chapter 3. From cocoon to artificial vessels: Electrospun silk derivatives as surface-tunable vascular graft materials

Landry, M.J.; Kok, M.; Potts K.P.; Gostick, J.T.; Lachapelle, K.; Barrett, C.J.; Leask, R.L. *Manuscript submitted for publication to Biomaterials.*

All polymer synthesis, materials preparation, and characterization were performed by Michael J. Landry and undergraduate student Karlie P. Potts. Matt Kok of McGill Chemical Engineering Department advised and aided Michael J. Landry with electrospinning experiments. Cell work was performed by Lisa Danielczak of the Chemical Engineering Department. and undergraduate Karlie Potts. Live/dead assays were performed by Michael J. Landry and Lisa

Danielczak. All cell imaging was performed by Michael J. Landry. Tensile testing of the material was performed by Michael J. Landry. Electron microscopy images of the material were collected by Michael J. Landry and Matt Kok. The first draft of the manuscript was prepared by Michael J. Landry, with additional first-writing supplied by Matt Kok (electrospinning methodology section), and Lisa Danielczak (cell methodology section). The manuscript was edited by Drs. Leask and Barrett. Drs. Leask and Barrett supervised the project. Michael J. Landry is first author.

Chapter 4. Photo-induced structural modification of silk gels containing azobenzene side groups

Michael J. Landry prepared the materials and performed the lithographic experiments. Graduate student Matt B. Applegate performed fluorescence experiments at Tufts University. Michael J. Landry prepared the first draft of the manuscript and Drs. Bushuyev, Omenetto, Kaplan, Cronin-Golomb and Barrett edited the manuscript. Dr. Cronin-Golomb (Tufts U.), a visiting Professor to McGill, and Dr. Barrett supervised the project. Michael J. Landry is first author.

Chapter 5. Micropatterning azobenzene-modified silk surfaces for optical control of cell guidance and growth

Landry, M.J.; Robert, A.; Noutsios, C.; Mubaid, F.; Brown, C.; Barrett, C.J. *Manuscript in preparation.*

Michael J. Landry, and undergraduate students Constantinos Noutsios and Anaïs Robert synthesized the azosilk materials and prepared each material into films. Anaïs Robert and Michael J. Landry performed the contact angle experiments. Michael J. Landry and Constantinos Noutsios patterned the azosilk substrates for cell culture. Firas Mubaid (McGill Faculty of Medicine) performed the Chinese hamster ovary cell culture, and Michael J. Landry and Firas Mubaid performed the live/dead assays. Michael J. Landry imaged the cell cultures and performed the data analysis. Michael J. Landry prepared the first draft of the manuscript. The manuscript was edited by Dr. Barrett. The project was supervised by Drs. Barrett and Brown (McGill Faculty of

Medicine). Michael J. Landry is first author.

Appendix 5. Surface-Plasmon-Mediated Hydrogenation of Carbonyls Catalyzed by Silver Nanocubes under Visible Light

The synthesis, characterization and materials preparation were completed by Michael J. Landry. Electron microscopy images were assisted by Moores Group graduate student Alexandra Gellé and undergraduate student Beryl Y. Meng, and these results are not planned to be included in A. Gelle's thesis. The optimization, scope and kinetics experiments were completed by Michael J. Landry. The first draft of the manuscript was prepared by Michael J. Landry and edited by Alexandra Gellé, Beryl Y. Meng, Dr. Barrett and Dr. Moores. The project was supervised by Drs. Barrett and Moores. Michael J. Landry is first author.

Chapter 1: Layers and multilayers: Self-assembled, soft, and wet designer neural cell growth surfaces

Chapter 1 is based on a published manuscript entitled 'Layers and multilayers of self-assembled polymers: tunable engineered extracellular matrix coatings for neural cell growth', published in *Langmuir* (Copyright 2018, American Chemical Society) and was co-authored by: Michael J. Landry, Frédéric-Guillaume Rollet, Prof. Timothy E. Kennedy and Prof. Christopher J. Barrett.

1.1 Abstract

Growing primary cells and tissue in long-term cultures, such as primary neural cell culture, presents many challenges. A critical component of any environment that supports neural cell growth *in vivo* is an appropriate 2-D surface or 3-D scaffold, typically in the form of a thin polymer layer that coats an underlying plastic or glass substrate and aims to mimic critical aspects of extracellular matrix. A fundamental challenge to mimicking a hydrophilic, soft natural cell environment is that materials with these properties are typically fragile, and difficult to adhere and stabilize on an underlying plastic or glass cell culture substrate. In this review, we highlight the current state of the art and overview recent developments of new artificial extracellular matrix (ECM) surfaces for *in vitro* neural cell culture. Notably, these materials aim to strike a balance between being hydrophilic and soft, while also being thick, stable, robust, and bound well to the underlying surface to provide an effective surface to support long-term cell growth. We focus on improved surface and scaffold coating systems that can mimic the natural physico-chemical properties that enhance neuronal survival and growth, applied as soft hydrophilic polymer coatings for both *in vitro* cell culture, and for implantable neural probes and 3-D matrices that aim to enhance stability and longevity to promote neural biocompatibility *in vivo*. Towards future developments, we outline four emerging principles that serve to guide the development of polymer assemblies that function well as artificial ECMs: a) design inspired by biological systems, and b) employing principles of aqueous soft-bonding and self-assembly, to achieve c) a high-water content 'gel-like' coating that is stable over time in a biological environment, and possessing d) a low modulus, to more closely mimic soft compliant real biological tissue. We then highlight two emerging classes of thick material coatings that have successfully captured these guiding principles: layer-by-layer deposited water-soluble polymers (LbL), and silk fibroin (SF) materials.

Both materials can be deposited from aqueous solution yet transition to a water-insoluble coating for long-term stability, while retaining a softness and water content similar to biological materials. These materials hold great promise as next generation bio-compatible coatings for tissue engineers, and chemists and biologists within the biomedical field.

1.2 Introduction

For over one hundred years researchers have employed *in vitro* cell culture methods to study neural cells; however, the artificial substrates and matrices typically used to maintain cell survival and differentiation provide a relatively poor approximation of biological tissue. Artificial polymer coatings are relatively inexpensive, stable, and straight-forward to prepare, yet typically provide a poor approximation of real soft and wet biological tissue, and thus often perform sub-optimally. A bare polystyrene plastic surface, for example, generally will not support living cells, and most thin polymer coatings, which are similarly hydrophobic and brittle, will not significantly extend cell viability. While systems that incorporate natural bio-sourced polymers have been developed, these are typically not stable over weeks, are difficult to work with, or are prohibitively expensive to purchase or manufacture in bulk. Poly-L-lysine (PLL), a homopolymer of the naturally occurring amino acid L-lysine, has long dominated the field as a gold standard; however, it is readily degraded by cellular proteases. The application of its 'mirror twin' poly-D-lysine (PDL) displays a similar efficacy yet is more resistant to proteolytic degradation than PLL. Advances in molecular biology have identified key components of extracellular matrix (ECM) that critically support cell survival, differentiation, and growth *in vivo*. Recent studies aim to capture the properties of natural ECM that enhance neuronal survival and growth, using novel soft water-soluble polymers to coat substrates for neural cell culture, implantable neural electrodes and probes, and 3-D matrices to enhance stability *in vivo* and increase neural biocompatibility. Here, we review recent advancements in the development of improved surface and scaffold coatings that employ principals of biomimicry at the molecular scale, with an ultimate goal of engineering a thick, soft, and wet transformative neural interface.

1.2.1 Background

The extracellular matrix (ECM) is a cell-type and tissue-specific organized array of proteins and polysaccharides secreted by cells that define the molecular composition of the local

environment and provide structural and biochemical support.[1] These macromolecular assemblies typically closely associate with cell surfaces, with some components binding directly to transmembrane receptors (Figure 1.1). Integrins, a key family of receptors, mediate cell adhesion *via* specific interactions with major ECM components that include members of the fibronectin, vitronectin, collagen and laminin protein families. Upon ligand binding, integrins initiate intracellular signal cascades that regulate the organization of the cytoskeleton, cell migration, the formation of specialized adhesive junctions, and the trafficking of secretory proteins and receptors to the plasma membrane.[1-2] Laminin superfamily members are core components of basal lamina ECM and are often employed in neuronal cell culture as a substrate to promote cell migration, adhesion, and neurite extension.[1] Fibronectin exists as either soluble plasma fibronectin or insoluble cellular fibronectin and influences cell adhesion, growth, differentiation, wound healing, embryonic development and migration.[1] Although the molecular composition of the ECM is complex and cell- and tissue-specific, synthetic ECM replacements have been used to support cell growth *in vitro* for many years.[3] The coatings produced by manufacturers are frequently proprietary and their exact compositions often remain trade secrets. With recent advancements in tissue engineering, ECM replacements have moved increasingly from two-dimensional films to three-dimensional scaffolds, with polymer chemists, cell biologists, and materials engineers working together to design materials that more realistically mimic tissue environments. The development of specialized materials to support three-dimensional artificial ECM presents an opportunity to create mimics of neuronal tissue that support the formation of three-dimensional networks of neurons and glial cells. Naturally derived polymers, such as hyaluronic acid (HA), a major component of the ECM in central nervous system (CNS),[4-5] have been employed with promise to improve neuronal cell culture, along with fibrous polymers such as collagen, fibronectin, and elastin.[6-7] However, these relatively large proteins are expensive, fragile, and can be difficult to prepare and store while maintaining their biological activity, compared to synthetic counterparts, and there has been relatively little research into chemical modifications to enhance their stability and ease of use. While the biochemical-structural components of ECM are complex, simple mimics of their basic mechanical and biochemical properties have been proposed in a variety of systems.[3,8] Critical features of materials that aim to mimic the ECM can be summarized by two guiding principles (self-assembly and bio-mimicry) and two key material properties (low modulus and high water content).

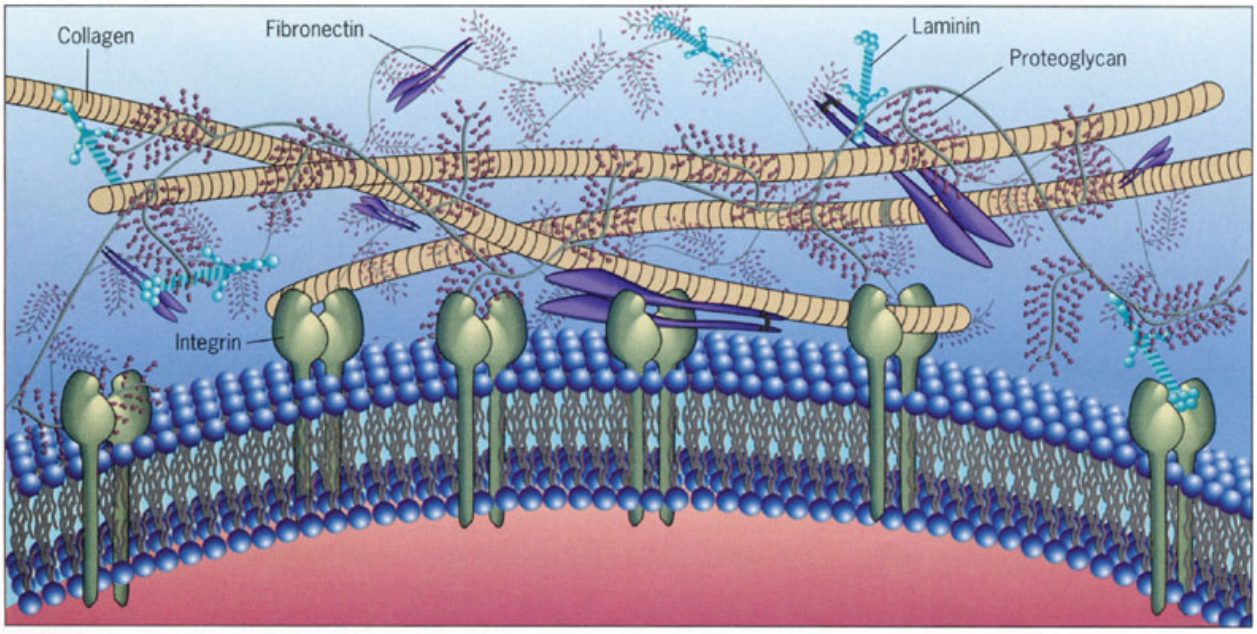

Figure 1.1. Schematic of the various components of ECM. Integrins bind extracellular proteins, such as collagen fibers decorated with proteoglycans. The specific proteins and glycans present differentiate ECMs found in different tissue types. Transmembrane integrin proteins are linked on the cytosolic side of the plasma membrane phospholipid bilayer to cytoskeletal elements, such as microfilaments composed of filamentous actin, intermediate filaments, or microtubules composed of polymerized tubulin. By linking the intracellular cytoskeleton to the local ECM, integrins transduce force across the plasma membrane. Adapted from Karp *et al.*[9] with permission from John Wiley and Sons, "Cell and Molecular Biology: Concepts and Experiments", 4th edition. Copyright 2006.

1.2.2 **Specific requirements of neural cells**

Neurons are highly specialized cells that are critical for sensation, movement, and cognition.[10] Loss of neurons and deficient neuronal function underlies neurodegenerative disorders such as Alzheimer's and Parkinson's diseases.[11] Developing materials that support neural growth and enhance neural biocompatibility may ultimately find utility in the treatment of neurodegenerative disease. Such materials will also facilitate the study of neural cells. Historically, neurons have been cultured on surfaces that attempted to capture and mimic critical physical or chemical aspects of a real ECM. During the first decade of the 20th century, the first experiments to visualize living neurons in cell culture utilized glass coverslips and a microscope, combined

with a technique pioneered by Ross Granville Harrison called a hanging drop – a technique that examined fragments of the embryonic nervous system within a liquid drop hanging from sterile coverslip inverted on a watch glass.[12] This technique allowed for small explants of living tissue to be viewed in three-dimensions rather than two. The neurons quickly died, however, due to the absence of adequate access to nutrition and mechanical support. At the time, it was not clear if the elaboration of a process by a neuron required a substrate, or alternatively if neurons might extend processes like a tree extends branches into the air. To determine if mechanical support is required, Harrison conducted a series of experiments using spider silk as a substrate for neural cell culture. Fibrous substrates were generated by having spiders spin a web across rings at the bottom of a jar, and once finished, tissue explants from embryonic chick or frog CNS were placed on top **(Figure 1.2, (A)** and **(B))**.[13] Processes from the excised tissue were observed to extend along the silk fibers, providing the first experimental evidence that neural cells utilize a mechanical substrate to extend processes.[13] Although not highlighted in these early papers at the time, they represent a foundational application of biomaterials to support the survival and growth of neurons *in vitro.*

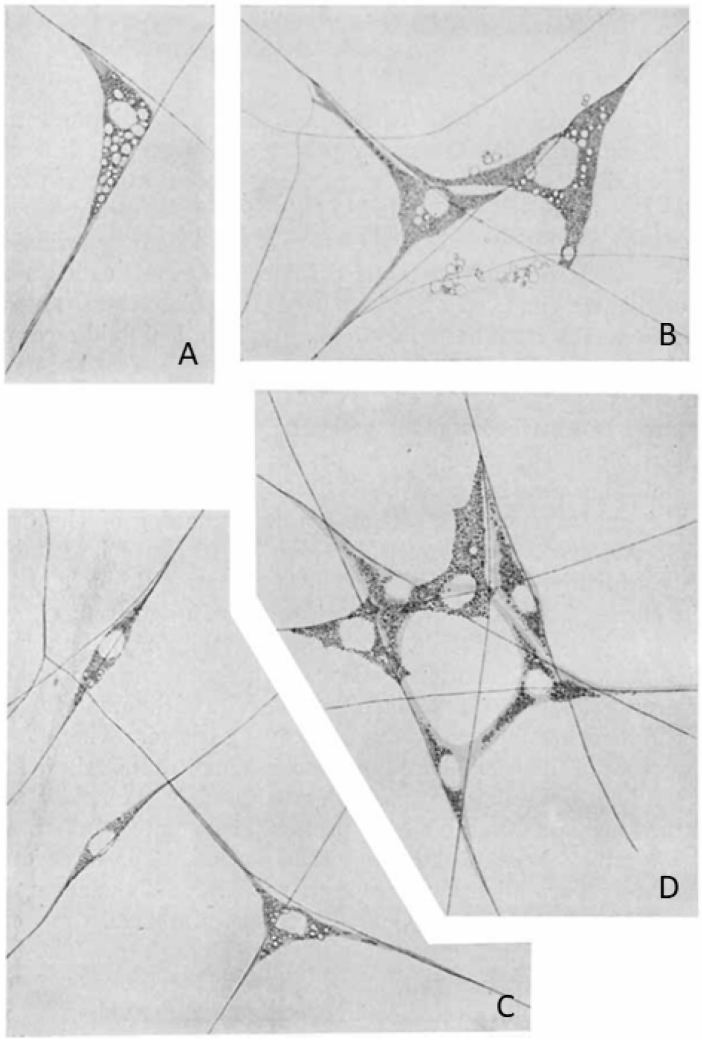

Figure 1.2. Illustrations from Harrison's pioneering paper entitled "The reaction of embryonic cells to solid structures" which demonstrates some of the first uses of artificial substrates for the cultivation of neural cells. **(A)** Cells from an explant of an embryonic frog CNS is cultured with serum on crossed spider webs (300 x). **(B)** Bipolar and tripolar cells from a medullary cord are attached to crossed webs at 8 days and **(C)** 2 days (both 300 x). **(D)** Drawing of the cells after 6 days, showing both 'pigment cell types' that Harrison noticed (300 x). Reprinted from Harrison *et al.*[13] with permission from John Wiley and Sons, *J. Exp. Zool*. Copyright 1914.

While the vast majority of subsequent studies of neurons in culture have employed one or two layers as a substrate, thicker biomaterial films are currently being explored as coatings to determine the effect of thickness and modulus on the longevity, connectivity, and density of neurons maintained *in vitro*. Many studies highlight the role of surface stiffness (measured as

modulus, the slope of a stress-strain curve) in neuronal cell survival and the formation of a neural network.[14] There are several definitions of a modulus, typically referring to how a material performs under a specific stress or load. Indentation moduli refer the response of a material under an indentation load (so called bulk modulus), while the Young's modulus describes the tensile elasticity of a material. The Young's modulus of elasticity tends to be defined also as the ratio of tensile stress to tensile strain. An ideal model system would permit a tunable modulus, to allow cultivation of neuronal (or other) cells in an environment *in vitro* that is as similar as possible to the specific moduli experienced *in vivo*, which can vary over a wide range, and to which cells appear to be surprisingly sensitive. Too soft an artificial surface can be just as inappropriate as too hard a surface, and the 'goldilocks zone' between them for successful growth appears to be limited to a narrow range of just 20-30% in modulus from an ideal target.[15,16]

1.2.3 **Classes of materials attempted as artificial ECM**

Systems such as silk fibroin (SF) and layer-by-layer deposition (LbL) polymers, in principle, possess the key characteristic of a tunable modulus, as both can be readily deposited or assembled from aqueous solution, yet each becomes adhered, stable, and insoluble while retaining soft gel-like properties that resemble a real ECM, to a controllable extent. Key to both systems is a complex sub-structure composed of soft-bonds that assemble during or following deposition, folding up into beta-sheets in the case of SF,[17] and pairing into ionic-bonded multiple layers in the case of LbL, the degree to which can be controlled precisely during fabrication to influence both the water content and the modulus.[18] Silk is a naturally derived and complex material which, while more traditionally challenging to work with, has recently been making important in-roads into the biomaterial and biomedical fields. LbL is an assembly technique that can be employed to construct multi-component systems of simple artificial and/or natural polyelectrolytes, including silk.

Silk fibroin from *Bombyx mori* silk worms is a polypeptide chain consisting of several domain specific sequences of amino acids that is carefully wound, as a single extruded filament, into a cocoon in preparation for metamorphosis in the *B. mori*'s life cycle. Compared to other polymers found to possess excellent properties as ECM for neurons, SF is inexpensive, relatively easy to process, and found to perform at least as well as PDL/PLL, a standard substrate for neuronal culture,[19] largely due to SF's soft modulus (ranging from 8-10 GPa elastic modulus[17] to as soft as 10-100 KPa[18] indentation modulus) and tunability. Layer-by-layer polymer deposition can be used

to build up self-assembled polymer coatings onto substrates through electrostatic interactions by alternating polyanionic and polycationic polymers. The loop length between attachment points, and thus the ability to hold water and the softness, can be tuned precisely by the conditions of chemical deposition, such as ionic strength or pH, in the dipping assembly baths. The influence of coating modulus on neuronal cells in culture has been well studied, with the general conclusion emerging that neurons grow best on softer materials, up to a specific maximal softness.[20,21] A thin layer of PLL on glass or plastic might serve to mask the hard SiO_2 or polystyrene surface chemically, yet the stiffness of such thin coatings generally still resembles that of the underlying hard support material. This stiffness is typically many MPa (the slope of indentation *vs* force), which can be a million or more times harder than the stiffness of living neural tissue, which is in the range of 10-100 Pa.[22] The key concept of modulus matching is to grow cells on surfaces and scaffolds that are as similar as possible to the modulus of the native tissue.[23,24]

While increasing evidence indicates that relatively low modulus materials generate better neuronal culture conditions, water content is a critical factor as well, though it is more challenging to obtain accurate measurements of water content to guide the development of enhanced cell culture substrates.[24,25] Another reason why modulus has been targeted to guide new material development is the stark disparity between some of the currently best available cell culture materials on the market, and real tissue; a difference in water content between real and artificial systems may be just a few tens of percent, while in contrast the stiffness of artificial systems is often mismatched by a factor of a million to that of real tissue.[22] Available high water content materials include hydrogels and layer-by-layer (LbL) systems. Both of these techniques afford good control over final properties during fabrication, allowing for highly tunable water content and moduli. High water content hydrogels have been rationally designed,[26] with upwards of 80% water content obtained in silk fibroin gels.[27] In spite of this, it remains a challenge to maintain the stability of such intrinsically hydrophilic material on a surface, with sufficient stability to limit re-arrangement and dissolution. For silk gels, two microstructures are present in equilibrium: blocks of hard insoluble beta sheets, and an amorphous entangled matrix of higher water content and lower modulus. The balance between the two phases is controlled by the ‘setting’ or ‘curing’ time, which governs the stability to re-dissolution, and also both the modulus and water content. Typically, SF ‘curing’ is achieved through methanol exposure or water annealing. Each technique allows further tailoring of the material’s properties either through treatment time, temperature or

concentration, which can heavily alter the water content and stability of SF-based materials. This inverse relationship between modulus and stability, and water content typically works in favor of the materials chemist, due to the goal of obtaining high water content materials with lower moduli. For LbL systems, varying the pH and salt conditions during the deposition of the polyelectrolyte multilayer film can be employed to control the final water content. These films have been shown to have high water content, while the exact roles of thickness, water content, and modulus have been explored combinatorially *via* 1-D and 2-D gradient films in LbL systems.[23,28]

Polymers that self-assemble into rationally-designed architectures often can be manipulated to possess a low modulus (100-800 kPa) and a high water content(<80 wt%). Such systems assemble into a thermodynamic minimum conformation, with a controllable, predictable spatial arrangement on a surface, leading to a stable and reproducible platform for investigating and optimizing cell compatibility. Natural polymers, such as ECM proteins and intracellular cytoskeletal proteins employ components that self-assemble and exert a profound influence on the modulus and structural integrity of neural tissues. Self-assembled systems characteristically employ hydrogen or ionic 'soft' bonding to generate precise yet reversible spatial arrangements of materials, such as the β-sheets in silk. Importantly, these 'soft bonds' are dynamic and can dissociate and re-bond depending on impinging stimuli, creating a dynamic system with the capacity to adapt and self-repair. Ionic bonds have been used to rationally design three-dimensional tailored materials, such as layer-by-layer (LbL) assembles that interact *via* electrostatic interactions between successive layers of alternately-charged polyelectrolytes. The capacity to engineer systems utilizing the flexibility of hydrogen and ionic bonding provides the potential to generate more complex rationally designed dynamic molecular architectures.

The fundamental mechanical properties of a polymer provide some insight into how well a material will perform under a stress or 'load'. There are several experiments designed to quantify the maximum extent to which a polymer can be strained, and the linear initial and reversible region of these stress-strain curves quantify how elastic or soft a material is, measuring a deformation experienced over the application of a force to a specific cross-sectional area of an object, and is expressed in terms of a force/area such as a Pascal (N/m^2). Strain is the material's dimensional response to a stress, and can be expressed as the percentage increase of a material's extension in the case of tension.[29] The elastic modulus is a measure of a polymer's resistance to being deformed

reversibly under stress, and is defined as the slope of the stress-strain curve in the elastic low-stress region. The Young's modulus describes the uniaxial tensile elasticity, and determines how elastic a material behaves under tensile stress, while a bulk modulus (or elastic modulus), perhaps more relevant to cell culture, describes an extension of the Young's modulus in three dimensions of elasticity and is typically determined through indentation. ECM components generally possess high tensile strength but low elastic modulus (i.e.: 'tough' polymers, typical for natural materials), and these attributes are what functional artificial ECM materials typically mimic.[30] The majority of biologically derived materials are soft yet tough, such as SF, HA, cellulose and spider silk. Structure-performance relationships have been studied between the softness of a material and how well it performs as an artificial ECM replacement for growing neuronal cells.[21]

Inspired by cell biology and biochemistry, we envision that an ideal system will possess a tunable modulus, high water content, and rely on efficient self-assembly. Typically, within natural systems, these guiding principles are highly prevalent, thus we believe it is important to design artificial systems with these design paradigms in mind. Of all of the various systems currently being studied, silk polymers, and LbL systems best fit these specifications. The LbL approach involves layering polycationic and polyanionic polymers in alternating secession, to generate multi-layered soft-bonded substrates that have much freedom in structure, so thus high water content, and low modulus. Both silk gels and LbL coatings have been shown to control predictably both the modulus and water content through a self-assembled process. We present a concise review firstly of silk-based materials, and then of LbL-based materials, for growing neuronal cultures.

1.3 **Silk as an artificial ECM material**

Naturally derived biomaterials have been extensively explored for use in biomedical applications,[31] cell guidance,[32] surface coatings,[4] and biomedical devices.[33] Silk embodies some of the best properties of successful artificial ECM. It is tough, having a high tensile modulus but low elastic modulus, possesses high water content, and can be processed into a variety of different forms and geometries.[34] Of all the types of SF being explored, *Bombyx mori* silk fibroin **(Figure 1.3 (A)** and **(B))** possesses perhaps the most ideal properties, while being a readily available, relatively inexpensive starting material, yet possessing a rich suite of material chemistry properties that are highly controllable through processing (**Figure 1.3, (C)**).

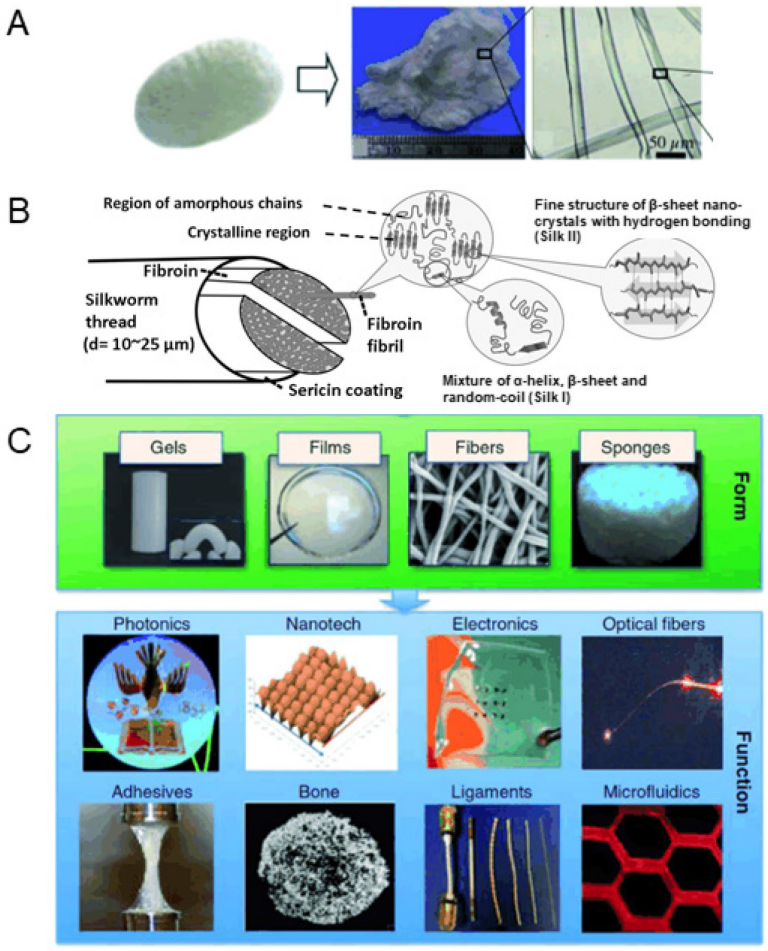

Figure 1.3. (A, left) A cocoon from a *B. mori* silk worm during metamorphosis. **(A, right)** Resulting material after degumming the silk cocoons and removing the sericin coating, and a light microscope image of the resulting bundled fibers after removal of sericin. **(B)** A schematic representation of the components comprising silk fibers. A bundle of fibers (d=10-25 μm) is surrounded with a coating of sericin. Fibroin contains multiple fibroin fibrils which have distinct packing motifs, including: amorphous chains, Silk I (mixture of α-helices, β-sheets and random-coil), and Silk II (β-sheet regions making dense crystalline regions). **(C)** Examples of 4 different platforms of silk (gels, films, fibers, sponges) and their corresponding potential applications (in photonics, nanotechnology, electronics, optical fibers, adhesives, bone scaffold materials, ligaments, and microfluidics). Adapted from **(A/C)** Ghezzi *et al.*[35] and **(B)** Volkov *et al.*[36] with permission from John Wiley and Sons, **(A/C)** *Isr. J. Chem.* Copyright 2013, and **(B)** *Macromol. Mater. Eng.* Copyright 2015.

Bombyx mori silk is a fibrous polymer chain of amino acids that possesses two unique structural motifs: well-defined crystalline phases, and an irregular amorphous phase in between.[37] The crystalline domain is composed of repeating units of glycine combined with alanine, serine or tyrosine (**Figure 1.3, (A)** and **(B)**). These repeating amino acid units produce different polymorphic domains, due to different packing motifs: Silk I, Silk II and Silk III.[37] Silk I is defined as the glandular state, a series of extended α-helices that are water soluble.[37] Silk II possess a well-defined β-sheet conformation, that is generally water insoluble, and Silk III is a threefold polyglycine II-like helix, that naturally occurs at the water-air interface during the process of spinning.[37] Silk III is the polymorphic form that *B. mori* silk worms excrete during pupation, and is generally water insoluble to protect the growing worm during the process of metamorphous. Although natural silk is largely composed of Silk III, a small amount of the crystalline region is also Silk II, allowing the material to be relatively water-impervious yet pliable.[38] Inter-conversion between Silk I to Silk II is achieved by gentle heating, and exposure to methanol or potassium chloride, producing water-stable films.[38] These films resist re-dissolution, yet present a platform to introduce water re-uptake into the film through water swelling, forming the various material classes into which silk can be processed.[39]

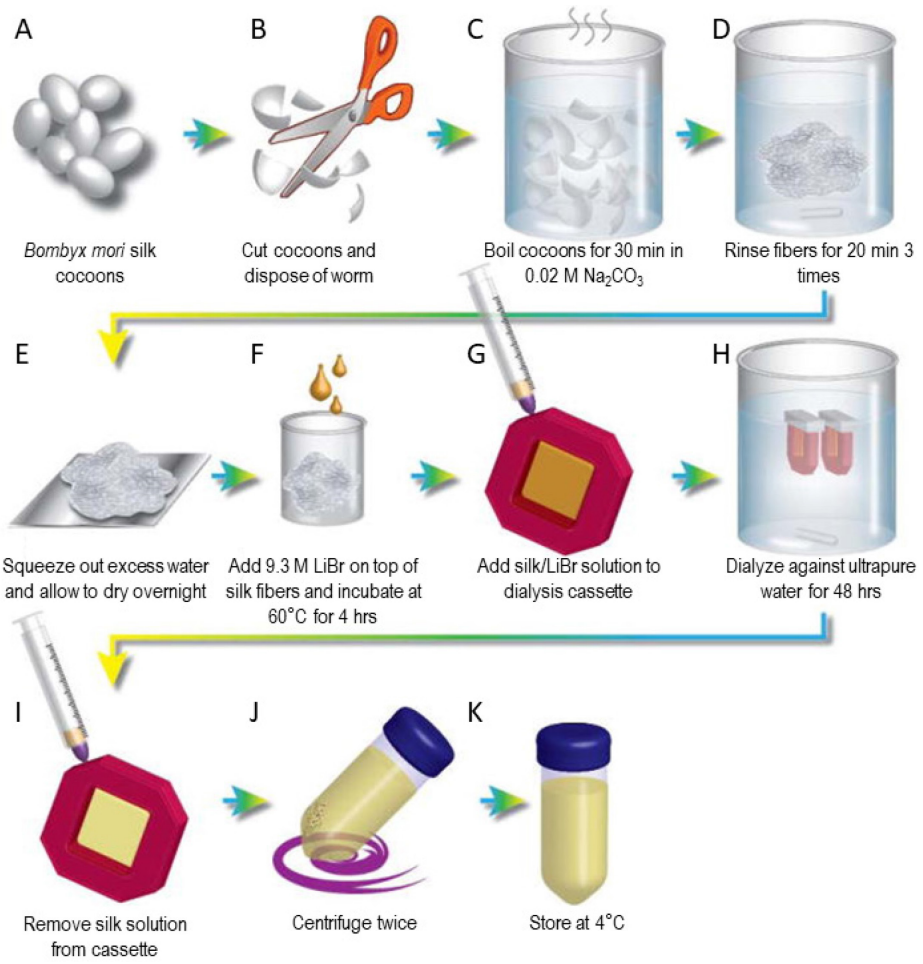

Figure 1.4. Procedure for extracting SF from *Bombyx mori* silk cocoons. **(A)** Whole *Bombyx mori* cocoons which are **(B)** cut up and the worm is removed. **(C)** The cocoons are boiled in a 0.02 M Na_2CO_3 solution to dissolve sericin from native silk fibers, and **(D)** the fibers are rinsed with distilled water to remove any additional base before **(E)** being left to dry overnight within a fumehood. **(F)** The dried and liberated fibers are dissolved with 9.3 M LiBr at 60°C for 4 hours, before **(G)** adding the solution to a dialysis cassette and **(H)** dialyzing against ultrapure water for 48 hours. **(I)** The solution is removed from the dialysis cassette and **(J)** centrifuged twice to remove any impurities (*i.e.* parts of the silk worm that made it through this process). **(K)** The finalized solution is stored at 4°C to prevent degradation. Adapted from Rockwood *et al.*[40] with permission from Macmillan Publishers Ltd., *Nat. Protocols.* Copyright 2011.

In order to process silk into various materials forms, an aqueous solution of silk is first required. Natural silk cocoons contain two polymeric components, silk fibroin and sericin, that must be separated prior to solubilizing the fibroin. Silk can be isolated by boiling the cocoons with Na_2CO_3, releasing the native silk fibers from their sericin 'glue', followed by dissolving into a 9.3 M solution of LiBr.[34] Purified silk is obtained by dialysis against water to remove the LiBr (**Figure 1.4**). Silk fibroin has been extensively processed into at least six different materials classes: films, microspheres, tubes, sponges, gels, and fibers (**Figure 1.3, (C)**).[41] Each of these different classes of materials possess a unique structure and set of properties, and each has been tested as ECMs for cell culture. Films of SF have been well studied, with a long tradition as a medium of choice to promote cell growth, including neuronal growth, in culture.[42] Transforming films into three-dimensional scaffolds can be achieved by creating materials such as gels and sponges from silk fibroin that allow for a variety of cells to be grown into a tissue in three-dimensions. A prime example of the use of 3-D silk scaffolds for neuroengineering is shown in work presented by Huang et *al*, using silk composite materials to grow and reconnect neural tissue in severed sciatic nerves *in vivo*.[43]

1.3.1 **Silk materials as artificial ECM 2-D coatings**

Thin films and coatings of silk have been extensively studied as an artificial ECM for a variety of cells, including Chinese hamster ovary,[44] endothelial,[45] and cardiac cells;[46] however, within the context of this review, we will focus on studies that culture neurons, highly specialized cells that are among the most demanding to maintain *in vitro*. A widely used standard substrate for neuronal cell culture is a coating of polylysine, either the naturally occurring poly-L-lysine (PLL), or it's artificial mirror form poly-D-lysine (PDL). These are stereochemically distinct, but otherwise chemically identical, and possess strong positive charges along the polymer chain that are thought to promote neuronal adhesion and be permissive for the extension of axons and dendrites. Silk does possess some of these characteristics: having amino acids that can be independently pH-adjusted to create positive charges along the polymer backbone to modify cell attachment. Silk's β-sheets allow for these polymers to remain water-insoluble yet swell with water to lower the elastic modulus.[39] A good examples of this was presented by Yang *et al* who explored the use of *B. mori* silk films as a growth promoting substrate for rat dorsal root ganglia (DRG)

sensory neurons from the peripheral nervous system (PNS).[47] Using these silk fiber films, they demonstrated excellent biocompatibility for DRG neurons and promoted the survival of Schwann cells (SC), with minimal cytotoxic effects on cell function. A subsequent paper extended these findings using CNS hippocampal neurons, again demonstrating good biocompatibility and minimal cytotoxicity as indicated by normal morphology and good cell viability compared to hippocampal neurons on PDL surfaces.[48] In both cases, the silk performed as well or better than the typical substrate used to grow these cells.

Thin films have been extensively studied as a coating for cell culture dishes; however, coatings that incorporate SF or SF-modified polymers have opened new avenues to coat other biomedical devices such as neuronal probes and electrodes,[42,49] and scaffolds for regenerative medicine.[43,50,51] SF has been used in conjunction with highly specialized neural probes as an inert, bio-compatible, pliable, and tough structural component.[49] Teshima and coworkers microfabricated small electrode cell culture substrates, called 'nanopallets', comprised of a highly cross-linked SF hydrogel matrix along with poly(3,4-ethylenedioxythiophene):polystyrene sulfonate (PEDOT:PSS) conductive polymers.[52] In this case, the SF hydrogel coats the conductive PEDOT:PSS fabricated electrodes, enhancing the biocompatibility of the device while minimizing electrical resistance and remaining essentially optically transparent. This allowed the authors to electrically stimulate the cells while monitoring the activation of voltage-sensitive Ca^{2+} channels with fluorescence (**Figure 1.5)**. In this example, the silk fibroin provides a soft and biocompatible coating for the hard and electronically conductive PEDOT:PSS nanoelectrodes.

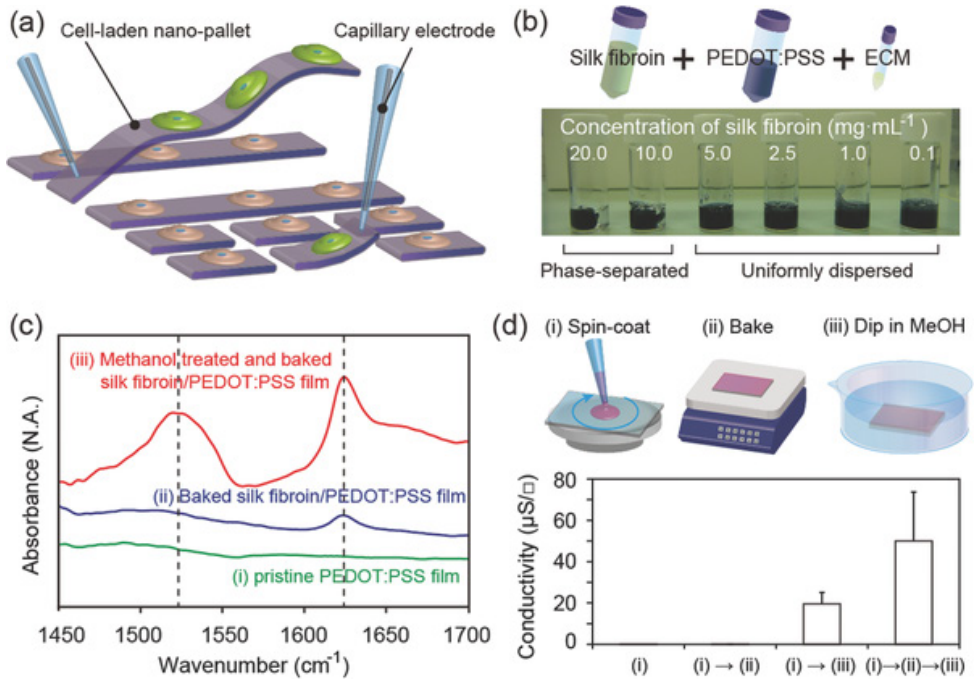

Figure 1.5 (a) Schematic representation of a device to observe an electrical stimulation of cells with voltage-gated Ca^{2+}-selective ion channels ($Ca_v2.1$). When the channel is closed, no florescence is detected, but as the channels opens, a signal is emitted by the Ca^{2+}-Fluo-4 dye complex (ex/em 494/506 nm) (**b)** Material composition of the mobile nano-pallets and photographs of the resulting dispersions of the nano-pallets in water. **(c)** FTIR spectra of the PEDOT:PSS film (green), baked SF/PEDOT:PSS film (blue), and methanol treated and baked SF/PEDOT:PSS film (red). These FTIR spectra show the development of the β-sheet domain, characteristic of water-insoluble silk. **(d)** The evolution of electrical conductivity that is accompanied by (i) spin-coating, (ii) baking and finally (iii) dipping in methanol. Reprinted from Teshima *et al*.[52] with permission from John Wiley and Sons, *Adv. Funct. Mater.* Copyright 2016.

1.3.2 **Patterned silk coatings for substrates**

Patterning SF to direct neuronal growth has been explored,[53,54] adding topographical features (so called '2.5-D surfaces') to flat 2-D films allows for more precise control over neuronal process extension and positioning. These techniques have been extensively investigated for applications that aim to promote axon regeneration. The capacity to effectively pattern SF coatings has been applied to direct neurite growth, and also as a means to roughen in order to present a

more biologically permissive surface. Tan *et al*. have suggested that patterned SF coatings could form highly permissive and effective cochlear implants by promoting the formation of long lasting associations with the spiral ganglion neurons that bridge peripheral and central auditory tissues.[55] Patterned cochlear implant coatings that increase surface roughness have promoted spiral ganglion attachment,[5556] yet directed neurite outgrowth has yet to be achieved by a similarly patterned surface, although several groups are actively pursuing this goal. Silk has emerged as the premiere material within this area and several techniques have been employed to create patterned SF, including soft lithography,[57-59] and physical processes.[60]

Hronik-Tupaj *et al* demonstrated SF patterning and daily uniaxial electrical stimulation promotes neuronal processes to align along surface groves (3.5 μm wide x 500 nm deep).[60] Alignment was only found on nano-patterned surfaces and the aligned neurons demonstrated an explicit response in the form of functional linear networks. It is also possible to pattern a surface by including a chemical gradient within the silk material. For example, the creation of a NaCl gradient generated a gradient of porosity within the resulting silk film. Neurons specifically grew best where the porosity was highest, showing a general trend towards higher salt content (higher numbers of pores).[61] Such patterned surfaces could direct neuronal process extension, with potential future materials being employed in neuro-regenerative medicine. A prime example of these neuronal guidance materials involves using aligned SF fibers that can act as physical guidance for growing neurites. Topographic patterns of the correct size regime, typically on the order of 100 μm,[62] have been extensively studied for their neurite outgrowth promoting, and synaptogenetic properties, yet few studies have combined topographically functionalized surface patterns with a chemoattractant with the goal of directing axon or dendrite guidance. With the goal of promoting regenerative growth in the CNS, Madduri and co-workers describe SF nanofibers functionalized with glial cell line-derived neurotrophic factor (GDNF) and nerve growth factor (NGF).[63] A series of experiments used aligned and non-aligned functionalized SF to examine neurite outgrowth from explants containing embryonic chick spinal cord motor neurons and embryonic PNS DRG neurons. Directional outgrowth was only observed along the aligned SF fibers as compared to the randomly arranged fibers which were no different than the control. This approach used SF-fibers patterned with NGF and GDNF to demonstrate the benefit of employing both chemo-attractant and physical cues to guide neurite outgrowth.

1.3.3 **Silk scaffolds in 3-D**

Transitioning from two-dimensional films to three-dimensional neural networks, scaffolds are being employed to investigate cellular mechanisms using culture conditions that aim to more closely mimic the native environment *in vivo*. This is especially important for neurons, since neural networks are inherently three-dimensional, rather than the thin relatively two-dimensional space presented by a typical cell culture dish surface. Three dimensional scaffolds may incorporate physical channels, grooves or supports. An example of such hapto-tactic physical guidance is the support of neuronal growth by uniaxial channels (~42-142 μm) within a silk sponge.[32] These structures were created by generating cylindrical ice crystals *via* a directional temperature field freezing technique. The material then functioned as a directional sponge, confining neuronal growth and directing neurite process extension along one axis. Using embryonic mouse CNS hippocampal neurons, axons projected along the sponge-scaffold holes. Such scaffolds were further refined by aiming to generate gels that mimic the modulus of human tissues, creating SF hydrogels that range from 4 to 33 kPa, while maintaining structural integrity.[64] In this study, explants of embryonic chick PNS DRGs were embedded in SF hydrogels and axon growth accessed. Modulus matching was found to promote outgrowth from the explants, with the best occurring on 2 and 4% silk hydrogels.

The potential of SF scaffolds to function as silk conduits to promote peripheral nerve regeneration in adult rats has recently been examined by several groups and silk is among one of the most promising materials for neuro-regenerative medicine currently being explored.[65,66] By employing SF in conjunction with a spider silk mimic (Spidrex®), Huang and coworkers were able to achieve partial axonal-regeneration across up to 13 mm long gaps in rat sciatic nerve.[43] In this study, regeneration was enhanced over the 12 week period monitored. Four-weeks after injury, Huang's best nerve-repairing conduits regenerated ~62% (mid conduit) and ~59% (distal to injury) of the previous neuronal density as compared to autologous nerve graph controls. Compared to the controls, the silk conduits limited the inflammatory macrophage response and supported colonization by Schwann cells, the myelinating glial cells that electrically insulate axons in the PNS (**Figure 1.6**). After 12-weeks, regenerated axons were myelinated to an extent similar to uninjured controls (81%). Such findings suggest that SF scaffolds have substantial potential to promote recovery following nerve damage.

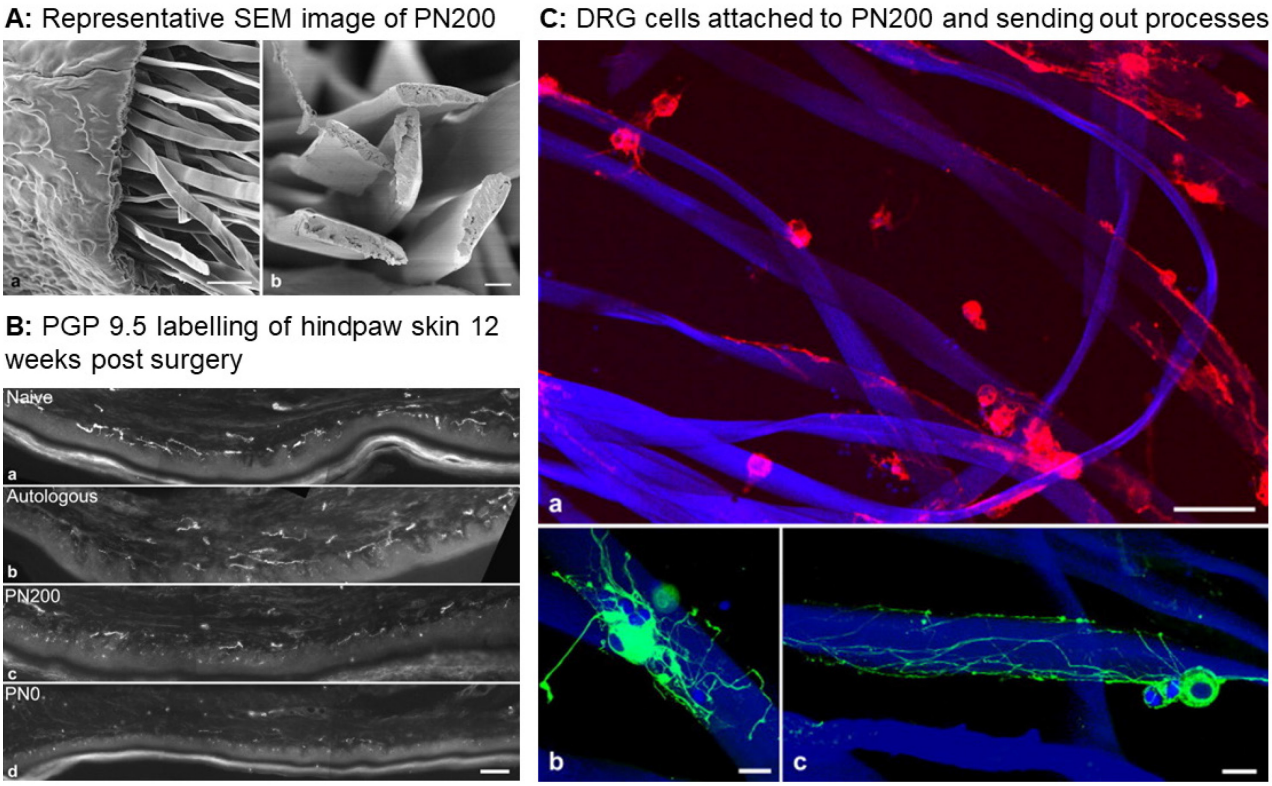

Figure 1.6. A composite figure demonstrating axon regeneration across 8 mm gaps in a rat sciatic nerve. **(A, left)** A representative scanning electron microscope image of PN200 (a graft consisting of 200 luminal silk fibres) graft displaying the outer sheath and (**A, right)** inner aligned luminal silk fibers. **(B)** Left hindpaw skin 12 weeks post-surgery labelled with PGP 9.5 to mark axons. The 4 conditions tested were: **(B, a)** naïve animal group, **(B,b)** autologous group **(B,c)** PN200 and **(B,d)** PN0 (a graft containing no luminal fibers). The autologous group **(B,b)** appears to have similar immunoreactivity as the naïve group **(B,a)**, while PN200 **(B,c)** demonstrated reduced PGP 9.5 immunoreactivity as compared to the autologous group. Few neurons were found on the PN0 group **(B,d)**. **(C)** Confocal images of adult DRG cells and their reaction with the silk graft. **(C,a)** Adult DRG cells attach to the degummed Spidrex® fibers and put out processes, as labelled by phalloidin (red). **(C,b)** Neurofilament labelling shows the long extended neurites wrapping along the luminal fibers and **(C,c)** the Spidrex® fibers. Adapted from Huang *et al.*[43] with permission from Elsevier, *Biomaterials.* Copyright 2012.

An example of the application of silk scaffolds to promote nerve regeneration by Gu and colleagues provides an innovative twist. By combining cell-derived ECM components with silk and chitosan, to further tailor the structure and modulus of the graft, they report regeneration across

up to ~10 mm gaps in adult rat peripheral nerve, similar to those described in Huang's paper.[43] While the two papers demonstrate similar methods to achieve comparable results, Gu's approach involves impregnating the graft with re-constituted ECM from Schwann cells or from acellular sources (e.g. NeuraGen® NeuroMatrix™, Neuroflex™, NeuraWrap™, and NeuroMend™, all proprietary and complex blends of polymers from cellular sources).[51] The chitosan and SF surfaces were cultured with SCs to create ECM derived exclusively from the cellular source, but subsequently decellularized to create ECM-functionalized chitosan - SF graft (**Figure 1.7**).[51] This approach provides two potential benefits: (1) it creates a highly-tailored nerve graft that can be derived from green, renewable feedstocks, and (2) histopathological and blood parameters indicated that this approach maximizes safety and limits macrophage response, which could lead to a rejection of the graft. Electrophysiological measurements confirm a sizable recovery over 12 weeks, albeit not to uninjured levels. Interestingly, using electrophysiological measurements as a matrix for recovery, naked scaffolds were significantly less effective than acellular and SC derived ECM; however, no significant difference was found between Schwann cell and acellular derived ECM.[51] The approach of using silk as a scaffold for cellular derived ECM is innovative and highlights silk's biocompatibility, since the naked silk-chitosan scaffolds do not evoke a significant immune-response.

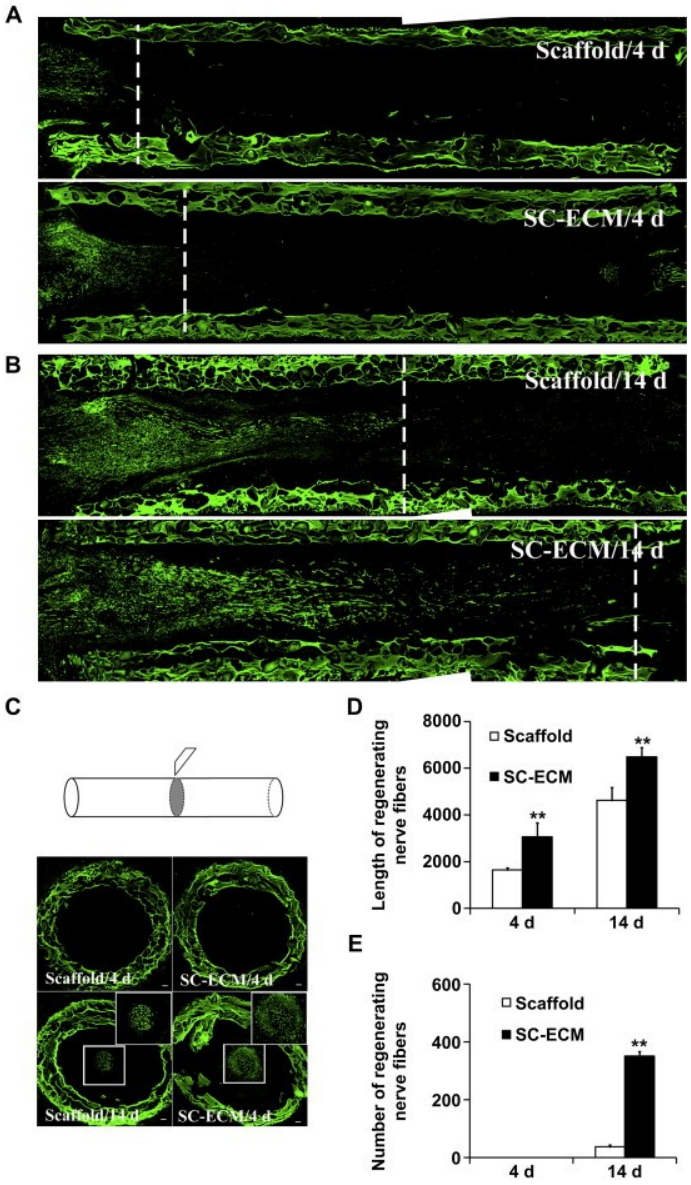

Figure 1.7. Neurofilament immunohistochemical staining of rat sciatic nerves within the bridged 10 mm gap. The dotted line represents the front of axon growth within the denoted period. **(A)** Longitudinal section of plain chitosan/silk graph (top) and the SC-ECM derived graph (bottom) after 4 days. **(B)** Sections of the plain chitosan/silk graph (top) and SC-ECM derived graph (bottom) after 14 days. **(C)** Transverse sections of the nerve graph showing the thickening edge with the SC-ECM compared to just the scaffold after 14 days. **(D)** Histogram of the length of regenerating axons *vs* the surgery date (4 and 14 days) and **(E)** number of regenerating nerve fibers. (**$p < 0.01$). Reprinted from Gu *et al.*[51] with permission from Elsevier, *Biomaterials*. Copyright 2014.

1.3.4 **SF-based composite materials**

While silk fibroin alone has proven to be a successful scaffold to support three-dimensional neuronal networks, multi-component composite materials allow further tailoring of the surface conditions to promote neuronal growth and survival. Ren *et al* employed a hyaluronic acid (HA), SF composite scaffold that exhibits particularly high porosity (~90%).[67] These highly porous scaffolds have a tunable HA content, which influences neuronal adhesion and attachment. Pore sizes ranged from 123 – 253 μm, allowing for large water content absorption, with the material swelling up to 10% in volume. Adding HA generated scaffolds that were more hydrophilic compared to similar SF-only electro-spun materials. SFs have also been incorporated into a variety of polymers such as chitosan and poly(L-lactic acid-co-ε-caprolactone) to modify their properties.[68-70] Some of these modified scaffolds have been tested for their capacity to promote axon regeneration in rat sciatic nerves following injury. One strategy employed chitosan/SF composite materials as a delivery vehicle for adipose-derived stem cells which promoted the repair of gaps in sciatic nerves across 10 mm distances.[71] Poly(L-latic acid-co-ε-caprolactone)/SF blends were employed in electro-spun peripheral nerve grafts, demonstrating enhanced regeneration and recovery of nerve function by 8 weeks following injury.[72] Wang *et al* attributed the enhanced regeneration to the alignment of the nanofibers in the SF-synthetic polymer blends, as well as using a combination of a soft material, such as SF, along with cell-philic poly(L-lactic acid-co- ε-caprolactone), which has recently been shown to dramatically increase adhesion of neural cells.[73] A final example of the application of SF composite materials is to support the generation of an engineered layered brain tissue.[74] This achievement capitalizes on a number of the best attributes of SF, in particular its soft modulus in conjunction with high water content, while the collagen was introduced to structure a layered toroidal 'donut'-like architecture that was used to model different parts of the brain by varying the modulus of each layer **(Figure 1.8)**.

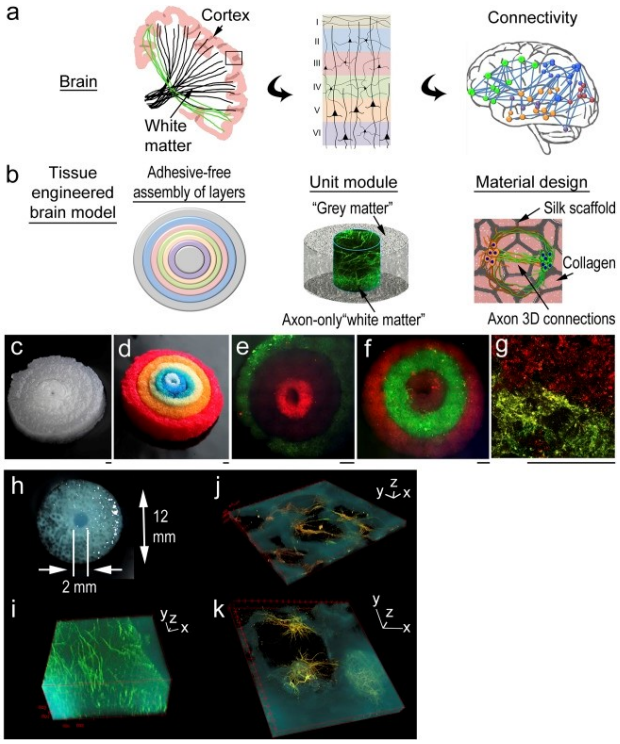

Figure 1.8. Using SF and collagen gels to create a modulus-matched toroid, generating cortical-like tissue organization *in vitro*. **(a)** Illustration of the organization of white matter and six layers of neocortex. **(b)** Design strategy that aimed to mimic these natural structures within a new material. **(left)** adhesive-free assembly of concentrically arranged layers (similar to the layers within the neocortex), and **(middle)** the unit module consisting of neuron-rich grey matter regions along with axon-only white matter regions. **(right)** Demonstration of the material design showing the scaffold and collagen gel composite material supporting connections in 3-D. **(c)** Photograph showing the three-dimensional silk scaffold and **(d)** a dyed version of the same layered toroid to aid in visualization. **(e)** Photograph of the toroid seeded with different primary rat cortical neurons (live-stained with DiI in red and DiO in green) and **(f)** a photograph after cells were grown. **(g)** A representative photograph of the interface between each of the populations (scale bar: 1 mm) **(h)** Photograph of the scaffold showing the dimensions along with **(i)** confocal z-stack multichannel images of 3-D brain like-tissues labeled with the axonal marker β3-tubulin in green and the dendritic marker microtubule-associated protein-2 in red. This confocal stack is from the center axon-only region, while **(j)** and **(k)** are from porous regions within the scaffold. Adapted from Tang-Schomer *et al.*[74] with permission from National Academy of Sciences, *Proc. Natl. Acad. Sci. U.S.A.* Copyright 2014.

1.4 Polyelectrolyte multilayers as tunable coatings

The previous section outlined how a naturally derived self-assembled polymer such as silk can be modified and employed as replacement for neural ECM. It is clear that cells respond to the stiffness of their substrate, and thus altering mechanical properties, such as Young's modulus, can directly impact cell survival and development.[75] A key technique to control the modulus and other properties of an engineered surface is to assemble polymers using a layer-by-layer approach. LbL assemblies were first introduced by Decher *et al.* in the early 1990s as a substitute for chemisorptions *via* the classical Langmuir-Blodgett technique. LbL assembly relies on electrostatic interactions between two oppositely-charged polyelectrolytes as the main driving force for a facile bottom-up method to prepare ultrathin films that removes the need for covalent bond formation and dependence on substrate size and morphology.[76] Other interactions such as hydrogen bonding, or charge-transfer interactions, can also drive the assembly process, highlighting the versatility of the LbL approach. Since the introduction of this technique, LbL assemblies have been used as an easy and inexpensive method to functionalize a wide variety of surfaces. The overall technique relies on dipping a surface into an aqueous solution of charged polymer, rinsing, followed by dipping into a solution that contains the complementary oppositely-charged polymer, the charge-overcompensating alternating process is then repeated until the desired number of layers have been deposited (**Figure 1.9, inset**). The properties of these surfaces can be easily tuned by modifying the nature of the interaction between the two polymer layers, the nature of the building blocks of the films, such as using synthetic polyelectrolytes,[77] polypeptides,[78,79] or polysaccharides,[80] and by tuning the preparation conditions.[81,82] Since its first description, structures more complex than simple films have been prepared using LbL techniques and these structures can be modified to be responsive to stimuli.[83] A summary of the scope of this technique is illustrated in **Figure 1.9.** Because the technique offers minute control over surface properties, a substantial amount of the research efforts towards these ultrathin films has focused on their potential application as biomaterials.[84] Previous studies took advantage of mechanical properties of LbL thin films, such as their dynamic stiffness,[85] or mechanical compliance,[86] to modulate cell adhesion. Published reviews offer comprehensive descriptions of LbL surfaces, focusing on their general physical, biochemical and mechanical properties.[87,88] A comprehensive review of biopolymer based LbL surfaces has been published,[83] and Silva *et al* has addressed their use as engineered extra-cellular matrices.[83]

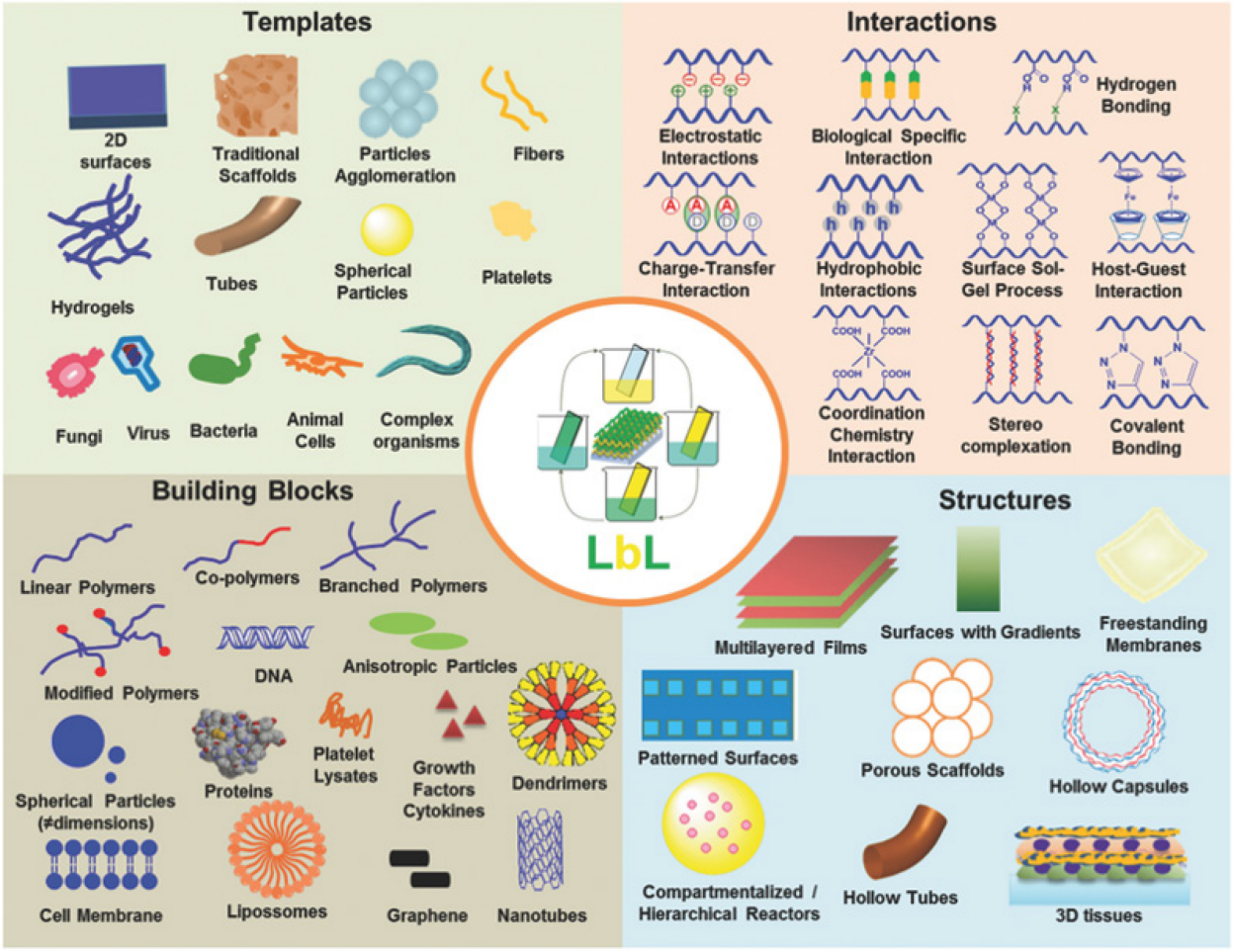

Figure 1.9. Summary of the scope of LbL assembly techniques showing possible interactions between polymer layers, the different building blocks available, the structures created and templates. Reprinted from Silva *et al.*[83] with permission from John Wiley and Sons, *Small*. Copyright 2016.

LbL derived films have been exploited as cell culture surfaces and coatings for a range of cell types;[83] however, a complete exploration as potential growth surfaces for neurons is lacking. LbL coatings offer an attractive interface between biological and artificial materials due to their versatility, and LbL deposition techniques have been used to create polymer assemblies in areas such as macromolecular encapsulation,[89,90] and biocompatible coatings for artificial implant materials.[90,91] Due to their complementary charges that can be controlled *via* the pH of the dipping baths, poly(acrylic acid) (PAA) and poly(allylamine hydrochloride) (PAH), simple polymers of acrylic acid or allylamine, respectively, are two of the most commonly used synthetic PEs in the

fabrication of PEMs. Research from our groups on PAA/PAH PEMs has shown that the fabrication conditions play a key role in altering PEM surface properties and modulus.[92,93] By varying the number of layers, the PEs used, or the deposition pH, an almost infinite number of physically unique PEMs can be created. Previous work in this field has focused mainly on the adhesion, viability, differentiation, and proliferation of neural cells on LbL thin films for use as ECMs.[87,94] Here, we highlight the more recent reports, and focus on the dependence of performance on the physical properties of the materials, and their suitability for potential use as surfaces to study the function of neural cells.

1.4.1 **Layer-by-layer coatings incorporating natural growth factors and polymers**

LbL assemblies can play host to a variety of different polymer combinations and properties dictated by assembly conditions, so that if carefully chosen these artificial polymers can take on the appearance and 'feel' of real ECM. One can mimic ECM by selecting soft and biologically permissive polymers (such as PLL and HA) and incorporating components of the natural ECM as a method to 'bio-camouflage' LbL assemblies on surfaces. In principal, these bio-camouflaged surfaces represent a more natural, albeit engineered, environment that can be tailored and optimized for neuronal survival and growth. Zhou and colleagues highlight the capacity of LbL assemblies to bio-functionalize surfaces for the survival and growth of neural progenitor cells (NPC).[95] Previous work has focused on the use of hard, yet supportive monolayers of bio-responsive polymers (such as PDL, PLL, HA, etc.), but Zhou *et al* focused on using cellular-derived ECM components in combination with a LbL approach, to support the growth of NPCs. Poly-ε-caprolactone, a material previously used both *in vitro* and *in vivo* for neural tissue engineering, was functionalized with a LbL thin film of PLL and heparin sulfate or brain derived neurotrophic factor (BDNF) with the aim of creating a coating that promotes regeneration while minimizing spinal cord injury inhibitory environments.[95] The effectiveness of this surface was assayed by quantifying the length of extending neurites and biochemical correlates of growth.

PLL was demonstrated to play a crucial role as a positively charged polyelectrolyte within a LbL assembly that supports the electrostatic binding of growth factors, while itself being a bio-permissive polymer.[83,95] Due to highly tailorable surface properties (such as charge, modulus and porosity), LbL thin films represent a promising platform for incorporating growth factors into a surface, due in part to adhesive ionic interactions on the surface and within the structure of these

films. Electrostatically bound small molecules, growth factors and drugs on highly charged LbL films have been investigated,[96] yet incorporation of ionically bound ECM components remains one area that has been sparsely developed for any cell type. Functionalizing a LbL thin film with biologically active proteins has substantial potential to optimize neuronal adhesion, survival and growth.[97,98] As a demonstration of this, Vodouhê and coworkers created a biofunctionalized LbL assembly composed of poly(ethylene-imine), PLL, or PAH as polycations and poly(sodium-4-styrenesulfonate) (PSS) or poly(L-glutamic acid), as polyanions along with BDNF and Semaphorin 3A as growth and tropic factors. Their approach embedded the proteins during the assembly process, with Zwitterionic interactions providing stability.[99] This proved to be a facile technique to create bioactive surfaces that present the growth factor and chemotropic factor, in conjunction with permissive polymers, to determine their influence on the growth of embryonic mouse spinal motoneurons.[99] Characterizing the morphology of cultured spinal motoneurons they found that BDNF containing surfaces enhanced survival above control (84% increased survival rate). The stability of BDNF in the substrate was found to be critical, as leaching of the incorporated BDNF significantly lowered the viability over time, and LbL assemblies containing PSS/BDNF exhibited minimal leaching and thus performed best, as compared to a PSS and PLL surfaces.[99]

Lee *et al.* developed a method to culture, differentiate, and promote neurite outgrowth using amino acid containing polymers such as PLL and poly-L-glutamic acid (PLGA). Assemblies of PLL and PLGA were layered onto supported lipid bilayers and used to induce neural stem/progenitor cells to migrate from cultured neurospheres and differentiate into neurons without the need for added serum or growth factors.[100] Neurite outgrowth length and the percentage of differentiated neurons were quantified relative to the number of layers of PLL/PLGA. Induction of differentiation occurred on films up to 8 layers thick. The charge of the last layer was found to influence neurite outgrowth and synaptogenesis, as positively-terminated surfaces (PLL) out-performed negatively terminated (PLGA) surfaces as measured by immunocytochemically labeling presynaptic synapsin I and dendritic MAP-2 (**Figure 1.10**). Lee, Vodouhê, and Zhou's work highlight the benefits of combining naturally derived ECM materials with synthetic polymers in LbL assembled materials and illustrates the flexibility, ease of use and power underlying the capacity of this technique to create highly functional surfaces/coatings to support neurons in cell culture.

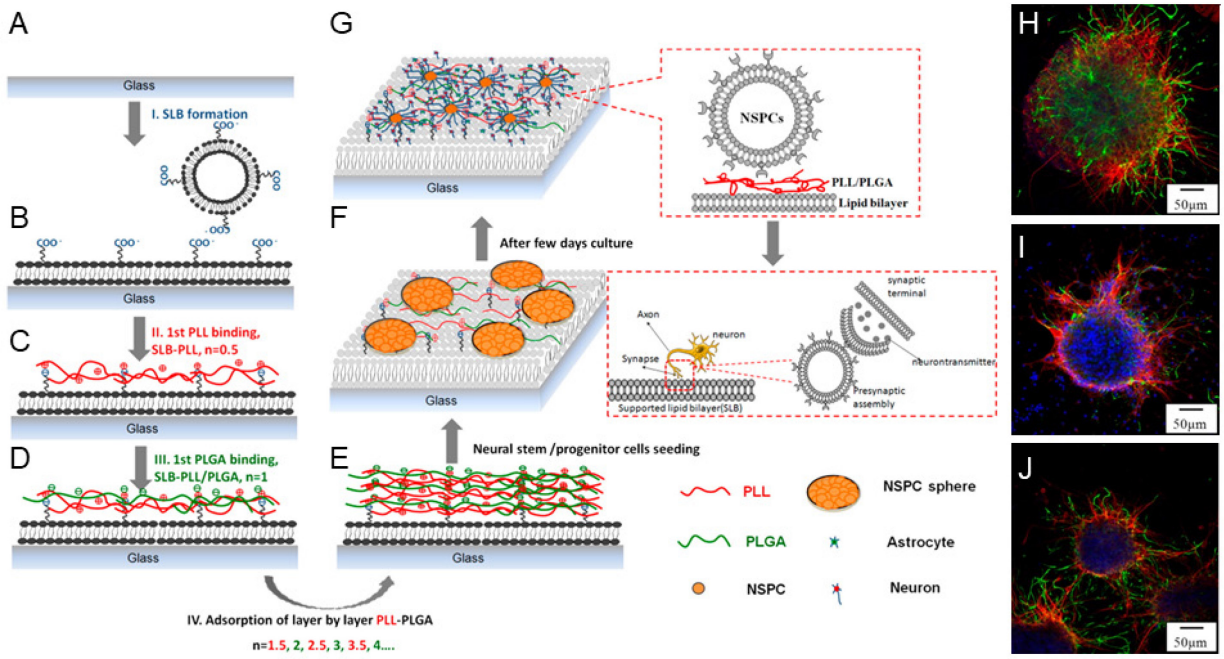

Figure 1.10. (A-G) A schematic representation of the fabrication processes of the multilayer coatings: **(A)** a fresh glass surface hosts a **(B)** supported lipid bilayer lysed onto the surface, exposing the functionalized negatively charged ($-COO^-$) groups and allows for **(C)** PLL (positively charged polymer) to layer onto the surface followed by **(D)** PLGA (negatively charged polymer). **(E)** The PLL/PLGA multilayer is built up to the desired number of layers before **(F)** NSPC spheres were cultured onto the plate. **(G)** A schematic view of the culture is seen with the resultant images shown on the left **(H-J)**. Fluorescence images show the cellular phenotypes that differentiated depending on the LbL surface conditions. Anti-MAP-2 (red, neurons) and anti-GFAP (green, astrocytes) label the differentiated cells. **(H)** A thinner surface results in more astrocytes (n=3.5), and **(I)** a supported LbL PEM of 7.5 layers and finally **(J)** a PEM with 8 bilayers. Adapted from Lee *et al.*[100] with permission from American Chemical Society, *ACS Appl. Mater. Interfaces.* Copyright 2014.

1.4.2 Tailored LbL assemblies to control surface charge

Multilayered surfaces can be tailored and specialized based on deposition parameters and even polymer choice, providing surfaces that can influence neural cell migration, adhesion, and differentiation. Cellular differentiation is an important aspect to study as surfaces have been found to influence the differentiation of neural stem/progenitor cells to functional neurons based on the physical properties of a LbL surface, such as charge,[101] modulus,[14] and chemical functionality.[102]

Since all of these physical properties can be highly tuned based on polymer choice or deposition parameters, LbL created assemblies remain the platform of choice for the exploration of these biological phenomena. Ren *et al.* studied the effect of changing pendant functional groups on polymeric assembles for the differentiation of NSCs to functional neurons.[103] The studied pendant side chain functionalities ranged from hydroxyl groups (-OH), sulfonic ($-SO_3H$), amino ($-NH_2$), carboxyl (-COOH), mercapto (-SH) and methyl ($-CH_3$) groups and demonstrated a range of contact angles revealed by measurements of neural stem cell morphology.[103] Sulfonic acid functionalized surfaces differentiated neural stem cells into oligodendrocytes, while carboxyl, amino, mercapto and methyl decorated LbL assemblies differentiated neural stem cells into a mixture of astrocytes and oligodendrocytes. Ren and coworkers hypothesized that the hydrophilicity of the surface had a dramatic effect on neural stem cell differentiation as evident from dramatic differences between the transformed cell types seen as a function of their contact angle (between methyl and sulfonic acid groups).[103]

While pendant side chain functionalities appear to have a significant influence on the differentiation of neural stem cells to neural cell types, other surface properties such as charge and modulus may also influence this process. Lee and coworkers investigated a PLL/HA system for the differentiation of neural stem/progenitor cells into different lineages (neurons, astrocytes and oligodendrocytes) by studying the effect of surface charge and number of layers in these LbL assembled systems.[4] Neural stem/progenitor cells were induced on films as thin as monolayers; however, the percentage of differentiated neurons increased with increasing coating thickness up to a maximum of 4 bilayers, after which no discernable difference was determined.[4] Single lineage induction was never achieved and only heterogeneous populations of differentiated cells were found. Cellular phenotypes were determined by immunostaining with MAP-2 (neuron) and GFAP (astrocyte), and film thickness, and as a result elastic modulus, was found to influence the ratio of neurons to astrocytes somewhat, with astrocyte counts decreasing with increasing film thickness. Charge was also studied and found, perhaps surprisingly, to have little influence on the ability for neural stem/progenitor cells to be induced, in contrast to findings from Ren and coworkers. While charge now appears to exert little effect over the differentiation of neural stem/progenitor cells to neurons, it does influence the length of processes, as evident by neurite outgrowth assays on negatively and positively terminated surfaces. The longest process extensions were found to occur on positively terminated surfaces, providing a demonstration of the explicit control over cellular

response as a function of the physical properties of a surface.[4]

1.4.3 **Tuning the stiffness of LbL coatings**

The physical and surface properties of LbL assembled materials influence cellular function.[14,23,31] While charge and chemical functionality have been extensively studied,[4,75,103] one might aim to study the elastic modulus of the supporting material independently of the surface properties. Importantly, this bulk property of a LbL film can be tuned based on layer thickness, water content and polymer selection.[104] As an example to illustrate the influence of modulus on neuronal differentiation, Leipzig *et al.* created a methyacrylamide and chitosan based biomaterial, with a tunable modulus (1-30 kPa), to study the influence of modulus on the differentiation of neural stem/precursor cells.[14,105] They found that stiffer polymeric surfaces (> 7 KPa) resulted in the differentiation of neural stem/precursor cells to oligodendrocytes, whereas softer surfaces promoted the generation of astrocytes (< 3.5 kPa).[14] LbL assembled films and coatings present a key opportunity to study the modulus of supportive coatings independent of surface properties (charge and chemical functionality) yet with distinctly reproducible elastic modulus.[106] However, due to the enormous parameter space involved for the preparation and fine-tuning of LbL thin films, we lack a clear structure-activity relationship between modulus and the viability of LbL film candidates, primarily due to the absence of specialized tools required to efficiently study each parameter.

To address this, Sailer and Barrett developed a combinatorial method to create gradient surfaces, with variable modulus and thickness, to facilitate studying large parameter spaces on a single film for high-throughput screening.[23,25] The method could also prepare 2-D gradient films, representing a parameter space equivalent to many thousands of uniform films, that allowed for high throughput combinatorial screening of film layering parameters and the identification of conditions that enhance cell viability. To achieve this, thin films of PAH and PAA were prepared slowly and vertically, filling from the bottom up and varying the pH and salt concentrations of the polyelectrolyte solutions during their deposition. By adding reagents (acids, bases, salts) with a syringe pump, this effectively changed the deposition conditions on-the-fly during film fabrication from bottom to top.[23,25] By rotating the film by 90˚ after each layer deposition, a full 2-D gradient surface could also be achieved. Cell viability was assayed using a HEK293 cell line, identifying the optimal pH range that created regions within the gradient film exhibiting the best survival. The

apex of cell viability was found within a small range of deposition pH (pH 4-6 for PAH and pH 4 for PAA), demonstrating the power of effectively screening the equivalent of over 10,000 single films on one gradient surface. This work was extended to identify surfaces of optimal viability for embryonic rat spinal commissural neurons, correlating surface energy (wettability), matrix stiffness and surface charge with cell survival and growth (**Figure 1.11**). For both HEK293 and commissural neurons, optimal growth was detected at an intermediate modulus between 500 and 800 kPa, and no cells survived in regions of the film that had a modulus below 500 kPa, consistent with a minimal level of mechanical support being required for attachment and growth.[23,25] This study supports the conclusion that survival and growth are highly influenced by modulus and was an important step towards attaining an in-depth understanding of cell-surface interactions.

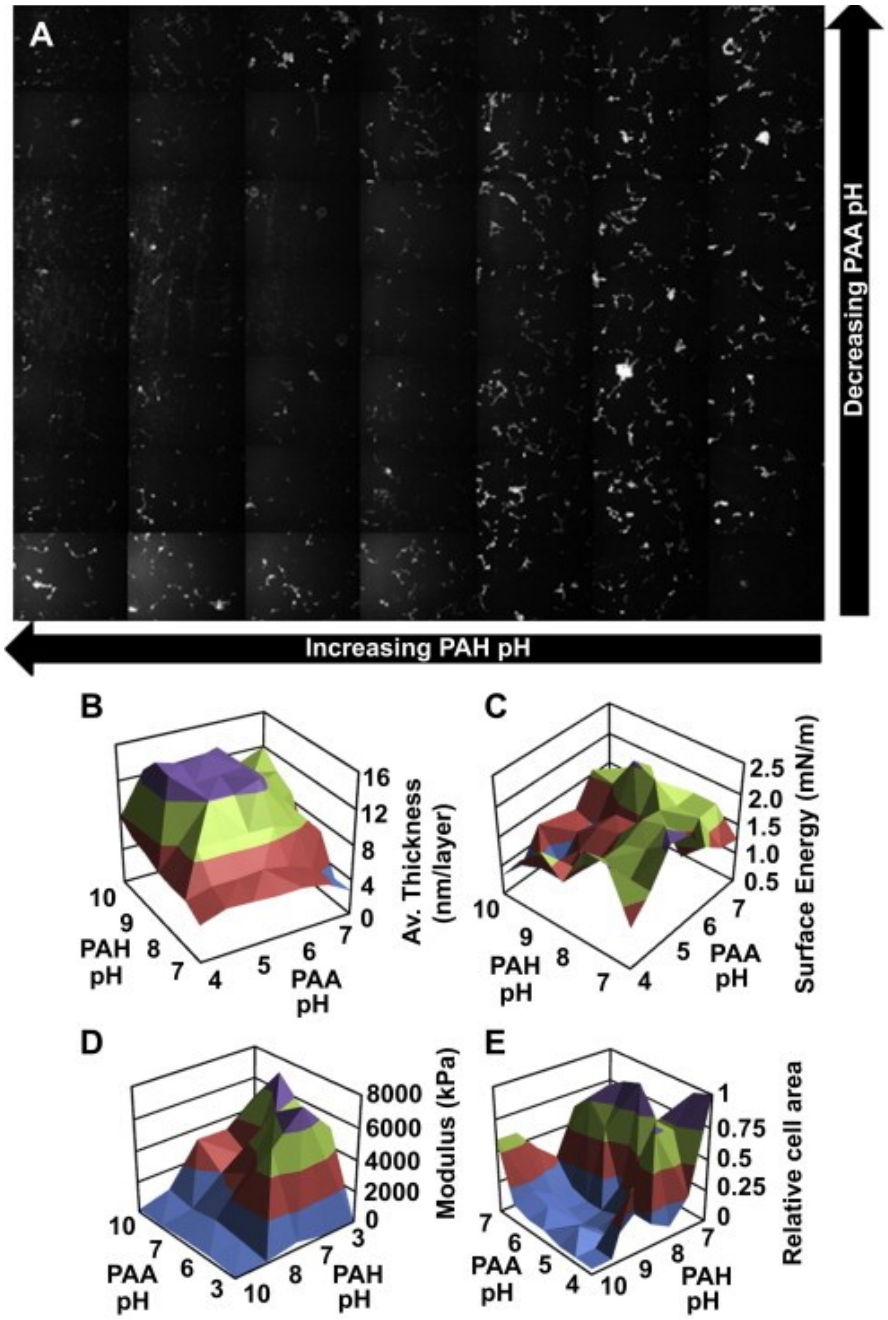

Figure 1.11. (a) Compilation of embryonic rat spinal commissural neuron morphologies at various points within the gradient surface. Microscope images shown in relation to 2-D properties of films depending on the pH of assembly of the polyelectrolytes. **(b-e)** A plot of **(b)** average thickness, **(c)** surface energy (mN/m) **(d)** modulus (kPa) and **(e)** relative cell coverage *vs* PAA and PAH deposition pH. Reprinted from Sailer *et al*.[23] with permission from Elsevier, *Biomaterials*. Copyright 2012.

1.4.4 **Advanced applications in biomedical devices**

This discussion of LbL-fabricated materials has focused primarily on the physical aspects of coatings and its subsequent effect on the viability of neural cells in culture. An additional attractive, key feature of LbL assemblies is their flexibility. LbL assemblies have been demonstrated to coat a variety of substrates and as a consequence, applications towards biomedical devices have been explored, due to the adaptability of LbL for creating coatings with enhanced biocompatibility on complex geometries, such as neural implants or electrodes.[101,107,108] Applications have also included the direct patterning of substrates to influence and guide neural cell growth, adhesion and viability. Kidambi *et al* addressed the impact of astrocytic oxidative stress on neurons by creating patterned co-cultures on LbL assembled structures.[109] This patterning occurred without the use of expensive proteins or ligands and was created by direct micro-contact printing of sulfonated poly(styrene) onto poly(diallyldimethylammoniumchloride) (PDAC)/sulfonated poly(styrene) surfaces. The placement of each member of the co-culture (astrocyte and neuron) was achieved by their binding preference for either a negatively charged or positively charged area within the patterned film. Primary neurons preferentially attached to the negatively charged PSS layers, while the astrocytes attached to either layer with no preference (**Figure 1.12**).[109] The patterned surface was used to study the neuronal response to high levels of reactive oxygen species that are associated with oxidative stress and contribute to neural pathogenesis and neurodegenerative diseases.[109] Using microcontact printed LbL assembled materials to precisely place neural cells in culture demonstrates both the utility and flexibility of this deposition technique.

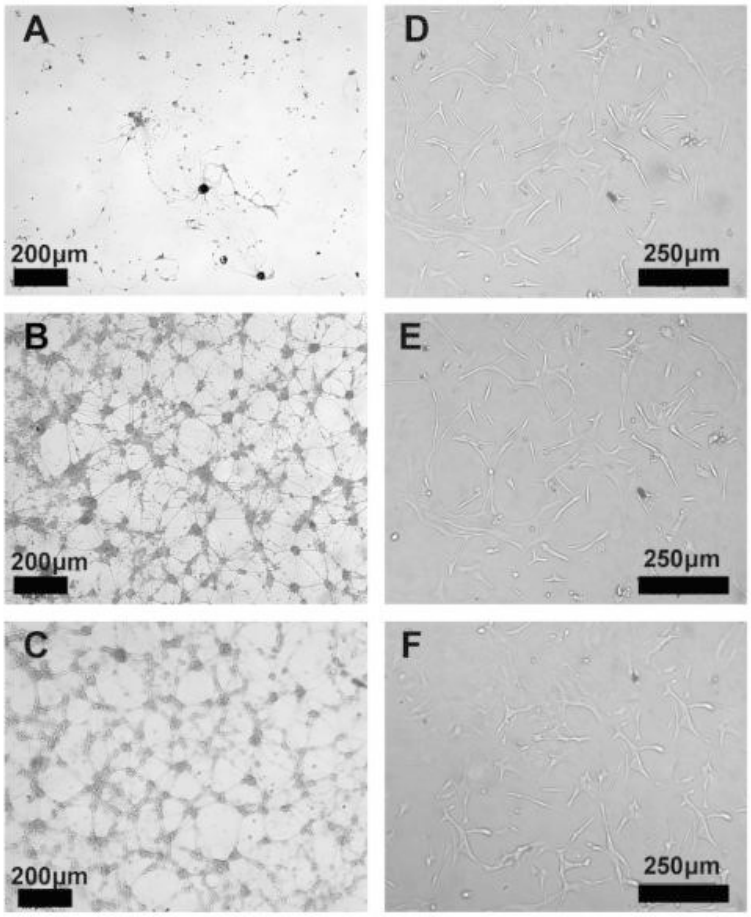

Figure 1.12. Phase contrast images of primary neurons and astrocytes after 7 days and 3 days respectively, illustrating their morphology and growth patterns determined by LbL substrate. Primary neurons were plated on: **(A)** 10.5 layers of PDAC/SPS showing PDAC as the topmost layer, **(B)** 10 layers of PDAC/SPS showing SPS as the topmost layer and, **(C)** PLL as a control. Astrocytes were plated on: **(D)** 10.5 layers of PDAC/SPS showing PDAC as the topmost layer, **(E)** 10 layers of PDAC/SPS showing SPS as the topmost layer and, **(F)** PLL control surface. Reprinted from Kidambi *et al.*[109] with permission from John Wiley and Sons, *Adv. Funct. Mater*. Copyright 2008.

Control over the resulting physical properties of a film can be achieved during the process of deposition, effectively locking in any physical property, such as modulus. This limits the capacity to fine tune surface properties post-production and can limit some of the applications for biomedical devices. LbL material can have dramatically different surface properties under direct electrical stimulation, thus the approach using a combination of an LbL assembled surface in

conjunction with direct electrical stimulation may be used to tune the surface properties of a coating post-production.[110,111] In fact, neural stem cell differentiation can be induced by surface properties and also by electrical stimulation. Lei and coworkers recently reported successfully controlling the differentiation of neural stem cells into functional neurons using a LbL assembled PLL/PLGA film along with direct electrical stimulation.[112] Films were layered on an indium tin oxide (ITO) substrate (a clear semiconductor, **Figure 1.13(A)** and **(B)**) and a microfluidic system was then built on top. By controlling the electrical stimulation, neural stem cells were differentiated and neurite extension assayed.[112] Following 80 mV electrical stimulation for 3 days, uniaxial neurite extension was achieved, with some processes extending well beyond 300 μm.[112] These findings demonstrate the capacity to apply an external stimulus to tailor a surface's properties, post-production, and thereby elicit a specific cellular responce (**Figure 1.13 (C)-(G)**).

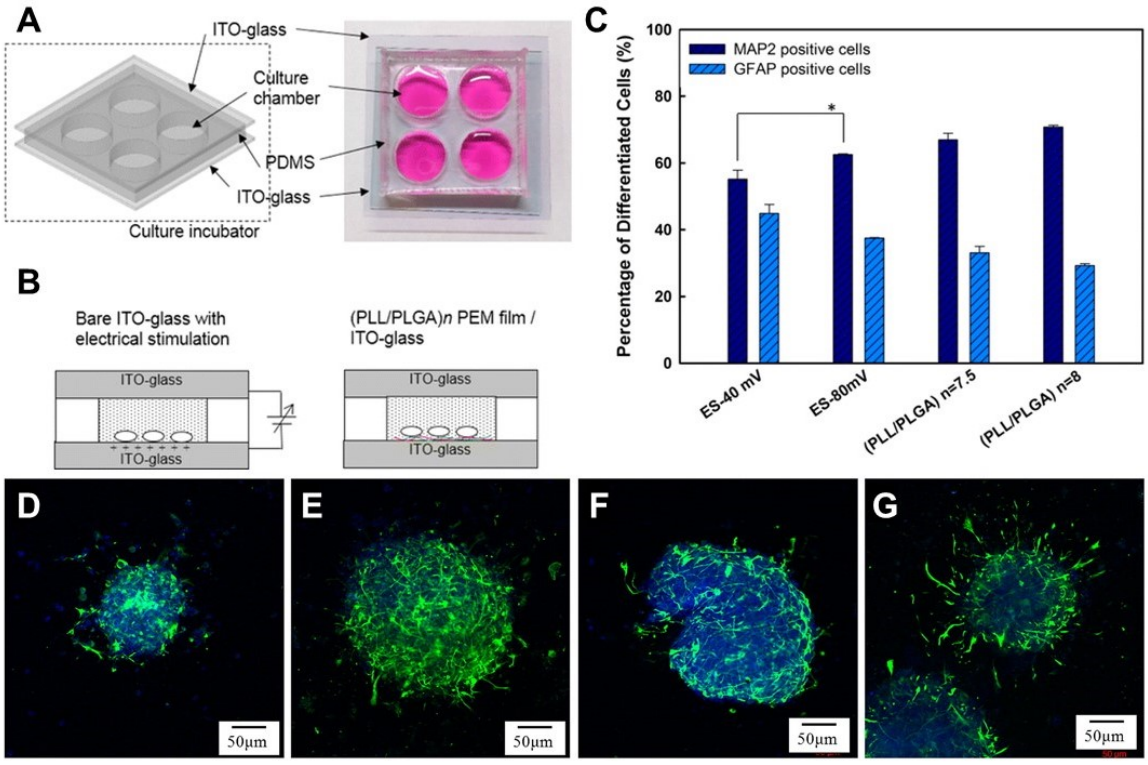

Figure 1.13. (A, left) Schematic drawing of the fabricated device showing the ITO glass and the PDMS chamber along with: **(A, right)** a photograph of the resulting fabricated device. **(B)** Schematic side-view of the device showing neurons plated on bare and LbL (PLL/PLGA) surfaces. **(C)** Quantification of the surfaces showing the distinct populations of neurons which were differentiated (neurons *vs* astrocytes) showing that the LbL-coated surfaces along with direct stimulation from the ITO allows for controlled differentiation into mainly neurons (n=8) or a co-culture with 50:50 differentiation with PLL and direct stimulation. **(D)** NSPCs cultured on bare ITO-glass with 40 mV electrical stimulation, and **(E)** 80 mV. Anti-MAP2 staining is in green (neurons) while anti-GFAP staining is in blue (astrocytes). **(F)** NSPCs cultured on PLL/PLGA on ITO-glass with 7.5 layers and **(G)** 8 layers. This demonstrates how critical the LbL surface is for the differentiation of neurons from NSPCs. Adapted from Lei *et al.*[112] with permission from American Chemical Society, *Langmuir.* Copyright 2014.

Finally, in a paper utilizing poly-ε-caprolactone spun nano-fibrous scaffolds for culturing primary cortical neurons, Zhou *et al.* demonstrated that LbL coatings do not impede electrical conductivity.[113] By using a highly engineered graphene-heparin/PLL system to coat the complex

nanofiberous scaffold, an electrically active, yet neural permissive scaffold was created. Graphene was chosen to impart electrical conductivity, while PLL was used to promote neural cell adhesion to the scaffold. This electrically active, yet neural cell culture permissive scaffold was found to perform similarly to PLL surfaces, while not impeding electrical conductivity, opening possibilities for electrically active coatings that direct neurite growth.[113] Zhou and coworkers were able to demonstrate substantial neurite outgrowth on their modified scaffolds, which did not statistically differ from graphene-free surfaces (61 ± 6 μm), providing that graphene is permissive for neuronal growth and development.[113]

1.5 Making wet *in situ* measurements of these layers

Towards the aim of rational development of new coatings, it is essential to elucidate structure-performance relationships between what can be measured and known about the physico-chemical properties of the polymer layers and multilayers, and the response of the cells in culture. It is thus essential to be able to make measurements of the relevant properties *in situ* - in the wet biological environment in which the coatings will be applied, as opposed to dry and cold, the usual standard conditions of traditional experimental physical chemistry. Historically, observing *in situ* has involved adapting the set of characterization tools typically used by spectroscopists to accommodate conditions more typical of living cells, i.e.: performing the characterization experiments in as close to a real biological environment as possible: at minimum in equilibrium completely underwater, and better at biological temperatures and in cell culture media if possible. Two of the key properties that need to be accurately measured are the water content in the layers, and stiffness. Other mechanical properties can also be of relevance, as well as the ion content and distribution, and knowing the acid-base and other dynamic equilibria in the coatings, which can often be markedly different than that in dilute solution. In general, the 'wetter' and the 'softer' the better, which also creates additional challenges as more sensitive measurements are often required than are typical.

Measurements of modulus are perhaps the most easily performed, as it has generally been fairly straightforward to adapt commercial nano-indentation tools to run in a liquid cell.[114] For more delicate measurements of coatings thinner than 1 micrometer, and/or soft moduli in the range of Pascals, more sensitive Atomic Force Microscopes (AFM) can be used in force-distance mode, underwater, and reasonable estimates of very soft moduli could be extracted statistically from

many 100s of indentations.[115] This AFM force-distance technique has the added benefit of the ability to record adhesion events during the tip retraction phase, and thus to measure surface 'stickiness' at the same time, if the AFM tip is also coated with cell-like LbL coatings.[115] In an experimental configuration already discussed for high-throughput combinatorial gradient 1-D and 2-D coating studies, one can simply automate the indent/retraction data collection concurrent with an x-y re-positionable sample stage, so that separate measurements spaced as closely as 1 millimeter apart can be made independently, and up to 10,000 such separate modulus measurements have been demonstrated in a 2-D 10 cm x 10 cm film.[25]

Towards development of coatings which are as stable as possible to de-sorption or rearrangement over time, it is also important to be able to characterize any dynamic equilibria that the coatings might form with the surrounding media, such as acid-base protonation or deprotonation. While direct measurement of this acid-base equilibria on cell culture surfaces is quite challenging, one can instead get adequate results from an analogous model system where the coatings are applied to small spherical nanoparticles of the same underlying substrate chemistries (silicates, plastics, etc), and then use electrophoresis to measure the zeta potential charge of the surface.[93,116] Making this measurement in a series of different pH environments allows one to construct a surface charge *vs* pH plot, to determine an 'apparent' pKa or pKb of the polymer coatings from the inflection points, which can be substantially different (1-3 log units) than the pKa and pKb values of the same polymers in dilute solution. This provides insight towards what rearrangements and equilibria might be expected at pH 7.4 in the cell culture, and rationalizes many physico-chemical properties that can be strongly non-equilibrium.[117]

The same layering-onto-nanoparticle approach can be used to take advantage of high surface-to-volume ratios of the small systems, to permit 'bulk' measurements to be applied to coatings of tens of nanometers or even less, for example by solid state NMR spectroscopy.[118,119] These sensitive NMR measurements can confirm internal bonding arrangements of polymer multilayer assembles, and structural composition if unknown, *via* either the proton,[118] or carbon signals.[119] Furthermore, solid state NMR can also yield information on the amount of water that is contained in the layers,[119] although this is not a true *in situ* measurement.

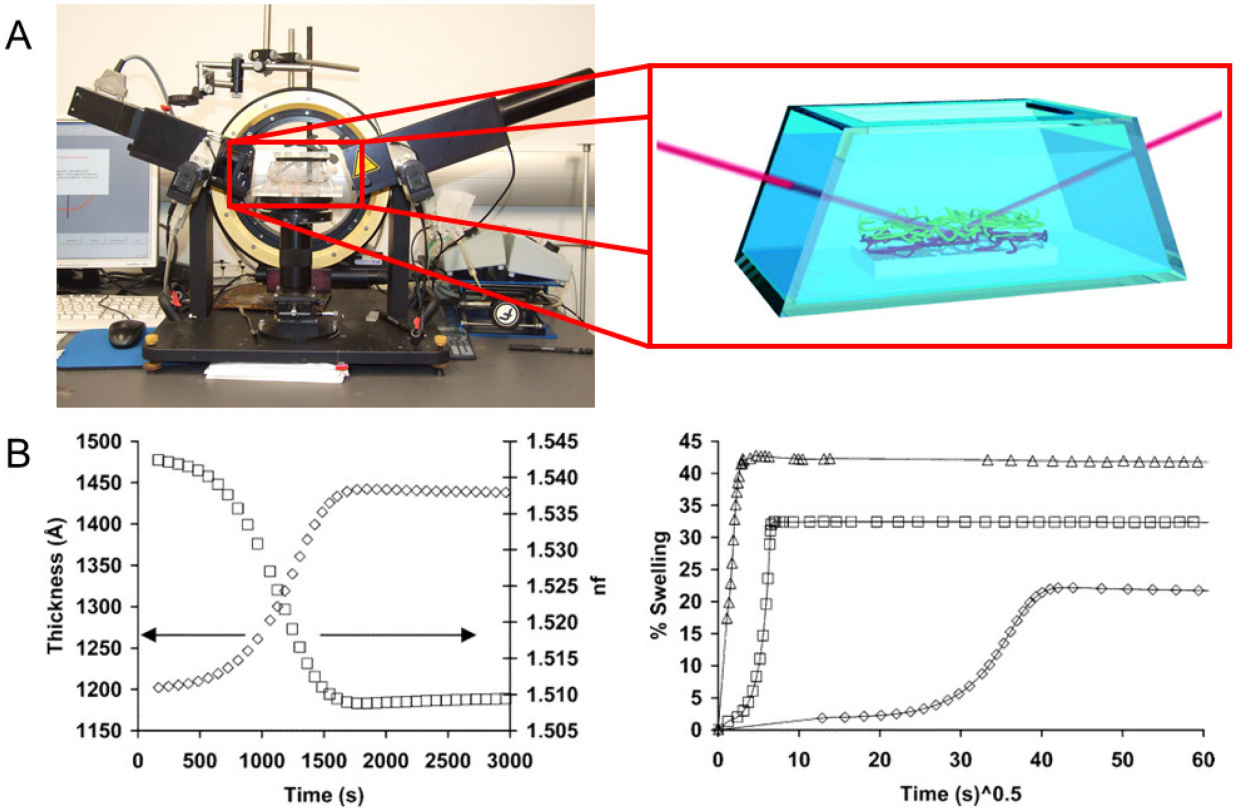

Figure 1.14. (A) Setup for in *situ* swelling measurement of the thickness (*h*) and refractive index of a film (*nf*) of LbL deposited polymers (PAH/PAA) with **(left)** a modified ellipsometer. **(right)** A schematic drawing of the liquid sample cell with the probe laser beam interfering with the LbL polymer surface under water to measure *h* and *nf*. **(B, left)** A curve showing a PAH/PAA surface (25 bilayers) swelling under water from time = 0. The thickness increases by 20% (diamonds) and the refractive index decreases proportionally (squares). **(B, right)** A demonstration of the vast difference (logarithmic scale) in swelling rate when PAH/PAA films assembled under different pH conditions and with a different number of layers. 25 bilayers, pH=3.5 (◇); 15 bilayers, pH=5.0(□); and 60 bilayers, pH=6.5 (▵). Adapted from Tanchak *et al.*[120] with permission from American Chemical Society, *Chem. Mater*. Copyright 2014.

In order to make a true wet *in situ* measurement of the water content of the real (flat, not spherical model) coatings, in as close an approximation as possible to the environment experienced in cell culture media, gentle radiation reflection techniques can be employed, such as ellipsometry, surface plasmon resonance spectroscopy, and neutron reflectometry.[28,120-123] One simply needs to

replace the instrument's dry sample holder with a liquid-holding cell with windows transparent to the radiation wavelengths employed, and to re-program the analysis and interpretation software to model the ambient medium as the refractive index properties of water, and not air. This can be accomplished most simply with a commercial ellipsometer,[120,121] with a home-build liquid sample holder with transparent and non-birefringent windows, aligned normal to the incident and output laser beams **(Figure 1.14 (A))**.[120] The cell can even be brought to biological temperatures, and more representative environments such as cell culture media used instead of water, as long as they are transparent in the visible, and the refractive index and extinction coefficients are known. Here, one measures the thickness and refractive index independently when wet, and compared to the known initial thickness and refractive index of the same coating in the dry state, this implies how much water penetrated in to both increase the thickness, and dilute the refractive index proportionally. Since measurements can be collected once per second or faster, this also permits real-time tracking of the dynamics of water-swelling from dry to hydrated, over seconds, minutes, or hours (**Figure 1.14, (B)**). In order to confirm these measurements by an independent and more powerful technique, a similar liquid cell can be home-built for variable angle neutron reflectometry,[122] where now any gradients in film composition can also be observed, in addition to confirming the results obtained by ellipsometry.[25] Good correlation was demonstrated by the 2 independent techniques, and water content levels from 5% to more than 80% could be measured, and coating fabrication protocols developed to tune the water content to desired intermediate values. Gradients of water profile throughout the coating, and distribution of ions, can also be ascertained by neutron reflectometry.[123]

1.6 Dynamic systems for next generation active surfaces

LbL thin films offer a versatile tool to functionalize surfaces and create soft, yet stable material coatings specifically aimed at mimicking neural ECM to create surfaces that support neuronal survival and growth. Control over the physical properties of a LbL film can be achieved during the process of deposition, effectively locking in any physical property, such as modulus, created by the depositing process. Future research directions towards permitting dynamic properties that can be 'post-modified' or 'post-processed' have been described that create reversible, stimuli-responsive, and externally addressable systems. Work reported by Wang *et al.* has presented an LbL thin film system with a dynamic stiffness based on labile disulfide bonds

that allow control of cell morphology and adhesion through chemical means.[85] While this work does allow for precise control over the material's moduli, we believe the most promising future systems will be controlled through external, localized, and non-interfering stimului, and not chemically. One such way to create an externally addressable system is through the addition of photo-switchable molecules, such as azobenzene, within a material.

Chromophores, such as azobenzene, can be added into the LbL assembly process through chemical means,[124] or through soft-bonds.[125] The addition of photo-switches into biologically relevant polymers creates new biomaterials that exhibit optical properties while remaining biologically permissive. This provides biomaterials that are: (1) externally addressable and (2) allows the experimenter to change/tune materials properties *in vitro* and on-the-fly, and (3) allows localized control of cell biology through single-cell 'switching' (e.g. light can modify the surface around a single cell and tune its properties relative to others around it). Published reviews have highlighted the use of such chromophores in biological systems for cellular control and sensing.[126,127] Polymers have been previously created with photo-responsive moieties as pendant groups, and were demonstrated to allow for the explicit control of modulus, and surface topology using laser irradiation as an external stimulus.[128] Azobenzene in particular is a dominant class of photo-isomerizing dyes that possesses the ability to switch reversibly quickly between distinct *trans* and *cis* geometries upon the absorption of low power light of the appropriate wavelength, including low-bio-interfering visible regions. Azo groups can also be co-polymerized with polyelectrolytes and assembled into thin film architectures to achieve similar control over surface energy as demonstrated by Sailer *et al.*, who reported the use of Disperse Red 2 dye co-polymerized with polyacrylic acid (DR2-co-PAA).[129] A 10% loading of the azo dye was sufficient to induce molecular orientation, and for the first time, resulting birefringence was measured and determined to be stable when completely under water, demonstrating that azobenzene can photo-switch and orient completely under water, extending its application potentials as externally and locally addressable biomaterials.[129]

More complex photo-switches can be functionalized into LbL systems to allow new avenues for targeted cellular control. Work by Goulet-Hanssens *et al* achieved dynamic control of cell adhesion when incorporating an azobenzene switch functionalized with a cyclic RGD peptide as a cell adhesive (**Figure 1.15**).[127] Low concentrations of dye of below 1% were sufficient to

control the adhesion of neural cells onto the LbL surface,[127] demonstrating in principle that light-responsive biomaterials can be capable of direct control over cellular function.

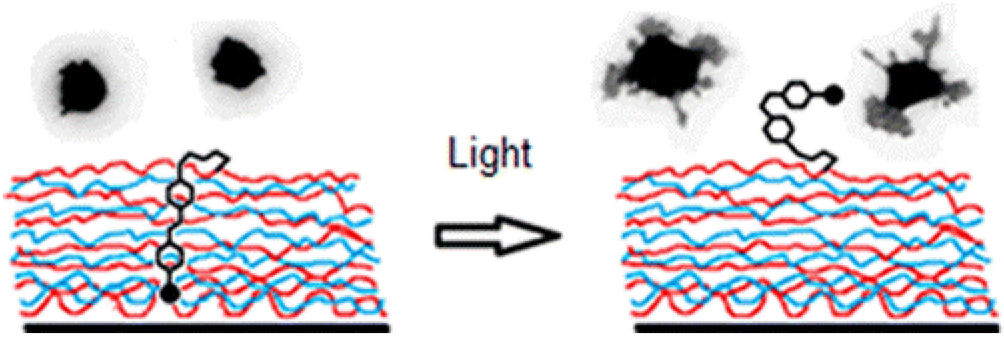

Figure 1.15. Schematic representation of a multilayer containing an azobenzene functionalize cyclic RGD that allows for photo-control over adhesion of NIH 3T3 cells to the surface. Reprinted from Goulet-Hanssens *et al.*[127] with permission from American Chemical Society, *Biomacromolecules*. Copyright 2012.

LbL assemblies with azobenzene have demonstrated the power of externally addressable biomaterials and the possibility to influence and dynamically control biological systems. Silk can also be modified with azobenzene chemically to create a dynamic biomaterial that is photo-responsive. This new material has been called 'azosilk', or 'opto-silk' and it combines the utility of azobenzene photo-reversible dyes with the natural biomaterial properties of silk.[130] While the majority of the previous applications of azosilk used the process of azobenzene functionalization as a means to tune the surface properties chemically, Landry *et al.* used azosilk as a means to achieve dynamic control over the topology and modulus of the surface using light as an external stimulus.[59] Upon exposure to 800 nm light, these silk surfaces expand and 'bubble' and can thus be patterned. The irradiated surface bubbles exhibit a greater than 10-fold decrease in modulus (from 12 kPa to 0.6 kPa).[59] This has the potential to locally manipulate cells by modifying the physical properties of the underlying growth substrate actively with light post-plating, in an active cell culture medium, for potential application to guide the migration of modulus sensitive cells such as neurons, as they grow and interact.

1.7 Conclusions

Throughout this literature review, we have identified a convergence of the field addressing artificial ECM materials, towards developing materials that are bio-inspired, self-assembled

through dynamic bonds, soft, and contain high amounts of water. The reports described demonstrate these guiding principles for developing enhanced methods to cultivate and study neurons using more complex and sophisticated means. Remarkably, some of the materials first used by Ross Harrison's pioneering work on neurite outgrowth in 1914 used biologically sourced spider silk, and 100 years later the field has return to silk as a promising 'material of the future'. Polymer chemists over the past 60 years have indeed provided novel new materials, yet traditionally ones that are hard, built from non-biological (foreign) chemical functionalities, while naturally derived polymers optimized through evolutionary processes have been harvested and post-engineered by humans for thousands of years. These biologically sourced and neurologically supportive materials may be a challenge to work with, yet we anticipate that the field can create highly viable and biologically supportive materials by taking inspiration from the structures and functionalities of complex natural materials. We believe that the design principles outlined here illustrate not only a growing trend of success achieved within the community towards developing and applying new and superior artificial ECM coating materials, but as an inspiring guide for future experimenters to pay attention to nature for the creation of next generation materials for interfacing with neural cells, and other fronts of the bio-interface.

1.8 Acknowledgements

TK and CB are grateful to the NSERC CREATE program (Canada) which funded interdisciplinary collaboration on Neuroengineering research between the MNI and McGill Faculty of Science.

1.9 Thesis scope and overview

The work presented in this thesis is an extension of previous research on optically active materials for interfacing with biological systems that was performed within our group over the last decade. Our first generation of biomaterials were based on polyelectrolyte multilayers, that were then modified by the addition of azobenzene complexes to create some of the first light-addressable polyelectrolyte multilayered coatings for culturing cells. This work will represent a new direction within our research group and within the field of optically addressable biomaterials, extending the previous knowledge of the photophysical properties of azobenzene containing polymers towards new materials which contain more biologically relevant polymers.

Culturing neuronal tissues, such as oligodendrocytes and cortical cells, rely on a small subset of coatings. These coatings are often unstable and expensive, but elicit a reproducible cellular response, and in general are well-tolerated. In the context of neurology, polylysine has high prevalence, and remains the current gold standard in the industry. Other notable brain implant coatings are Parylene C, polydimethylsiloxane (PDMS) and off-stoichiometry thiol-ene polymers (OSTE) These polymers are stable, cheap, easy to manufacture as coatings, and are found to create an inert and sterile interface when implanted. While each of these coatings have several benefits, they also have several disadvantages, including low patency rates, resulting in rejection due to histochemical responses. These undesirable outcomes stem from a poor understanding of how materials interface with biological tissues.

Polylysine coatings play a key role in culturing neurons, and as well as other cell tissue culturing cell types. A few simple questions arise from this statement – why is polylysine used, and what makes it a decent polymer for use in tissue culturing? One may look at the structure of the polymer and find that it is composed as a homopolymer of lysine, a positively charge naturally occurring amino acid. This amino acid plays an important role in proteinogenesis, yet also in collagen crosslinking, and in other structural proteins responsible for cell movement and attachment. Its positive charge is thought to aid in cell attachment through electrostatic interactions with the phospholipid bilayer. Additionally, degradation of polylysine leads back to its monomer, lysine, which has minimal cytotoxicity effects. Thus, monolayers of such a positively charged polymer aid in attachment, although due to its naturally derived peptide linkages, polylysine is prone to degradation. As a method to avoid this, non-natural stereoisomers of lysine (D-lysine) have been synthesized into its corresponding homopolymer (poly-D-lysine). PDL has shown some promise to slow degradation *in vitro*, yet degradation can still occur, albeit slowly.

Other polymers such as PDMS or Parylene C do show promise as alternative coatings for neural probes and other biomedical devices. Parylene C is very stable, showing minimal degradation potential *in vivo*, but is difficult to synthesize, and only small coated objects can be created. Paralyene C coatings are created through chemical vapor deposition, typically of poly(p-xylylene) polymers, and this synthesis requires harsh conditions (550 °C in vacuum). PDMS has been used in numerous applications in biomedical devices, ranging from wound dressing to contact lenses. These polymers provide a hydrophobic and chemically inert coating, which is very stable.

However, as discussed in Chapter 1, to create an interface between biological systems and materials, one must mimic and blend the barrier between the two.

In order to create a long lasting, stable and biologically permissive interface between tissues and biomedical devices, one must blur the boundary between cell and material. Cells and tissues are wet, soft, compliant and made from amino acids, so an ideal coating material would embrace these qualities. Within Chapter 1, we explored a set of principles that highlighted this, relying on the extensive literature on artificial extracellular matrix materials for interfacing with neurology. Mimicking the physical characteristics of the artificial extracellular matrix allowed for the creation of these long lasting, stable interfaces with biology. The triumph of polylysine and other protein coatings for cell biology can be attributed to the use of bio-derived materials to create these interfaces. The typical characteristics of these proteins and biomolecular assemblages are wet, high water containing and minimize compliance and modulus mismatches with the surrounding tissues. The research within our group has focused for the last decade on creating high water containing and soft materials for optics, mostly created through a layer-by-layer approach. Previous research has focused on measuring the modulus of such polymer assemblies, and in addition, create assemblies which had the capacity to support attachment and growth of tissues. By understanding and quantifying the physical properties of artificial extracellular matrix materials, better and augmented cell growth can be achieved. By employing these wet and soft polymer coatings, we can blur the boundary between tissue and implant, effectively bio-camouflaging an object. As mentioned in Chapter 1, few synthetic materials are capable of 'bio-camouflaging' an object. Specifically, this thesis will aim on developing novel bio-inspired replacements for PDL, using materials such as silk fibroin from *Bombyx mori* silk worms.

Silk-based biomaterials offer a platform which is renewable, flexible, cheap and can be tailored using synthetic chemistry to create a vast family of optically distinct materials to interface with biology. *B. mori* silk possesses three specific domains: Silk I (random-coil or unordered structure), Silk II (crystalline and beta sheet regions), and Silk III (unstable structure). Within the silk worm itself, a liquid version of silk in a Silk I and Silk III form is found, which is spun through its spinnerets into a structure mostly consisting of Silk II. This transformation from a water-soluble silk towards something more water-stable is important and used to prevent their cocoon from unravelling during a rain storm. Crystalline regions (Silk II) are held in place in more amorphous

structured Silk I domains, allowing the material to strength and be flexible. This Silk I/Silk II bundled fibre is arranged into larger and larger bundles, held completely together with sericin, an additional protein. In Chapter 1, a list of the most impactful artificial extracellular matrix replacements for culturing neurons was gathered, and their material properties were distilled into a set of guidelines. These guidelines could be used to create and engineer superior materials for interfacing with biology, and all point towards an interesting and developing new class of materials, silk fibroin from *Bombyx mori* silk worms. Silk can be self-assembled into high water-containing and low modulus materials, all properties which are possessed by natural tissue environments. Combining azobenzene chromophores with silk polymers creates a material called 'azosilk', which will be explored as a potential second generation optically active biomaterial.

One specific question that will be addressed within the context of this thesis is the effectiveness of silk materials against previously tested solutions for culturing cells. Chapter 2 will tackle this question, addressing new methodologies for accessing the performance of cell surfaces. Previously researched polymers will be explored along with newly synthesized silk-based ionomers to create new assemblages of polymer coatings for supporting neural cell culture. This chapter will highlight the physical aspects of the materials, rationalizing their performance based on mechanical data.

The mechanical properties of each of these materials is an important aspect to explore, as mechanical properties such as Young's modulus, compressibility and indentation/bulk modulus can affect both cellular growth and proliferation. However, the modulus of a material can be dramatically affected by the amount of water that is present within the polymer matrix, and thus can be decreased dramatically based on the amount of swelling experienced by the coating or scaffold. In order to characterize the amount of swelling, thermogravimetric analysis can shed some insight into the total water content trapped within the polymer chains. This can be and will be used to characterize specific water content of silk and PEM coatings within the following chapters. Additionally, the modulus of a given material can decrease based on the swelling of the polymer, so in order to characterize this decrease in modules, AFM indentation experiments must be explored using underwater AFM characterization.

AFM indentation is a technique to explore the hardness of a surface within a local

environment. It is similar to traditional indentation experiments, where an increasing load is placed on an indenter tip as the tip penetrates further into a sample. The stress experienced by the tip is expressed as the depth at which the probe can indent, and this is a function of the amount of load placed. AFM indentation occurs using a AFM tip to indent into smaller and microscopic features that are present within a sample. This is perfect for exploring nano-sized features or general inhomogeneity within a sample's surface. Additionally, since underwater probes are available, underwater indentation can be achieved through contacting the surface of the swollen polymer and indenting into it. The generated indentation data is in the form of a force-deflection curve, where the initial linear portion can generate the bulk or indentation modulus assuming different fitting parameters. Parameters such as tip volume/shape, spring constant, and indentation speed matter, as softer materials have viscoelastic components which require modelling. Hertz models are simple and provide an estimate of the elastic behavior of such materials, but in the case of soft materials with viscoelastic responses, a Johnson-Kendall-Roberts (JKR) model may provide better insight. Thus, for the exploration of our silk materials, we will employ nanoindentation using submerged AFM probes and model their deflection using such a JKR model.

There are some limitations within the context of creating 2-D growth surfaces for interfacing with biological tissues. While coating materials provide necessary interfaces with cells, native tissues are a 3-D arrangement of cells in space, and thus coatings unnecessarily restrict the normally 3-D tissues into a 2-D coverage of cells. From 2-D coatings towards 3-D scaffolds, Chapter 3 will explore and tackle the creation of electrospun materials made from azosilk and address some of the problems associated with electrospinning such water-soluble polymers into insoluble and swellable materials. This chapter will also begin the discussion of the interaction of azosilk with light, and the photomechanical properties that are exhibited by azosilk.

The electrospinning of silk materials is complicated, as shown within Chapter 1. One must balance the cohesivity of the spin-dope solution while maintaining volitivity in order to create dry electrospun mats. 2-D surfaces, such as those explored in Chapter 2 and the beginning of Chapter 3, have several limitations, including their inability to be used as scaffolds for growing more exotic tissues, and their inability to represent a real mechanically supportive biological environment. Naturally, biology exists in three-dimensions such as those tissues found in the vascular system. As a proof of principle that our material could be used as a scaffold for culturing more exotic

tissues, we will electrospin our newly formed azosilk polymers into a family of azosilk nanofibrous materials. As a trial to explore the use of our newly created azosilk materials, we decided to assess their viability as vascular tissue support materials. The vascular system demands materials which have the correct tensile strength, while maintaining adequate bulk modulus and minimal cytotoxicity effects. While this is a large departure from the original subject matter of PEM coatings for neurology, we believe that the selection of a new class of silk materials may provide an avenue towards three-dimensional applications such as tissue engineering. The goal in mind was to create a new platform of photo-responsive biomaterials, thus the ability to have three-dimensional and free-standing materials which are available for implantation is important.

Finally, Chapters 4 and 5 will explore the photo-responsive aspects of azosilk in detail, delving into the possibility of interfacing with biological tissues using azosilk and light. Chapter 4 will examine the photomechanical properties of azosilk materials, and potential applications will be discussed in the context of biomedical research. These potential applications will be explored and refined within Chapter 5, where the plausibility of using the photomechanical properties researched in Chapter 4 will be discussed and highlighted. In conclusion, Chapter 7 will discuss the potential applications of azosilk, heavily setting the stage for new applications of these photo-responsive polymers, and the plausibility for designing additional photo-responsive materials for the future.

1.10 References

1. Hynes, R. O.; Yamada, K. M., *Extracellular matrix biology*. Cold Spring Harbor Laboratory Press: Cold Spring Harbor, New York, **2012**.
2. Hynes, R. O., Integrins: a family of cell surface receptors. *Cell* **1987**, *48* (4), 549–554.
3. Lutolf, M. P.; Hubbell, J. A., Synthetic biomaterials as instructive extracellular microenvironments for morphogenesis in tissue engineering. *Nat. Biotech.* **2005**, *23* (1), 47–55.
4. Lee, I. C.; Wu, Y. C.; Cheng, E. M.; Yang, W. T., Biomimetic niche for neural stem cell differentiation using poly-L-lysine/hyaluronic acid multilayer films. *J. Biomater. Appl.* **2015**, *29* (10), 1418–1427.
5. Suri, S.; Schmidt, C. E., Cell-laden hydrogel constructs of hyaluronic acid, collagen, and laminin for neural tissue engineering. *Tissue Eng. Part A* **2010**, *16* (5), 1703–1716.

6. Wei, K.; Kim, B. S.; Kim, I. S., Fabrication and biocompatibility of electrospun silk biocomposites. *Membranes (Basel)* **2011**, *1* (4), 275–298.

7. Gao, M.; Tao, H.; Wang, T.; Wei, A.; He, B., Functionalized self-assembly polypeptide hydrogel scaffold applied in modulation of neural progenitor cell behavior. *J. Bioact. Compat. Polym.* **2016**, *32* (1), 45–60.

8. Maniotis, A. J.; Folberg, R.; Hess, A.; Seftor, E. A.; Gardner, L. M.; Pe'er, J.; Trent, J. M.; Meltzer, P. S.; Hendrix, M. J., Vascular channel formation by human melanoma cells *in vivo* and *in vitro*: vasculogenic mimicry. *Am. J. Pathol.* **1999**, *155* (3), 739–752.

9. Karp, G., *Cell and molecular biology: concepts and experiments*. 4th Ed.; John Wiley & Son: Hoboken, New Jersey, **2006**.

10. Kandel, E. R.; Schwartz, J. H.; Jessell, T. M., *Principles of neural science*. 4th Ed.; McGraw-Hill: New York, **2000**.

11. Yates, D., Neurodegenerative disease: neurodegenerative networking *Nature Rev. Neurosci.* **2012**, *13* (5), 288–289.

12. Millet, L. J.; Gillette, M. U., Over a century of neuron culture: from the hanging drop to microfluidic devices. *Yale J. Biol. Med.* **2012**, *85* (4), 501–521.

13. Harrison, R. G., The reaction of embryonic cells to solid structures. *J. Exp. Zoolog. Part. A Comp. Exp. Biol.* **1914,** *17* (4), 521–544.

14. Leipzig, N. D.; Shoichet, M. S., The effect of substrate stiffness on adult neural stem cell behavior. *Biomaterials* **2009**, *30* (36), 6867–6878.

15. Wang, H.-B.; Dembo, M.; Wang, Y.-L., Substrate flexibility regulates growth and apoptosis of normal, untransformed cells. *Am. J. Physiol., Cell Physiol.* **2000,** *279* (5), 1345–1350.

16. Yeung, T.; Georges, P. C.; Flanagan, L. A.; Marg, B.; Ortiz, M.; Funaki, M.; Zahir, N.; Ming, W.; Weaver, V.; Janmey, P. A., Effects of substrate stiffness on cell morphology, cytoskeletal structure, and adhesion. *Cell Motil. Cytoskeleton* **2005**, *60* (1), 24–34.

17. He, Y. X.; Zhang, N. N.; Li, W. F.; Jia, N.; Chen, B. Y.; Zhou, K.; Zhang, J.; Chen, Y.; Zhou, C. Z., N-terminal domain of *Bombyx mori* fibroin mediates the assembly of silk in response to pH decrease. *J. Mol. Biol.* **2012**, *418* (3), 197–207.

18. Farhat, T.; Yassin, G.; Dubas, S. T.; Schlenoff, J. B., Water and ion pairing in polyelectrolyte multilayers. *Langmuir* **1999**, *15* (20), 6621–6623.

19. Rodríguez-Lozano, F. J.; García-Bernal, D.; Aznar-Cervantes, S.; Ros-Roca, M. A.; Algueró, M. C.; Atucha, N. M.; Lozano-García, A. A.; Moraleda, J. M.; Cenis, J. L., Effects of composite films of silk fibroin and graphene oxide on the proliferation, cell viability and mesenchymal phenotype of periodontal ligament stem cells. *J. Mater. Sci. Mater. Med.* **2014,** *25* (12), 2731–2741.

20. Banerjee, A.; Arha, M.; Choudhary, S.; Ashton, R. S.; Bhatia, S. R.; Schaffer, D. V.; Kane, R. S., The influence of hydrogel modulus on the proliferation and differentiation of encapsulated neural stem cells. *Biomaterials* **2009**, *30* (27), 4695–4699.

21. Saha, K.; Keung, A. J.; Irwin, E. F.; Li, Y.; Little, L.; Schaffer, D. V.; Healy, K. E., Substrate modulus directs neural stem cell behavior. *Biophys. J.* **2008**, *95* (9), 4426–4438.

22. Levental, I.; Georges, P. C.; Janmey, P. A., Soft biological materials and their impact on cell function. *Soft Matter* **2007**, *3* (3), 299–306.

23. Sailer, M.; Lai Wing Sun, K.; Mermut, O.; Kennedy, T. E.; Barrett, C. J., High-throughput cellular screening of engineered ECM based on combinatorial polyelectrolyte multilayer films. *Biomaterials* **2012**, *33* (24), 5841–5847.

24. Georges, P. C.; Janmey, P. A., Cell type-specific response to growth on soft materials. *J. Appl. Physiol.* **2005**, *98* (4), 1547–1553.

25. Sailer, M.; Barrett, C. J., Fabrication of two-dimensional gradient layer-by-layer films for combinatorial biosurface studies. *Macromolecules* **2012**, *45* (14), 5704–5711.

26. Wang, Q.; Mynar, J. L.; Yoshida, M.; Lee, E.; Lee, M.; Okuro, K.; Kinbara, K.; Aida, T., High-water-content mouldable hydrogels by mixing clay and a dendritic molecular binder. *Nature* **2010**, *463* (7279), 339–343.

27. Su, D.; Yao, M.; Liu, J.; Zhong, Y.; Chen, X.; Shao, Z., Enhancing mechanical properties of silk fibroin hydrogel through restricting the growth of β-Sheet domains. *ACS Appl. Mater. Interfaces* **2017**, *9* (20), 17489–17498.

28. Tanchak, O. M.; Yager, K. G.; Fritzsche, H.; Harroun, T.; Katsaras, J.; Barrett, C. J., Water distribution in multilayers of weak polyelectrolytes. *Langmuir* **2006**, *22* (11), 5137–5143.

29. Jordan, J.; Jacob, K. I.; Tannenbaum, R.; Sharaf, M. A.; Jasiuk, I., Experimental trends in polymer nanocomposites—a review. *Mat. Sci. Eng. A* **2005**, *393* (1), 1–11.

30. Kolacna, L.; Bakesova, J.; Varga, F.; Kostakova, E.; Planka, L.; Necas, A.; Lukas, D.; Amler, E.; Pelouch, V., Biochemical and biophysical aspects of collagen nanostructure in the extracellular matrix. *Physiol. Res.* **2007**, *56*, 51–60.

31. Georges, P. C.; Miller, W. J.; Meaney, D. F.; Sawyer, E. S.; Janmey, P. A., Matrices with compliance comparable to that of brain tissue select neuronal over glial growth in mixed cortical cultures. *Biophys. J.* **2006,** *90* (8), 3012–3018.

32. Zhang, Q.; Zhao, Y.; Yan, S.; Yang, Y.; Zhao, H.; Li, M.; Lu, S.; Kaplan, D. L., Preparation of uniaxial multichannel silk fibroin scaffolds for guiding primary neurons. *Acta Biomater.* **2012**, *8* (7), 2628–2638.

33. Kundu, B.; Kurland, N. E.; Bano, S.; Patra, C.; Engel, F. B.; Yadavalli, V. K.; Kundu, S. C., Silk proteins for biomedical applications: bioengineering perspectives. *Prog. Polym. Sci.* **2014**, *39* (2), 251–267.

34. Li, Z.-H.; Ji, S.-C.; Wang, Y.-Z.; Shen, X.-C.; Liang, H., Silk fibroin-based scaffolds for tissue engineering. *Front. Mater. Sci.* **2013**, *7* (3), 237–247.

35. Ghezzi, C. E.; Rnjak-Kovacina, J.; Weiss, A. S.; Kaplan, D. L., Multifunctional silk-tropoelastin biomaterial systems. *Isr. J. Chem.* **2013**, *53* (9), 777–786.

36. Volkov, V.; Ferreira, A. V.; Cavaco-Paulo, A., On the routines of wild-type silk fibroin processing toward silk-inspired materials: a review. *Macromol. Mater. Eng.* **2015**, *300* (12), 1199–1216.

37. Asakura, T.; Yao, J.; Yamane, T.; Umemura, K.; Ulrich, A. S., Heterogeneous structure of silk fibers from *Bombyx mori* resolved by ^{13}C solid-state NMR spectroscopy. *J. Am. Chem. Soc.* **2002**, *124* (30), 8794–8795.

38. Yan, L. P.; Oliveira, J. M.; Oliveira, A. L.; Caridade, S. G.; Mano, J. F.; Reis, R. L., Macro/microporous silk fibroin scaffolds with potential for articular cartilage and meniscus tissue engineering applications. *Acta Biomater.* **2012**, *8* (1), 289–301.

39. Freddi, G.; Pessina, G.; Tsukada, M., Swelling and dissolution of silk fibroin (*Bombyx mori*) in N-methyl morpholine N-oxide. *Int. J. Biol. Macromol.* **1999**, *24* (2), 251–263.

40. Rockwood, D. N.; Preda, R. C.; Yucel, T.; Wang, X.; Lovett, M. L.; Kaplan, D. L., Materials fabrication from *Bombyx mori* silk fibroin. *Nat. Protoc.* **2011**, *6* (10), 1612–1631.

41. Ude, A. U.; Eshkoor, R. A.; Zulkifili, R.; Ariffin, A. K.; Dzuraidah, A. W.; Azhari, C. H., *Bombyx mori* silk fibre and its composite: a review of contemporary developments. *Mater. Des.* **2014**, *57*, 298–305.

42. Servoli, E.; Maniglio, D.; Motta, A.; Predazzer, R.; Migliaresi, C., Surface properties of silk fibroin films and their interaction with fibroblasts. *Macromol. Biosci.* **2005**, *5* (12), 1175–1183.

43. Huang, W.; Begum, R.; Barber, T.; Ibba, V.; Tee, N. C.; Hussain, M.; Arastoo, M.; Yang, Q.; Robson, L. G.; Lesage, S.; Gheysens, T.; Skaer, N. J.; Knight, D. P.; Priestley, J. V., Regenerative potential of silk conduits in repair of peripheral nerve injury in adult rats. *Biomaterials* **2012,** *33* (1), 59–71.

44. Wang, Z.; Park, J. H.; Park, H. H.; Tan, W.; Park, T. H., Enhancement of recombinant human EPO production and sialylation in chinese hamster ovary cells through *Bombyx mori* 30Kc19 gene expression. *Biotechnol. Bioeng.* **2011**, *108* (7), 1634–1642.

45. Young, E. W.; Wheeler, A. R.; Simmons, C. A., Matrix-dependent adhesion of vascular and valvular endothelial cells in microfluidic channels. *Lab. Chip.* **2007**, *7* (12), 1759–1766.

46. Patra, C.; Talukdar, S.; Novoyatleva, T.; Velagala, S. R.; Muhlfeld, C.; Kundu, B.; Kundu, S. C.; Engel, F. B., Silk protein fibroin from *Antheraea mylitta* for cardiac tissue engineering. *Biomaterials* **2012,** *33* (9), 2673–2680.

47. Yang, Y.; Chen, X.; Ding, F.; Zhang, P.; Liu, J.; Gu, X., Biocompatibility evaluation of silk fibroin with peripheral nerve tissues and cells *in vitro*. *Biomaterials* **2007,** *28* (9), 1643–1652.

48. Tang, X.; Ding, F.; Yang, Y.; Hu, N.; Wu, H.; Gu, X., Evaluation on *in vitro* biocompatibility of silk fibroin-based biomaterials with primarily cultured hippocampal neurons. *J. Biomed. Mater. Res. A* **2009,** *91* (1), 166–174.

49. Lecomte, A.; Degache, A.; Descamps, E.; Dahan, L.; Bergaud, C., *In vitro* and *in vivo* biostability assessment of chronically-implanted parylene C neural sensors. *Sens. Actuactors B Chem.* **2017**, *251* (Supplement C), 1001–1008.

50. Xue, C.; Ren, H.; Zhu, H.; Gu, X.; Guo, Q.; Zhou, Y.; Huang, J.; Wang, S.; Zha, G.; Gu, J.; Yang, Y.; Gu, Y.; Gu, X., Bone marrow mesenchymal stem cell-derived acellular matrix-coated chitosan/silk scaffolds for neural tissue regeneration. *J. Mater. Chem. B* **2017**, *5* (6), 1246–1257.

51. Gu, Y.; Zhu, J.; Xue, C.; Li, Z.; Ding, F.; Yang, Y.; Gu, X., Chitosan/silk fibroin-based, Schwann cell-derived extracellular matrix-modified scaffolds for bridging rat sciatic nerve gaps. *Biomaterials* **2014**, *35* (7), 2253–2263.

52. Teshima, T.; Nakashima, H.; Kasai, N.; Sasaki, S.; Tanaka, A.; Tsukada, S.; Sumitomo, K., Mobile silk fibroin electrode for manipulation and electrical stimulation of adherent cells. *Adv. Funct. Mater.* **2016**, *26* (45), 8185–8193.

53. Gupta, M. K.; Khokhar, S. K.; Phillips, D. M.; Sowards, L. A.; Drummy, L. F.; Kadakia, M. P.; Naik, R. R., Patterned silk films cast from ionic liquid solubilized fibroin as scaffolds for cell growth. *Langmuir* **2007**, *23* (3), 1315–1319.

54. Beh, W. S.; Kim, I. T.; Qin, D.; Xia, Y.; Whitesides, G. M., Formation of patterned microstructures of conducting polymers by soft lithography, and applications in microelectronic device fabrication. *Adv. Mater.* **1999**, *11* (12), 1038–1041.

55. Tan, F.; Walshe, P.; Viani, L.; Al-Rubeai, M., Surface biotechnology for refining cochlear implants. *Trends Biotechnol.* **2013**, *31* (12), 678–687.

56. Zhu, W.; O'Brien, C.; O'Brien, J. R.; Zhang, L. G., 3D nano/microfabrication techniques and nanobiomaterials for neural tissue regeneration. *Nanomedicine (Lond)* **2014**, *9* (6), 859–875.

57. Perry, H.; Gopinath, A.; Kaplan, D. L.; Dal Negro, L.; Omenetto, F. G., Nano- and Micropatterning of optically transparent, mechanically robust, biocompatible silk fibroin films. *Adv. Mater.* **2008**, *20* (16), 3070–3072.

58. Galeotti, F.; Andicsova, A.; Yunus, S.; Botta, C., Precise surface patterning of silk fibroin films by breath figures. *Soft Matter* **2012**, *8* (17), 4815–4821.

59. Landry, M. J.; Applegate, M. B.; Bushuyev, O. S.; Omenetto, F. G.; Kaplan, D. L.; Cronin-Golomb, M.; Barrett, C. J., Photo-induced structural modification of silk gels containing azobenzene side groups. *Soft Matter* **2017**, *13* (16), 2903–2906.

60. Hronik-Tupaj, M.; Raja, W. K.; Tang-Schomer, M.; Omenetto, F. G.; Kaplan, D. L., Neural responses to electrical stimulation on patterned silk films. *J. Biomed. Mater. Res. A* **2013**, *101* (9), 2559–2572.

61. Byette, F.; Bouchard, F.; Pellerin, C.; Paquin, J.; Marcotte, I.; Mateescu, M. A., Cell-culture compatible silk fibroin scaffolds concomitantly patterned by freezing conditions and salt concentration. *Polym. Bull.* **2011**, *67* (1), 159–175.

62. Lucido, A. L.; Suarez Sanchez, F.; Thostrup, P.; Kwiatkowski, A. V.; Leal-Ortiz, S.; Gopalakrishnan, G.; Liazoghli, D.; Belkaid, W.; Lennox, R. B.; Grutter, P.; Garner, C. C.; Colman, D. R., Rapid assembly of functional presynaptic boutons triggered by adhesive contacts. *J. Neurosci.* **2009**, *29* (40), 12449–12466.

63. Madduri, S.; Papaloizos, M.; Gander, B., Trophically and topographically functionalized silk fibroin nerve conduits for guided peripheral nerve regeneration. *Biomaterials* **2010**, *31* (8), 2323–2334.

64. Hopkins, A. M.; De Laporte, L.; Tortelli, F.; Spedden, E.; Staii, C.; Atherton, T. J.; Hubbell, J. A.; Kaplan, D. L., Silk hydrogels as soft substrates for neural tissue engineering. *Adv. Funct. Mater.* **2013**, *23* (41), 5140–5149.

65. Yao, M.; Zhou, Y.; Xue, C.; Ren, H.; Wang, S.; Zhu, H.; Gu, X.; Gu, X.; Gu, J., Repair of rat sciatic nerve defects by using allogeneic bone marrow mononuclear cells combined with chitosan/silk fibroin scaffold. *Cell Transplant.* **2016**, *25* (5), 983–993.

66. Bini, T. B.; Gao, S.; Xu, X.; Wang, S.; Ramakrishna, S.; Leong, K. W., Peripheral nerve regeneration by microbraided poly(L-lactide-co-glycolide) biodegradable polymer fibers. *J. Biomed. Mater. Res. A* **2004**, *68* (2), 286–295.

67. Ren, Y. J.; Zhou, Z. Y.; Liu, B. F.; Xu, Q. Y.; Cui, F. Z., Preparation and characterization of fibroin/hyaluronic acid composite scaffold. *Int. J. Biol. Macromol.* **2009**, *44* (4), 372–378.

68. Tanaka, K.; Sata, M.; Komuro, I.; Saotome, T.; Yamashita, Y.; Asakura, T., P5377 Biodegradable extremely small diameter vascular graft made of silk fibroin leads rapid vascular remodeling; a preliminary evaluation. *Eur. Heart J.* **2017**, *38*, 1137.

69. Cai, Z.-X.; Mo, X.-M.; Zhang, K.-H.; Fan, L.-P.; Yin, A.-L.; He, C.-L.; Wang, H.-S., Fabrication of chitosan/silk fibroin composite nanofibers for wound-dressing applications. *Int. J. Mol. Sci.* **2010**, *11* (9), 3529–3539.

70. Schnell, E.; Klinkhammer, K.; Balzer, S.; Brook, G.; Klee, D.; Dalton, P.; Mey, J., Guidance of glial cell migration and axonal growth on electrospun nanofibers of poly-ε-caprolactone and a collagen/poly-ε-caprolactone blend. *Biomaterials* **2007**, *28* (19), 3012–3025.

71. Wei, Y.; Gong, K.; Zheng, Z.; Wang, A.; Ao, Q.; Gong, Y.; Zhang, X., Chitosan/silk fibroin-based tissue-engineered graft seeded with adipose-derived stem cells enhances nerve regeneration in a rat model. *J. Mater. Sci. Mater. Med.* **2011**, *22* (8), 1947–1964.

72. Wang, C. Y.; Zhang, K. H.; Fan, C. Y.; Mo, X. M.; Ruan, H. J.; Li, F. F., Aligned natural-synthetic polyblend nanofibers for peripheral nerve regeneration. *Acta Biomater.* **2011,** *7* (2), 634–643.

73. Zhang, K.; Wang, H.; Huang, C.; Su, Y.; Mo, X.; Ikada, Y., Fabrication of silk fibroin blended P(LLA-CL) nanofibrous scaffolds for tissue engineering. *J. Biomed. Mater. Res. A* **2010**, *93* (3), 984–993.

74. Tang-Schomer, M. D.; White, J. D.; Tien, L. W.; Schmitt, L. I.; Valentin, T. M.; Graziano, D. J.; Hopkins, A. M.; Omenetto, F. G.; Haydon, P. G.; Kaplan, D. L., Bioengineered functional brain-like cortical tissue. *Proc. Natl. Acad. Sci. U.S.A.* **2014**, *111* (38), 13811–13816.

75. Ren, K.; Crouzier, T.; Roy, C.; Picart, C., Polyelectrolyte multilayer films of controlled stiffness modulate myoblast cells differentiation. *Adv. Funct. Mater.* **2008**, *18* (9), 1378–1389.

76. Decher, G.; Hong, J. D.; Schmitt, J., Buildup of ultrathin multilayer films by a self-assembly process: III. Consecutively alternating adsorption of anionic and cationic polyelectrolytes on charged surfaces. *Thin Solid Films* **1992**, *210*, 831–835.

77. Thebaud, N. B.; Bareille, R.; Daculsi, R.; Bourget, C.; Remy, M.; Kerdjoudj, H.; Menu, P.; Bordenave, L., Polyelectrolyte multilayer films allow seeded human progenitor-derived endothelial cells to remain functional under shear stress *in vitro*. *Acta Biomater.* **2010**, *6* (4), 1437–1445.

78. Richert, L.; Lavalle, P.; Vautier, D.; Senger, B.; Stoltz, J. F.; Schaaf, P.; Voegel, J. C.; Picart, C., Cell interactions with polyelectrolyte multilayer films. *Biomacromolecules* **2002**, *3* (6), 1170–1178.

79. Tsai, H. A.; Wu, R. R.; Lee, I. C.; Chang, H. Y.; Shen, C. N.; Chang, Y. C., Selection, enrichment, and maintenance of self-renewal liver stem/progenitor cells utilizing polypeptide polyelectrolyte multilayer films. *Biomacromolecules* **2010**, *11* (4), 994–1001.

80. Almodovar, J.; Bacon, S.; Gogolski, J.; Kisiday, J. D.; Kipper, M. J., Polysaccharide-based polyelectrolyte multilayer surface coatings can enhance mesenchymal stem cell response to adsorbed growth factors. *Biomacromolecules* **2010**, *11* (10), 2629–2639.

81. Jaklenec, A.; Anselmo, A. C.; Hong, J.; Vegas, A. J.; Kozminsky, M.; Langer, R.; Hammond, P. T.; Anderson, D. G., High throughput layer-by-layer films for extracting film forming parameters and modulating film interactions with cells. *ACS Appl. Mater. Interfaces* **2016**, *8* (3), 2255–2261.

82. Decher, G., Fuzzy nanoassemblies: toward layered polymeric multicomposites. *Science* **1997**, *277* (5330), 1232–1237.

83. Silva, J. M.; Reis, R. L.; Mano, J. F., Biomimetic extracellular environment based on natural origin polyelectrolyte multilayers. *Small* **2016**, *12* (32), 4308–4342.

84. Mendelsohn, J. D.; Yang, S. Y.; Hiller, J.; Hochbaum, A. I.; Rubner, M. F., Rational design of cytophilic and cytophobic polyelectrolyte multilayer thin films. *Biomacromolecules* **2003**, *4* (1), 96–106.

85. Wang, L.-M.; Chang, H.; Zhang, H.; Ren, K.-F.; Li, H.; Hu, M.; Li, B.-C.; Martins, M. C. L.; Barbosa, M. A.; Ji, J., Dynamic stiffness of polyelectrolyte multilayer films based on disulfide bonds for *in situ* control of cell adhesion. *J. Mater. Chem. B* **2015**, *3* (38), 7546–7553.

86. Thompson, M. T.; Berg, M. C.; Tobias, I. S.; Rubner, M. F.; Van Vliet, K. J., Tuning compliance of nanoscale polyelectrolyte multilayers to modulate cell adhesion. *Biomaterials* **2005**, *26* (34), 6836–6845.

87. Gribova, V.; Auzely-Velty, R.; Picart, C., Polyelectrolyte multilayer assemblies on materials surfaces: from cell adhesion to tissue engineering. *Chem. Mater.* **2012**, *24* (5), 854–869.

88. Borges, J.; Mano, J. F., Molecular interactions driving the layer-by-layer assembly of multilayers. *Chem. Rev.* **2014**, *114* (18), 8883–8942.

89. Sukhorukov, G. B.; Antipov, A. A.; Voigt, A.; Donath, E.; Möhwald, H., pH-controlled macromolecule encapsulation in and release from polyelectrolyte multilayer nanocapsules. *Macromol. Rapid Commun.* **2001**, *22* (1), 44–46.

90. Ai, H.; Jones, S. A.; Lvov, Y. M., Biomedical applications of electrostatic layer-by-layer nano-assembly of polymers, enzymes, and nanoparticles. *Cell Biochem. Biophys.* **2003**, *39* (1), 23–43.

91. Choy, K. L.; Schnabelrauch, M.; Wyrwa, R., Bioactive coatings, in *Biomaterials in clinical practice: advances in clinical research and medical devices*, Zivic, F.; Affatato, S.; Trajanovic, M.; Schnabelrauch, M.; Grujovic, N.; Choy, K. L., Eds. Springer International Publishing: Cham, Switzerland, **2018**; pp 361–406.

92. Mermut, O.; Barrett, C. J., Effects of charge density and counterions on the assembly of polyelectrolyte multilayers. *J. Phys. Chem. B* **2003**, *107* (11), 2525–2530.

93. Burke, S. E.; Barrett, C. J., Acid−base equilibria of weak polyelectrolytes in multilayer thin films. *Langmuir* **2003**, *19* (8), 3297–3303.

94. Reyes, D. R.; Perruccio, E. M.; Becerra, S. P.; Locascio, L. E.; Gaitan, M., Micropatterning neuronal cells on polyelectrolyte multilayers. *Langmuir* **2004**, *20* (20), 8805–8811.

95. Zhou, K.; Sun, G. Z.; Bernard, C. C.; Thouas, G. A.; Nisbet, D. R.; Forsythe, J. S., Optimizing interfacial features to regulate neural progenitor cells using polyelectrolyte multilayers and brain derived neurotrophic factor. *Biointerphases* **2011**, *6* (4), 189–199.

96. Delcea, M.; Mohwald, H.; Skirtach, A. G., Stimuli-responsive LbL capsules and nanoshells for drug delivery. *Adv. Drug Deliv. Rev.* **2011**, *63* (9), 730–747.

97. Luna-Acosta, J. L.; Alba-Betancourt, C.; Martínez-Moreno, C. G.; Ramírez, C.; Carranza, M.; Luna, M.; Arámburo, C., Direct antiapoptotic effects of growth hormone are mediated by PI3K/Akt pathway in the chicken bursa of Fabricius. *Gen. Comp. Endocrinol.* **2015**, *224* (Supplement C), 148–159.

98. Milkova, V.; Radeva, T., Influence of charge density and calcium salt on stiffness of polysaccharides multilayer film. *Colloids Surf. A Physicochem. Eng. Asp.* **2015**, *481* (Supplement C), 13–19.

99. Vodouhê, C.; Schmittbuhl, M.; Boulmedais, F.; Bagnard, D.; Vautier, D.; Schaaf, P.; Egles, C.; Voegel, J.-C.; Ogier, J., Effect of functionalization of multilayered polyelectrolyte films on motoneuron growth. *Biomaterials* **2005**, *26* (5), 545–554.

100. Lee, I. C.; Wu, Y. C., Assembly of polyelectrolyte multilayer films on supported lipid bilayers to induce neural stem/progenitor cell differentiation into functional neurons. *ACS Appl. Mater. Interfaces* **2014**, *6* (16), 14439–14450.

101. Gheith, M. K.; Sinani, V. A.; Wicksted, J. P.; Matts, R. L.; Kotov, N. A., Single-walled carbon nanotube polyelectrolyte multilayers and freestanding films as a biocompatible platform for neuroprosthetic implants. *Adv. Mater.* **2005**, *17* (22), 2663–2670.

102. Dierich, A.; Le Guen, E.; Messaddeq, N.; Stoltz, J. F.; Netter, P.; Schaaf, P.; Voegel, J. C.; Benkirane-Jessel, N., Bone formation mediated by synergy-acting growth factors embedded in a polyelectrolyte multilayer film. *Adv. Mater.* **2007**, *19* (5), 693–697.

103. Ren, Y. J.; Zhang, H.; Huang, H.; Wang, X. M.; Zhou, Z. Y.; Cui, F. Z.; An, Y. H., *In vitro* behavior of neural stem cells in response to different chemical functional groups. *Biomaterials* **2009**, *30* (6), 1036–1044.

104. Nolte, A. J.; Cohen, R. E.; Rubner, M. F., A two-plate buckling technique for thin film modulus measurements: applications to polyelectrolyte multilayers. *Macromolecules* **2006**, *39* (14), 4841–4847.

105. Yu, L. M. Y.; Leipzig, N. D.; Shoichet, M. S., Promoting neuron adhesion and growth-Review. *Mater. Today* **2008**, *11* (5), 36–43.

106. Schneider, A.; Francius, G.; Obeid, R.; Schwinte, P.; Hemmerle, J.; Frisch, B.; Schaaf, P.; Voegel, J. C.; Senger, B.; Picart, C., Polyelectrolyte multilayers with a tunable Young's modulus: influence of film stiffness on cell adhesion. *Langmuir* **2006**, *22* (3), 1193–1200.

107. He, W.; Bellamkonda, R. V., Nanoscale neuro-integrative coatings for neural implants. *Biomaterials* **2005**, *26* (16), 2983–2990.

108. Jan, E.; Hendricks, J. L.; Husaini, V.; Richardson-Burns, S. M.; Sereno, A.; Martin, D. C.; Kotov, N. A., Layered carbon nanotube-polyelectrolyte electrodes outperform traditional neural interface materials. *Nano Lett.* **2009**, *9* (12), 4012–4018.

109. Kidambi, S.; Lee, I.; Chan, C., Primary neuron/astrocyte co-culture on polyelectrolyte multilayer films: a template for studying astrocyte-mediated oxidative stress in neurons. *Adv. Funct. Mater.* **2008**, *18* (2), 294–301.

110. Chluba, J.; Voegel, J.-C.; Decher, G.; Erbacher, P.; Schaaf, P.; Ogier, J., Peptide hormone covalently bound to polyelectrolytes and embedded into multilayer architectures conserving full biological activity. *Biomacromolecules* **2001**, *2* (3), 800–805.

111. Schmidt, D. J.; Moskowitz, J. S.; Hammond, P. T., Electrically triggered release of a small molecule drug from a polyelectrolyte multilayer coating. *Chem. Mater.* **2010**, *22* (23), 6416–6425.

112. Lei, K. F.; Lee, I. C.; Liu, Y. C.; Wu, Y. C., Successful differentiation of neural stem/progenitor cells cultured on electrically adjustable indium tin oxide (ITO) surface. *Langmuir* **2014**, *30* (47), 14241–14249.

113. Zhou, K.; Thouas, G. A.; Bernard, C. C.; Nisbet, D. R.; Finkelstein, D. I.; Li, D.; Forsythe, J. S., Method to impart electro- and biofunctionality to neural scaffolds using graphene-polyelectrolyte multilayers. *ACS Appl. Mater. Interfaces* **2012**, *4* (9), 4524–4531.

114. Cavelier, S.; Barrett, C. J.; Barthelat, F., The mechanical performance of a biomimetic nanointerface made of multilayered polyelectrolytes. *Eur. J. Inorg. Chem.* **2012**, *2012* (32), 5380–5389.

115. Mermut, O.; Lefebvre, J.; Gray, D. G.; Barrett, C. J., Structural and mechanical properties of polyelectrolyte multilayer films studied by AFM. *Macromolecules* **2003**, *36* (23), 8819–8824.

116. Burke, S. E.; Barrett, C. J., pH-responsive properties of multilayered poly(L-lysine)/hyaluronic acid surfaces. *Biomacromolecules* **2003**, *4* (6), 1773–1783.

117. Burke, S. E.; Barrett, C. J., Controlling the physicochemical properties of weak polyelectrolyte multilayer films through acid/base equilibria. *Pure Appl. Chem.* **2004**, *76* (7-8), 1387–1398.

118. Rodriguez, L.; De Paul, S.; Barrett, C. J.; Reven, L.; Spiess, H. W., Fast magic-angle spinning and double-quantum ^{1}H solid-state NMR spectroscopy of polyelectrolyte multilayers. *Adv. Mater.* **2000**, *12* (24), 1934–1938.

119. McCormick, M.; Smith, R.; Graf, R.; Barrett, C. J.; Reven, L.; Spiess, H. W., NMR studies of the effect of adsorbed water on polyelectrolyte multilayer films in the solid state. *Macromolecules* **2003**, *36* (10), 3616–3625.

120. Tanchak, O. M.; Barrett, C. J., Swelling dynamics of multilayer films of weak polyelectrolytes. *Chem. Mater.* **2004**, *16* (14), 2734–2739.

121. Burke, S. E.; Barrett, C. J., Swelling behavior of hyaluronic acid/polyallylamine hydrochloride multilayer films. *Biomacromolecules* **2005**, *6* (3), 1419–1428.

122. Harroun, T.; Fritzsche, H.; Watson, M.; Yager, K.; Tanchak, O.; Barrett, C. J.; Katsaras, J., Variable temperature, relative humidity (0%–100%), and liquid neutron reflectometry sample cell suitable for polymeric and biomimetic materials. *Rev. Sci. Instrum.* **2005**, *76* (6), 065101.

123. Tanchak, O. M.; Yager, K. G.; Fritzsche, H.; Harroun, T.; Katsaras, J.; Barrett, C. J., Ion distribution in multilayers of weak polyelectrolytes: A neutron reflectometry study. *J. Chem. Phys.* **2008**, *129* (8), 084901.

124. Ahmed, N. M.; Barrett, C. J., Novel azo chromophore-containing polymers: synthesis and characterization. *Polym. Mater. Sci. Eng.* **2001**, *85*, 607–608.

125. Schoelch, S.; Vapaavuori, J.; Rollet, F. G.; Barrett, C. J., The orange side of disperse red 1: humidity-driven color switching in supramolecular azo-polymer materials based on reversible dye aggregation. *Macromol. Rapid Commun.* **2017**, *38* (1), 1600582.

126. Goulet-Hanssens, A.; Barrett, C. J., Photo-control of biological systems with azobenzene polymers. *J. Polym. Sci. A* **2013**, *51* (14), 3058–3070.

127. Goulet-Hanssens, A.; Lai Wing Sun, K.; Kennedy, T. E.; Barrett, C. J., Photoreversible surfaces to regulate cell adhesion. *Biomacromolecules* **2012**, *13* (9), 2958–2963.

128. Fernandez, R.; Ocando, C.; Fernandes, S. C.; Eceiza, A.; Tercjak, A., Optically active multilayer films based on chitosan and an azopolymer. *Biomacromolecules* **2014**, *15* (4), 1399–1407.

129. Sailer, M.; Fernandez, R.; Lu, X.; Barrett, C. J., High levels of molecular orientation of surface azo chromophores can be optically induced even in a wet biological environment. *Phys. Chem. Chem. Phys.* **2013**, *15* (46), 19985–19989.

130. Murphy, A. R.; St John, P.; Kaplan, D. L., Modification of silk fibroin using diazonium coupling chemistry and the effects on hMSC proliferation and differentiation. *Biomaterials* **2008**, *29* (19), 2829–2838.

Rationale for Chapter 2: Polyelectrolyte multilayers promote superior growth of rodent neural cells

Polyelectrolyte multilayers have been previously investigated as a support for cell growth, yet a broader investigation of the precise physical properties of such materials which are conducive to neural compatibility and augmented growth are currently still under investigation. Within the introduction of this thesis a set of guiding principles for creating effective extracellular matrix-mimicking materials was constructed. The idea of 'biocamouflaging', matching biochemical and biophysical properties of polymers to their native tissue-specific environment, was also investigated in detail. In the introduction, silk materials as well as layer-by-layer deposited materials were highlighted, and the materials' properties which create superior neurophilic coatings and scaffolds were elucidated. Within Chapter 2, we explore the use of layer-by-layer deposited synthetic polymers and natural polymers along with their optimized and characterized properties. We employ imaging quantification and film characterization to determine which polyelectrolyte polymers hold promise to create effective replacements for the unstable and easily degradable standards currently in use. The prepared manuscript 'Polyelectrolyte multilayers promote superior growth of rodent neural cells', was co-authored by Michael J. Landry, Kaien Gu, Stephanie N. Harris, Laila Al Alwan, Laura Gutsin, Daniele de Biasio, Bernie Jiang, Diane S. Nakamura, Dr. T. Christopher Corkery, Prof. Timothy E. Kennedy, and Prof. Christopher J. Barrett, and provides a means to quantify the best supportive materials we created and rationalized their performance using modulus measurements.

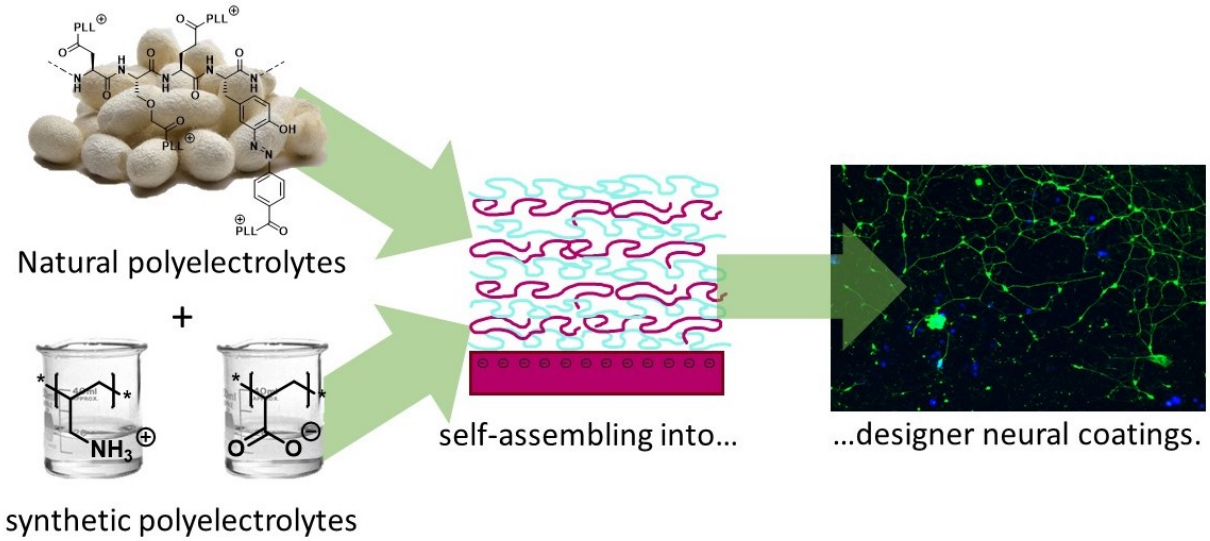

Chapter 2: Polyelectrolyte multilayers promote neural cell growth and survival

Chapter 2 is based on a manuscript entitled 'Polyelectrolyte multilayers promote neural cell growth and survival', and was co-authored by: Michael J. Landry, Kaien Gu, Stephanie N. Harris, Laila Al Alwan, Laura Gutsin, Daniele de Biasio, Bernie Jiang, Diane S. Nakamura, Dr. T. Christopher Corkery, Prof. Timothy E. Kennedy, and Prof. Christopher J. Barrett.

2.1 Abstract

Poly-D-lysine (PDL) and poly-L-lysine (PLL) are standard surfaces for culturing neural cells; however, both are relatively unstable, costly, and the coated surface typically must be prepared immediately before use. Here, we employ polyelectrolyte multilayers (PEMs) as highly stable, relatively inexpensive, alternative substrates to support primary neural cell culture. Initial findings identified specific silk-based PEMs that significantly outperform the capacity of PDL to promote neuronal survival and process extension. Based on these results, we generated a library of PEM variants, including commercial and bio-sourced polyelectrolytes, and identified three that substantially outperform PDL as a substrate for primary neurons in cell culture: PLL/poly(acrylic acid)-co-DR1A, silk fibroin-poly-L-lysine/silk fibroin-poly-D-glutamic acid, and silk fibroin-poly-L-lysine/poly(acrylic acid)-co-DR1A. Further, testing these PEM variants as substrates for primary oligodendrocyte progenitors demonstrated that silk fibroin-poly-L-lysine/poly(acrylic acid)-co-DR1A functioned significantly better than PDL. These findings reveal specificity of cellular responses, indicating that PEMs may be tuned to optimally support different cell types. PEMs are relatively inexpensive, highly stable, proteolysis resistant surfaces that may be prepared in advance in bulk and employed as an effective substrate for efficient long-term maintenance of primary neural cells in culture.

2.2 Introduction

Precise conditions of temperature, humidity, and nutrition are essential for successful cell culture, along with adequate mechanical support. The physical properties of a cellular support material are critical, as cells and tissues are sensitive to the modulus of the surface on which they are cultivated.[1-4] Therefore, controlling the surface properties of a cell culture substrate, such as surface energy and Young's modulus, impacts cell survival and development. Some cells are more difficult to maintain and grow in cell culture than others, with mammalian primary neural cells

being particularly challenging. These include neurons and oligodendrocytes, which are neural cell types directly associated with neurodegenerative disorders such as Alzheimer's and Parkinson's diseases, and multiple sclerosis.[5] The study of neurodegenerative disorders will be facilitated by an *in vitro* environment that closely mimics the *in vivo* conditions found within tissue, to provide an optimal platform for testing potential therapeutics. Currently, only a small set of substrate surfaces are typically employed to culture primary neural cells.

A typical 'state of the art' culture substrate for primary neural cells is produced by first cleaning a glass surface, and then applying a single layer of poly-D-lysine (PDL) prior to plating the cells. These layers are not robust, can be damaged by drying or UV, are ultimately degraded by proteolysis, and are not stable in long-term storage. They must, therefore, be prepared immediately prior to plating the cells onto the surface. PLL and its 'mirror twin' PDL are widely used as standard surfaces to culture neural cells.[6-7] These polypeptide substrates are thought to function as non-specific attachment factors for cells, driven by electrostatic attraction between the positively charged lysine groups and the electronegative phospholipid bilayer of the plasma membrane.[8-9] These electrostatic interactions are strong attractive force between oppositely charged molecules. The strength of this phenomenon diminishes quickly ($1/r^2$) with respect to distance from the charged surface. Thus, these interactions are optimal for assembling multilayered structures composed of positively and negatively charged polymers; however, long range effects from charge are not seen.[9]

There is an opportunity to create improved substrates to: (1) better support the growth of neural cells, (2) to improve experimental reproducibility, and (3) facilitate easy neural cell cultivation. An ideal system would use inexpensive, degradation-resistant substrates that are easy to process. Peptides present one class of options, yet protein-decorated surfaces are expensive to produce and suffer from the same degradation limitations as poly-lysine. Previous studies have revealed that materials of relatively low modulus and high-water content perform significantly better as cell culture substrates, and that there is a 'Goldilocks' zone that best promotes cell survival.[10-11] One method that allows for tailoring of both modulus and water content of polymer coatings is by using a layer-by-layer (LbL) approach to create polyelectrolyte multilayers (PEMs) from charged polyelectrolytes.[12]

PEMs are films fabricated from polyelectrolytes (PEs), water-soluble polymers that contain a significant proportion of ionizable groups, and are assembled using a LbL method.[13-14] PEs can either be polyanionic or polycationic, and their degree of ionization is controlled by pH. PEM deposition can be used to build up self-assembled polymer coatings onto substrates through electrostatic interactions by alternating polyanionic and polycationic polymers. (**Figure 2.1**, top). Since being developed in the 1990s, PEMs have been used in areas such as macromolecular encapsulation,[15-18] drug delivery,[19-20] and biocompatible coatings for artificial implants.[21-22] Much recent work has aimed to use PEMs as a 'biocamouflage' coating between biological cells or tissues and engineered materials. Modulation of PEM fabrication conditions, such as deposition pH and choice of PEs, dramatically affects the resulting mechanical properties of the created PEM.[23] Previous work has investigated cellular adhesion, proliferation, and differentiation of neural stem and progenitor cells, and subtypes of neural lineages (i.e. neurons, astrocytes and oligodendrocytes) by tuning the Young's modulus.[24-25]

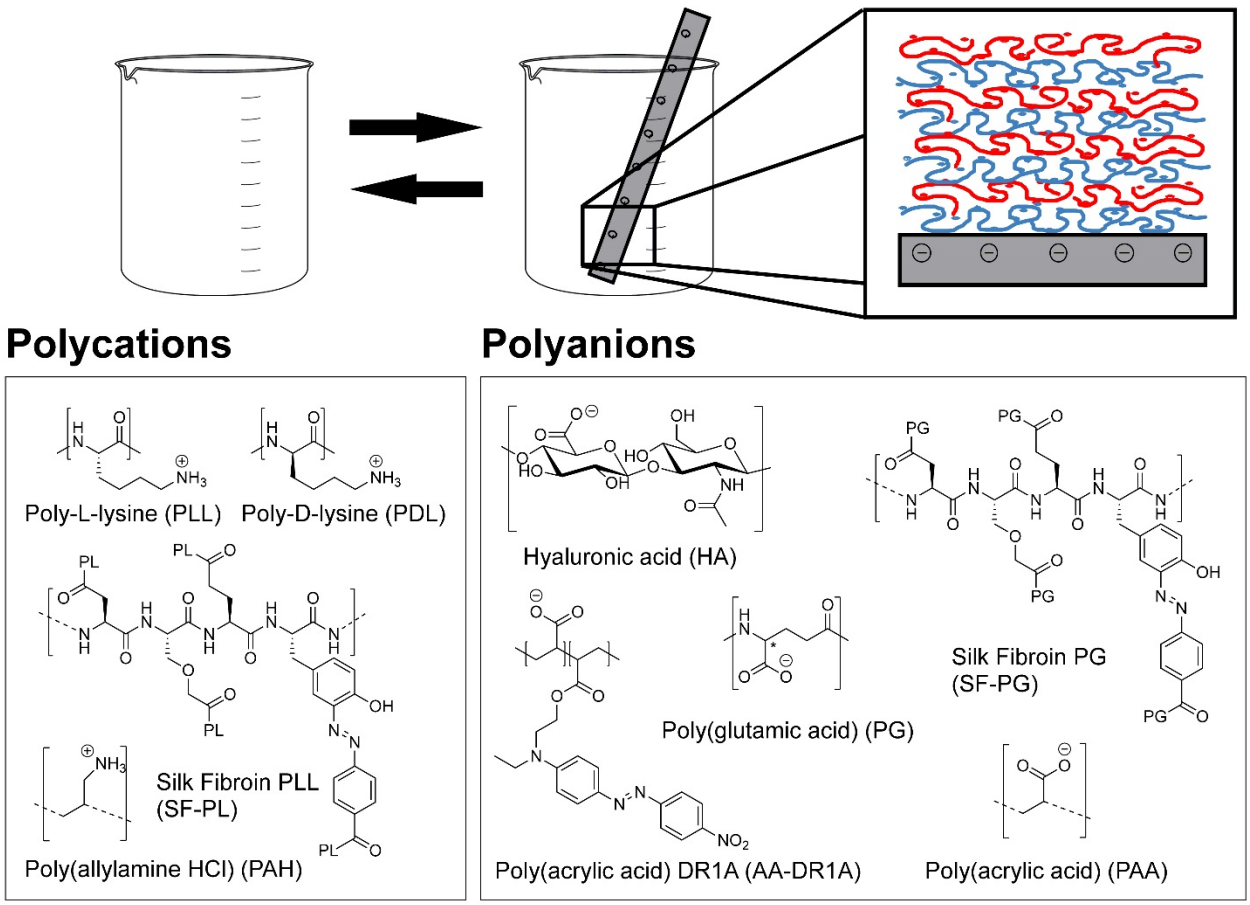

Figure 2.1. (Top) Schematic depicting layer-by-layer assembly of PEM films, beginning with a negatively charged substrate (glass or silicon) being dipped in a polycation solution. (Bottom) Illustration of biologically relevant polycationic and polyanionic polymers used in this study and their acronyms.

While PEMs have enjoyed a long history as coatings for biomedical applications,[26] substantially less work has been conducted with neural cells from the central nervous system (CNS). Previous work attempted to use PEMs as a platform for neural cell proliferation and differentiation.[27-29] Zhou *et al* used a LbL assembled film of poly-ε-caprolactone, PLL, and heparin sulfates with the aim of increasing attachment, differentiation and neurite outgrowth from neural progenitor cells (NPCs).[27-28] Ren and colleagues studied the contribution of surface effects from chemically distinct polymers on the differentiation and migration behavior of neural stem cells.[30-31] Sailor *et al* developed methodologies to create 2-D polyacrylic acid (PAA) and poly(allylamine hydrochloride (PAH) gradient films. These gradient films present the equivalent of over 10 000

single film experiments as one gradient surface and were used to determine the optimal assembly conditions for substrates that support the growth of HEK293 cells and embryonic rat spinal commissural neurons.[10-11]

Here, we assessed PEM surfaces as substrates for neural cell growth, aiming to identify substrates that are more stable and robust than PDL. We employed a set of guiding principles that aim to effectively 'biocamouflage' less-than-optimal surfaces and create materials that are soft, wet and 'ECM-like' using a LbL approach. We evaluated the capacity of a catalogue of PEMs to support neural growth and survival while rationalizing performance using the physico-mechanical properties of the different substrates. Our findings identify PEMs that exhibit enhanced neural biocompatibility and function as a highly effective substrate to cultivate primary neural cells.

2.3 Materials and methods

2.3.1 Materials

All polymers, reagents and salts used in the fabrication of PEM films were purchased from Sigma-Aldrich. Silk fibroin with appended polyglutamate (SF-PG) and silk fibroin with appended poly-L-lysine (SF-PL) were synthesized as described,[32] with some modifications (**Section 2.2.3)**. Silk fibroin for these procedures was provided by Tajima Shoji LTD (Yokohama, Japan). Polyacrylic acid-co-DR1A (19:1) (AA-DR1A) was prepared by as described.[33] 24-well glass bottom plates were purchased from Greiner Bio-One (Monroe, US).

2.3.2 Equipment, instrumentation and software

Distilled water was purified by a Milli-Q purification system (Millipore, Billerica, US) for the preparation of all solutions. The pH of all solutions was measured using a SympHony B10P pH meter with an immersion probe and a KI electrolyte solution (VWR, Radnor, US). Film thickness was measured using a M-033K001 Optrel Multiskop ellipsometer (Sinzing, DE). Glass coverslip substrates were cleaned using a plasma cleaner (Harrick Plasma, Ithaca, US) prior to PEM deposition. Images were acquired using an Axiovert 100 inverted fluorescence microscope (Carl Zeiss Canada, Toronto, CA) with a MagnaFire CCD camera and MagnaFire 4.1C imaging software (Optronics, Goleta, US). Images were further processed using ImageJ 2.0 (Open-Source, Madison, USA) and CellProfiler Version 2.0 (Open-Source, Cambridge, USA) for cell counting.

2.3.3 **Silk fibroin-co-poly-L-glutamate and silk fibroin-co-poly-L-lysine synthesis**

Methods for the preparation of silk solutions from *Bombyx mori* silkworm cocoons were based on protocols from Rockwood *et al*.[34] Both SF-PG and SF-PL were synthesized as previously described[32] with some modifications. To a vial equipped with a stir bar, 1.25 mL of a 0.2 M 4-aminobenzoic acid solution (in acetonitrile) was added along with 625 µL of a 1.6 M p-toluene sulfonic acid aqueous solution. The resulting solution was cooled to 5 °C in an ice bath. 625 µL of a 0.2 M $NaNO_2$ aqueous solution was added to the cooled flask dropwise which produced a bright yellow diazonium salt solution. The solution was stirred for 25 min on ice. 2 mL of a 5% w/v silk solution and 0.25 mL of a 1 M boric acid/sodium borate buffer solution was added to a separate vial, mixed, and cooled to 5 °C. The silk solution was adjusted to pH 9 and 0.5 mL of the diazonium salt solution was added dropwise over 2 min. This addition produced a bright red solution that was stirred for 30 min on ice. The red, azobenzene-modified silk solution was purified using desalinating columns (NAP-25, VWR International) with distilled water as the eluent.

Once the azobenzene-modified silk solution was purified, enough chloroacetic acid was added to produce a 1.0 M solution (roughly 1.2 mL). Immediately after the addition, a white precipitate formed, that slowly dissolved back into solution with additional stirring. The solution was stirred for 1 h at room temperature and produced a hazy orange colored solution. The resulting solution was loaded into a Slide-A-Lyzer® dialysis cassette (3500 MW, 3-12 mL) and was dialyzed against water for 72 h (the water was changed 3 times).

The resulting solution was divided into two batches; one for producing SF-PL, and one for producing SF-PG. Roughly 3 mL of the mother solution was added to each 8 dram vial and stirred. 0.502 g of PDL was added to one vial and 0.532 g of PG was added to the other. The pH of the resulting solutions was adjusted to 6 using dilute HCl and 60 mg of EDC (1-ethyl-3-(3-dimethylaminopropyl)carbodiimide) added to both vials and stirred at rt for 8 h. After the reaction was completed, the resulting polymer solution was dialyzed against water for 72 hrs and the water was changed twice. The solution was diluted to 0.5 mg/mL for use in PEM fabrication. NMR of the final product was taken by adding 10% deuterated water and adding an insert of deuterated benzene. NMR signals corresponded to literature values.[23] SF-PL: ^{1}H NMR (300 MHz, 10% D_2O, Benzene-d6 insert): δ 0.71 (br, Val), 1.25−1.31 (m, Lys), 1.55 (m, Lys/Lys), 2.84 (m,br, Lys), 3.55 (s, -CH_2-COO), 3.73 (m, Ser/Gly), 4.15 (m, Lys), 6.81−7.05 (m,trace, Tyr + Azo). SF-PG:

^{1}H NMR (300 MHz, 10% D_2O, Benzene-d6 insert): δ 0.71 (br, Val), 1.21 (br, Ala), 1.52−2.05 (m, Glu), 2.13 (m, Glu), 3.55 (s, -CH_2-COO), 3.78 (m, Ser/Gly), 4.16 (m, Glu), 6.81−7.07 (m,trace, Tyr + Azo).

2.3.4 **PEM fabrication**

Polyelectrolyte solutions were prepared at a concentration of 0.5 mg/mL using Milli-Q deionized water. The pH of the deposition solution was adjusted to the desired value using 1 M NaOH or 1 M HCl solutions. Each surface was cleaned with a plasma cleaner prior to use. 1 mL of the positive PE solution was placed onto the surface of choice and allowed to self-assemble into a layer for 10 min. The positive PE solution was then removed with a pipette, and the surface was washed three times (3 x 1 mL) with deionized water. Filtered air was used to dry the surface prior to the deposition of the negative PE solution onto the surface for 10 min. The negative PE solution was then removed with a pipette and the surface washed in the same manner as with the positive PE solution. This procedure was repeated until the desired number of layers was built up.

2.3.5 **Ellipsometry measurement**

The thickness of fabricated PEM surfaces was measured using a single wavelength (633 nm, non-absorbing) null-ellipsometer (Optrel Multiskop, Germany) using a fixed angle of 70˚ (140˚ between source and detector). Measurements were performed on dried samples, using a model that had 2 layers on silicon (n = 3.42, k = -0.011): silicon dioxide (t = 2.3 nm, n = 1.54), and an unknown polymer layer (t = x, n = y), under air (n = 1.00). The model was fit assuming the refractive index of the PEM was the average of the two polymers separately and was used as a starting point for data fitting. **Table A1.1** shows the combinations of averaged film thicknesses, and each noted thickness was calculated from a series of three measurements from three prepared samples.

2.3.6 **Neural cell culture**

Oligodendroglial and cortical neuronal cell cultures were derived from Sprague-Dawley® rats (Charles River, Senneville, CA). All procedures were performed in accordance with the Canadian Council on Animal Care guidelines for the use of animals in research and approved by the Montreal Neurological Institute Animal Care Committee and the McGill Animal Compliance Office. Embryonic rat cortical neurons were obtained by dissection of embryonic day 16-17

(E16/17) Sprague-Dawley® rat brain (Charles River, Senneville, CA) as previously described.[35] Prepared 24-well plates were irradiated for 20 min to ensure sterility of the surfaces. Neurons were plated at a density of 50 000 cells per well. Cultures were maintained for 14 days in Neurobasal medium containing 1% B27 (Life Technologies, Carlsbad, US), 1% penicillin/streptomycin (Life Technologies), 0.5% N-2 supplement (Life Technologies), 0.25% GLUTAmax™ (Life Technologies,), and 0.2% Fungizone® antimycotic (Life Technologies) in a 37°C incubator with 5% carbon dioxide (Thermo Fisher Scientific).

Oligodendrocyte precursor cells were obtained from mixed glial cultures derived from postnatal day 0 (P0) rat pups and grown in oligodendrocyte defined medium (OLDEM) as described[36-37] with 0.1% fetal bovine serum (FBS) included to initiate differentiation. Oligodendrocytes were plated at a density of 40 000 cells per well. Cells were fixed by immersion in a 4% solution of paraformaldehyde (PFA) (Thermo Fisher Scientific, Waltham, US) in phosphate buffered saline (PBS) for 20 min. PFA was removed, and the surfaces washed twice for 10 min with PBS. Blocking was then performed for 1 hr using a solution of 0.25% Triton X-100 (Thermo Fisher Scientific) and 3% horse serum (HS) (Life Technologies) in PBS. Secondary antibody was prepared using Alexa Fluor® Phalloidin 488 (Life Technologies) at a concentration of 1:1000 and Hoescht 33258 (Life Technologies) at a concentration of 1:3000 in PBS with 1% HS. The secondary antibody was incubated for 2 hrs, and surfaces washed 3 times for 10 min with PBS. Surfaces were then immersed in PBS in preparation for imaging.

2.3.7 **Image processing**

Cells were imaged using an Axiovert 100 inverted fluorescence microscope (Carl Zeiss Canada, Toronto, CA) with a Magnafire CCD camera and MagnaFire 4.1C imaging software (Optronics, Goleta, US). To assess the effectiveness of each multilayer system, cells were stained with Hoechst 33258 (nuclear stain) and with Alexa Fluor® Phalloidin 488 labelling of F-actin and quantified using Cell Profiler™ (Broad Institute, Cambridge, US) and Fiji version 1.0.[38] A series of 6 micrographs were taken from each well to ensure each studied surface was captured effectivity, by an individual blind to the experimental conditions. Two characteristics of each image were assessed: the average number of adherent cells (Hoechst 33258) and total surface area of the cell body including processes (Alexa Fluor® Phalloidin 488). Both values were calculated using the Cell Profiler™ application. To standardize, the number of nuclei and surface area were

tabulated from each image and averages calculated per condition. This average was calculated for each surface condition and compared against a control of PDL. Each condition was replicated three times to ensure reproducibility. Statistical analyses, such as analysis of variance (ANOVA, least significant difference), were performed using SPSS 21 (IBM, Armonk, US).

2.4 Results and discussion

2.4.1 Initial PEM screening

To identify PEMs that support neural cell attachment and survival, we began with the results of previous studies of gradient PAH/PAA systems and the best conditions identified from combinatorial pH assays of HEK293 cells and rat spinal commissural neurons.[10-11] Due to the documented effectiveness of SF as an artificial ECM, we included two silk PEs: silk fibroin-co-poly-L-lysine (SF-PL) and silk fibroin-co-poly-L-glutamate (SF-PG). These specialized silk polymers were synthesized following published protocols with some modifications (see **Section 2.2.3**). All PEMs were assembled on plasma cleaned coverslips (see **Section 2.2.4**) to a thickness of 10 bilayers. Embryonic rat cortical neurons were cultured on each condition. Based on the gradient PAH/PAA films, the pH of deposition for PAH was chosen to be 5.5, and the pH of PAA was varied (5.0, 5.5, and 6.0). The deposition pH changes the charge density along each PE and alters the layer thickness by limiting attachment points to the surface (effecting how 'loopy' each layer becomes). At the pKa of a PE, half of the possible ionizable groups on a PE are charged. For PAA, the pKa is roughly 5.5 so pH values of deposition below 5.5 will make the polyanion less charged (longer loop length) and pH values above the pKa will make PAA more negatively charged (shorter loop length).[11] The degree of charge along the backbone, and thus the loop length, influences modulus, thickness and water content, which are key properties governing the capacity of these surfaces to support cell survival and growth.[39-40] We varied the PAA deposition pH and examined the resultant capacity of the surfaces to support neuronal viability. For the silk polymers, the deposition pH was set to 7.4 based on previous investigation of PDL/PG multilayers.[32] Neurons were cultured for 6 days before being fixed and stained with Alexa Fluor® 488 Phalloidin to visualize F-actin and Hoechst 33258 to label nuclei. **Figure 2.2** illustrates neurons grown on each PEM compared to the control (PDL) and a blank coverslip. Based on qualitative assessment, films created using a PAA deposition pH of 5.0 exhibited poor growth and attachment, while higher cell density and networks of neurites were present for substrates assembled using a PAA deposition pH of 5.5 and 6.0 (**Figure 2.2 A-C**). To quantify the number of cells present, Hoechst 33258

stained nuclei were imaged and counted using Cell profiler™ software. This assay was used as a rapid screen for the capacity of a surface to promote cell attachment and survival. In the PAH/PAA pH study, cell survival and attachment decreased on films constructed with a PAA deposition pH of 5.0. Films generated with PAA deposition pHs of 5.5 and 6.0 were not significantly different from each other or the control (**Figure 2.2 G**). Compared to the control, films constructed with pH values of 5.5 and pH 6.0 PAA deposition conditions were not significantly different in their capacity to support cell attachment and survival than PDL (ns). From previous work, we discovered that films assembled with a deposition pH corresponding to that of the PE's pKa supported maximum cellular survival and attachment. SF-PL/SF-PG performed similarly to the control condition (PDL, ns). All conditions promoted cell attachment and survival better than an uncoated glass substrate ($P < 0.01$). This screen optimized the deposition pH and identified several materials that perform as least as well as PDL.

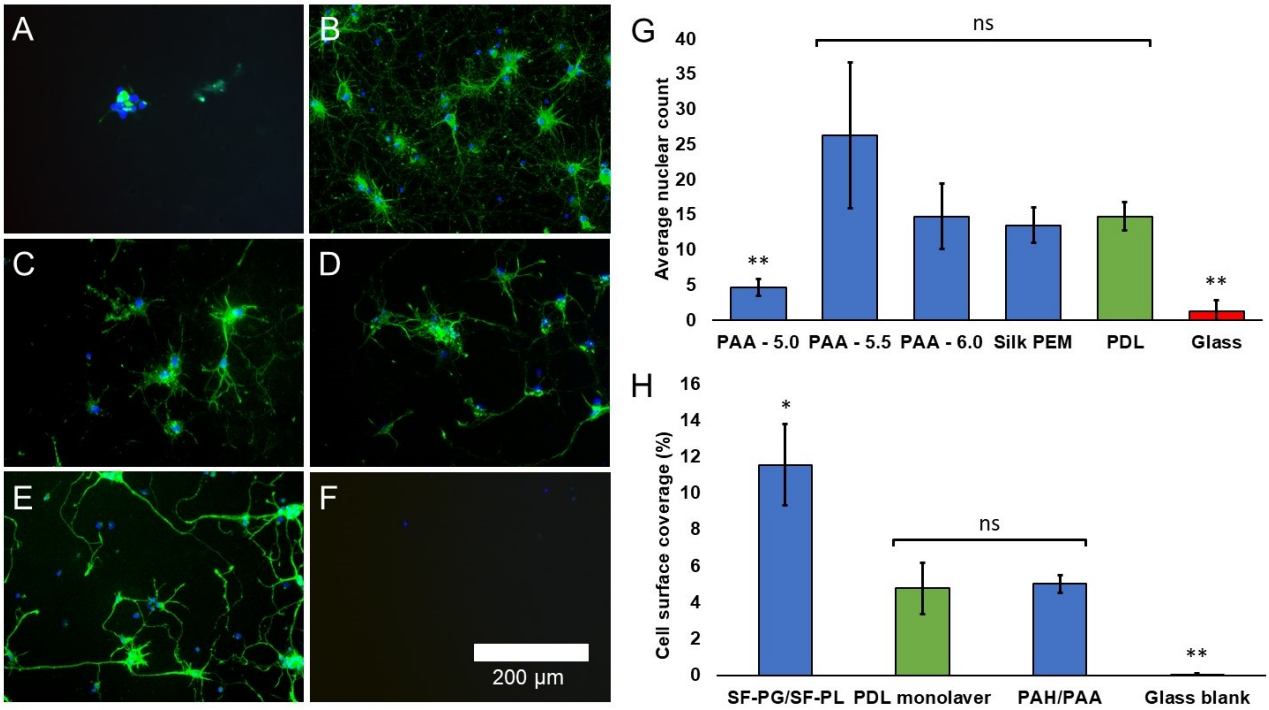

Figure 2.2. Assessing the survival (nuclei count) and growth (cell surface coverage) of the PAH/PAA and silk PEMs. Both materials perform competitively with PDL when quantifying nuclei count and cell surface coverage. All PEMs were 10 bilayers thick. **(A-F)** Images of various PEM conditions. Cells were stained with Hoechst 33258 (blue) to label nuclei and phalloidin Alexa Fluor® 488 (green) to label F-actin. PEM conditions tested were: **(A)** PAH/PAA with PAA at pH 5.0, **(B)** PAH/PAA with PAA at pH 5.5, **(C)** PAH/PAA with PAA at a pH 6.0, **(D)** PDL coated coverslip, **(E)** SF-PL and SF-PG PEM (both at pH 7.0) and **(F)** blank coverslip. **(G)** Quantifying cell surface coverage to compare PDL and silk-based and PAH/PAA-based PEMs. Compared to controls, SF-PG/SF-PL performed best and was significantly different than PDL and uncoated glass. PAH/PAA was better than bare glass but not significantly different than PDL. **(H)** Surface area of phalloidin Alexa Fluor® 488 staining to provide an estimate of cell size. ns ($P > 0.05$), * ($P \leq 0.05$), ** ($P \leq 0.01$), *** ($P \leq 0.001$).

2.4.2 **Optimizing substrates to promote cell survival and growth**

We alter the thickness, and as a result, the water content and modulus of each film by changing the deposition pH of each PE. Since each of the created films have the same number of layers, changes in thickness can be a pseudo-qualitative measurement of the water content of a

film. As a method to characterize the substrates, the thickness of each film was measured by ellipsometry **(Figure A1.1)**. The best performing surface was generated using pH 5.5 for both PAH and PAA deposition, resulting in a 51 ± 1 nm thick film. The SF-PL/SF-PG film thickness was found to be 50 ± 6 nm, within the same range as the best PAH/PAA film. We detected a linear trend of increasing thickness with increasing pH for the PAH/PAA systems that correlated with increased cellular viability. A similar effect occurred using SF-PL/SF-PG, although not as pronounced as the viability trend for PAH/PAA pH.

To better understand how the assembly conditions of PEM films influence neuronal survival and growth, we conducted a set of experiments that altered the number of bilayers. The performance of 2.5, 4.5, 8.5 and 12.5 bilayers were examined along with changing the deposition pH between the systems: PAH/PAA (pH = 4.5, 5.5, 6.5) and SF-PL/SF-PG (pH = 6.0, 7.0, 8.0). We chose to study the number of bilayers *vs* pH deposition, creating a pseudo-gradient of thickness for this screen. Cortical neurons were cultured on these surfaces, and the number of surviving cells counted and averaged over three cultures (**Table A1.2** and **Figure A1.2**). Counting the number of nuclei on each surface revealed a general trend; films created with 4.5 bilayers typically performed better than films created with 2.5 bilayers. Yet any number of bilayers above 4.5 showed no significant change in cell count. In general, a single monolayer of PDL (control) did not significantly differ from films with at least 4.5 bilayers (averaged).

Counting nuclei provides an easily automated measure of cell survival for each film. To assess the capacity of surfaces to promote process extension, we visualized the F-actin cytoskeleton by staining with fluorescent phalloidin. Interestingly, the surface with the most attached cells was not the same as the surface promoting the highest surface coverage (**Figure 2.2 H**). SF-PL/SF-PG PEM performed markedly better than controls (PDL $P < 0.05$, and glass $P < 0.01$) and PAH/PAA performed similar to PDL (ns). While silk-based PEMs promoted cell attachment and viability similar to PDL, the capacity to support higher surface coverage was better than PAH/PAA surfaces. In contrast, PAH/PAA surfaces appear to be more adhesive, but are less effective at supporting cell spreading and process extension. A possible explanation is that PAH/PAA films may be substantially more adhesive than the SF films created, to the extent that they arrest neurite extension, while SF films are sufficiently adhesive to support cell survival, yet not to the extent that they inhibit cell and axon motility.

While the number of layers beyond 4.5 bilayers had no specific effect on viability, we can further test and tailor our surfaces by modifying PEM surface charge. So far, the terminal layer was always polycationic, but by adding an additional layer of polyanion, we can, in principal, change the surface to be negatively charged without significantly changing the thickness of the material. Previous research indicated that positively charged surfaces promote neuronal attachment,[41-42] and support the formation of high-density neural networks in culture. These studies utilized single monolayers of cationic PDL/PLL. In contrast, the multilayered materials we use here can partially mask the electrostatic charge of the outer layer that encounters the cellular plasma membrane. Typically, due to the plasma membrane phospholipid bilayer, cells exhibit a negative surface charge, perhaps accounting for positively charged polymers promoting cellular attachment.[8, 43-44] Within a PEM, the charge of the outer surface layer may be partially masked by polymers extruded from the oppositely charged layer below, resulting in surface charge weakening with each subsequent layer.

To determine if neurons exhibit a preference for negative or positive outer layers on a PEM surface, we altered which layer was topmost for PAH/PAA and SF-PL/SF-PG PEMs. Neurons were then cultured on these surfaces for 12 days before fixation, stained and quantified. Perhaps surprisingly, our findings indicate that the positive and negative terminated PEMs resulted in no significant difference in the number of nuclei present (**Figure 2.3 B**). For the PEMs studied, the charge of the terminal layer did not appear to influence either the number of adherent cells (**Figure 2.3 B**) or cell surface area (**Figure 2.3A**). It has been previously shown that negative charges within monolayered polymer materials perform poorly compared to polycationic polymers such as PLL/PDL;[42] however, polyanionic polymers within multilayered materials support cellular attachment of neural cells.[7, 25] Interestingly, the absence of an effect of the charge of the outer layer extends to other PEM combinations, with cells generally showing little to no preference for positive and negatively terminated PEMs (**Figures A1.3** and **A1.4**). This lack of preference for culturing neurons on PEMs may be due to the assemblage of serum proteins onto the surface of charged PEM growth substrates during culturing. As the number of layers increases, interpenetration of once discrete positive and negative polymer layers occurs, and thus creates a diminished formal charge of the surface. This diminished surface charge is further masked by serum proteins, which assemble close to the surface of the PEM and maybe the reason that we observe no difference between the terminal charge of the surfaces for cell growth and proliferation.

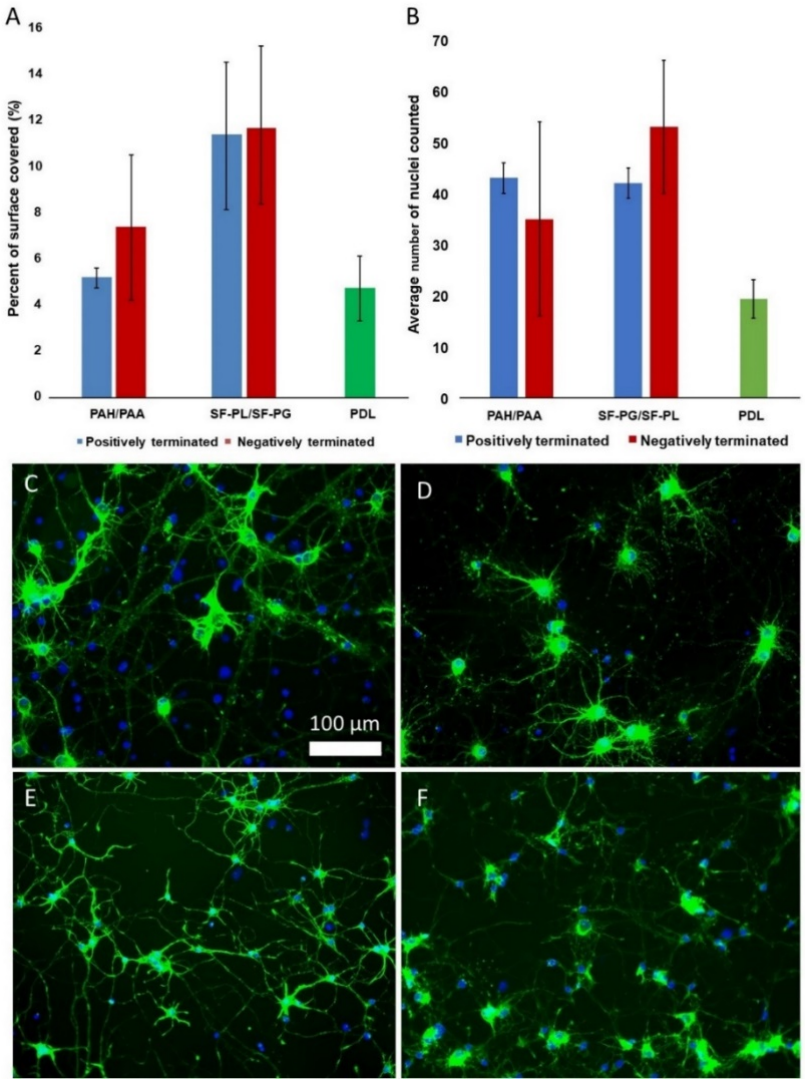

Figure 2.3. The charge of the terminal layer exhibits no significant effect on the growth and surface coverage of neural cells on PEM surfaces. **(A)** No significant difference in cell surface coverage was found between positive or negative terminated PEMs composed of PAH/PAA or SF-PL/SF-PG. Comparison to PDL reveals that the silk-based PEMs perform significantly better for the positive and negative terminated surfaces ($P < 0.05$). **(B)** No significant difference in the number of nuclei present was detected between positive or negative terminated PEMs composed of PAH/PAA or SF-PL/SF-PG. Compared to PDL, either silk-based PEM performed significantly better for both positive and negative terminated surfaces ($P < 0.05$). **(C-F)** Representative images of each of the surfaces with the plated cortical neurons: **(C)** PAH/PAA positively terminated, **(D)** PAH/PAA negatively terminated, **(E)** SF-PL/SF-PG positively terminated, and **(F)** SF-PL/SF-PG negatively terminated.

2.4.3 **Mechanical characterization of PEMs**

Modulus matching can enhance material biocompatibility for designer tissue engineering.[27, 45] Modulus matching has been used to mask implants from rejection and aid in the generation of lab-derived tissues. The importance of modulus within a material stems from an inverse relationship with water content. Higher water content materials tend to have lower modulus and high modulus materials tend to have lower water content. To characterize the material generated here, we performed nano-indentation on the SF-PL/SF-PG and PAH/PAA surfaces using an Asylum Research MFP-3D AFM to determine the modulus. Each film was created three times and measured at 9 different points. Indentation was performed using a BL-TR400PB tip (Asylum Research, k = 0.11 N/m) at an indentation rate of 5 μm/s. An average of the indented values was calculated, and the standard error is presented for each value. We measured freshly made PAH/PAA films and obtained a value of 870 ± 50 kPa, which is consistent with previous characterization of PAH/PAA surfaces.[46] Values for SF-PL/SF-PG PEM were found to be substantially softer than PAH/PAA (510 ± 55 kPa). Comparing the Young's modulus of both materials indicated that the softer SF-PL/SF-PG PEM better supported cell spreading and process outgrowth compared to the stiffer PAH/PAA multilayer. These findings are in contrast with previous studies of endothelial cells which exhibit increased spreading on harder substrates.[46] A meaningful comparison of the modulus of these multilayers to a single layer of PDL is essentially impossible, due to the difficulty of indenting a single layer of PDL on a glass substrate, where substrate effects overwhelm the measure and compromise obtaining an accurate indentation profile. A single molecular layer of PDL would be expected to exhibit the same high modulus as the underlying substrate.

2.4.4 **Exploring other bio-inspired PEMs**

In the process of investigating the effect of terminal charge on growth and attachment of neural cells, we tried other polyelectrolytes such as hyaluronic acid and chitosan. Surprisingly, we found that films made from these alternative PEs supported cell attachment and growth as well as PDL or better. We then explored other sources of PEs and expanded the family by including a large host of naturally derived and bio-sourced polymers. To standardize inclusion within this study, we employed the previously optimized parameters: 4.5 bilayers with positively terminated surfaces. All PEs used in this broader study are illustrated in **Figure 2.1**, including positively

charged (poly-L-lysine [PLL], hyaluronic acid [HA]), and negatively charged poly(glutamic acid) [PG], poly(acrylic acid)-co-DR1A [PAA-co-DR1A], and chitosan [CHI]). A combinatorial approach was employed, testing all possible polyanion and polycation combinations in a 24-well cell culture plate (**Figure A1.5**). Each multilayer was made by flooding the internal well with the PE of choice, waiting 5 minutes and aspirating the excess away. After washing twice with water, the alternative PE was added to the well, repeating the process till 4.5 bilayers were generated. Embryonic rat cortical neurons were plated and cultured for 12 days. The cultures were then fixed, stained and quantified (**Tables A1.6** and **A1.7)**. PEMs containing HA as a polyanion performed significantly worse than PDL ($P < 0.001$), while polymers containing silk PEs, in general, performed significantly better than control. Neuronal viability was best when cultured on the SF-PL/AA-DR1A PEM, which achieved a 3-fold increase in surface coverage as compared to PDL ($P < 0.001$). Notably, all PEMs that performed better than PDL contained a naturally derived PE (silk-based, PG, PDL or PLL). The best performing materials exhibited increased cell numbers and promoted higher surface coverage ($P < 0.05$). **Figure 2.4** illustrates the PEMs in ascending order of surface coverage, assayed using F-actin labelled with fluorescent phalloidin, with the PDL control colored red.

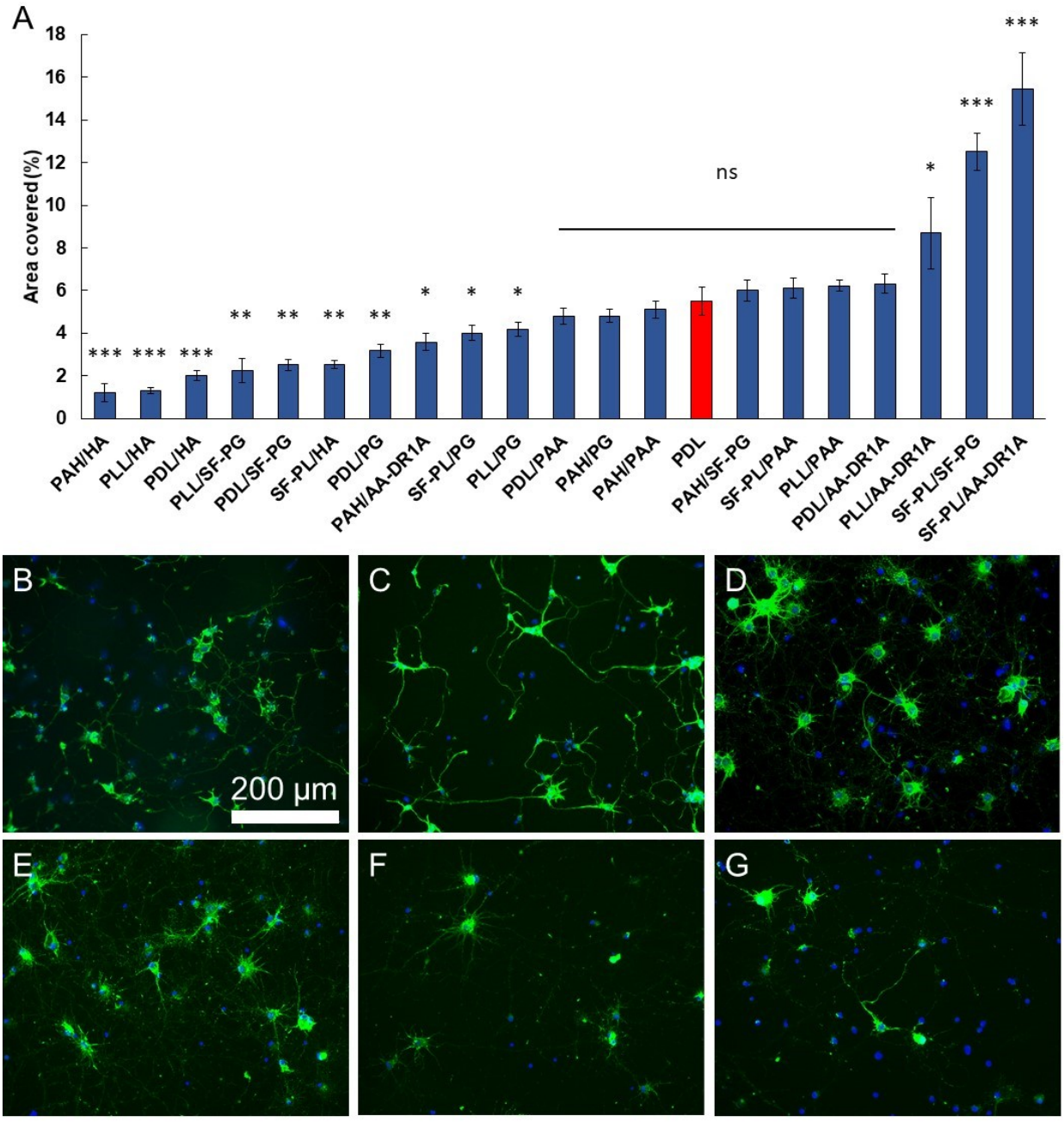

Figure 2.4. Combinatorial study of PEs ranking cell surface coverage. **(A)** Histogram showing PEMs ranked in ascending order of surface coverage. PDL control is red. All surfaces are 4.5 bilayers thick, positively charged, with deposition pH at the pKa of the polymer. (B-G) Select images are shown for the following systems: **(B)** PLL/SF-PG, **(C)** SF-PL/PAA-co-DR1A, **(D)** SF-PG/SF-PL, **(E)** PAA/PAH, **(F)** HA/PLL, and **(G)** Control (PDL). ns ($P > 0.05$), * ($P \leq 0.05$), ** ($P \leq 0.01$), *** ($P \leq 0.001$).

Although a number of surfaces did not differ significantly from PDL, three PEMs performed significantly better (**Figure 2.4)**. PLL/PAA-DR1A, SF-PL/SF-PG, and SF-PL/PAA-DR1A exhibited greatly enhanced cell growth when compared to PDL. Notably, all contain naturally derived polymers. The best among these was SF-PL/PAA-DR1A, which performed 3x better than PDL ($P < 0.001$) when comparing surface coverage. This trend was similar when counting the number of surviving cells (**Figure A1.6**), with the exception of PLL/PAA-DR1A PEM, which dropped a few places in the ranking compared to the two top PEMs. Interestingly, the structures of the SF-PG and SF-PL polymers consist of a silk backbone with pendant co-polymers (either PG or PLL), in a 'bottle brush' configuration, with silk as a backbone from which PG or PLL side-chains extend. However, each of the silk-based polymers performs markedly better than either PDL, or a film created from both PG and PL ($P < 0.05$). If performance was solely based on which surface was present, we would expect that the silk-based polymers would present similar results to that of the control or that of PLL/PG surfaces, which they do not. Notably, the best performing materials contained peptide linkages, which may contribute to these being particularly well tolerated by the neurons. The majority of the silk fibroin residues are neutral and not charged, thus, adding PDL or PG through typical peptide linkage chemistry is one way to augment the charge capability.

2.4.5 **Identifying an optimal surface for oligodendrocytes**

By examining cortical neuron growth, we identified three multilayer systems that outperform a standard PDL monolayer and identified specific attributes of these systems that affect performance: thickness, chemical composition and modulus. We then tested these systems using primary rat oligodendrocytes to determine if the enhanced substrate performance of the identified PEMs might generalize to this important vertebrate CNS glial cell type. Our findings indicated that oligodendrocytes exhibit some specificity for surface characteristics, but similar to the neurons, PAA-DR1A/SF-PL PEM ranked highest in measures of extension and growth **(Figure 2.5)**. Unlike the cortical neurons, this was the only PEM that scored significantly better than the PDL control ($P < 0.05$), while two other high-performing surfaces were not significantly different from control (ns). HA-based PEMs again performed poorly, while PAH/PAA-based PEMs performed poorly as well. Silk-based PEs performed well, along with the majority of PEMs containing PDL or PLL. The capacity for these PEMs to be interchangeable while maintaining

similar performance between vastly different neuronal cell types is a clear strength of this system. SF systems exhibited the best performance for both cell types, and specifically the best and most optimized system, SF-PL/AA-DR1A, was the top performer for both cell types.

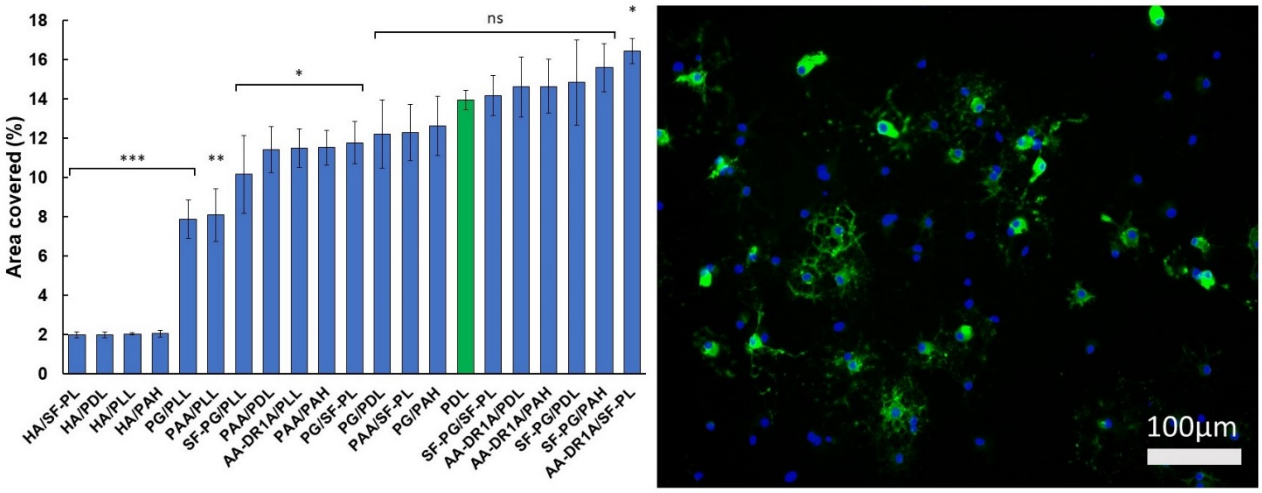

Figure 2.5. Oligodendrocytes cultivated on AA-DR1A/SF-PL films exhibit significantly better area coverage compared to PDL ($P < 0.05$). Combinatorial study ranking cell surface coverage for each PEM for rodent oligodendrocytes. (left). Histogram shows PEMs ranked in ascending order of surface coverage. PDL control is green. All surfaces are 4.5 bilayers thick, positively charged, and the deposition pH is the pKa of the polymer. (right) Representative micrograph of the AA-DR1A/SF-PL PEM showing F-actin labelling (green) and nuclear stain (blue). ns ($P > 0.05$), * ($P \leq 0.05$), ** ($P \leq 0.01$), *** ($P \leq 0.001$).

2.5 **Discussion**

Systematic optimization of our PEM coatings using bio-inspired PEs has identified three coatings, each of which performs significantly better than PDL: SF-PL/SF-PG ($P \leq 0.001$), PLL/AA-DR1A ($P < 0.05$), and SF-PL/AA-DR1A ($P \leq 0.001$). While the synthetic PEM (PAH/PAA) performed similarly to PDL when measuring cellular attachment, ultimately silk-based PEMs proved to be significantly better than PDL or synthetic PEs when measuring surface coverage. These results were the cumulation of several rounds of development, which required the optimization of the number of layers, the pH of deposition and modification of terminal charge. The assembly of PEMs onto a non-compatible surface functions as biocamouflage, making the new coated surface soft, wet, with a composition that resembles an ECM. All of these properties

contribute to creating an effective and functional synthetic ECM substrate for neural cells.

The Young's modulus, chemical functionality and water content all play major roles in biocamouflage and we varied each of these properties within our study with the aim of creating superior substrate coatings for neural cell culture. Low modulus materials have been previously shown to affect the motility and physical spreading of cells.[47-50] Further, relatively low modulus gels have shown promise to prevent astrocyte spreading and to reduce astrocyte recruitment during gliosis, effectively delaying the formation of a glial scar.[51] We found that the SF-PG/SF-PL PEM has an indentation modulus that is significantly softer than PAH/PAA at 510 ± 55 kPa. This value for the optimal silk surfaces corresponds well with an optimal range of 500-800 kPA previously identified for cultured embryonic rat spinal commissural interneurons.[10] Intriguingly, the high-functioning PAA/PAH surfaces possess a modulus of 870 ± 50 kPa, which is slightly outside the previously identified ideal range, suggesting that it may be possible to further optimize these surfaces. Striking the appropriate balance between being not too soft or too stiff is important, as modulus can prevent cells from adhering or from extending processes and thereby limit neural network formation.[47-48, 52]

Chemically similar polymer coatings have been found to elucidate dramatically different cellular responses, and thus, polymer selection can dramatically affect the success of neural regeneration or cultivation.[51, 53] Since a wide range of responses can be found, we used a combinatorial approach for screening the viability of each PEM coating. We found that in general, HA-based PEMs performed significantly worse than PDL and were the lowest performing materials. This was surprising as HA is a major structural component within the CNS; however, it may function more as a structural scaffold for other macromolecules *in vivo*, rather than directly interacting with cells to promote adhesion and process extension.[54] A striking finding we obtained is that any PE which contained a peptide backbone performed as well or better than PDL. Our combinatorial search highlighted silk-based PEMs, suggesting that these are promising materials for coatings. Silk has been previously explored as a functional material for numerous applications including regenerative medicine,[55-57] functioning as an artificial extracellular matrix, specifically designed to promote the growth of neural tissues. Notably, Gu and colleagues have employed the lower modulus of *B. mori* silk in conjunction with cellulose and relatively high tensile strength of spider silk to create nerve grafts.[55, 57] Cellulose and spider silk provide a rope-like physical

guidance scaffold, while *B. mori* silk provides an optimal growth medium with low modulus.

Poly-lysine has remained a standard material for coating substrates for several decades; however, PDL and PLL both are relatively expensive to produce and are prone to degradation and thus the coated substrates need to be made immediately prior to use. The PEM coating materials we describe here are based on silk-fibroin, a relatively inexpensive natural polymer source. When assembled into a PEM, a relatively simple coating of SF-PL/SF-PG performs significantly better than PDL. These materials can be assembled weeks prior to plating and are relatively shelf stable as compared to less robust PL coatings. Silk fibroin is a polypeptide, and therefore is prone to proteolytic degradation, yet when assembled into a thick PEM coating, it can last for several months.[58] Further, PEM formation is not limited to substrates, but have the capacity to coat irregular surfaces. Silk-based PEMs may also have substantial potential as coatings to promote the neural-biocompatibility of biomedical devices implanted in the CNS *in vivo*.

2.6 **Conclusions**

By optimizing pH of deposition, number of layers and PE combinations, we identified a new set of PE combinations to create a PEM that performs significantly better as a substrate for neural cell growth than PDL. This was measured on two matrices of quantification: a survival assay (number of nuclei present), and a growth assay (surface area of cell coverage). PEMs created with SF-PL (a polymer containing silk fibroin from *B. mori* silk worms co-polymerized with PLL) and PAA-DR1A or SF-PG substantially outperformed PDL. The silk polymers themselves contain PG and PLL (depending on PE) as a co-polymer, yet perform better than either PDL and PG together on all matrices measured. We demonstrate that employing silk results in a softer modulus for the assembled PEM (510 ± 55 kPa *vs* 870 ± 50 kPa). These newly developed materials have potential applications to support neural cell culture *in vitro* and also as coatings for devices and implants to enhance neural biocompatibility *in vivo*.

2.7 Acknowledgements

We are grateful to Dr. Beatrice Lego and Mohini Ramkaran for their help with the AFM indentation experiments. The project was supported by a Collaborative Health Research Program (CHRP) grant from the Canadian Institutes of Health Research (CIHR 357055) and the Natural Sciences and Engineering Research Council (NSERC 493633-16). TCC, TEK and CJB are grateful to the NSERC CREATE program (Canada) for supporting interdisciplinary collaboration through the McGill/MNI Training Program in NeuroEngineering.

2.8 References

1. Landry, M. J.; Rollet, F.-G.; Kennedy, T. E.; Barrett, C. J., Layers and multilayers of self-assembled polymers: Tunable engineered extracellular matrix coatings for neural cell growth. *Langmuir* **2018**, *34* (30), 8709–8730.

2. Aamodt, J. M.; Grainger, D. W., Extracellular matrix-based biomaterial scaffolds and the host response. *Biomaterials* **2016**, *86*, 68–82.

3. Bellamkonda, R.; Ranieri, J. P.; Bouche, N.; Aebischer, P., Hydrogel-based three-dimensional matrix for neural cells. *J. Biomed. Mater. Res.* **1995**, *29* (5), 663–671.

4. Gil, E. S.; Park, S. H.; Marchant, J.; Omenetto, F.; Kaplan, D. L., Response of human corneal fibroblasts on silk film surface patterns. *Macromol. Biosci.* **2010**, *10* (6), 664–673.

5. Yates, D., Neurodegenerative disease: Neurodegenerative networking. *Nat. Rev. Neurosci.* **2012**, *13* (5), 288–289.

6. Yavin, Z.; Yavin, E., Survival and maturation of cerebral neurons on poly(L-lysine) surfaces in the absence of serum. *Dev. Biol.* **1980**, *75* (2), 454–459.

7. Roach, P.; Parker, T.; Gadegaard, N.; Alexander, M. R., Surface strategies for control of neuronal cell adhesion: A review. *Surf. Sci. Rep.* **2010**, *65* (6), 145–173.

8. Kim, Y. H.; Baek, N. S.; Han, Y. H.; Chung, M. A.; Jung, S. D., Enhancement of neuronal cell adhesion by covalent binding of poly-D-lysine. *J. Neurosci. Methods* **2011**, *202* (1), 38–44.

9. Millet, L. J.; Gillette, M. U., Over a century of neuron culture: From the hanging drop to microfluidic devices. *Yale J. Biol. Med.* **2012**, *85* (4), 501–521.

10. Sailer, M.; Lai Wing Sun, K.; Mermut, O.; Kennedy, T. E.; Barrett, C. J., High-throughput cellular screening of engineered ECM based on combinatorial polyelectrolyte multilayer films. *Biomaterials* **2012**, *33* (24), 5841–5847.

11. Sailer, M.; Barrett, C. J., Fabrication of two-dimensional gradient layer-by-layer films for combinatorial biosurface studies. *Macromolecules* **2012**, *45* (14), 5704–5711.

12. Karlsson, A. J.; Flessner, R. M.; Gellman, S. H.; Lynn, D. M.; Palecek, S. P., Polyelectrolyte multilayers fabricated from antifungal β-peptides: Design of surfaces that exhibit antifungal activity against *Candida albicans*. *Biomacromolecules* **2010**, *11* (9), 2321–2328.

13. Decher, G., Fuzzy nanoassemblies: Toward layered polymeric multicomposites. *Science* **1997**, *277* (5330) 1232–1237.

14. Decher, G.; Hong, J. D.; Schmitt, J., Buildup of ultrathin multilayer films by a self-assembly process: III. Consecutively alternating adsorption of anionic and cationic polyelectrolytes on charged surfaces. *Thin Solid Films* **1992**, *210* (2), 831–835.

15. Radtchenko, I. L.; Sukhorukov, G. B.; Leporatti, S.; Khomutov, G. B.; Donath, E.; Möhwald, H., Assembly of alternated multivalent ion/polyelectrolyte layers on colloidal particles. Stability of the multilayers and encapsulation of macromolecules into polyelectrolyte capsules. *J Colloid Interface Sci.* **2000**, *230* (2), 272–280.

16. Sukhorukov, G. B.; Antipov, A. A.; Voigt, A.; Donath, E.; Möhwald, H., pH-Controlled macromolecule encapsulation in and release from polyelectrolyte multilayer nanocapsules. *Macromol. Rapid Commun.* **2001**, *22* (1), 44–46.

17. Volodkin, D. V.; Petrov, A. I.; Prevot, M.; Sukhorukov, G. B., Matrix Polyelectrolyte microcapsules: New system for macromolecule encapsulation. *Langmuir* **2004**, *20* (8), 3398–3406.

18. Zhu, H.; McShane, M. J., Macromolecule Encapsulation in diazoresin-based hollow polyelectrolyte microcapsules. *Langmuir* **2005**, *21* (1), 424–430.

19. Almodóvar, J.; Bacon, S.; Gogolski, J.; Kisiday, J. D.; Kipper, M. J., Polysaccharide-based polyelectrolyte multilayer surface coatings can enhance mesenchymal stem cell response to adsorbed growth factors. *Biomacromolecules* **2010**, *11* (10), 2629–2639.

20. De Koker, S.; Hoogenboom, R.; De Geest, B. G., Polymeric multilayer capsules for drug delivery. *Chem. Soc. Rev.* **2012**, *41* (7), 2867–2884.

21. Jagur-Grodzinski, J., Polymers for tissue engineering, medical devices, and regenerative medicine. Concise general review of recent studies. *Polym. Adv. Technol.* **2006**, *17* (6), 395–418.

22. Schultz, P.; Vautier, D.; Richert, L.; Jessel, N.; Haikel, Y.; Schaaf, P.; Voegel, J.-C.; Ogier, J.; Debry, C., Polyelectrolyte multilayers functionalized by a synthetic analogue of an anti-

inflammatory peptide, α-MSH, for coating a tracheal prosthesis. *Biomaterials* **2005**, *26* (15), 2621–2630.

23. Thompson, M. T.; Berg, M. C.; Tobias, I. S.; Rubner, M. F.; Van Vliet, K. J., Tuning compliance of nanoscale polyelectrolyte multilayers to modulate cell adhesion. *Biomaterials* **2005**, *26* (34), 6836–6845.

24. Gribova, V.; Auzely-Velty, R.; Picart, C., Polyelectrolyte multilayer assemblies on materials surfaces: From cell adhesion to tissue engineering. *Chem. Mater.* **2012**, *24* (5), 854–869.

25. Kidambi, S.; Lee, I.; Chan, C., Primary neuron/astrocyte co-culture on polyelectrolyte multilayer films: A template for studying astrocyte-mediated oxidative stress in neurons. *Adv. Funct. Mater.* **2008**, *18* (2), 294–301.

26. Boudou, T.; Crouzier, T.; Ren, K.; Blin, G.; Picart, C., Multiple functionalities of polyelectrolyte multilayer Films: New biomedical applications. *Adv. Mater.* **2010**, *22* (4), 441–467.

27. Zhou, K.; Sun, G. Z.; Bernard, C. C.; Thouas, G. A.; Nisbet, D. R.; Forsythe, J. S., Optimizing interfacial features to regulate neural progenitor cells using polyelectrolyte multilayers and brain derived neurotrophic factor. *Biointerphases* **2011**, *6* (4), 189–199.

28. Zhou, K.; Thouas, G. A.; Bernard, C. C.; Nisbet, D. R.; Finkelstein, D. I.; Li, D.; Forsythe, J. S., Method to impart electro- and biofunctionality to neural scaffolds using graphene-polyelectrolyte multilayers. *ACS Appl. Mater. Interfaces* **2012**, *4* (9), 4524–4531.

29. Ren, K.; Crouzier, T.; Roy, C.; Picart, C., Polyelectrolyte multilayer films of controlled stiffness modulate myoblast cells differentiation. *Adv. Funct. Mater.* **2008**, *18* (9), 1378–1389.

30. Ren, Y. J.; Zhang, H.; Huang, H.; Wang, X. M.; Zhou, Z. Y.; Cui, F. Z.; An, Y. H., *In vitro* behavior of neural stem cells in response to different chemical functional groups. *Biomaterials* **2009**, *30* (6), 1036–1044.

31. Ren, Y.-J.; Zhou, Z.-Y.; Liu, B.-F.; Xu, Q.-Y.; Cui, F.-Z., Preparation and characterization of fibroin/hyaluronic acid composite scaffold. *Int. J. Biol. Macromol.* **2009**, *44* (4), 372–378.

32. Serban, M. A.; Kaplan, D. L., pH-Sensitive ionomeric particles obtained *via* chemical conjugation of silk with poly(amino acid)s. *Biomacromolecules* **2010**, *11* (12), 3406–3412.

33. Ahmad, N. M.; Saqib, M.; Barrett, C. J. Novel azobenzene functionalized polyelectrolytes of different substituted head groups 3: Control of properties of self assembled multilayer thin films. *J. Macromol. Sci., Pure Appl. Chem.* **2010**, 47, 571–579.

34. Rockwood, D. N.; Preda, R. C.; Yucel, T.; Wang, X.; Lovett, M. L.; Kaplan, D. L., Materials fabrication from *Bombyx mori* silk fibroin. *Nat. Protoc.* **2011**, *6* (10), 1612–1631.

35. Goldman, J. S.; Ashour, M. A.; Magdesian, M. H.; Tritsch, N. X.; Harris, S. N.; Christofi, N.; Chemali, R.; Stern, Y. E.; Thompson-Steckel, G.; Gris, P.; Glasgow, S. D.; Grutter, P.; Bouchard, J. F.; Ruthazer, E. S.; Stellwagen, D.; Kennedy, T. E., Netrin-1 promotes excitatory synaptogenesis between cortical neurons by initiating synapse assembly. *J. Neurosci.* **2013**, *33* (44), 17278–17289.

36. Armstrong, R. C., Isolation and characterization of immature oligodendrocyte lineage cells. *Methods* **1998**, *16* (3), 282–292.

37. Jarjour, A. A.; Manitt, C.; Moore, S. W.; Thompson, K. M.; Yuh, S.-J.; Kennedy, T. E., Netrin-1 is a chemorepellent for oligodendrocyte precursor cells in the embryonic spinal cord. *J. Neurosci.* **2003**, *23* (9), 3735–3744.

38. Schindelin, J.; Arganda-Carreras, I.; Frise, E.; Kaynig, V.; Longair, M.; Pietzsch, T.; Preibisch, S.; Rueden, C.; Saalfeld, S.; Schmid, B.; Tinevez, J.-Y.; White, D. J.; Hartenstein, V.; Eliceiri, K.; Tomancak, P.; Cardona, A., Fiji: an open-source platform for biological-image analysis. *Nat. Methods* **2012**, *9*, 676–682.

39. Engler, A. J.; Richert, L.; Wong, J. Y.; Picart, C.; Discher, D. E., Surface probe measurements of the elasticity of sectioned tissue, thin gels and polyelectrolyte multilayer films: Correlations between substrate stiffness and cell adhesion. *Surf. Sci.* **2004**, *570* (1-2), 142–154.

40. Mermut, O.; Lefebvre, J.; Gray, D. G.; Barrett, C. J., Structural and mechanical properties of polyelectrolyte multilayer films studied by AFM. *Macromolecules* **2003**, *36* (23), 8819–8824.

41. Valentini, R. F.; Vargo, T. G.; Gardella, J. A.; Aebischer, P., Patterned neuronal attachment and outgrowth on surface modified, electrically charged fluoropolymer substrates. *J. Biomater. Sci., Polym. Ed.* **1994**, *5* (1-2), 13–36.

42. Webb, K.; Hlady, V.; Tresco, P. A., Relative importance of surface wettability and charged functional groups on NIH 3T3 fibroblast attachment, spreading, and cytoskeletal organization. *J. Biomed. Mater Res.* **1998**, *41* (3), 422–430.

43. Letourneau, P. C., Possible roles for cell-to-substratum adhesion in neuronal morphogenesis. *Dev. Biol.* **1975**, *44* (1), 77–91.

44. Yavin, E.; Yavin, Z., Attachment and culture of dissociated cells from rat embryo cerebral hemispheres on polylysine-coated surface. *J. Cell Biol.* **1974**, *62* (2), 540–546.

45. Etienne, O.; Schneider, A.; Kluge, J. A.; Bellemin-Laponnaz, C.; Polidori, C.; Leisk, G. G.; Kaplan, D. L.; Garlick, J. A.; Egles, C., Soft tissue augmentation using silk gels: An *in vitro* and *in vivo* study. *J. Periodontol.* **2009**, *80* (11), 1852–1858.

46. Schneider, A.; Francius, G.; Obeid, R.; Schwinté, P.; Hemmerlé, J.; Frisch, B.; Schaaf, P.; Voegel, J.-C.; Senger, B.; Picart, C., Polyelectrolyte multilayers with a tunable Young's modulus: Influence of film stiffness on cell adhesion. *Langmuir* **2006**, *22* (3), 1193–1200.

47. Bai, S.; Zhang, W.; Lu, Q.; Ma, Q.; Kaplan, D. L.; Zhu, H., Silk nanofiber hydrogels with tunable modulus to regulate nerve stem cell fate. *J. Mater. Chem. B Mater. Biol. Med.* **2014**, *2* (38), 6590–6600.

48. Banerjee, A.; Arha, M.; Choudhary, S.; Ashton, R. S.; Bhatia, S. R.; Schaffer, D. V.; Kane, R. S., The influence of hydrogel modulus on the proliferation and differentiation of encapsulated neural stem cells. *Biomaterials* **2009**, *30* (27), 4695–4699.

49. Cheng, M.; Deng, J.; Yang, F.; Gong, Y.; Zhao, N.; Zhang, X., Study on physical properties and nerve cell affinity of composite films from chitosan and gelatin solutions. *Biomaterials* **2003**, *24* (17), 2871–2880.

50. Leipzig, N. D.; Shoichet, M. S., The effect of substrate stiffness on adult neural stem cell behavior. *Biomaterials* **2009**, *30* (36), 6867–6878.

51. Fitch, M. T.; Silver, J., CNS injury, glial scars, and inflammation: Inhibitory extracellular matrices and regeneration failure. *Exp. Neurol.* **2008**, *209* (2), 294–301.

52. Yu, T. T.; Shoichet, M. S., Guided cell adhesion and outgrowth in peptide-modified channels for neural tissue engineering. *Biomaterials* **2005**, *26* (13), 1507–1514.

53. Huang, W.; Begum, R.; Barber, T.; Ibba, V.; Tee, N. C.; Hussain, M.; Arastoo, M.; Yang, Q.; Robson, L. G.; Lesage, S.; Gheysens, T.; Skaer, N. J.; Knight, D. P.; Priestley, J. V., Regenerative potential of silk conduits in repair of peripheral nerve injury in adult rats. *Biomaterials* **2012**, *33* (1), 59–71.

54. Wang, X.; He, J.; Wang, Y.; Cui, F.-Z., Hyaluronic acid-based scaffold for central neural tissue engineering. *Interface Focus* **2012**, *2* (3), 278–291.

55. Wang, C. Y.; Zhang, K. H.; Fan, C. Y.; Mo, X. M.; Ruan, H. J.; Li, F. F., Aligned natural-synthetic polyblend nanofibers for peripheral nerve regeneration. *Acta Biomater.* **2011**, *7* (2), 634–643.

56. Wang, Y.; Rudym, D. D.; Walsh, A.; Abrahamsen, L.; Kim, H. J.; Kim, H. S.; Kirker-Head, C.; Kaplan, D. L., *In vivo* degradation of three-dimensional silk fibroin scaffolds. *Biomaterials* **2008**, *29* (24-25), 3415–3428.

57. Wei, Y.; Gong, K.; Zheng, Z.; Wang, A.; Ao, Q.; Gong, Y.; Zhang, X., Chitosan/silk fibroin-based tissue-engineered graft seeded with adipose-derived stem cells enhances nerve regeneration in a rat model. *J. Mater. Sci. Mater. Med.* **2011**, *22* (8), 1947–1964.

58. Arai, T.; Freddi, G.; Innocenti, R.; Tsukada, M., Biodegradation of *Bombyx mori* silk fibroin fibers and films. *J. Appl. Polym. Sci.* **2004**, *91* (4), 2383–2390.

Appendix 1: Supplemental information for Chapter 2

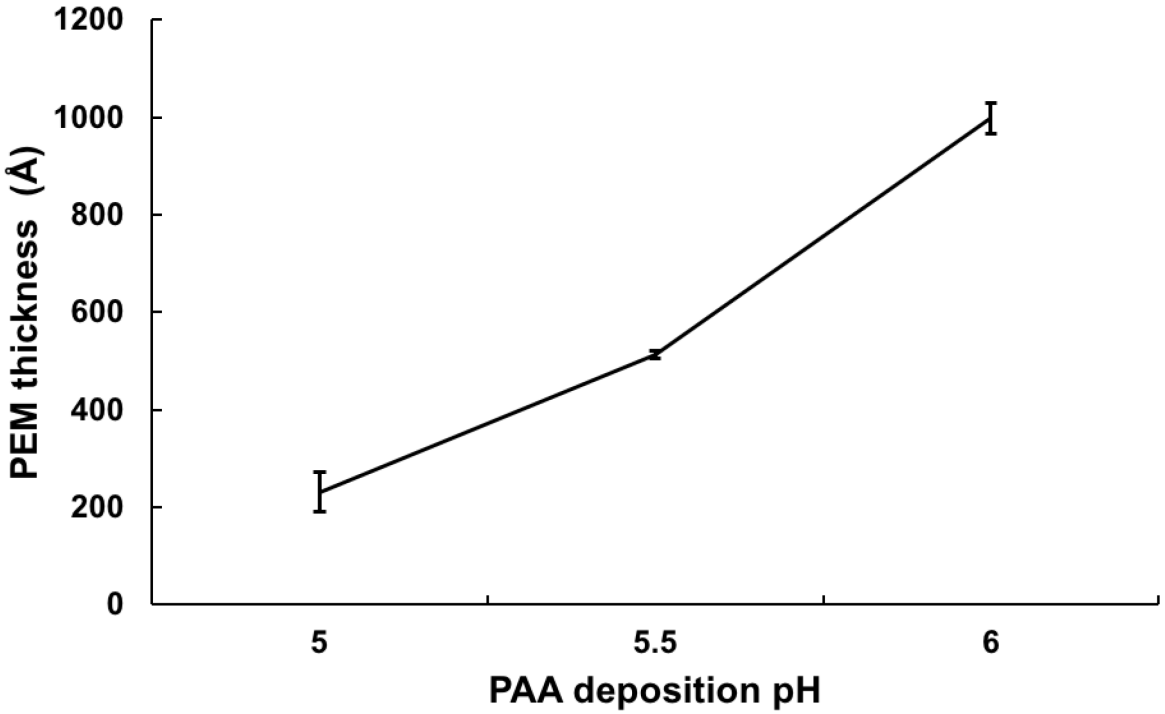

Figure A1.1. Thickness measurement of PEMs fabricated from PAH and PAA where the pH of deposition of PAH was kept constant at 5.5 and the pH of deposition of PAA was varied (5.0, 5.5 and 6.0).

Table A1.1. Thickness measurements of PEMs created from a series of polyanionic and polycationic polymers. Each measurement was obtained from ellipsometry experiments and denoted in nanometers. Each measurement was performed in triplite on three samples and the materials were measured when fully dry.

	PAA	**HA**	**SF-PL**	**PDL**	**PLL**
SF-PG	32 ± 1	32 ± 1	39 ± 2	84 ± 2	86 ± 2
PAH	49 ± 8	75 ± 4	32 ± 1	35 ± 2	33 ± 2
CHI	36 ± 6	32 ± 1	32 ± 1	31 ± 0	33 ± 1
AA-DR1A	30 ± 0	30 ± 1	86 ± 0	66 ± 3	86 ± 1

Table A1.2. Cell counts of Hoechst 33258 stained nuclei. PEMs were fabricated by varying the pH of deposition and bilayer number.

	pH of deposition for PAH			**pH of deposition for SF-PL**		
Bilayer structure	**pH 4.5**	**pH 5.5**	**pH 6.5**	**pH 6.0**	**pH 7.0**	**pH 8.0**
2.5 bilayers	43 ± 5	69 ± 9	65 ± 17	41 ± 22	37 ± 11	96 ± 63
4.5 bilayers	59 ± 11	96 ± 10	95 ± 12	73 ± 20	61 ± 9	58 ± 10
8.5 bilayers	48 ± 20	116 ± 35	67 ± 23	83 ± 42	52 ± 20	122 ± 31
12.5 bilayers	70 ± 11	95 ± 25	46 ± 7	62 ± 25	117 ± 16	73 ± 22

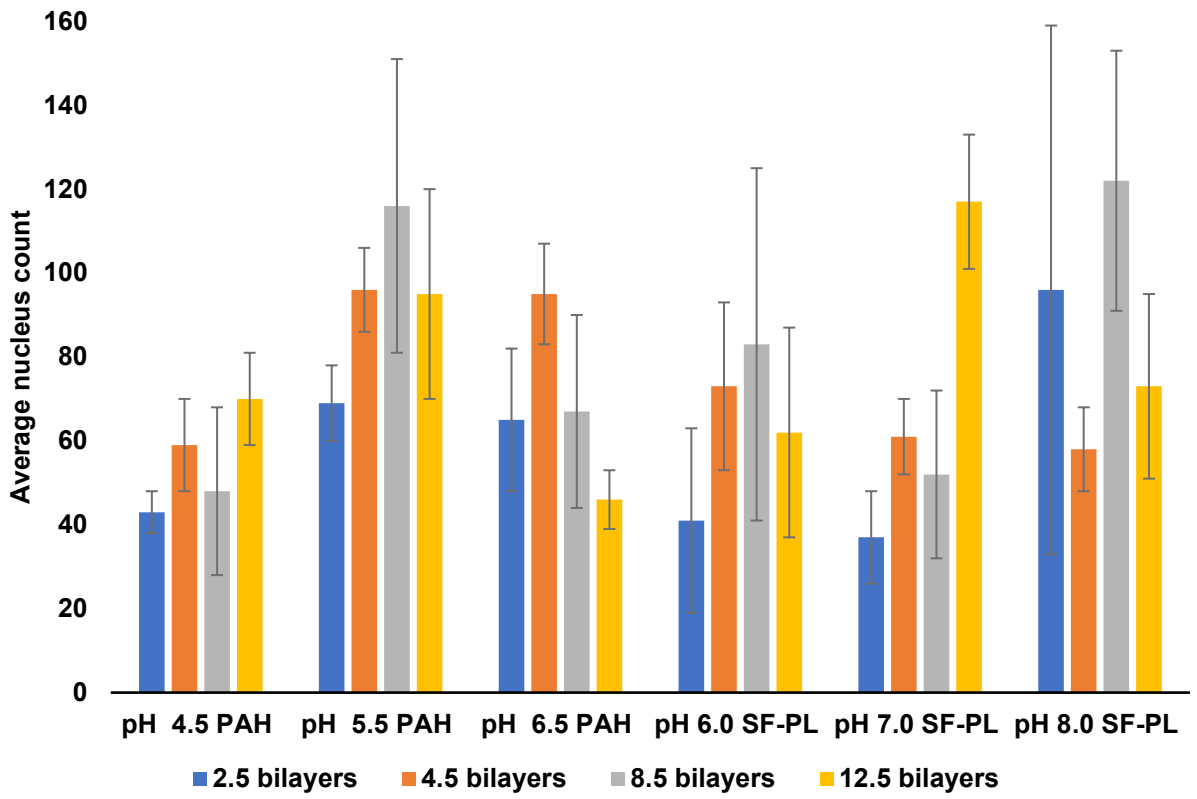

Figure A1.2. Graphical representation of **Table A1.2** showing the average number of nuclei on each of the studied substrates. There was no significant correlation between number of layers and cell viability.

Table A1.3. Cell counts of Hoechst 33258 stained nuclei. Data was obtained from negatively terminated PEMs.

	PAA	**HA**	**SF-PL**	**PDL**	**PLL**
SF-PG	14 ± 1	16 ± 9	53 ± 13	30 ± 5	32 ± 17
PAH	35 ± 19	20 ± 5	26 ± 7	26 ± 5	46 ± 14
CHI	11 ± 6	23 ± 5	37 ± 6	46 ± 9	30 ± 9
AA-DR1A	10 ± 6	10 ± 5	73 ± 41	70 ± 16	92 ± 12
Blank	16 ± 17		**PDL**	36 ± 11	

Table A1.4. Cell counts of Hoechst 33258 stained nuclei. Data was obtained from positively terminated PEMs.

	PAA	HA	SF-PL	PDL	PLL
SF-PG	14 ± 1	16 ± 9	42 ± 3	37 ± 8	39 ± 5
PAH	43 ± 3	14 ± 13	26 ± 7	26 ± 5	48 ± 24
CHI	29 ± 9	18 ± 2	37 ± 6	46 ± 9	30 ± 9
AA-DR1A	10 ± 6	10 ± 5	68 ± 15	39 ± 7	51 ± 6

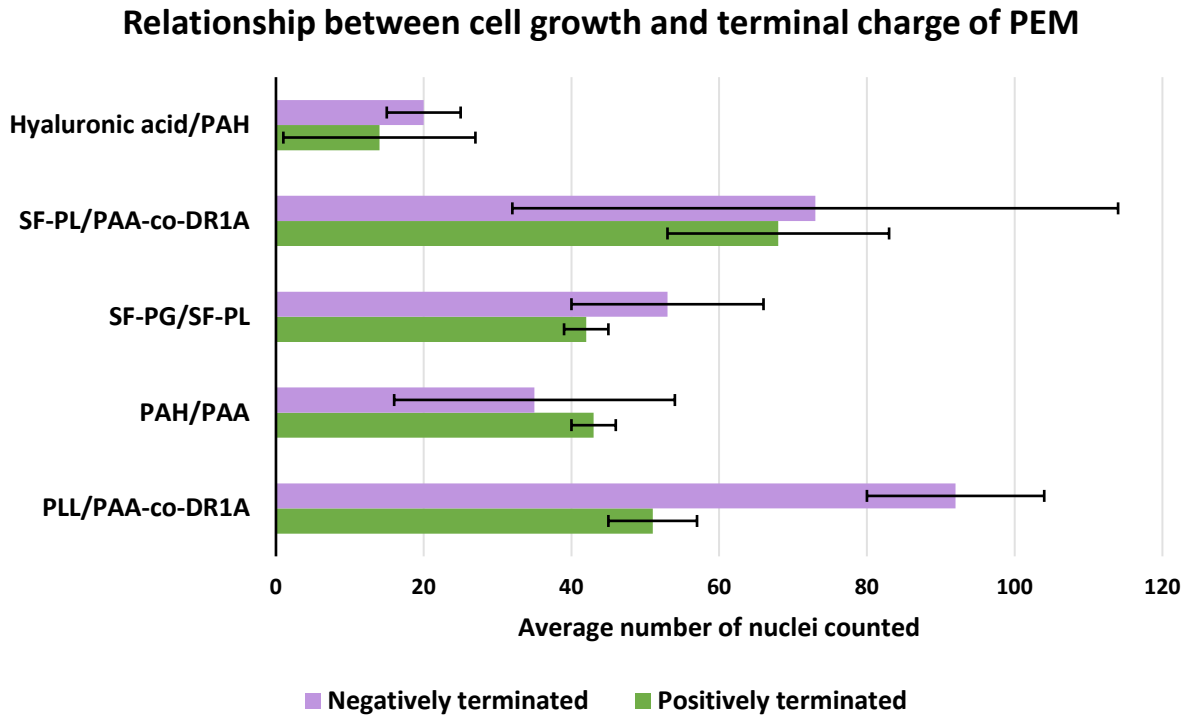

Figure A1.3. The charge of the terminal layer exhibits no significant effect on the growth and surface coverage of neural cells on PEM surfaces. The average number of nuclei was counted for negatively terminated (purple) and positively terminated (green) PEMs created from different choice surfaces.

Table A1.5. Quantification of Alexa Fluor phalloidin 488 stained cortical neurons. Numbers represent the total area stained in square millimeters. Data was obtained from negatively terminated PEMs. Data from the blank and PDL control conditions is also presented.

	PAA	**HA**	**SF-PL**	**PDL**	**PLL**
SF-PG	2.3 ± 1.2	5.5 ± 3.3	11.7 ± 2.9	13.6 ± 1.2	8.1 ± 2.4
PAH	7.4 ± 4.7	3.3 ± 1	3.9 ± 1.5	3.8 ± 0.9	7.4 ± 4.0
CHI	1.4 ± 1.3	2.4 ± 0.4	6.2 ± 4.3	9.5 ± 1.4	9.2 ± 1.8
AA-DR1A	2.6 ± 2.5	1.8 ± 1.5	13.4 ± 10.4	1 ± 0.1	6.8 ± 0.6
Blank	1.4 ± 1.7		**PDL**	4.2 ± 0.3	

.

Table A1.6. Quantification of Alexa Fluor phalloidin 488 stained cortical neurons. Numbers represent the total area in square millimeters that was stained. Data was obtained from positively terminated PEMs.

	PAA	**HA**	**SF-PL**	**PDL**	**PLL**
SF-PG	2.2 ± 2.0	0.2 ± 0.1	11.4 ± 2.7	10.0 ± 3.3	6.7 ± 7.2
PAH	5.2 ± 0.5	0.3 ± 0.3	3.3 ± 1.0	6.8 ± 4.4	3.6 ± 0.5
CHI	2.1 ± 1.2	1.2 ± 0.7	4.0 ± 1.5	3.8 ± 0.9	3.7 ± 0.2
AA-DR1A	1.4 ± 0.6	0.9 ± 0.4	12.8 ± 1.5	7.9 ± 2.1	14.0 ± 4.5

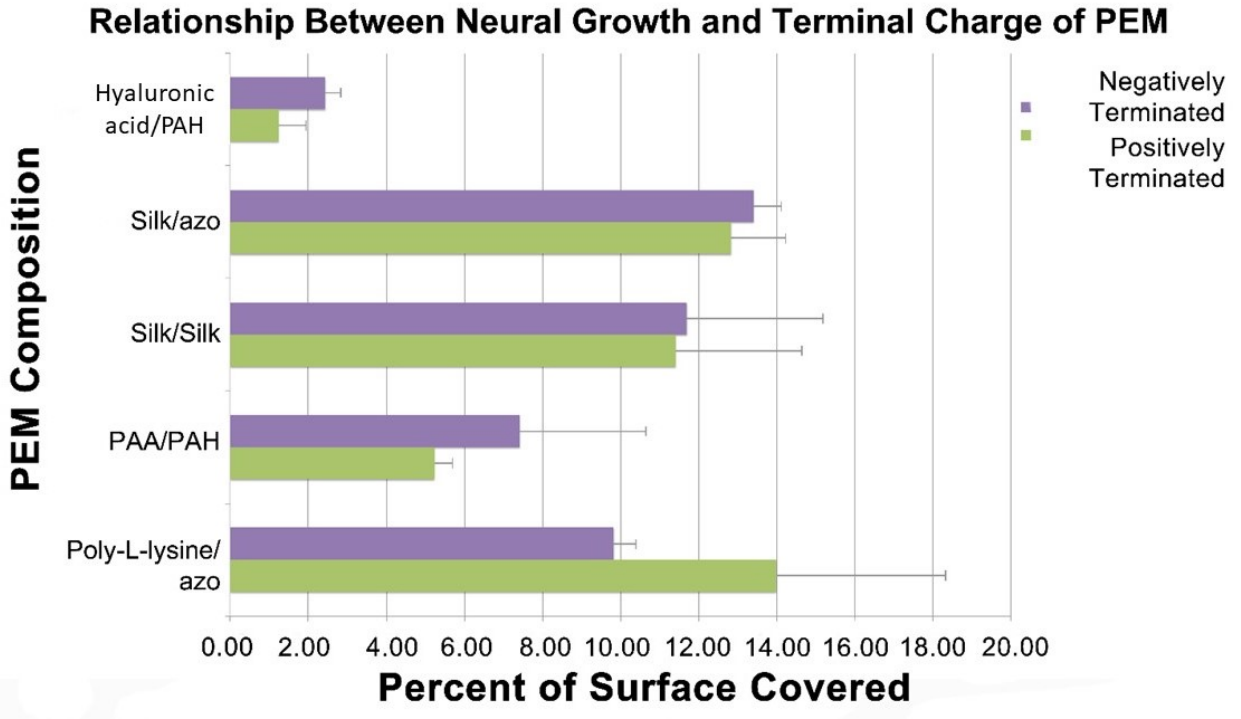

Figure A1.4. The effect of terminating a PEM either by the polycationic or polyanionic polymer through quantification of surface coverage. No significant difference was found between either the polycation or polyanion terminated PEMs when the percentage of surface covered was quantified. 'Azo' polymer denotes PAA-co-DR1A polymer which is a modified PAA polymer.

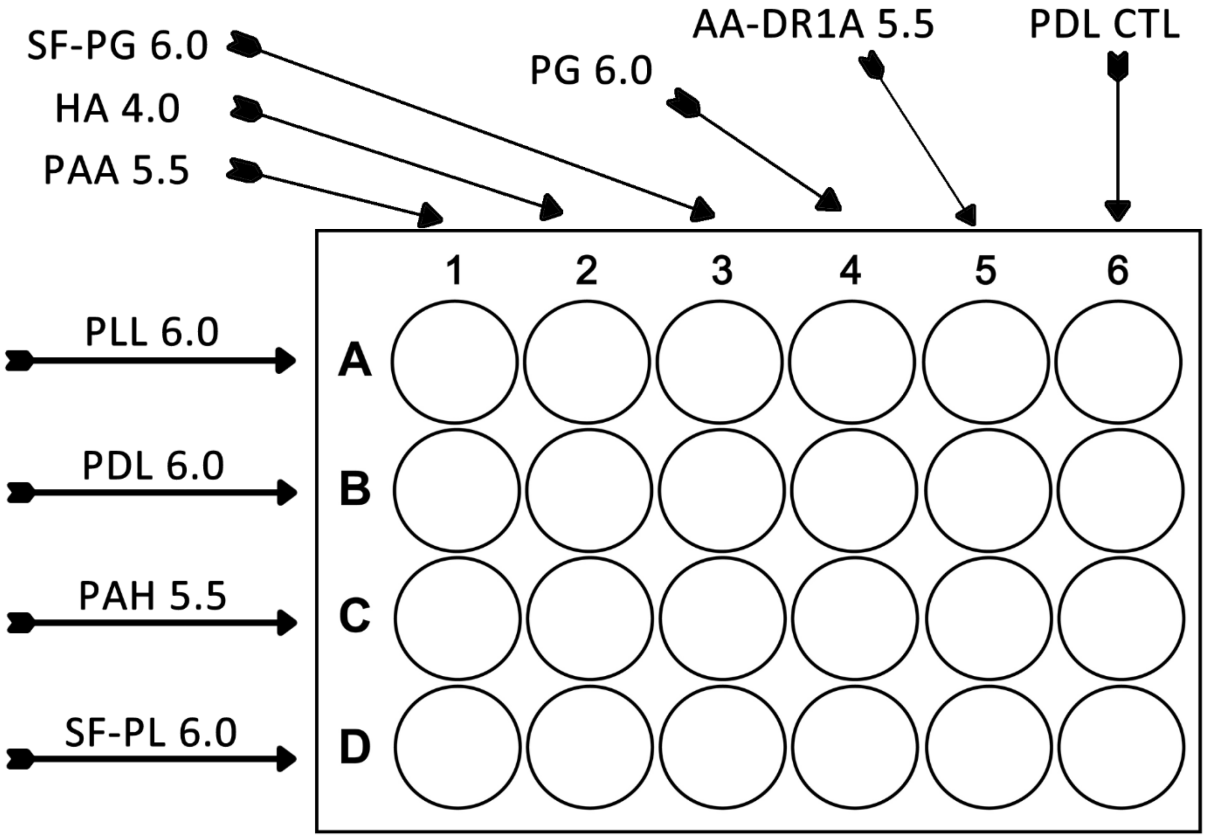

Figure A1.5. Schematic overview of the 24-well plate used to culture cells. Each combination, and pH of deposition are noted on the outside of the plate. Quantification of the plate is found in **Table A1.6**.

Table A1.7. Quantification study showing the full range of tested PEs. Cortical neurons were stained with Alexa Fluor phalloidin 488 and the stained cell surface area counted and standardized per surface. Values within this table are the percentage of the surface covered with cellular phalloidin staining.

	PAA	**HA**	**SF-PG**	**PG**	**PAA-DR1A**
PLL	6.2±0.3	1.3±0.1	2.2±0.6	4.2±0.3	8.7±1.7
PDL	4.8±0.4	2.0±0.2	2.5±0.3	3.2±0.3	6.3±0.5
PAH	5.1±0.4	1.2±0.4	6.0±0.5	4.8±0.3	3.6±0.4
SF-PL	6.1±0.5	2.5±0.2	12.5±0.9	4.0±0.4	15.5±1.7

Table A1.8. Quantification study showing the full range of tested PEs. Cortical neurons were stained with Hoechst 33258 and the nuclei were counted and averaged for each surface. Values here are from three 24 well plates with 3 images each, averaged.

	PAA	HA	SF-PG	PG	PAA-DR1A
PLL	24.3±12.9	7.7±3.0	42.0±2.7	37±8.2	38.7±5.0
PDL	43.3±3.2	14.0±13.1	21.3±1.5	27.3±4.0	30.3±9.3
PAH	29.3±9.5	17.7±1.5	41.7±5.1	40.3±26.6	43.3±15.3
SF-PL	9.7±4.0	13.3±2.1	68.0±14.8	39.0±7.2	50.7±6.4

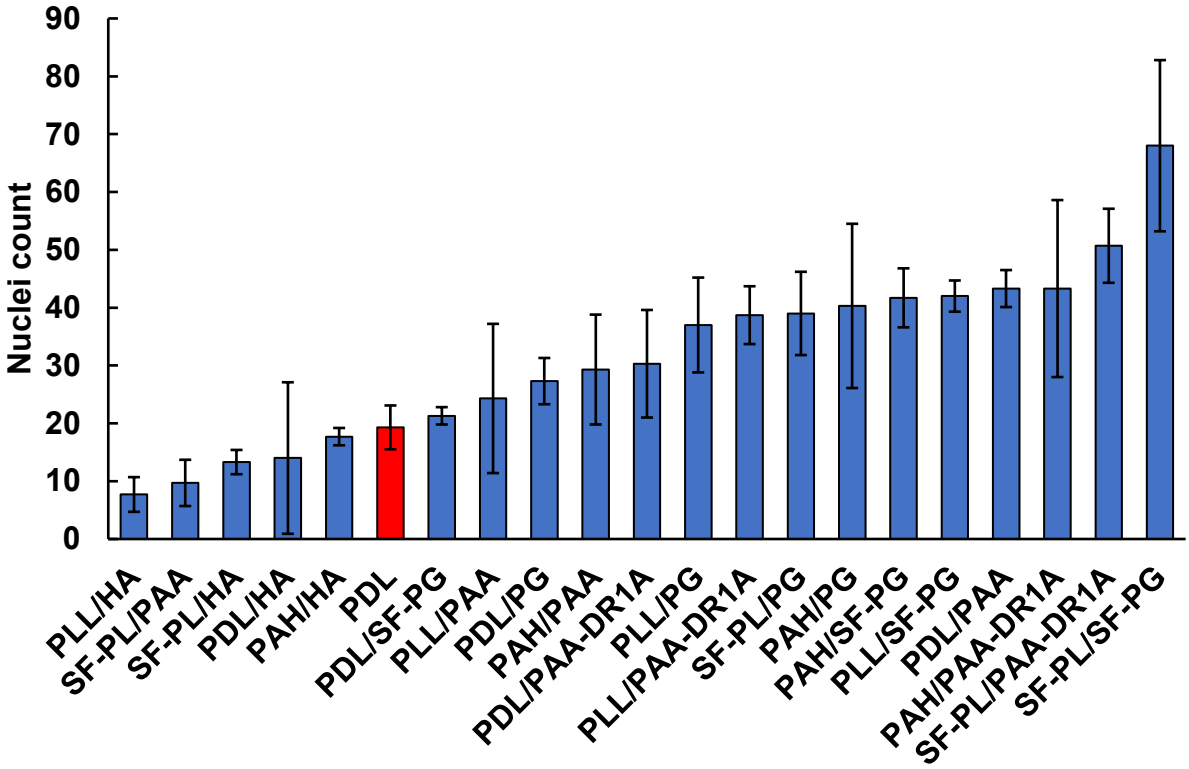

Figure A1.6. Quantification of second 24-well study showing a histogram of the full range of tested PEs. The data corresponds to **Table A1.6** PDL control in red.

Rationale for Chapter 3: From cocoon to artificial vessels: Electrospun silk derivatives as surface-tunable vascular graft materials

Chapter 2 explored the creation and optimization of surfaces specifically for the cultivation of neuronal cells and investigated the precise layering conditions required for creating optimal surfaces. These films were adhesive enough to allow cells to adhere, whilst not being so adhesive as to prevent process extension. Not only were the materials assessed for their capacity to support neural cells; their thickness (and therefore water content) and moduli were measured and used as rationales for supporting the reasoning why our new multilayer surfaces performed superiorly to PDL. Silk fibroin-based materials were found to be among the highest performing materials. Silk fibroin has been previously shown to be amendable to synthetic tailoring and processing into different biomaterial forms, other than films. This ability to be tailored further into chemically distinct materials and processed into a variety of different forms is explored in Chapter 3. Previously, we developed neural supportive materials, and we extend this knowledge into creating coatings and scaffolds for artificial vascular support materials. By screening a variety of chemically distinct polymers, we intend on selecting one which will be electrospun into a network of fibers. This extension of a naturally 2-D material into a porous 3-D scaffold material was only possible based on previous the knowledge of adhesion gained in Chapter 2. The prepared manuscript 'From cocoon to artificial vessels: Electrospun silk derivatives as surface-tunable vascular graft materials' was co-authored by Michael J. Landry, Matthew Kok, Karlie P. Potts, Prof. Jeff T. Gostick, Dr. Kevin Lachapelle, Prof. Christopher J. Barrett, and Prof. Richard L. Leask, and provides insight into how to create a 3-D scaffold material created from water soluble silk polymers with suitable mechanical properties for suturing and implantation.

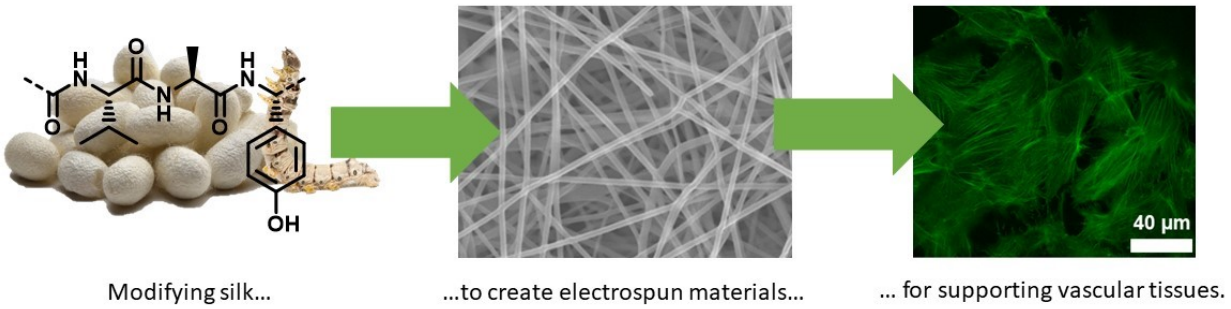

Chapter 3: From cocoon to artificial vessels: Electrospun silk derivatives as surface-tunable vascular graft materials

Chapter 3 is based on a manuscript entitled 'From cocoon to artificial vessels: Electrospun silk derivatives as surface-tunable vascular graft materials', and was co-authored by: Michael J. Landry, Matthew Kok, Karlie P. Potts, Prof. Jeff T. Gostick, Dr. Kevin Lachapelle, Prof. Christopher J. Barrett, and Prof. Richard L. Leask.

3.1 Abstract

Bombyx mori silk fibroin is a natural biopolymer well suited for incorporation into biomedical devices and tissue engineering scaffolds. We report here a series of azobenzene dye-modified silk polymers (so called 'azosilk') which exhibit a wide range of wettability (2 ° – 120 ° contact angle) due to functionalization with various chemical 'headgroups'. The viability of human abdominal aortic endothelial cells (HAAECs) on 16 members of this family of azosilks demonstrated a linear relationship of cell viability with respect to contact angle ($R^2 = 0.675$, $P < 0.01$). A sodium sulfanilate azobenzene derivative showed the highest viability (~90% alive) and was selected to be processed into electrospun mats, with a mean fiber diameter of 140 ± 15 nm. Mechanical properties were tested and revealed a low indentation modulus (16 kPa), with a suitable stiffness (230 ± 43 MPa, as measured by uniaxial tensional stressing). When processed into electropsun spun mats, our azobenzene-modified silk improves the biocompatibility and mechanical properties of this natural biopolymer and is a suitable vascular graft material.

3.2 Introduction

Atherosclerosis is the major etiology of cardiovascular disease, manifesting as the pathological remodeling of arteries which can lead to events such as occlusion (i.e. heart attack or stroke), dissection, or rupture of a vessel. Vascular grafts have been used to replace or bypass diseased blood vessels since the 1950's.[1-3] Autologous arteries and veins are the best conduits but may not always be available and there is a need for reasonable synthetic alternatives. Although synthetic grafts can be used in large arteries (> 8 mm in diameter) with very good patency rates, their use in small arteries (< 3 mm in diameter), such as those in the heart and lower limbs, are not very successful and succumb to early thrombosis. The challenge is to develop a non-thrombotic synthetic graft which could be used on small arteries such as the coronary arteries.[4-5]

Original synthetic vascular graft materials used to replace blood vessels have included: glass, aluminum, gold-plate, silver, poly(methyl methacrylate), and nylon tubes.[1] Many improvements have been made to make synthetic vascular grafts more biocompatible and functional. The literature contains many examples of promising materials, surface functionalization techniques, and drug/biomolecule implantation aimed at producing a viable small vessel (< 8 mm diameter) synthetic graft.[6] Large vessel graft materials continue to be dominated by poly(ethylene terephthalate) (PET or Dacron) or poly(tetrafluoroethylene)-PTFE (Gortex and Teflon). These materials are relatively biocompatible, easy to manipulate by the surgeon, durable, and have low surgical mortality when used in large vessels. The results have been in general quite satisfactory,[7] however these materials have been shown to be unsuitable for application as small diameter grafts.[4-5]

The major challenge for small diameter grafts is to create a conduit that has sufficient strength and suture retention that has similar compliance to native vessels, while maintaining an antithrombotic lumen,[5] and a soft texture that increases biocompatibility. Indeed, this is perhaps the key balance to achieve in development of such biomaterials- optimizing the tradeoff between 'soft' and 'wet' materials, the 2 properties key for good biocompatibility,[8] yet remaining strong enough to survive surgical application. Typical artificial materials are either strong *or* 'soft and wet', while many natural biopolymers, such as silk, cellulose, and chitosan, do possess this combination of ideal mechanical properties for implantation,[9-12] and yet are of low-enough modulus and high-enough water content to resemble biological tissue sufficiently to be well tolerated and reduce rejection rates. Silk fibroin in particular has demonstrated great potential as a bio-sourced engineered tissue scaffold, and has been explored as a graft material because of its combination of excellent mechanical properties, and biocompatibility.[5, 8] Silk fibroin can be readily fabricated into porous scaffolds with suitable mechanical properties for graft material by weaving, knitting, or electrospinning.[13-17]

Electrospinning silk fibroin creates roughened, high surface area materials with good porosity and tunable mechanical properties suitable for vascular grafts.[18] The surface of nanofibers from silk fibroin can be post-modified with sulfate groups to improve blood compatibility and anticoagulant activity.[19] Silk fibroin is also amendable to selective modification via amino acid chemistry, that can be used to tailor and fine-tune surface and bulk polymer properties of graft

materials. Aromatic amino acids in particular offer facile targets for electrophilic substitution reactions, yielding well-controlled and selective chemical modifications of the silk. One such modification demonstrated recently, is a functionalization with photo-reversible azobenzene (azo) dyes, that respond to low-power visible light to locally and selectively unfold some of the self-assembled beta sheet regions of silk structure, causing these regions to expand and swell with water, greatly reducing modulus near the surface of the material to that mimicking biological tissue.[20] This results in the surface of the implanted material to possess a 'gel-like' high water content (>80%), and a much lower modulus (>10x less) than the bulk material, matching the 'soft and wet' properties of the biological environment surrounding the implant, while retaining the bulk mechanical strength needed for tissue repair and implantation. This azobenzene-modified silk or so-called 'azosilk' preparation has been reported,[20] and the post-processing light-triggered surface softness and wetness enhancement demonstrated for applications as externally addressed biomaterials,[21] and as a synthetic tag to further modify silk into other materials classes such as ionomers.[22] Typically, the pendant amino acid side chains are facile to modify, as each is chemically distinct. Azobenzene-functionalization of silk occurs through the electrophilic attack of tyrosine, an aromatic amino acid, by diazonium salts under aqueous conditions. The creation of diazonium salts requires an activated aniline derivative and stoichiometric sodium nitrate and allows for the creation of families of azosilks by switching the aniline derivative in this reaction (**Figure 3.1**). Using azobenzene coupling reactions is a powerful tool that can be exploited to create chemically distinct, tailored, and optically addressable biomaterials, in a quick and facile manor – typically only requiring 30 minutes for a reaction to create a specified azosilk solution.[21] Each 'headgroup' (aniline derivative coupled to the tyrosine sidechain) can be used to add biologically relevant molecules onto silk or can be used to further tune the physico-chemical properties of silk. Surface properties, such as hydrophilicity (measured as a water drop contact angle), can affect adhesion of biomolecules and, as a result, cell felicity adjacent to the surface of the implant material.

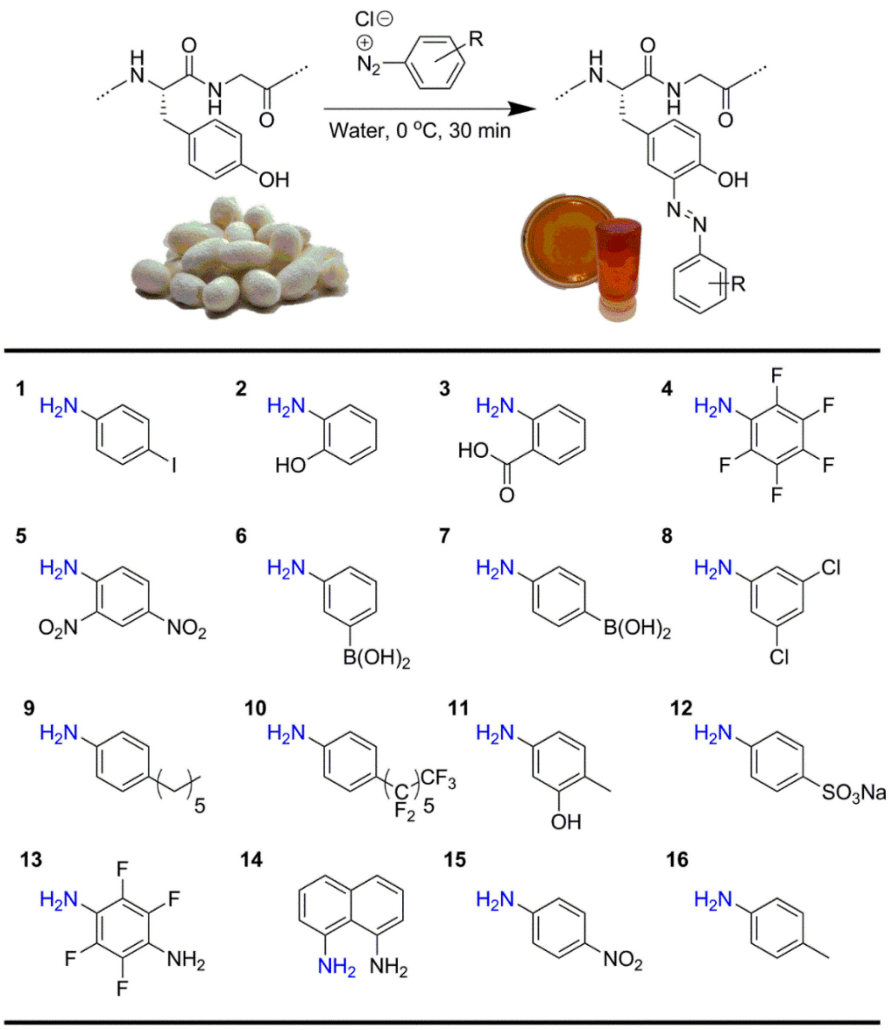

Figure 3.1. (Top) Reaction scheme and **(bottom)** resulting family of various 'headgroup' azosilk materials that were studied as endothelial cell growth surfaces. The amino group (blue label) on each substrate is where the diazonium salt is formed, and thus where the attachment to tyrosine links the azosilk pendant group.

In this paper, we describe the application of azobenzne-modified silk (azosilk) derivatives as implantable materials that can later transform their surface properties with light to enhance biocompatibility. A wide range of variable head-group azosilk derivatives was prepared and screened for suitability to apply as permissive electrospun materials for supporting endothelial cells in artificial vascular tissues, with optimized physical properties to support superior HAAECs growth. We then selected the top cell growth assay performer to then optimize for electrospinning properties to create mats with viable mechanical properties for vascular graft materials, artificial

vascular coatings, or as scaffolds for engineered vascular tissues.

3.3 Materials and methods

3.3.1 Materials, equipment, and instrumentation

All materials and reagents used in the synthesis or processing of materials were purchased from Sigma-Aldrich unless indicated otherwise. Silk fibroin cocoons were purchased from Tajima Shoji Ltd. (Yokohama, JP). Corning Costar flat bottom cell culture plates (12-well) were purchased from Fisher Scientific (Waltham, MA, US). Distilled water was purified by a MilliQ Academic purification system (Millipore, Billerica, US) and was used in the preparation of all aqueous solutions.

Scanning electron microscopy images were taken on a SU3500 Hitachi (Hitachi Ltd., Tokyo, Japan) scanning electron microscope. FTIR spectra were collected using a Vertex 70v FTIR spectrometer (Bruker, Billerica, US). Atomic force microscopy images and indentations were conducted using an MFP-3D SA atomic force microscope with molecular force probe 3D controller (Asylum Research, Santa Barbara, CA). The goniometer used in the contact angle measurements was a Techspec goniometer with a rotating stage (Edmund optics, Barrington, US). The tensile strength was measured experimentally using a Shimadzu EZ test tensile tester (Shimadzu, Kyoto, JP) using tensile strength mode. Cell images were acquired using an Axiovert 100 inverted fluorescence microscope (Carl Zeiss Canada, Toronto, CA). Images of the 12 well cell culture plates were taken using an ImageXpressMicro (Molecular Devices, Sunnyvale, US) and processed using MetaMorph® microscopy automation and image analysis software (MetaMorph®, Sunnyvale, US). Images were further processed using ImageJ 2.0 (Open-Source, Madison, US).

3.3.2 Isolation of silk fibroin and synthesis of azosilk

Preparation of the silk solutions from *Bombyx mori* silkworm cocoons was based on the protocol from Rockwood et al. with minor modifications.[23] 1.25 mL of a 0.2 M aniline derivative solution (in water or an appropriate solvent, i.e. acetonitrile/acetone) and 625 µL of 1.6 M aqueous toluenesulfonic acid (TSA) was added to a 9.5-dram vial. The solution was stirred and cooled in an ice bath to 4°C. 625 µL of 0.2 M aqueous $NaNO_2$ solution was added to the vial dropwise, producing a bright yellow diazonium salt solution. This was then stirred for 25 minutes on ice. In

a separate vial, 2 mL of a 5% w/v silk solution was cooled to 4°C. 0.25 mL of a boric acid/sodium borate buffer was added to the silk solution, and the resulting solution was adjusted to a pH of 8-9. Over 2 minutes, 0.5 mL of the diazonium salt was added dropwise to the silk solution, producing a bright red colour. The solution was then stirred for 30 minutes on ice, to ensure complete reaction. The azobenzene-modified silk solution was purified using desalinating columns, NAP-25 (VWR International), with borate buffer as the eluent.

3.3.3 Preparation of insoluble films for initial biological testing

The azosilk solutions were fabricated into drop cast films in 12 or 24-well plates for initial cell felicity testing. This was accomplished by pipetting 250 µL of the azosilk solution into each well. The plate was then covered with parafilm, and small air holes were poked into each well to ensure slow drying over 4-5 days. The dried films were placed into an oven at 45°C overnight, which produced water stable films. To ensure the asosilk film was successfully annealed to the well, 2mL of 1X PBS buffer was added to the well and placed in an incubator overnight. The buffer was removed prior to cell culture.

3.3.4 Preparation of spin-dope solutions

To a 50 mL Eppendorf centrifuge tube, 10 mL of azosilk (see **Section 3.3.2**) and 0.5 g of poly(ethylene oxide) (90 k MW) were added and stirred overnight. 0.25 mL of water was then added to ensure dissolution of the PEO into the viscous solution. (Note: an additional 24 hours was often required to ensure complete re-dissolution of the polymer into the azosilk solution.) Once a clear and viscous PEO/azosilk solution was prepared, 5-15 wt% of DMF was added to the solution. DMF was used as a co-solvent to reduce the vapor pressure of the spin dope, improving the solutions capability to be electrospun.[24] To ensure minimal bubble formation, 2-3 drops of common commercial dish soap (Softsoap®, a source of sodium laureth sulfate) were added to the solution before loading it into a syringe. The tube was tumbled gently to ensure minimal bubble formation. Adding the dish soap was found to be key, as it acted as a surfactant to reduce the surface tension of the spin dope, allowing the fibers to be formed.

3.3.5 Electrospinning azosilk into fibers

A 25 mL plastic syringe with an inner diameter of 21 mm was utilized for the electrospinning. 10-15 mL of the spin-dope solution was added to the syringe and left until the

bubbles were removed. The syringe plunger was carefully pressed into the shaft, and all bubbles were removed again. A 22-gauge hollow metallic needle was attached to the end and mounted onto a syringe pump. A collection plate was placed 15 cm from the tip of the needle. The collection plate was made of a conductive metal plate, covered with aluminum foil, and was then connected to a high voltage power supply. The set-up was grounded via a connection to the end of the needle and to the syringe pump. The flow rate of the syringe pump set to 0.1 mL/hr. The high voltage power supply was initiated and slowly ramped to 35 kV, at which point the polymer/spin-dope mixture transitioned into a Taylor cone.[25] The polymer mixture was sprayed onto the collection plate for 12 hours, and the resulting material was then imaged or further processed for plating. the electrospun mats were then placed into a solution of methanol for 20 minutes, effectively creating water-insoluble mats. The mats ere further treated by being heated at 45 °C under house vacuum for 3 days to ensure complete evaporation of methanol.

3.3.6 **Mechanical testing of bulk materials and fibers**

The tensile strength was measured experimentally using Shimadzu EZ test tensile tester using tensile strength mode with a maximum load of 5.5 N. The samples were loaded into the machine, their thickness, length and GL were measured and used to calculate the cross-sectional area. To minimize slippage of our samples in the tensile tester, the sample ends were covered in medium grit sandpaper and loaded tightly into the holder. A maximum strain rate of 5 mm/min is used. Each sample was extended until failure and their tensile strength calculated in triplicate.

3.3.7 **Contact angle measurements**

The contact angle of the studied azosilk surfaces were measured by placing a 50 μL drop of water onto the surface and a photo was taken after waiting 30 seconds for the water to settle. This process was repeated three times and the angle which the surface and the water drop made was measured and averaged three times. Table S2 (Supplementary information) contains the complete dataset of contact angles of the studied azosilks.

3.3.8 **Cell culture of HAAECs**

Human abdominal aortic endothelial cells (HAAECs) (AG09799; Coriell, Camden, NJ, US) were cultured in endothelial growth medium (C-22010; Promocell, Hiedelberg, Germany), supplemented with 10% fetal bovine serum (SH3007003; GE Healthcare, Little Chalfont, UK) and

1% penicillin-streptomycin (15-140-122; Gibco, Waltham, US) in tissue culture flasks coated with 0.1% pig gelatin at 37°C and 5% CO_2. At confluence, cultures were rinsed with phosphate buffered saline solution (PBS) and harvested with 0.25% Trypsin-EDTA (25-200-072, Gibco, Waltham, US). The electrospun mats were sterilized by UV irradiation (UV-C radiation, 253.7 nm) in a cell culture hood for 30 minutes, followed by being submerged in endothelial growth medium for 1 hour prior to seeding. HAAECs were seeded onto the surfaces (electrospun mat or azosilk films) at a concentration of 5 x 10^5 cells/mL and allowed to adhere overnight before changing the media. The plate was incubated (37°C and 5% CO_2) for 48 hours and then fixed for 20 minutes in 1% paraformaldehyde (Alfa Aesar, Cambridge, MA). The wells were then washed 3x with PBS and stored in PBS at 4°C until staining. The cells were permeabilized with 0.1% Triton-X for 15 minutes and washed twice with 0.05% Tween-20. They were then stained with 1/200 FITC-phalloidin and 1/1000 DAPI for 1 hour before washing three times with 0.05% Tween-20. The samples were imaged within 36 hours.

3.3.9 **Live/dead viability assay**

After the initial cells were cultured and viewed on a light microscope, a LIVE/DEAD viability/Cytotoxicity kit (L3224, ThermoFisher) was applied to each surface. The dye was prepared using the outlined protocols with the following components: 20 µL of 2 mM ethdium homodimer-1, and 5 µL of 4 mM calcein AM solution to 10 mL of 1 X PBS solution. After the addition of 100 µL of the dying solution to each well, the plates were transferred to a live cell imaging chamber. The cells were maintained with CO_2 and a humidity chamber during the live cell imaging. The plate was allowed to acclimate for 30 minutes, and then images were taken hourly of each well (9 random images per well) for 6 hours. Images were analyzed through automated software (MetaXpress®) which quantified the fractions of alive and dead cells (**Table A2.3**).

3.4 **Results and discussion**

3.4.1 **Initial screen of azosilks on endothelial cells**

To identify azosilk materials that best supported HAAECs growth, a range of target head groups (the functionality at the end of the azobezene group) was selected. A series of hydrophilic, hydrophobic, electron-donating and electron-withdrawing substituents was chosen, generating a family of 16 diazonium salts based on the aniline substrate (**Figure 3.1**). Each salt was processed

into azosilk solutions, plated onto a plasma-treated 24 well plate, and allowed to slow-dry over 5 days at room temperature before being further dried using a 45°C vacuum oven overnight. This slow-drying technique allowed for the assembly of β-sheets, a critical requirement for the formation of water-resistant films suitable for cell culture. HAAECs were plated onto the azosilk surfaces and cultured for 2 days in an incubator (37°C, 5% CO_2). The cytotoxicity of each azosilk polymer film was assayed using a live/dead assay kit consisting of calcein AM (live) and ethdium homodimer-1 (dead) (**Table A2.2**). As an initial screen, the 16 azosilk variations were assayed for their cell viability, resulting in a large range of survival rates observed (**Figure A2.2**). Several of the azosilk materials were found to perform at a level as the control of the proprietary coatings on the cell culture dishes (**Figure A2.2**).

Survival rates for the cultured HAAECs varied from 20-90% between the 16 prepared surfaces. A trend emerged when considering the structure of each headgroup and their corresponding viability rates, with the more hydrophobic 'Teflon-like' 4-(perfluorohexyl)aniline (#**10**) and 4-hexylaniline (#**9**) derivatives recording the lowest survival ratios, whilst the more hydrophilic sodium sulfanilate (#**12**) and 2-aminobenzoic acid (#**3**) derivatives achieved the highest survival ratios. The hydrophilic derivatives were determined to not be significantly different than the proprietary cell culture dishes coatings (control, $P > 0.05$). Each of the derivatives was purified using desalinating columns and their purity confirmed using ^{1}H NMR spectroscopy (see **Appendix 2**), yet a large variance of survival rates was observed. The conversion rate from silk to azosilk is nearly quantitative as a large excess of diazonium is used (20-30 eq), while the content of tyrosine within silk is low, typically 2-5% of the total residues (by mass).[21, 26] There is a large variance of survival rates considering the transformation of a small quantity (5 wt%) of the total amount of amino acid residues to the corresponding azobenzene. This suggests that the cytotoxicity of the polymer or the surface properties change with azobenzene functionalization. To quantify the cytotoxicity and surface properties of these polymers, the contact angle of the various azosilk films (surface energy) were measured.

Azosilk films were fabricated on coverslips and the contact angle of the surfaces were measured using the static sessile drop method (**Table A2.3**). A wide range of contact angles were observed, from strongly hydrophilic (#**12** (2°) and #**3** (12°)) to hydrophobic (#**4** (120°) and #**10** (129°)). The large variance of the observed contact angles demonstrates the tunabilty of the azosilk

system through headgroup modification. This is likely due to hydrophobic moieties self-assembling at the water-air interface. In the case of the hydrophobic surfaces, this self-assembly creates a surface which is predominantly alkyl and fluoroalkyl at the surface with silk below. This phase separation is an effect similar to what is observed in block-co-polymers and Langmuir-Blodgett films.[27] The capability to tune the hydrophobicity (i.e. contact angle) of a biomaterial is important considering each cell type and lineage uniquely responds to the surface properties they are cultured on. The optimal contact angle for culturing cells on a surface may vary up to 25 degrees.[28] This specificity is dictated by the different integrin proteins expressed by each cell type, which vary significantly.[29] To quantify the question of hydrophobicity affecting cell adhesion, and thus cell survival, the contact angle (as a measure of hydrophobicity) *vs* cell survival is plotted (**Figure 3.2**).

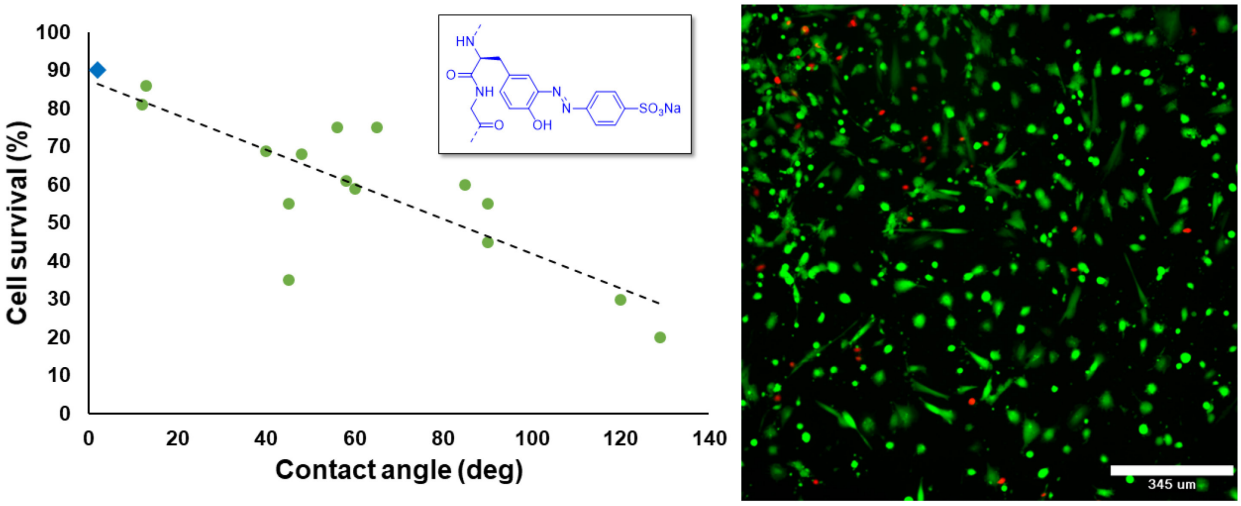

Figure 3.2. (Left) Correlation between contact angle of azosilk film materials and the viability of HAAECs quantified with calcein AM (live) and ethdium homodimer-1 and counted automatically using automated software. Cell viability was inversely correlated with contact angle (hydrophilic) ($P<0.01$, $R^2=0.675$). The chemical structure of the highest performing azosilk **(left, inset)** was found to be a sodium sulfanilate-based group. **(Right)** A representative image showing a live/dead assay employing ethdium homodimer-1 (dead, compromised membranes) and calcein AM (alive, esterases convert to calcein) of the sodium sulfanilate best performing film.

Figure 3.2 demonstrates a correlation between contact angle (a measure of hydrophobicity) and cell survival. Hydrophobicity influences cell adhesion and thus survival of adherent cells (including endothelial cells). In order to survive, HAAECs must excrete and assemble a basement membrane onto the surface.[30-32] In the case of the most hydrophobic surfaces (#**3** and #**12**), the excreted ECM proteins from the HAAECs are not able to sufficiently assemble onto the surface to create a basement layer enabling cell adhesion. In the case of the hydrophilic surfaces, their surface energy and charged surfaces resemble their native ECM proteins,[33-35] which enables the HAAECs adhering and growing to confluence. Tidwell and coworkers note that functionalities which are charged ($–COO^-$, $–SO_3^-$, $–NH_3^+$) have the most impact on cell growth,[36] whereas adhesion of cells onto naked and non-protein functionalized, hydrophobic surfaces net low adhesion and survival.[32] This study provided us a methodical approach for the selection of azosilk family members for further refinement (**Figure 3.2, inset**), which included our best performing polymer – a sodium sulfanilate derivative – which achieved the highest survival.

3.4.2 **Processing azosilk materials into electrospun mats**

Starting from our selected azosilk family member (#**12**), we began the optimization of the electrospinning parameters to create nanofiberous mats of our materials.[37] Aqueous spin-dope solutions were created following previous literature protocols, with the exception of using azosilk in place of non-functionalized silk and using 5 wt% poly(elthyleneoxide) (PEO, 90 k MW) – a previously explored water soluble spin-aid polymer.[37-38] The gap width between collector and tip was adjusted to 15 cm, the flow rate was regulated to 0.02 mL/min, and the biased collection plate was adjusted to 35 kV to begin electrospinning. One problem that affected the formation of well-defined fibers was the significant surface tension at the air-water interface. To overcome the surface tension problem, several additives were screened. Among the successful candidate additives, DMF yielded the most promising results, however it did not create a fully stable spinning system. DMF spin-dope solutions of 5% and 10% were screened, as well as the addition of a few drops of liquid detergent. This detergent was used to decrease the surface tension, while DMF was used to increase the cohesivity of the polymer during spinning. **Figure 3.3** shows the resulting fibrous mats after successful optimization of the spinning parameters; achieved using a spin solution containing: 5 wt% PEO in 20 wt% azosilk (#**12**) and 5 wt% DMF with three drops of aqueous dish soap. A 22-gauge needle was used, and the spin dope solution was excreted at a rate

of 1.30 mL/hr with a gap width of 15 cm from a 35 kV positively charged metallic collection plate. The resulting fibers were relatively monodispersed and found to be 140 ± 15 nm thick from a series of 100 measurements. These fibers are significantly smaller than those reported previously.[39]

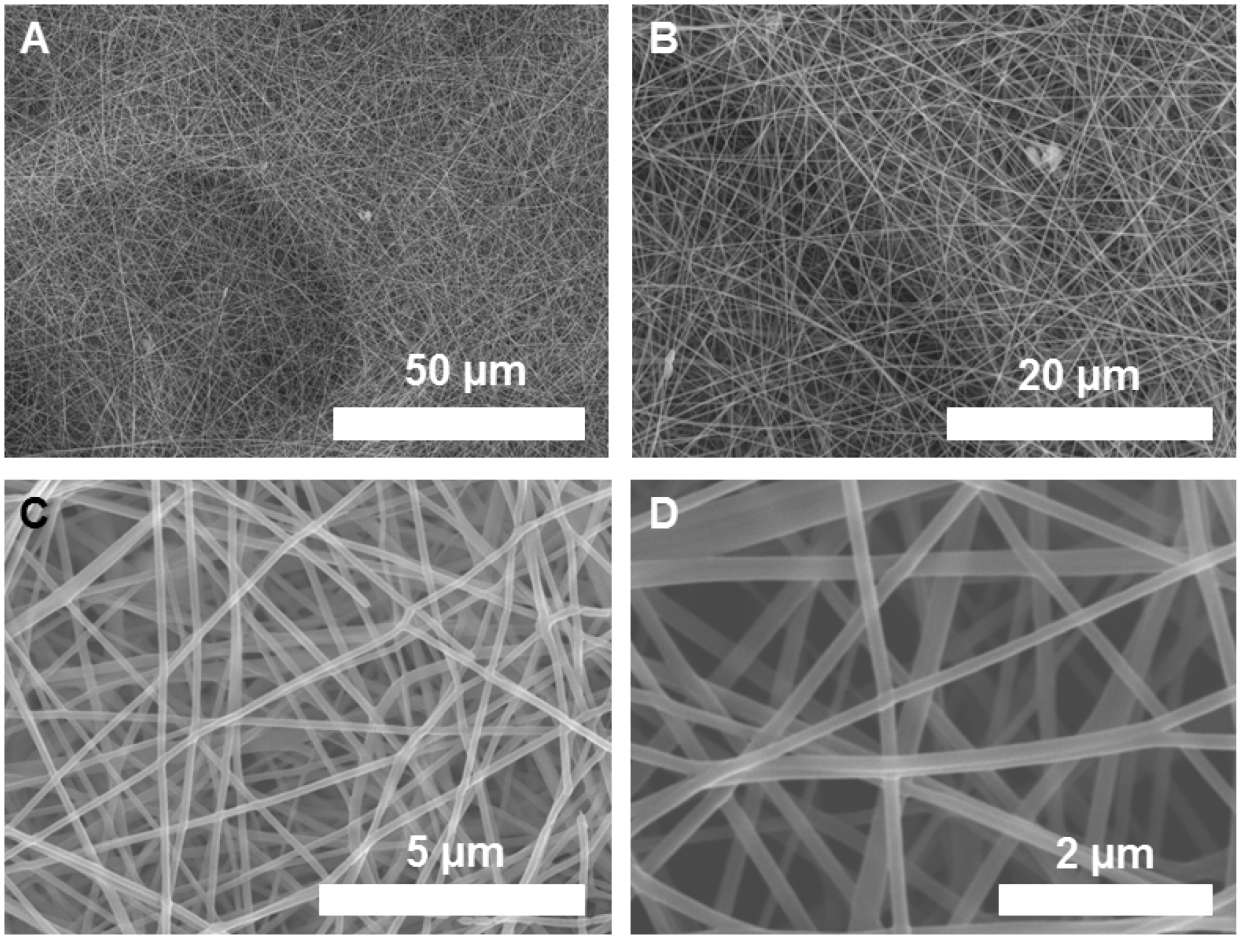

Figure 3.3. Scanning electron microscopy images of the azosilk fibers formed from electrospinning. The fibers formed from this process are relatively monodispersed (140 ± 15 nm) and the mat shows no preferential alignment of the fibers.

FTIR (**Figure 3.4A**) and solid-state UV-vis spectroscopy (**Figure 3.4B**) were used to characterize the fibers and to verify: (a) the protein secondary structure that the spun fibers were formed into and, (b) to verify the incorporation of the sodium sulfanilate azobenzene chromophore into the silk scaffold. The IR spectrum was measured on the 'as made' material after spinning. Several key characteristics of our material are demonstrated, including a dramatic shift in the amide region of the IR spectrum (**Figure 3.4A**) that signifies both a Silk I and II structure (ν =

1650 cm^{-1}, 1627 cm^{-1}, 1535 cm^{-1}) which suggests that the as made material is a mixture of water soluble and water insoluble silk.[40] Water insolubility is important in scaffold materials to ensure the durability of the structure of the scaffold during cell culture. Presence of the sulfate group on the end of the azobenzene (#**12**) was seen at 1340 cm^{-1}, suggesting the incorporation of the azobenzene was successful. This was also confirmed by solid state UV-vis spectrophotometry measurements, demonstrating an absorbance side band that is characteristic of the sodium sulfanilate (#**12**) azosilk as seen from previous optical measurements (410 nm) in solution, and within solid-state swollen films.[21] Yet, the predominate absorbance bands found in the UV spectrum are 260 and 320 nm, characteristic of the silk fibroin amino acid absorptions.[41] The identified Silk II structure suggests water insolubility, however to transform any remaining Silk I structure, and to sterilize the mats, the material was soaked in methanol for 20 minutes, a process previously shown to transform a water-soluble Silk I structure to the water-stable Silk II structure (ν = 1650 cm^{-1} and 1535 cm^{-1}).[42] The methanol treatment did not result in changes to the IR spectrum. Mats of the methanol and non-methanol treated electrospun materials were submerged under 1X PBS buffer overnight in an incubator at 37°C. The next morning, the methanol-treated materials were found to be intact and only a trace of dissolved azosilk polymer (yellow color) was found in the buffer, suggesting that only a small amount of the polymer had dissolved. Subsequent washings resulted in no transfer of this color, thus no dissolution of the silk polymer into solution.

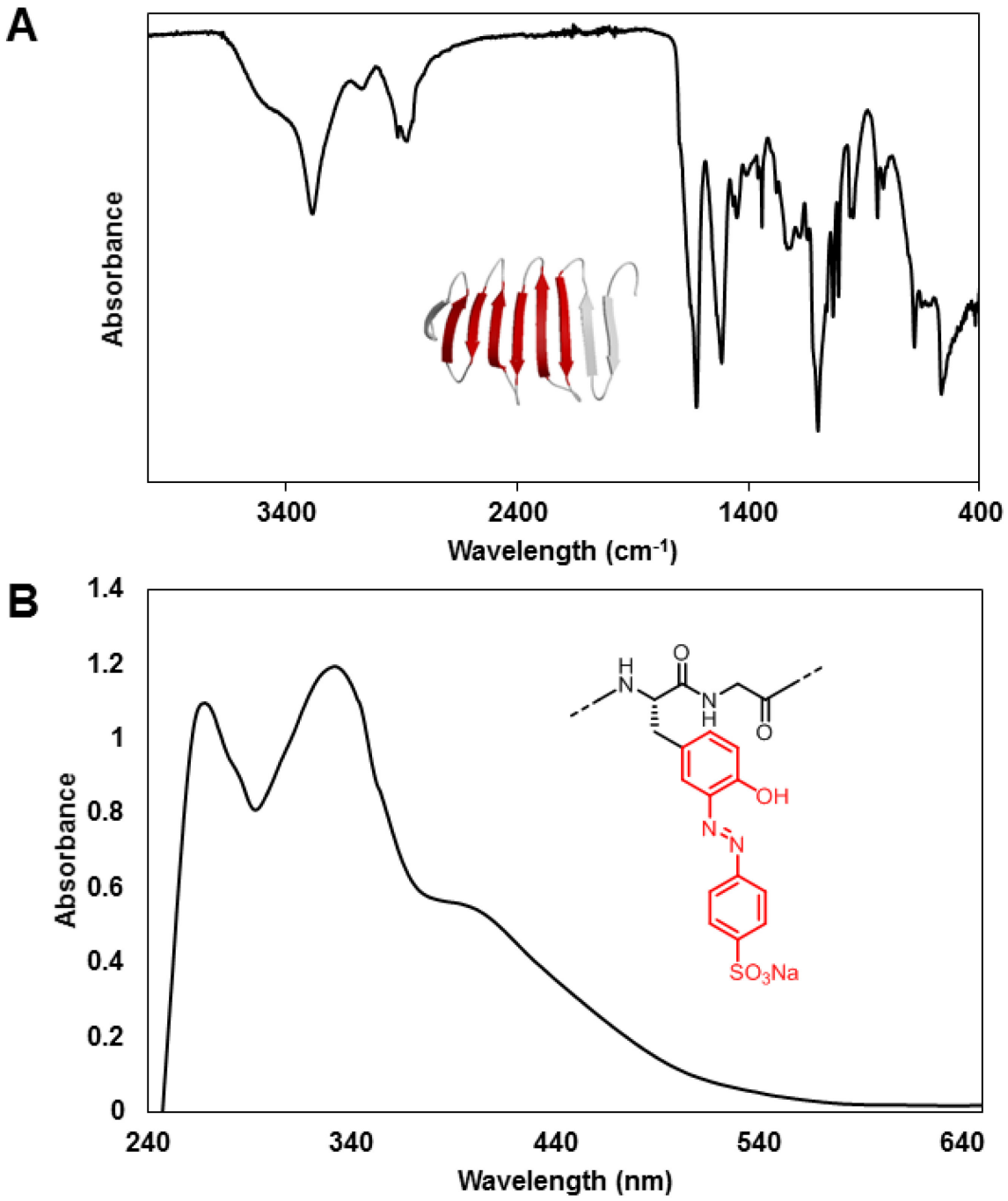

Figure 3.4. Characterization of the prepared azosilk (**#12**) nanofibers using **(A)** FTIR spectroscopy, and **(B)** UV-vis spectroscopy. **(A)** The characteristic vibration from Silk II amide structures (ν = 1650 cm^{-1}, 1627 cm^{-1}, 1535 cm^{-1}) is highly suggestive that the as-is made fibers are water resistant. Nevertheless, the fibers are treated with methanol and no change in the IR spectrum is observed. **(B)** UV-vis spectroscopy shows the characteristic sideband structure of azobenzene-modified silk.

3.4.3 **Assessing the mechanical properties of azosilk spun mats**

Ideal successful vascular support materials should be: (a) durable and possess a high tensile strength whilst maintaining a stiffness similar to native tissue (ideally 60-200 MPa Young's modulus and 1-3 MPa ultimate tensile strength),[43-45] while (b) maintaining structural integrity in a biological environment as well as, (c) possess adequate mechanical properties required for structural implantation into the body, and (d) exhibit a high surface area and porous structure that is semi-impermeable. To measure the mechanical characteristics for the azosilk grafts, uniaxial tensile testing was done until ultimate failure. To compare to previous measurements of the elastic (tensile) modulus of electrospun silk grafts, a linear regression analysis was performed on the linear portion of stress *vs* strain curves at 1% extension of the polymer. This was performed in triplicate and resulted in a tensile modulus of 230 ± 43 MPa, significantly below that of unmodified silk fibroin (515 MPa).[46] The characteristic yield strength typically occurred at 1.5% extension of the polymer (30 MPa), while the ultimate tensile strength was found to be 450 ± 50 MPa, from a series of 4 measurements. **Figure 3.5** shows a typical stress *vs* strain curve created by the thickest electrospun mat and identifies the elastic (shown in blue) and non-elastic (black) portions of the stress/strain curve. Electrospinning azosilk exhibits a reduced stiffness compared to the bulk films of silk and a specific stiffness less than Dacron – an industry standard. The reduced stiffness induced by electrospinning should aid in achieving a better compliance match with native vascular tissue and limit the pathological responses seen with compliance mismatch.[47]

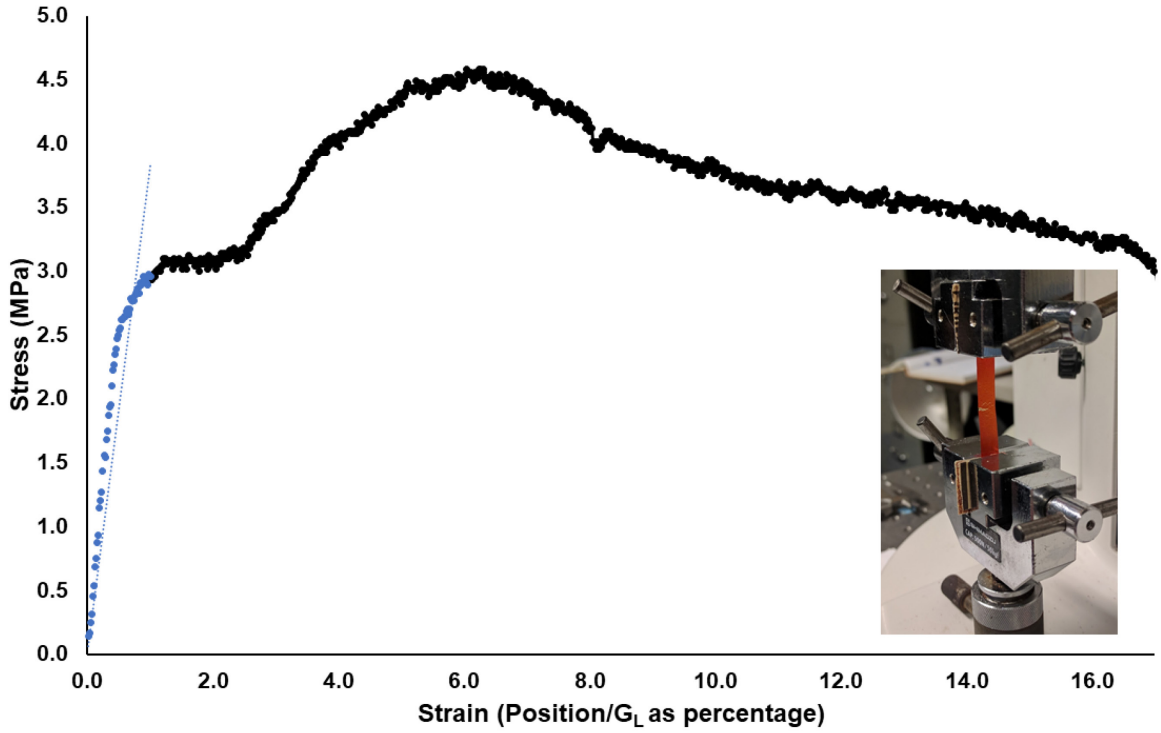

Figure 3.5. Stress vs strain curve of a mat of electrospun fibers showing the distinctive elastic region, yield strength, non-elastic region and ultimate tensile strength. The trend line illustrates the elastic region and where the Young's modus values are based from. From a series of data sets, a value of 230 ± 43 MPa is found. The inset image shows a photograph of azosilk mats being extended until ultimate failure.

The tensile elastic modulus of our material is well within the range expected for a vascular graft material. In addition to the bulk tensile properties, vascular graft material should support endothelial cell growth which is dependent on the surface mechanical properties. Substrate surface hardness can be used to elicit a wide variety of cellular responses, such as differentiation, motion and division. These cellular responses can be controlled with a surprisingly small range of hardness.[48-51] To explore the mechanical surface properties of our azosilk material, a series of 4 underwater AFM nanoindentations are conducted on drop-cast films. Bulk azosilk films were chosen as the substrate of choice for AFM indentation, as our electrospun mats contained a majority of azosilk polymer and minimal spin-aid polymer (5 wt%). The geometry of the electrospun fibres also proved to be difficult to indent into as the surface was found to be rough and inhomogeneous, thus it was difficult to determine the first contact point of the AFM tip to the

surface (BL-TR400PB tip, Asylum Research, k = 0.11 N/m at an indentation rate of 5 μm/s to a depth of 50 μm). The average of the indentation modulus of our azosilk film was calculated to be 12 kPa, which was found to be similar to previous hydrated silk measurements using the same method,[21] and is well within a range indicated to provide adequate mechanical support for endothelial cells. Further tuning of the modulus was achieved by irradiating the surface of the azosilk film with a two-photon confocal microscope (800 nm, 100 $\mu J/\mu m^2$) (**Figure 3.6**). **Figure 3.6A** is a pseudo-three-dimensional confocal microscope image of the irradiated surface. The irradiated area has risen above the film and created small fluid-filled microbubbles that was confined to the irradiated region of interest. AFM surface imaging of the interface between the irradiated microblisters and the non-irradiated surface is shown in **Figure 3.62B**, along with points where AFM indentation which was performed to determine modulus. Within the confines of the irradiated section, an elastic modulus was measured to be 0.6 kPa and demonstrated a significant photo-soften effect.

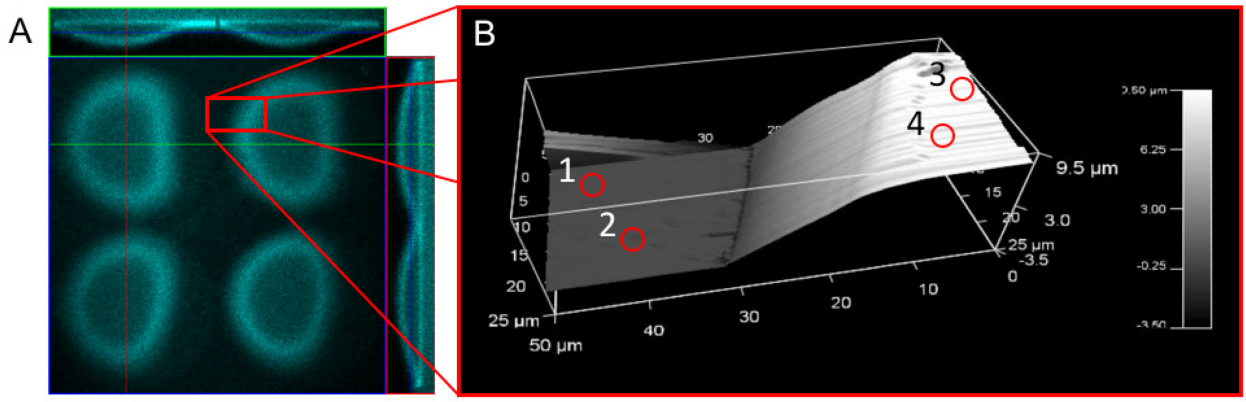

C

Indentation number	AFM modulus	Condition
1	11 kPa	Dark
2	12 kPa	Dark
3	0.65 kPa	Irradiated
4	0.60 kPa	Irradiated

Figure 3.6. Studying the effect of light on bulk azosilk materials using AFM indentation. **(A)** A confocal image demonstrating the effect of irradiating into films near the surface. A pseudo-three-dimensional representation of the surface is reconstructed by taking imaging slices of the irradiated film. Raised bubbles can be seen near the surface. **(B)** An AFM image of the surface of the film at the interface of the irradiated (bubble) and non-irradiated surface of the film. AFM indentation is performed in duplicate on both the irradiated (3 and 4) and non-irradiated surfaces (1 and 2). **(C)** The resulting table with each of the indentations and the resulting AFM moduli.

3.4.4 **Assessing the materials as viable supports for HAAECs**

Due to the nature of electrospinning, the graft material is porous and requires soaking with media before culturing HAAECs. This porosity allows for further tailoring of the supportive layer by loading growth factors into the scaffold. As a method to increase viability of the graft, they were soaked in HAAECs media (Promocell supplemented with 10% fetal bovine serum and 1% penicillin-streptomycin), which promotes adhesion and growth due to the added nutrients. **Figure 3.7** illustrates representative images of the HAAECs plated on the sodium sulfanilate azosilk mat. The cells were grown for 2 days in an incubator before being fixed and stained with FITC-phalloidin to visualize the F-actin within the material. The excitation of the FITC-phaloidin stained cells (488 nm) resulted in the electrospun material fluorescing, making it difficult to visualize the

f-actin-stained cells under excitation. Azosilk has been previously shown to fluoresce, when excited with 400 – 520 nm, and thus background fluorescence was found to be an issue.[21] Consequently, a background image of the azosilk submerged in PBS was taken and subtracted from each image. **Figure 3.7A** and **Figure 3.7B** show the actin staining on the surface and marks the cell placement. Cells are spread in their typical cobblestone shape. Large uni-axial F-actin fibers are present and end in dense peripheral actin bands onto the surface where the buildup of F-actin indicates attachment and focal adhesion. **Figure 3.7 C-D** is a representative pseudo-three-dimensional image that shows the surface and the cells built up onto it. The cells form a fairly uniform monolayer and spread across the fibrous surface. X and Y projections of **Figure 3.7C** show these monolayers along with multiple cells forming thicker layers.

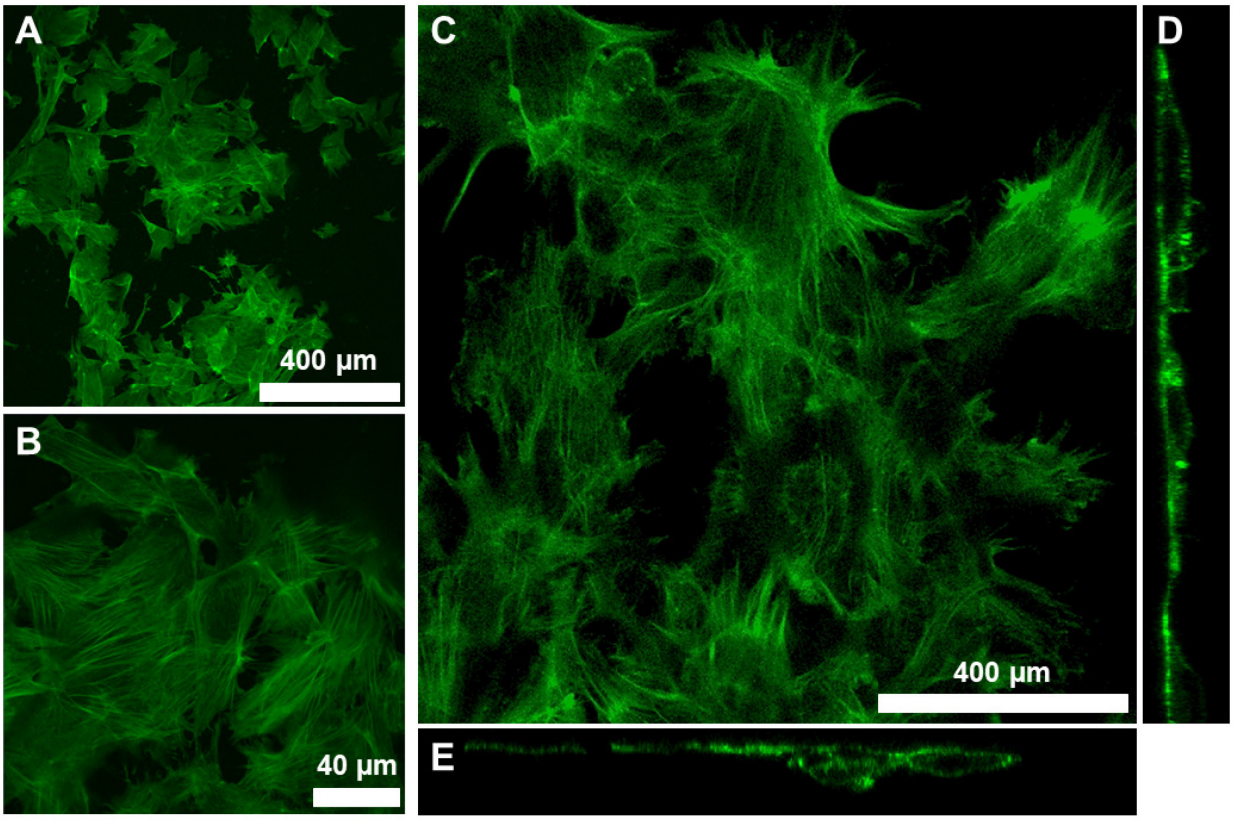

Figure 3.7. Representative images HAAECs seeded onto the electrospun azosilk material at a density of 5 x 10^5 cells/mL. Cells are stained with FITC-phallodin as a mark for F-actin. **(A)** Representative images at 100 x showing the overall density found for the cells, and **(B)** 630 x showing the fiberous f-actin staining on the surface/cell interact. Images in **(C-E)** represent a pseudo-three-dimensional reproduction of the cells on the surface with **(C)** representing the XY plan, **(D)** representing the YZ plane, and **(E)** represents the XZ plane. Each of the planes shows the buildup of the cells onto the surface, and attachment along the plane of the surface.

3.5 Conclusion

A series of azo-dye functionalized silks were prepared, assessed for their cellular viability, and the highest performing material was electrospun into mats. The electrospun silk was demonstrated to have suitable mechanical characteristics for vascular reconstruction surgery and possess optimal surface properties that improve hemocompatibility. Electrospinning of this biomaterial allowed for the creation of a graft that is easy to post-process and is compatible with industrial scale processes for vascular grafts. We believe that the formation of this new family of

azosilk materials, along with our process to spin them into effective supportive scaffolds for tissues holds promise as an effective tool to study and create grafts of HAAECs for biomedical devices, stent coatings and as effective materials that are useful in vascular surgical applications where effective endothelialization is crucial.

3.6 **Acknowledgements**

The project was support by a Collaborative Health Research Program (CHRP) grant from the Canadian Institutes of Health Research (CIHR 357055) and the Natural Sciences and Engineering Research Council (NSERC 493633-16, 261938-13).

3.7 **References**

1. Friedman, S. G., *A History of Vascular Surgery*. Blackwell Futura: New York, **2008**.

2. Voorhees, A. B.; Jaretzki, A.; Blakemore, A. H., The use of tubes constructed from vinyon "N" cloth in bridging arterial defects: a preliminary report. *Ann. Surg.* **1952**, *135* (3), 332–336.

3. Stoney, R. J.; Albo, R. J.; Wylie, E. J., False aneurysms occurring after arterial grafting operations. *Am. J. Surg.* **1965**, *110* (2), 153–161.

4. Weyand, M.; Kerber, S.; Schmid, C.; Rolf, N.; Scheld, H. H., Coronary artery bypass grafting with an expanded polytetrafluoroethylene graft. *Ann. Thorac. Surg.* **1999**, *67* (5), 1240–1244.

5. Wang, X.; Lin, P.; Yao, Q.; Chen, C., Development of small-diameter vascular grafts. *World J. Surg.* **2007,** *31* (4), 682–689.

6. Hehrlein, F.; Schlepper, M.; Loskot, F.; Scheld, H.; Walter, P.; Mulch, J., The use of expanded polytetrafluoroethylene (PTFE) grafts for myocardial revascularization. *J. Cardiovasc. Surg.* **1984,** *25* (6), 549–553.

7. DeBakey, M. E.; Cooley, D. A.; Crawford, E. S.; Morris, G. C., Jr., Aneurysms of the thoracic aorta; analysis of 179 patients treated by resection. *J. Thorac. Surg* **1958,** *36* (3), 393–420.

8. Landry, M. J.; Rollet, F.-G.; Kennedy, T. E.; Barrett, C. J., Layers and multilayers of self-assembled polymers: Tunable engineered extracellular matrix coatings for neural cell growth. *Langmuir* **2018**, *34* (30), 8709–8730.

9. Hubbell, J. A., Biomaterials in Tissue Engineering. *Bio/technology* **1995**, *13*, 565–576.

10. Schmidt, C. E.; Baier, J. M., Acellular vascular tissues: natural biomaterials for tissue repair and tissue engineering. *Biomaterials* **2000**, *21* (22), 2215–2231.

11. Shin, H.; Jo, S.; Mikos, A. G., Biomimetic materials for tissue engineering. *Biomaterials* **2003**, *24* (24), 4353–4364.

12. Akintewe, O. O.; Roberts, E. G.; Rim, N.-G.; Ferguson, M. A. H.; Wong, J. Y., Design approaches to myocardial and vascular tissue engineering. *Annu. Rev. Biomed. Eng.* **2017**, *19* (1), 389–414.

13. Sato, M.; Nakazawa, Y.; Takahashi, R.; Tanaka, K.; Sata, M.; Aytemiz, D.; Asakura, T., Small-diameter vascular grafts of *Bombyx mori* silk fibroin prepared by a combination of electrospinning and sponge coating. *Mater. Lett.* **2010**, *64* (16), 1786–1788.

14. Yagi, T.; Sato, M.; Nakazawa, Y.; Tanaka, K.; Sata, M.; Itoh, K.; Takagi, Y.; Asakura, T., Preparation of double-raschel knitted silk vascular grafts and evaluation of short-term function in a rat abdominal aorta. *J. Artif. Organs* **2011**, *14* (2), 89–99.

15. Aytemiz, D.; Sakiyama, W.; Suzuki, Y.; Nakaizumi, N.; Tanaka, R.; Ogawa, Y.; Takagi, Y.; Nakazawa, Y.; Asakura, T., Small-diameter silk vascular grafts (3 mm diameter) with a double-Raschel knitted silk tube coated with silk fibroin sponge. *Adv. Healthcare Mater.* **2013**, *2* (2), 361–368.

16. Zhang, X.; Baughman, C. B.; Kaplan, D. L., *In vitro* evaluation of electrospun silk fibroin scaffolds for vascular cell growth. *Biomaterials* **2008**, *29* (14), 2217–2227.

17. Wang, D.; Liu, H.; Fan, Y., Silk fibroin for vascular regeneration. *Microsc. Res. Tech.* **2017,** *80* (3), 280–290.

18. Wendorff, J. H.; Agarwal, S.; Greiner, A., *Electrospinning: materials, processing, and applications*. John Wiley & Sons: Hoboken, NJ. **2012**.

19. Liu, H.; Hsieh, Y.-L., Ultrafine fibrous cellulose membranes from electrospinning of cellulose acetate. *J. Polym. Sci. B.* **2002**, *40* (18), 2119–2129.

20. Murphy, A. R.; John, P. S.; Kaplan, D. L., Modification of silk fibroin using diazonium coupling chemistry and the effects on hMSC proliferation and differentiation. *Biomaterials* **2008**, *29* (31), 2829–2838.

21. Landry, M. J.; Applegate, M. B.; Bushuyev, O. S.; Omenetto, F. G.; Kaplan, D. L.; Cronin-Golomb, M.; Barrett, C. J., Photo-induced structural modification of silk gels containing azobenzene side groups. *Soft Matter* **2017,** *13* (16), 2903–2906.

22. Serban, M. A.; Kaplan, D. L., pH-Sensitive ionomeric particles obtained *via* chemical conjugation of silk with poly(amino acid)s. *Biomacromolecules* **2010,** *11* (12), 3406–3412.

23. Rockwood, D. N.; Preda, R. C.; Yucel, T.; Wang, X.; Lovett, M. L.; Kaplan, D. L., Materials fabrication from *Bombyx mori* silk fibroin. *Nat. Protoc.* **2011**, *6* (10), 1612–1631.

24. Bhardwaj, N.; Kundu, S. C., Electrospinning: A fascinating fiber fabrication technique. *Biotechnol. Adv.* **2010**, *28* (3), 325–347.

25. Yarin, A. L.; Koombhongse, S.; Reneker, D. H., Taylor cone and jetting from liquid droplets in electrospinning of nanofibers. *J. Appl. Phys.* **2001**, *90* (9), 4836–4846.

26. Koh, L.-D.; Cheng, Y.; Teng, C.-P.; Khin, Y.-W.; Loh, X.-J.; Tee, S.-Y.; Low, M.; Ye, E.; Yu, H.-D.; Zhang, Y.-W.; Han, M.-Y., Structures, mechanical properties and applications of silk fibroin materials. *Prog. Polym. Sci.* **2015**, *46*, 86–110.

27. Albert, J. N. L.; Epps, T. H., Self-assembly of block copolymer thin films. *Mater. Today* **2010**, *13* (6), 24–33.

28. Grinnell, F.; Feld, M., Fibronectin adsorption on hydrophilic and hydrophobic surfaces detected by antibody binding and analyzed during cell adhesion in serum-containing medium. *J. Biol. Chem.* **1982**, *257* (9), 4888–4893.

29. Arima, Y.; Iwata, H., Effect of wettability and surface functional groups on protein adsorption and cell adhesion using well-defined mixed self-assembled monolayers. *Biomaterials* **2007**, *28* (20), 3074–3082.

30. Aamodt, J. M.; Grainger, D. W., Extracellular matrix-based biomaterial scaffolds and the host response. *Biomaterials* **2016,** *86*, 68–82.

31. Karp, G., *Cell and molecular biology: Concepts and experiments.* John Wiley & Son: Hoboken, NJ. 2006.

32. Van Wachem, P. B.; Beugeling, T.; Feijen, J.; Bantjes, A.; Detmers, J. P.; van Aken, W. G., Interaction of cultured human endothelial cells with polymeric surfaces of different wettabilities. *Biomaterials* **1985,** *6* (6), 403–408.

33. Roach, P.; Parker, T.; Gadegaard, N.; Alexander, M. R., Surface strategies for control of neuronal cell adhesion: A review. *Surf. Sci. Rep.* **2010**, *65* (6), 145–173.

34. Valentini, R. F.; Vargo, T. G.; Gardella, J. A.; Aebischer, P., Patterned neuronal attachment and outgrowth on surface modified, electrically charged fluoropolymer substrates. *J. Biomater. Sci., Polym. Ed.* **1994**, *5* (1-2), 13–36.

35. Webb, K.; Hlady, V.; Tresco, P. A., Relative importance of surface wettability and charged functional groups on NIH 3T3 fibroblast attachment, spreading, and cytoskeletal organization. *J. Biomed. Mater. Res.* **1998**, *41* (3), 422–430.

36. Tidwell, C. D.; Ertel, S. I.; Ratner, B. D.; Tarasevich, B. J.; Atre, S.; Allara, D. L., Endothelial cell growth and protein adsorption on terminally functionalized, self-assembled monolayers of alkanethiolates on gold. *Langmuir* **1997**, *13* (13), 3404–3413.

37. Jin, H.-J.; Fridrikh, S. V.; Rutledge, G. C.; Kaplan, D. L., Electrospinning *Bombyx mori* silk with poly(ethylene oxide). *Biomacromolecules* **2002**, *3* (6), 1233–1239.

38. Chen, C.; Chuanbao, C.; Xilan, M.; Yin, T.; Hesun, Z., Preparation of non-woven mats from all-aqueous silk fibroin solution with electrospinning method. *Polymer* **2006**, *47* (18), 6322–6327.

39. Meine, A.J.; Kubow, K.E.; Klotzsch, E.; Garcia-Fuentes, M.; Smith, M.L.; Vogel, V.; Merkle, H.P.; Meinel, L. Optimization strategies for electrospun silk fibroin tissue engineering scaffolds. *Biomaterials* **2009**, *30* (17), 3058–3067.

40. Asakura, T.; Yao, J.; Yamane, T.; Umemura, K.; Ulrich, A. S., Heterogeneous structure of silk fibers from *Bombyx mori* resolved by ^{13}C solid-state NMR Spectroscopy. *J. Am. Chem. Soc.* **2002**, *124* (30), 8794–8795.

41. Diao, Y. Y.; Liu, X. Y.; Toh, G. W.; Shi, L.; Zi, J., Multiple structural coloring of silk-fibroin photonic crystals and humidity-responsive color sensing. *Adv. Funct. Mater.* **2013**, *23* (43), 5373–5380.

42. Freddi, G.; Pessina, G.; Tsukada, M., Swelling and dissolution of silk fibroin (*Bombyx mori*) in N-methyl morpholine N-oxide. *Int. J. Biol. Macromol.* **1999,** *24* (2-3), 251–263.

43. Nolte, A. J.; Treat, N. D.; Cohen, R. E.; Rubner, M. F., Effect of relative humidity on the Young's modulus of polyelectrolyte multilayer films and related nonionic polymers. *Macromolecules* **2008**, *41* (15), 5793–5798.

44. Sailer, M.; Lai Wing Sun, K.; Mermut, O.; Kennedy, T. E.; Barrett, C. J., High-throughput cellular screening of engineered ECM based on combinatorial polyelectrolyte multilayer films. *Biomaterials* **2012**, *33* (24), 5841–5847.

45. Schneider, A.; Francius, G.; Obeid, R.; Schwinté, P.; Hemmerlé, J.; Frisch, B.; Schaaf, P.; Voegel, J.-C.; Senger, B.; Picart, C., Polyelectrolyte multilayers with a tunable Young's modulus: Influence of film stiffness on cell adhesion. *Langmuir* **2006**, *22* (3), 1193–1200.

46. Ayutsede, J.; Gandhi, M.; Sukigara, S.; Micklus, M.; Chen, H.-E.; Ko, F., Regeneration of *Bombyx mori* silk by electrospinning. Part 3: characterization of electrospun nonwoven mat. *Polymer* **2005**, *46* (5), 1625–1634.

47. Tremblay, D.; Zigras, T.; Cartier, R.; Leduc, L.; Butany, J.; Mongrain, R.; Leask, R. L., A comparison of mechanical properties of materials used in aortic arch reconstruction. *Ann. Thorac. Surg.* **2009**, *88* (5), 1484–1491.

48. Bai, S.; Zhang, W.; Lu, Q.; Ma, Q.; Kaplan, D. L.; Zhu, H., Silk nanofiber hydrogels with tunable modulus to regulate nerve stem cell fate. *J. Mater. Chem. B Mater. Biol. Med.* **2014**, *2* (38), 6590–6600.

49. Banerjee, A.; Arha, M.; Choudhary, S.; Ashton, R. S.; Bhatia, S. R.; Schaffer, D. V.; Kane, R. S., The influence of hydrogel modulus on the proliferation and differentiation of encapsulated neural stem cells. *Biomaterials* **2009**, *30* (27), 4695–4699.

50. Gao, M.; Tao, H.; Wang, T.; Wei, A.; He, B., Functionalized self-assembly polypeptide hydrogel scaffold applied in modulation of neural progenitor cell behavior. *J. Bioact. Compat. Polym.* **2016**, *32* (1), 45–60.

51. Leipzig, N. D.; Shoichet, M. S., The effect of substrate stiffness on adult neural stem cell behavior. *Biomaterials* **2009**, *30* (36), 6867–6878.

Appendix 2: Supplemental information for Chapter 3

Materials characterization

Materials were characterized using standard characterizing techniques, including topographical and structural information, chemical properties, surface properties, and mechanical properties.

Electron microscopy images

A dye was used to cut out a circular piece of the electrospun material and the sample was sputter-coated and a piece of conductive tape was used to ground the sample to the SEM. The sample was imaged on a SU3500 Hitachi scanning electron microscopy, and an assortment of extra images were collected and shown in **Figure A2.1**.

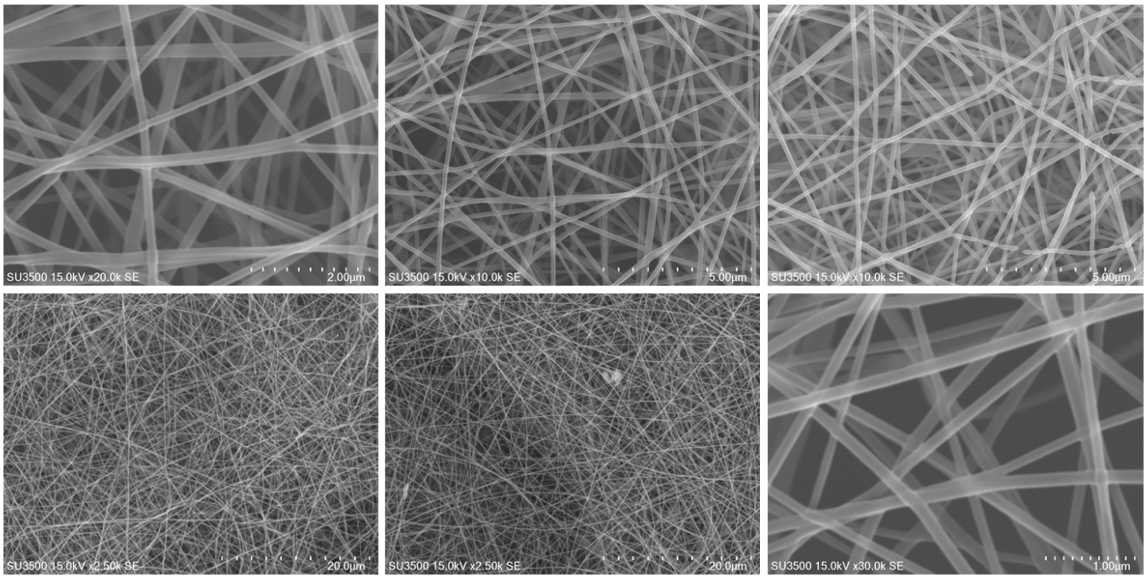

Figure A2.1. Scanning electron microscopy images of the optosilk mats created from the procedure outlined in **Section 3.2.5**. Images were taken on SU3500 Hitachi SEM using a specialized setup which is outlined in **Section 3.2.6**.

Tensile strength measurement

The tensile strength was measured experimentally using Shimadzu ez test tensile tester in tensile strength mode with a maximum load of 5.5 N. The samples were loaded into the machine, their thickness, length and G_L was measured and used to calculate the cross-sectional area. Each

sample was extended until failure and their tensile strength calculated in triplicate. **Table A2.1** shows the resulting data subset.

Table A2.1. Table denoting the cross-sectional area, initial length and calculated tensile strength as determined from regression analysis of stress vs strain curves generated by stretching optosilk electrospun mats. Regression analysis is performed on data generated from 1% extension of the polymer. Standard error is shown for the total population.

Sample	Cross-sectional area (mm^2)	G_L (mm)	Tensile strength (MPa)
Opto-silk fibres 1	0.33	12.3	283 ± 15
Opto-silk fibres 2	0.41	13.3	147 ± 4
Opto-silk fibres 3	0.25	9.6	269 ± 14
Average			233 ± 43

Contact angle measurements

Contact angle measurements were performed on family of opto-silk surfaces. The contact angle was measured by placing the studied surface onto a level surface and a 50 μL drop of water was placed onto the surface and a photo was taken. This process was repeated three times, and the angle which the surface and the water drop made was measured and averaged three times. **Table A2.2** contains the complete dataset of contact angles of the studied opto-silks.

Table A2.2. Contact angle of the select members of the opto-silk family. Each structure of the headgroups are presented along-side the measured contact angle. Each measurement is performed three times and the average value is presented with standard deviation.

Substrate number	Head group structure	Contact angle (deg)
1	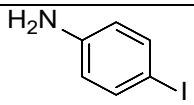	**48 ± 2**
2	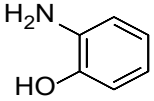	**56 ± 1**
3	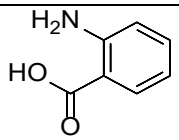	**12 ± 3**
4	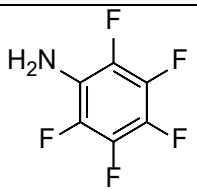	**120 ± 3**
5	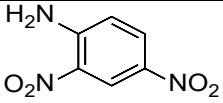	**45 ± 4**
6	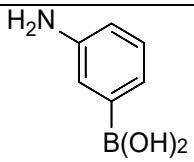	**40 ± 2**
7	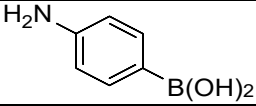	**45 ± 5**
8	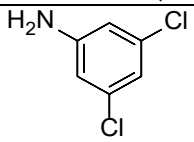	**85 ± 0**
9	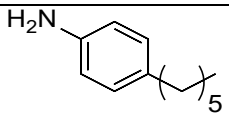	**90 ± 1**
10	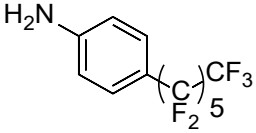	**129 ± 2**
11	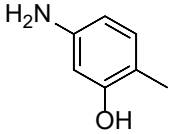	**60 ± 3**

12	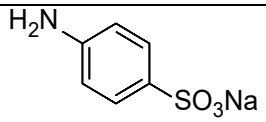	**2 ± 2**
13	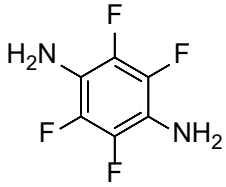	**13 ±4**
14	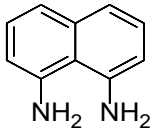	**90 ± 4**
15	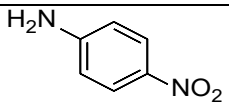	**58 ± 4**
16	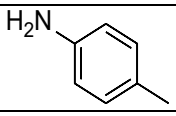	**65 ± 2**
Silk	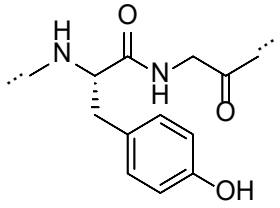	**74 ± 5**
Blank		**85 ± 4**

NMR of the opto-silk material

A solution of purified opto-silk (**Section 3.3.2**) was mixed with D_2O (10%) and placed into a NMR tube. A proton NMR spectrum was acquired using a "Wet 1D" pulse sequence which suppresses signal occurring from water. A HSQC spectrum was also acquired using pre-saturation of the water signal. A complex spectrum of amino acids was observed from the 1D ^1H NMR spectrum. The distinct lack of peaks associated with 4-aminobenzenesulfonate or 4-hydrobenzenesulfonate were seen, the only possible impurities associated with the synthesis of opto-silk (used in the formation of the diazonium salt).

^1H NMR (500 MHz, Deuterium Oxide) δ 7.01 – 6.80 (m, 4H), 6.25 – 6.66 (m, 4H), 4.64 (d, J = 6.1 Hz, 1H), 4.19 (dq, J = 16.3, 7.3 Hz, 1H), 3.93 – 3.60 (m, 5H), 1.25 (q, J = 11.4, 9.0 Hz, 4H), 0.85 – 0.57 (m, 1H).

AFM imaging and modulus measurement

Water stable films were created from azosilk (**#12**) and irradiated with a confocal microscope (Zeiss Axioexaminer upright microscope, equipped with a Chameleon direct-coupled multiphoton laser). Films are irradiated using 800 nm light (100 μJ/μm2) within a controlled region of interest. After films were irradiated, the sample was imaged using an MFP-3D SA atomic force microscope with molecular force probe 3D controller (Asylum Research, Santa Barbara, CA). A tip (BL-TR400PB, Asylum Research, k = 0.11 N/m) was used to image the surface (Figure 6, main text), and a series of in situ underwater AFM indentations were conducted. 2 indentations were conducted on a non-irradiated area, and 2 were conducted on an area which was irradiated. The sample indentation and retraction curves were fitted assuming a Hertz model (Hertz area = 12.8 μm^2, with a sample Poisson ratio of 0.33. The tip's Poisson ratio was found to be 0.2.

Live/Dead Assay

Table A2.3. Alive and dead percentages for each of the head groups of opto-silk. A dramatic difference between is observed between each head group illustrating either the physical properties of the films or the cytotoxicity of the film materials.

Substrate number	Head group structure	Alive (%)	Dead (%)
1	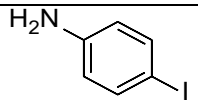	68 ± 8	32 ± 8
2	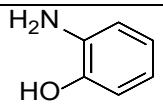	75 ± 5	25 ± 5
3	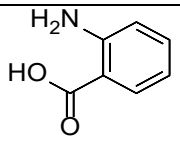	81 ± 6	19 ± 6
4	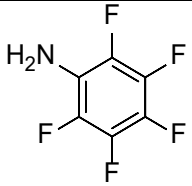	30 ± 6	70 ± 6
5	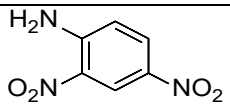	55 ± 5	45 ± 5

6	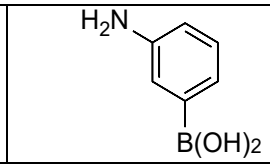	69 ± 3	31 ± 3
7	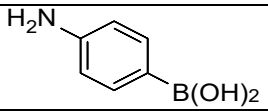	35 ± 10	65 ± 10
8	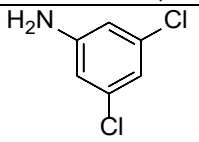	60 ± 5	40 ± 5
9	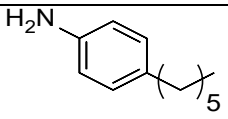	55 ± 6	45 ± 6
10	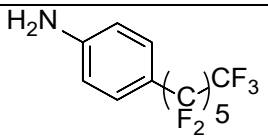	20 ± 5	80 ± 5
11	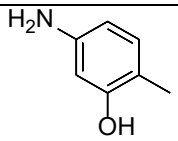	59 ± 5	41 ± 5
12	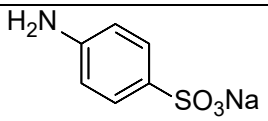	90 ± 5	10 ± 5
13	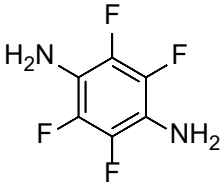	86 ± 5	14 ± 5
14	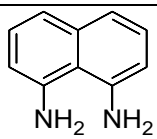	45 ± 4	55 ± 4
15	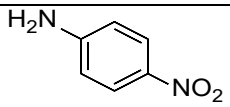	61 ± 6	39 ± 6
16	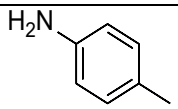	75 ± 8	25 ± 8
Silk	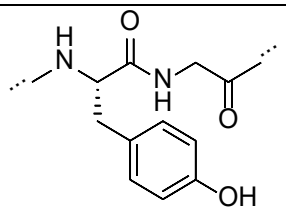	85 ± 2	15 ± 2
Blank		45 ± 3	55 ± 3

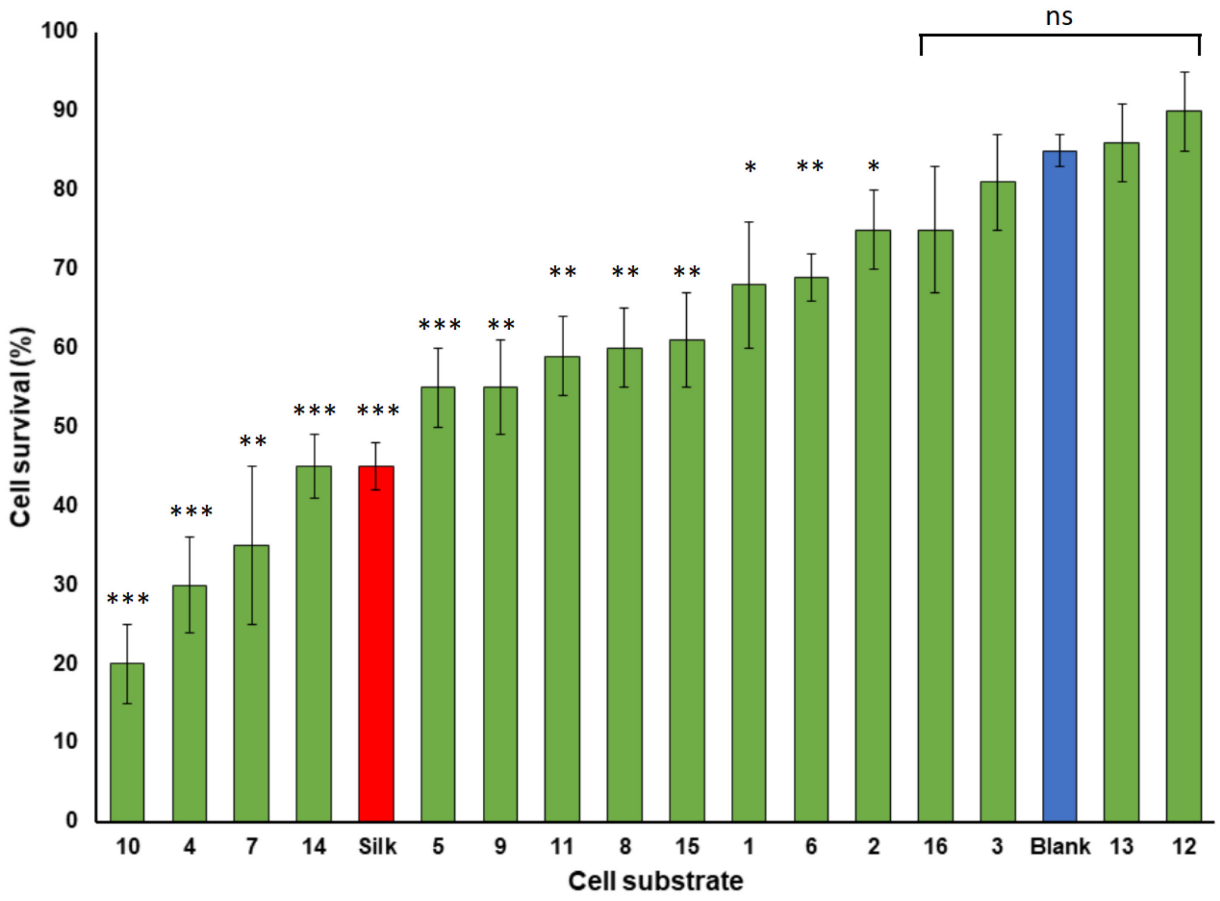

Figure A2.2. Histogram depicting the values from **Table A2.2** noted with standard deviation. The statistics shown are comparing with the proprietary film coating (Blank) of the 24 well plate. $P > 0.05$ (ns), $P \leq 0.05$ (*), $P \leq 0.01$ (**), and $P \leq 0.001$ (***).

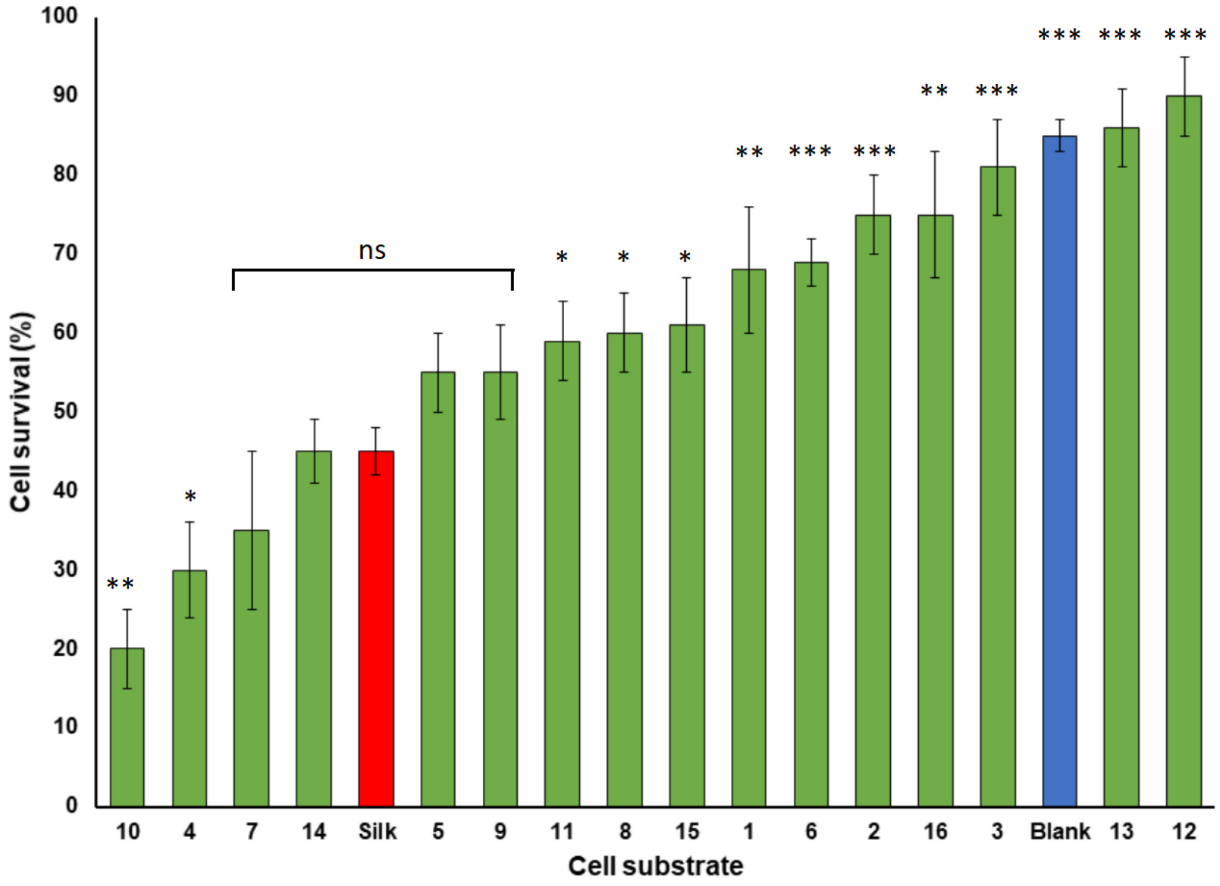

Figure A2.3. Histogram depicting the values from **Table A2.2** noted with standard deviation. The statistics shown are comparing with a film created from non-functionalized silk which has been slow-dried to maximum β-sheet formation. $P > 0.05$ (ns), $P \leq 0.05$ (*), $P \leq 0.01$ (**), and $P \leq 0.001$ (***).

Rationale for Chapter 4: Photo-induced structural modification of silk gels containing azobenzene side groups

Within Chapter 3, we investigated the effect of electrospinning our best performing azosilk polymers into a three-dimensional supportive material for culturing and supporting endothelial cell growth. This investigation led us to the creation of a material with the correct tensile and elastic modulus for creating cell-supportive materials for cell culture with appropriate mechanical properties for suturing and implantation. The investigation of cell-substrate interactions within biological materials is a fascinating tissue engineering topic. Having an exact and precise control over the surface morphology can aid in guiding cells and hence allow the study of specific cell-cell interactions or cell-surface interactions. The majority of the work within this field revolves around using intricate and often expensive clean-room techniques that employ harsh chemicals and reagents which are usually cytotoxic. The work on creating soft, wet and supportive materials (Chapter 3) is extended to Chapter 4, where we explore the photomechanical properties of our most highly supportive azosilk. We envisioned creating an externally addressable and tunable biomaterial to avoid the use of lengthy and expensive clean-room techniques and, at the same time, to possess direct control over the topology and morphology of the surface. The contribution 'Photo-induced structural modification of silk gels containing azobenzene side groups' was co-authored by Michael J. Landry, Matthew B. Applegate, Dr. Oleksandr S. Bushuyev, Prof. Fiorenzo G. Omenetto, Prof. David L. Kaplan, Prof. Mark Cronin-Golomb, and Prof. Christopher J. Barrett, and published in *Soft Matter*, and provides a means to modify topology, morphology and modulus of a biomaterial using two-photon excitation from a standard confocal microscope.

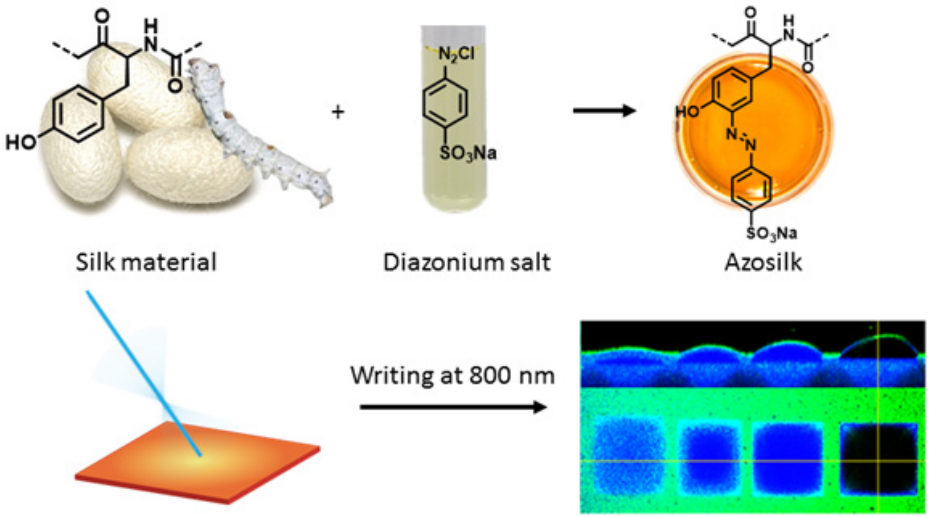

Chapter 4: Photo-induced structural modification of silk polymer gels containing azobenzene side groups

Chapter 4 is based on a published manuscript entitled 'Photo-induced structural modification of silk polymer gels containing azobenzene side groups', published in *Soft Matter* (Copyright 2017 Royal Society of Chemistry), and was co-authored by: Michael J. Landry, Matthew B. Applegate, Dr. Oleksandr S. Bushuyev, Prof. Fiorenzo G. Omenetto, Prof. David L. Kaplan, Prof. Mark Cronin-Golomb, and Prof. Christopher J. Barrett.

4.1 Abstract

Azobenzene modification of *Bombyx mori* silkworm silk creates a photo-responsive 'azosilk' biomaterial, allowing for 3D laser patterning. Written regions fluoresce and become fluid-filled raised 'micro-blisters' with a 10-fold photo-softening effect of the modulus. Patterning is facile and versatile, with potential applications as soft tunable materials for dynamic cell guidance and microfluidics.

4.2 Introduction

Silk fibroin from *Bombyx mori* silkworms is a versatile biocompatible material receiving recent interest in tissue engineering, bioelectronics and optics.[1–4] The optical clarity of silk films and gels make it attractive for applications in the design of some biomedical devices, particularly implantable optical components requiring soft biocompatible parts.[5–8] Many of these applications require the ability to pattern the material and thus several methods have been reported including soft lithography,[9,10] nano-imprinting,[11,12] electron lithography,[13,14] chemical modification of silk to form methacrylate-based photoresists,[15] and optical micromachining in cross-linked silk hydrogels.[16]

When silk is processed into useful materials such as films, microspheres, sponges, tubes, gels and fibers, it can retain the elastic properties related its secondary structure. Silk possesses regions of highly repetitive sequences of amino acids, which lead to well-defined structural domains. This offers the potential for facile and controllable chemical modifications with photo-active compounds, to introduce the ability to post-engineer its physical properties using light. A convenient method for this is to use diazonium coupling to the tyrosine residues, effectively incorporating light-responsive azobenzene into the silk structure. Azobenzene and its derivatives

see wide use in developing optically sensitive materials for applications including optical storage, holography,[17,18] and optically actuated micro-mechanical systems (MEMS),[19–21] based on reversible photo-switching between the trans and cis geometric isomers. The recent demonstration of the functionalization of silk with various azobenzene moieties (azosilk) provides a facile route to incorporate the optical properties of azobenzene into silk.[22,23]

Azosilk has previously been shown to exhibit optically-induced birefringence and holographic recording in dry thin films.[23] In this paper, we report the discovery that permanent three-dimensional topographic micro-patterning in hydrated azosilk films can be achieved through photo-induced physical modification of azosilk films using the photolithographic capabilities of a nonlinear scanning microscope. We observed two newly discovered light-induced changes: a significant shift in fluorescence emission wavelength, and key to proposed applications: volume morphology changes, which subsequently control surface stiffness over a wide range. The morphology changes are in the form of raised blisters, which have the potential to guide cells through modulus and topography changes on the surface of the silk films.

4.3 Results and discussion

We prepared azosilk materials following previous literature protocols,[22] with some modifications (see **Appendix 3**) and cast them into thin films. Films were submerged into water to ensure even hydration and a dipping lens was used to minimize scattering during the writing. The water content of these films was found to comprise 77 wt% of the material from TGA characterization (**Figure A3.4**). While studying the optical properties of these azosilk films with a nonlinear scanning microscope using a femtosecond mode-locked laser at 800 nm, we observed that the regions under observation fluoresced with peak emission at 625 nm corresponding to the known fluorescence of azobenzene,[24] but over time developed significantly increased fluorescence accompanied by a shift of the emission peak to 520 nm (**Figure A3.1**). Desired areas could be patterned using a Zeiss Axioexaminer nonlinear optical scanning microscope, with specific regions of interest exposed to laser light to form precise and arbitrary composite patterns.[25] This lithographic technique allows for the creation of complex patterns by combining numerous programmable exposure areas referred to in the software as ‘regions of interest’. These regions are generated by a Matlab code[25] from a black and white image, thus allowing for the programmable patterning of complex and arbitrary written areas within the film. **Figure 4.1** presents an example

where such spatial control over laser irradiation enables the inscription of the test words “McGill” and “Tufts” at different depths in the film composed of more than 200 regions of interest. The fluorescent patterns were formed using two-photon femtosecond pulse excitation at 800 nm at 80 MHz repetition rate within these regions of interest. The width of the pulses was 250 fs after including the dispersive effects of the objective lens and the acousto-optic modulator in the microscope after the laser (Chameleon by Coherent). The fluorescence patterns that result represent a facile marker of visually tracking the inscribed areas. When the writing energy was increased to 100 μJ μm^{-2} (2500 pulses), a more important physical effect was observed; the film would form large soft raised blisters on the surface of the material, coincident with the lithographic irradiation pattern. These blisters were filled with a fluorescent liquid whose peak emission wavelength closely matched those of plain silk photo-irradiated by more intense 800 nm light (900 μJ μm^{-2}).

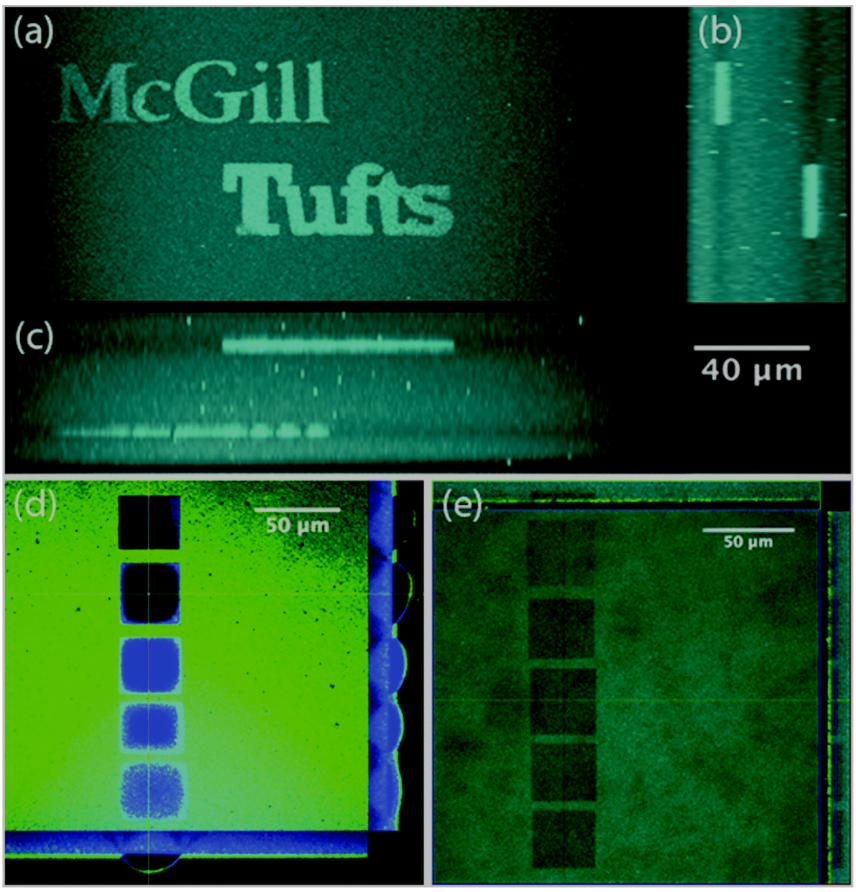

Figure 4.1. (a) Written areas of the hydrated azosilk film show increased fluorescence compared to the unwritten areas at two different depths within the hydrated film. The darkening shown in the writing planes is an artifact of the software. **(b)** Vertical projection of three-dimensional photolithography image of **(a)**. **(c)** Horizontal projection of the image shown in **(a)**. **(d)** Confocal fluorescence image at 488 nm excitation (blue) and reflectance image (green) of hydrated azosilk with photo-modified regions. From top to bottom, each rectangle is written 1 µm deeper into the azosilk. The cross-sections of the film show the development of blisters whose thickness decreases with writing depth. Each 37 µm × 37 µm rectangle takes 1.5 seconds of writing time. Each 0.4 µm × 0.4 µm pixel receives 2500 pulses each with 1.25 nJ energy and 250 fs pulse width. **(e)** Confocal fluorescence imaging at 488 nm excitation (blue) and reflectance image (green) of hydrated unmodified silk pattern-irradiated in the same manner as **(a)**, showing lack of blistering.

To study the blister formation, a set of 5 rectangles was written (**Figure 4.1 (d)**). The rectangle at the top of the figure was written just under the surface, and subsequent rectangles presented below it were written at increasing depth in the film in steps of 1 µm. While the axial

resolution of the microscope under the conditions used is only about 1 μm, the peak intensity of the beam can still be stepped in down in 1 μm increments, with corresponding shifts in the mean depth of illumination and pattern writing. Within **Figure 4.1 (d)** and **Figure 4.1 (e)**, green colour indicates the surface of the film by reflectance confocal while blue corresponds to broadband fluorescence excited at 488 nm, showing signals from the unexposed azosilk as well as fluorescence from the exposed areas. The film expands vertically (parallel to the axis of the laser beam) to form blisters with the height of 13 μm for samples irradiated near surface. The blister height decreases upon an increase in writing depth presumably because stronger physical confinement deep in the hydrated film. The uniformity of fluorescence in the material within the blisters suggests that they are liquid-filled. The top two bubbles appeared to be so thin that their porosity allowed the fluorescent contents to escape into the surrounding water solution, while the lower three blisters remained intact and fluid-filled.

To determine the contents of the fluid-filled blisters, a series of 100 disc shaped blisters were created and their liquid was manually extracted using a micro-needle. NMR analysis was conducted on the withdrawn liquid and it was concluded that the fluorescent liquid was mainly water along with some trace amino acid residues (see **Appendix 3**). Fluorescence lithography was also performed in hydrated unmodified silk as a control, with very different results observed at the same writing parameters than for azosilk (**Figure 4.1 (e)**). In this case, fluorescence peaking at 470 nm is simply diminished in intensity, and no blistering is observed. When the writing energy is increased to 900 μJ μm^{-2}, the plain silk films sustain observable structural damage that does not conform closely to the lithography pattern (**Figure A3.3**, **Appendix 3**). There is a simultaneous increase in fluorescence intensity in the damaged regions accompanied by a 20 nm shift towards shorter wavelengths. Irradiation of hydrated films of azosilk produces permanent fluorescent blisters written into them, with patterns still easily observable after 3 months as long as they are kept under water. The fluorescence spectra (**Figure A3.1**) of written and unwritten regions in various samples were recorded using the microscope's emission spectroscopy mode with two-photon excitation at 800 nm. Unmodified silk shows an emission spectrum peaking at 470–500 nm, unwritten azosilk shows a fluorescence peak at 640 nm, while written azosilk shows fluorescence at 520 nm and 560 nm.

While there have been previous observations of fluorescence in azobenzene and azobenzene-containing polymers,[24,26] the observed fluorescence in azosilk appears to be closely analogous to that obtained in experiments with silk treated with horseradish peroxidase (HRP).[27] HRP has been shown previously to convert unmodified silk solutions into a fluorescent hydrogel with dityrosine crosslinks.[27,28] However, in the case of azosilk, the azobenzene pendant groups on the tyrosine residues extend the pi-system and lead to a broader fluorescence signal. We hypothesize that the optically-induced modifications observed in azosilk are due to the two-photon absorption of the azobenzene in the azosilk, and reaction of the resulting photo-excited radicals on tyrosine moieties to form dityrosine, leading to disruption of the self-assembled structure, then expansion and blistering. This is consistent with the fluorescence effects observed in HRP cross-linked silk where the HRP produces dityrosine bonds and results in enhanced blue fluorescence.[27]

To test the hypothesis that photo-induced fluorescence changes are due to photo-crosslinking of radical species, the radical marker TEMPO ((2,2,6,6-tetramethylpiperidin-1-yl)oxyl) was added to hydrated films. At high concentrations of TEMPO (10 wt%), writing into the film was not observed but could be re-established by washing out the TEMPO from within the film with a 50 : 50 water : ethanol solution. This may be due to TEMPO competing for the radicals that would otherwise be used by the excited tyrosine when crosslinking into dityrosine. Fluorescence modification is re-established with decreasing TEMPO concentrations. When the concentration of the added TEMPO drops below 1 wt%, fluorescence modification is induced; however, blistering is not observed regardless of irradiation power. At higher concentrations of TEMPO (5–10 wt%), fluorescence decreases upon illumination by the mode-locked laser. Writing was not observed within an azosilk sample prepared with 10% TEMPO at any power. To confirm the role of water during blister formation, films were exposed to 800 nm irradiation under dry conditions (**Figure A3.5**). Written areas in dry films exhibit the same fluorescence shift as seen for hydrated azosilk films (**Figure A3.6)**, but no blistering occurs. This supports our hypothesis that water is required for the blistering to occur, and allows us to separate the two effects of the fluorescence shifts and the blistering.

AFM force imaging (**Figure 4.2**, Asylum Research MFP-3D) showed that the modulus of the azosilk in unwritten areas was 12 ± 1 kPa. This decreased to 0.6 kPa in the photo-modified areas and the measurement was replicated in many different areas to ensure consistency. To our

knowledge, controlled photo-softening of this magnitude has not previously been observed in any silk material. This is an interesting feature for potential cell-guidance control applications, as variations in modulus have been shown to exert influence over various cell processes and functions, including growth orientation of neural cells.[29–31] One could easily envisage that this softening effect could be controlled to vary predictably with writing depth from the surface, in addition to the power and duration of irradiation, to tune this photo-softening in the patterns.

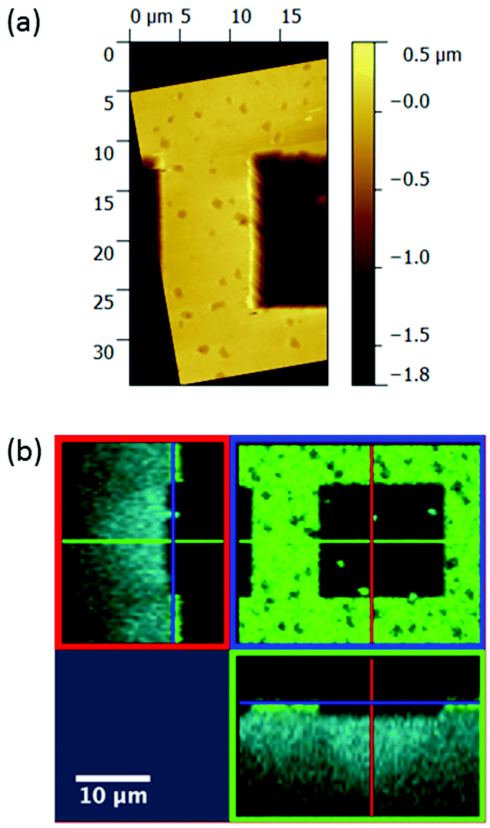

Figure 4.2. (a) AFM image of photo-inscribed areas of azosilk **(b)** the corresponding confocal image. Blue channel: fluorescence at 488 nm excitation. Green channel: reflectance image. The blister top has completely separated from surface in this case.

In summary, we have found that the azobenzene in azosilk can act as a photo-sensitizer that produces a photolithographic material exhibiting a new physical 'soft blistering' effect previously unreported or explored in any azopolymers. It enables visible light to be used in a precise and localized manner to inscribe programmable patterns and morphologies on silk biomaterials in a single post-processing step. These blisters are inflated into soft, water-filled blisters through a

osmotic pressure mechanism, similarly to previously PEG-based materials.[32] There are several potential applications for such photo-induced blisters that could readily be envisaged in addition to cell influence, for example this effect might be used to form microfluidic channels in the same way that multi-photon absorption can be used to form channels in horseradish peroxidase (HRP) crosslinked silk.[16] As an illustration of this potential application, we wrote a microfluidic test pattern[33] in azosilk (**Figure 4.3**) based on a standard test device design. The image of the pattern was recorded with an ordinary wide field microscope, indicating that patterns can be easily observed using conventional microscopy. In this case, the size of the microfluidic chamber would be limited by the field of view of the objective used on the microscope being used for lithography, unless indexed and moved, but otherwise unlimited in 2-D patterns possible and so represents a facile method to fabricate microfluidic chambers without the use of expensive photo-resist masks and clean room procedures, similar to previously found methods,[34] however using synthetically modified silk.

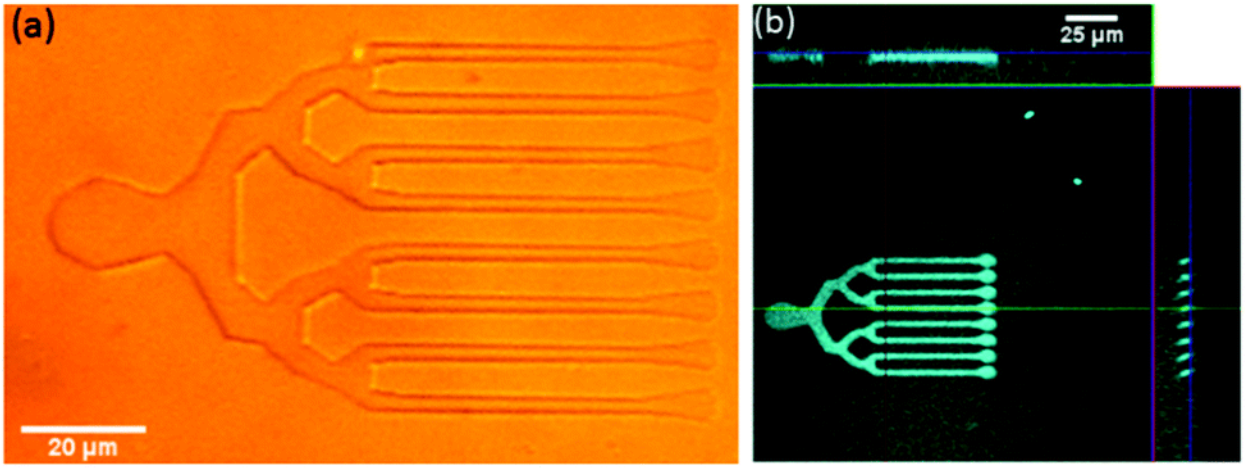

Figure 4.3. (a) Bright field image of a microfluidic-inspired pattern made through the ocular of the microscope, demonstrating that the photo-inscribed structures can be easily visualized with an ordinary wide field microscope, so they can be readily found for later processing. **(b)** Cross sectional image of a microfluidic pattern written within the hydrated azosilk film showing the increased fluorescence obtained by irradiating several regions of interest. This image was written into an azosilk film at a depth of 5 µm from the surface and consisted of over 100 regions of interest. The background fluorescence signal was subtracted from the image to better visualize the three-dimensional form of the chamber.

4.4 Conclusions

In conclusion, photo-induced patterning in azosilk materials provides optically tunable surfaces and topologies generated by laser light irradiation. These photo-inscribed regions also show a controlled decreased modulus, illustrating a tunable photo-softening effect. This patterning of azosilk films can be readily accomplished through a one-step two-photon process, and provides promising surfaces for a wide variety of potential applications such as microfluidic inscription, dynamic directed cell-growth surfaces, and in general as localized optically-modifiable soft biomaterials.

4.5 Acknowledgements

Images were collected, processed, and analyzed for this manuscript in the McGill University Life Sciences Complex Advanced BioImaging Facility (ABIF). We thank the AFOSR (Tufts) and NSERC Canada (McGill) for support of this work. CJB and MCG are grateful for funding from FQRNT Quebec Canada, which assisted a sabbatical stay at McGill University's

Centre for Self-Assembled Chemical Structures. CJB is grateful to the Artisans d'Angkor and Kolbe Foundations for enabling a visit to Bombyx Mori silkworm farms and silk harvesting facilities in Cambodia, with in-kind supply of silk cocoons.

4.6 References

1. Li, Z.-H.; Ji, S.-C.; Wang, Y.-Z.; Shen, X.-C.; Liang, H., Silk fibroin-based scaffolds for tissue engineering. *Front. Mater. Sci.* **2013**, *7* (3), 237–247.

2. Ude, A. U.; Eshkoor, R. A.; Zulkifili, R.; Ariffin, A. K.; Dzuraidah, A. W.; Azhari, C. H., *Bombyx mori* silk fibre and its composite: A review of contemporary developments. *Mater. Des.* **2014**, *57*, 298–305.

3. Van Vlierberghe, S.; Dubruel, P.; Schacht, E., Biopolymer-based hydrogels as scaffolds for tissue engineering applications: a review. *Biomacromolecules* **2011**, *12* (5), 1387–1408.

4. Omenetto, F. G.; Kaplan, D. L., New opportunities for an ancient material. *Science* **2010**, *329* (5991), 528–531.

5. Bray, L. J.; George, K. A.; Ainscough, S. L.; Hutmacher, D. W.; Chirila, T. V.; Harkin, D. G., Human corneal epithelial equivalents constructed on *Bombyx mori* silk fibroin membranes. *Biomaterials* **2011**, *32* (22), 5086–5091.

6. C., D. P.; Younjin, M.; J., I. D.; T., H. P., Implantable silk composite microneedles for programmable vaccine release kinetics and enhanced immunogenicity in transcutaneous immunization. *Adv. Healthcare Mater.* **2014**, *3* (1), 47–58.

7. Mauney, J. R.; Cannon, G. M.; Lovett, M. L.; Gong, E. M.; Di Vizio, D.; Gomez, P.; Kaplan, D. L.; Adam, R. M.; Estrada, C. R., Evaluation of gel spun silk-based biomaterials in a murine model of bladder augmentation. *Biomaterials* **2011**, *32* (3), 808–818.

8. Bai, L.; Zhu, L.; Min, S.; Liu, L.; Cai, Y.; Yao, J., Surface modification and properties of *Bombyx mori* silk fibroin films by antimicrobial peptide. *Appl. Surf. Sci.* **2008**, *254* (10), 2988–2995.

9. Galeotti, F.; Andicsova, A.; Yunus, S.; Botta, C., Precise surface patterning of silk fibroin films by breath figures. *Soft Matter* **2012**, *8* (17), 4815–4821.

10. Sakakibara, K.; Hill, J. P.; Ariga, K., Thin-film-based nanoarchitectures for soft matter: Controlled assemblies into two-dimensional worlds. *Small* **2011**, *7* (10), 1288–1308.

11. Ding, G.; Jin, Q.; Chen, Q.; Hu, Z.; Liu, J., The fabrication of ordered bulk heterojunction solar cell by nanoimprinting lithography method using patterned silk fibroin mold at room temperature. *Nanoscale Res. Lett.* **2015**, *10* (1), 491.

12. Perry, H.; Gopinath, A.; Kaplan, D. L.; Dal Negro, L.; Omenetto, F. G., Nano- and micropatterning of optically transparent, mechanically robust, biocompatible silk fibroin films. *Adv. Mater.* **2008**, *20* (16), 3070–3072.

13. Kim, S.; Marelli, B.; Brenckle, M. A.; Mitropoulos, A. N.; Gil, E. S.; Tsioris, K.; Tao, H.; Kaplan, D. L.; Omenetto, F. G., All-water-based electron-beam lithography using silk as a resist. *Nat. Nanotechnol.* **2014**, *9* (4), 306–310.

14. Liu, J.; Shao, J.; Zheng, J., Radiation grafting/crosslinking of silk using electron-beam irradiation. *J. Appl. Polym. Sci.* **2004,** *91* (3), 2028–2034.

15. Kurland, N. E.; Dey, T.; Kundu, S. C.; Yadavalli, V. K., Precise patterning of silk microstructures using photolithography. *Adv. Mater.* **2013**, *25* (43), 6207–6212.

16. Applegate, M. B.; Coburn, J.; Partlow, B. P.; Moreau, J. E.; Mondia, J. P.; Marelli, B.; Kaplan, D. L.; Omenetto, F. G., Laser-based three-dimensional multiscale micropatterning of biocompatible hydrogels for customized tissue engineering scaffolds. *Proc. Natl. Acad. Sci. U. S. A.* **2015**, *112* (39), 12052–12057.

17. Audorff, H.; Kreger, K.; Walker, R.; Haarer, D.; Kador, L.; Schmidt, H.-W., Holographic Gratings and data storage in azobenzene-containing block copolymers and molecular glasses. Müller, A. H. E.; Schmidt, H.-W., Eds. Springer Berlin Heidelberg: Berlin, Heidelberg, 2010; Vol. 228, 59–121.

18. Shishido, A., Rewritable holograms based on azobenzene-containing liquid-crystalline polymers. *Polym. J.* **2010**, *42* (7), 525–533.

19. Ye, X.; Kuzyk, M. G., Photomechanical response of disperse red 1 azobenzene dye-doped PMMA polymer fiber. *Opt. Commun.* **2014**, *312*, 210–215.

20. Priimagi, A.; Barrett, C. J.; Shishido, A., Recent twists in photoactuation and photoalignment control. *J. Mater. Chem. C* **2014**, *2* (35), 7155–7162.

21. Krasnov, I.; Krekiehn, N. R.; Krywka, C.; Jung, U.; Zillohu, A. U.; Strunskus, T.; Elbahri, M.; Magnussen, O. M.; Müller, M., Optically switchable natural silk. *Appl. Phys. Lett.* **2015**, *106* (9), 093702.

22. Murphy, A. R.; St John, P.; Kaplan, D. L., Modification of silk fibroin using diazonium coupling chemistry and the effects on hMSC proliferation and differentiation. *Biomaterials* **2008**, *29* (19), 2829–2838.

23. Cronin-Golomb, M.; Murphy, A. R.; Mondia, J. P.; Kaplan, D. L.; Omenetto, F. G., Optically induced birefringence and holography in silk. *J. Polym. Sci. B: Polym. Phys.* **2012**, *50* (4), 257–262.

24. Satzger, H.; Spörlein, S.; Root, C.; Wachtveitl, J.; Zinth, W.; Gilch, P., Fluorescence spectra of trans- and cis-azobenzene – emission from the Franck–Condon state. *Chem. Phys. Lett.* **2003**, *372* (1-2), 216–223.

25. Culver, J. C.; Hoffmann, J. C.; Poche, R. A.; Slater, J. H.; West, J. L.; Dickinson, M. E., Three-dimensional biomimetic patterning in hydrogels to guide cellular organization. *Adv. Mater.* **2012**, *24* (17), 2344–2348.

26. Zhao, R.; Zhan, X.; Yao, J.; Sun, G.; Chen, Q.; Xie, Z.; Ma, Y., Reversible photo-controlled mass transfer in a photo-responsive conjugated main-chain polymer film for high contrast surface patterning. *Polym. Chem.* **2013**, *4* (21), 5382–5386.

27. Partlow, B. P.; Hanna, C. W.; Rnjak-Kovacina, J.; Moreau, J. E.; Applegate, M. B.; Burke, K. A.; Marelli, B.; Mitropoulos, A. N.; Omenetto, F. G.; Kaplan, D. L., Highly tunable elastomeric silk biomaterials. *Adv. Funct. Mater.* **2014**, *24* (29), 4615–4624.

28. Harms, G. S.; Pauls, S. W.; Hedstrom, J. F.; Johnson, C. K., Fluorescence and rotational dynamics of dityrosine. *J. Fluoresc.* **1997**, *7* (4), 283–292.

29. Tomba, C.; Villard, C., Brain cells and neuronal networks: Encounters with controlled microenvironments. *Microelectron. Eng.* **2015**, *132*, 176–191.

30. Georges, P. C.; Miller, W. J.; Meaney, D. F.; Sawyer, E. S.; Janmey, P. A., Matrices with compliance comparable to that of brain tissue select neuronal over glial growth in mixed cortical cultures. *Biophys. J.* **2006**, *90* (8), 3012–3018.

31. Georges, P. C.; Janmey, P. A., Cell type-specific response to growth on soft materials. *J. Appl. Physiol.* **2005**, *98* (4), 1547–1553.

32. Ming, G.; Pegoraro, A.F.; Mao, A.; Zhou, E. H.; Arany, P. R.; Han, Y.; Burnette, D.T.; Jensen, M. H.; Kasza, K. E.; Moore, J. R.; Mackintosh, F. C.; Fredberg, J. J.; Mooney, D. J.; Lippincott-Schwartz, J.; Weitz, D. A., Cell volume thourgh water efflux impacts cell stiffness and stem cell fate. *Proc Natl Acad Sci U. S. A.* **2017**, *114* (41), E8618–E8627.

33. Young, E. W.; Wheeler, A. R.; Simmons, C. A., Matrix-dependent adhesion of vascular and valvular endothelial cells in microfluidic channels. *Lab Chip* **2007**, *7* (12), 1759–1766.
34. Bélisle, J.M.; Kunik, D.; Constantino, S., Rapid multicomponent optical protein patterning. *Lab Chip* **2009**, *9*, 3580–3585.

Appendix 3: Supplemental information for Chapter 4
Experiment Section: Methods and Materials

All chemicals were purchased from Sigma-Aldrich and used without further purification. The Bombyx mori cocoons were purchased from Tajima Shoji Co., LTD. Cell culture plates were purchased from Falcon (60 x 15 mm Style, treated by vacuum gas plasma) and used without further sterilization. Water used within the experiments was provided by a MilliQ water purification system. Imaging was performed on a Multi-Photon LSM: Zeiss Axioexaminer upright microscope using 800 nm as the writing and reading beam during experiments.

Preparation of silk solutions

Methods for the preparation of silk solutions from *Bombyx mori* silkworm cocoons were based on protocols from Rockwood *et al*.[1]

Preparation of azosilk solutions

The general procedure for making azosilk solutions was adapted from Murphy *et al.* with some modifications. The procedure used here instead was for the fabrication of azosilk-SO_4Na however, but can be generalized made by replacing the sulfanilic sodium salt with an alternate aniline in an appropriate solvent that is miscible with water (e.g. acetonitrile, acetone, or ethanol). Three solutions were prepared: 0.2 M aqueous solution of sulfanilic sodium salt, 1.6 M aqueous solution of p-toluenesulfonic acid, and an aqueous solution of 0.8 M $NaNO_2$. The 0.8 M $NaNO_2$ was cooled in an ice bath until a temperature of 5°C was achieved. Subsequently, 625 μL of the 1.6 M p-toluenesulfonic acid solution and 1.25 mL of 0.2 M sulfanilic sodium salt were briefly mixed by vortexing to produce a homogeneous solution. Then 625 μL of 0.8 M $NaNO_2$ solution was added and then submerged into an ice bath. The solution was let to react for 15 min or until a drop of the solution reacted positively on a piece of starch iodide paper. While this solution was reacting, 2 mL of silk solution was added to a vial and its pH was adjusted to a pH = 10. Once the diazonium solution was ready, 0.5 mL was added to the silk solution dropwise over 60 seconds duration, and vortexed quickly before adding it back to an ice bath. This solution could be used without further purification for optical experiments; however, it was further purified for biological experiments. For this process, 1-2 mL aliquot of the aqueous solution was added to Sephadex size exclusion columns (NAP-25, GE HealthCare), preequilibrated with pH 8 boric acid/borate buffer solution at 0.1 M.

Preparation of azosilk films

Water-stable films were prepared in by adding 1–3 mL of the prepared azosilk solution to a 30 mm petri dish and allowing drying over 5 days. Nine small holes were drilled into the cover to prevent quick drying, since films that dry slowly (over 5 days) are found to be insoluble in water due to more complete self-assembly of the β-sheets within the silk material.[2] Films that are dried in less than 5 days are found to dissolve in water.

Writing in azosilk films

Once the films were dried in the petri dish, they were hydrated by adding 5–10 mL of Milli-Q water to a depth of about 5 mm and mounted onto the microscope. Either 10 or 40x water dipping lenses (Zeiss W N-Achroplan 10x/0.3 M27, W Plan Apochromat 40X/1.0 DIC M27) were used in conjunction with a mode-locked Ti-sapphire laser (Coherent Chameleon, 140 fs, 80 MHz repetition rate) tuned to 800 nm as a two-photon writing/reading beam. After 10000 fs^2 dispersion by the microscope's acousto-optic modulator and 5000 fs^2 dispersion by the objective lens the pulses were broadened to approximately 250 fs at the sample. Single photon fluorescence images were also taken at 488 nm. The laser powers measured before the objective lens used for writing and reading are typically 100 mW and 10 mW respectively, with pixel dwell times in the 3 to 5 microsecond range. Patterning was carried out using the method described by Culver *et al*.[3] Approximately 2500 pulses, each with 4.3 $nJ/\mu m^2$ were used to form blistering for a total energy of 100 $\mu J/\mu m^2$. Fluorescence emission spectra of various areas of the observed images were taken using the microscope's spectroscopic lambda mode at 10 mW excitation power.

Characterization of fluorescent liquid

To characterize the fluorescent liquid present in the written bubbles, a series of 100 disc shaped blisters were created and their liquid was extracted using a needle. A few drops of the liquid were added to D_2O and 1H NMR spectroscopy was performed. The presence of 4 amino acids were determined (alanine, valine, tyrosine and glycine) in trace amounts along with the presence of a large amount of water.

^{1}H NMR (D_2O, 400 MHz): δ 1.39 (br, 1H), 2.13 (s, 1H), 3.38 (m, 1H), 4.72 (H_2O, s, 30H), 6.88 (d, 1H, J=8 Hz), 7.15 (d, 1H, J= 8 Hz), 8.39 (br, 1H).

In this case, alanine corresponds to the NH peak found at 8.39 ppm, and the methyl peak at 1.39 ppm, valine's CH is found at 2.13 ppm, tyrosine's aromatic peaks are found at 6.88 and 7.15 ppm and finally glycine's CH2 is found at 3.38 ppm. The peptide's backbone peaks were not found due to the high rate of exchange between D_2O.

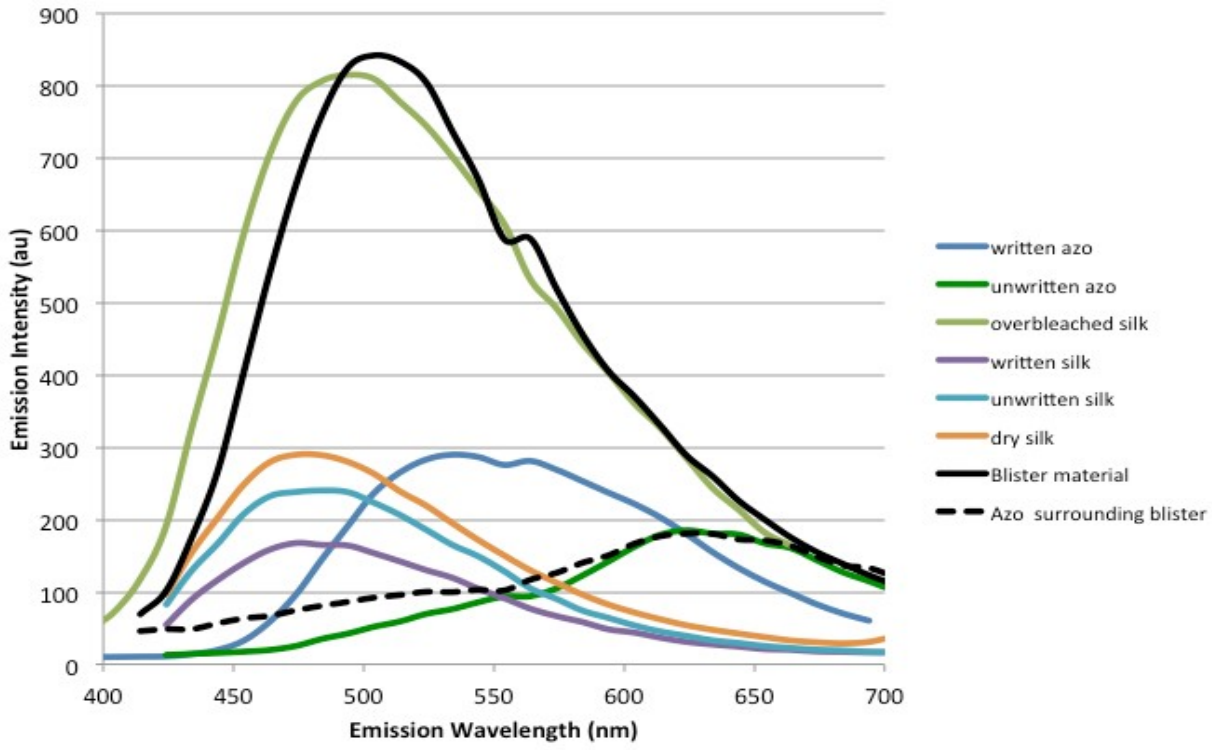

Figure A3.1. Emission spectra variously of: written azosilk, unwritten azosilk, over-bleached (photo-damaged) silk, written slow-dried silk, unwritten slow-dried silk, and liquid material captured from within the blisters, depicting the spectral shift of azosilk with increasing exposure to mode locked 800 nm light. Unexposed hydrated azosilk shows weak fluorescence peaking at 625 nm, then upon illumination with the 800 nm femtosecond beam, the fluorescence peak strengthens and blueshifts to 520 nm. This fluorescence shift is restricted to the illuminated region: silk regions above and below the irradiated areas retain their original fluorescence spectrum, thereby allowing the material to be used as a three-dimensional patterning medium, as indicated in **Figure 4.1 (a)** in which the 'McGill' and 'Tufts' logos are written in different depth planes.

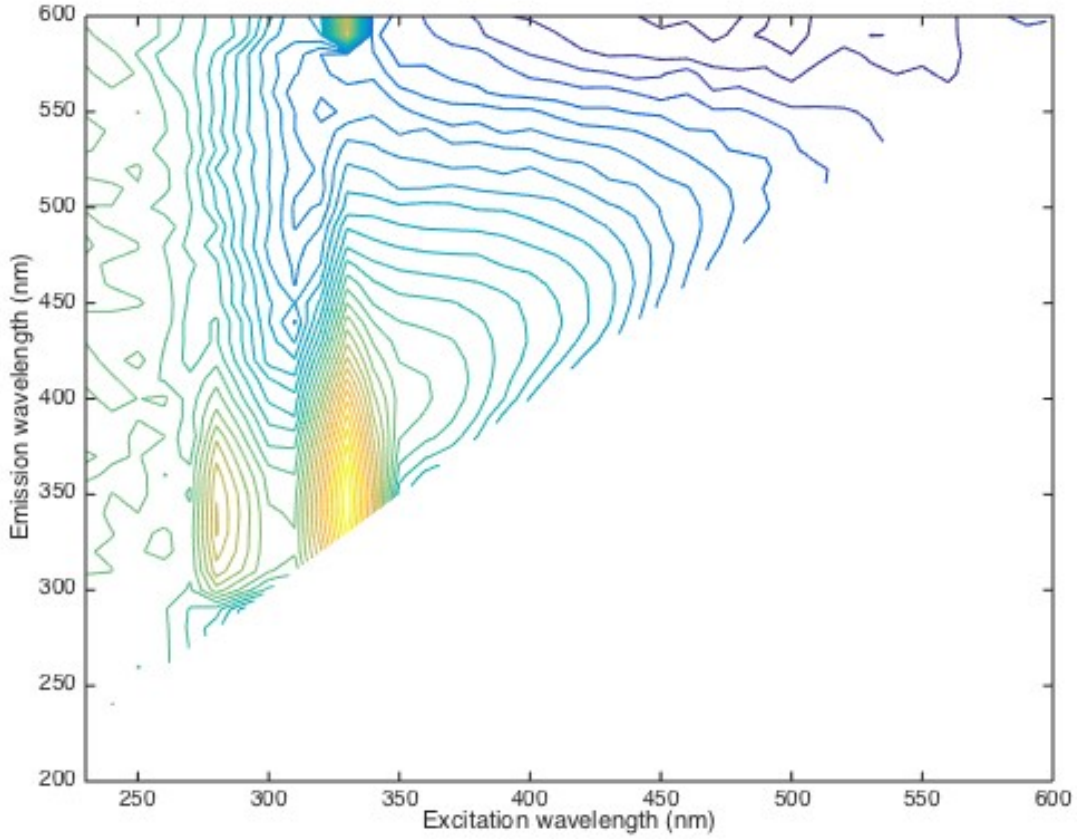

Figure A3.2. Excitation emission spectrum of 5% aqueous silk solution (logarithmic scale). Note the principal peak is centered at excitation wavelength 325 nm and emission at 340 nm, while the low intensity ridge is shifted by 50 nm from the excitation wavelength.

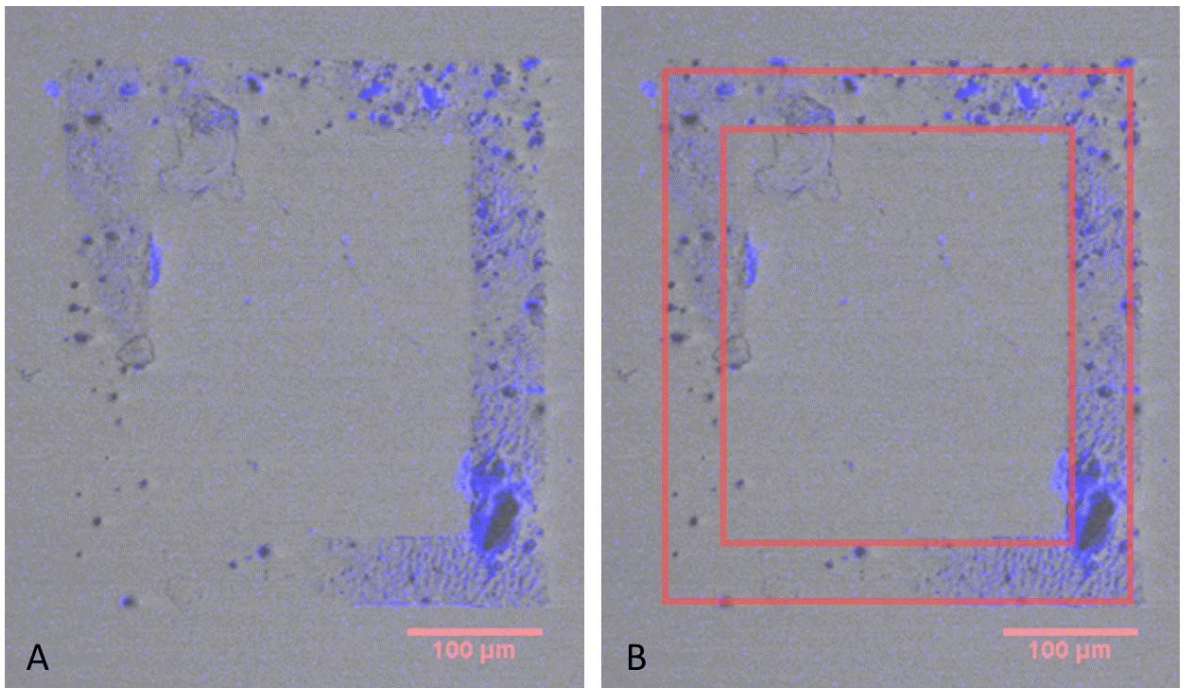

Figure A3.3. Image of structural damage on silk caused by laser irradiation at 900 µJ/µm^2. **(a)** shows the region of interest where irradiation occurred, and **(b)** shows the resulting fluorescence pattern from irradiation. Structural damage is observed extending outside the lithographic regions of interest from the higher power used.

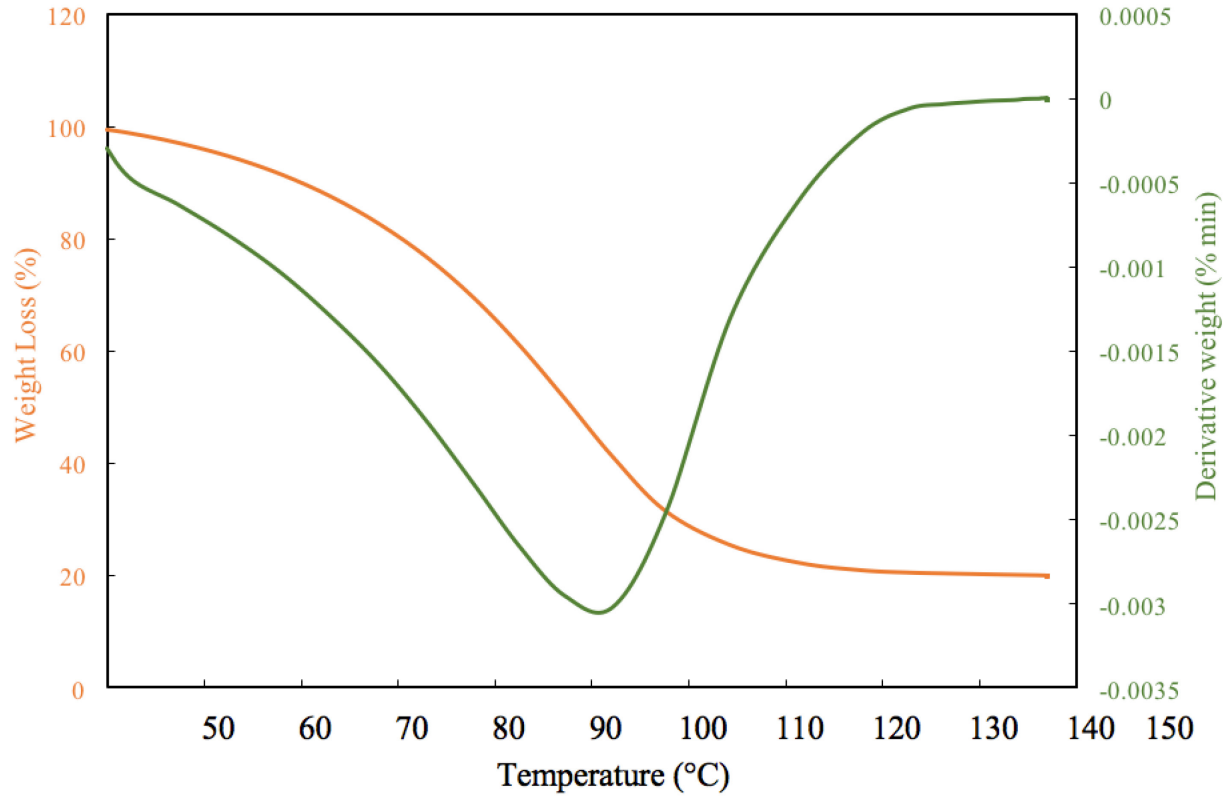

Figure A3.4. TGA experimental weight loss vs. Temperature curve (orange) to estimate the water content of the azosilk (left y axis). The sample analyzed was cut from a film that was hydrated in water for 30 minutes. Total water content was found to be 77% by heating 21.31 mg of sample to 150 °C and held isothermally at 150 °C for 45 minutes. The first derivative of weight loss is plotted in green to show the weight loss rate vs temperature (right y axis).

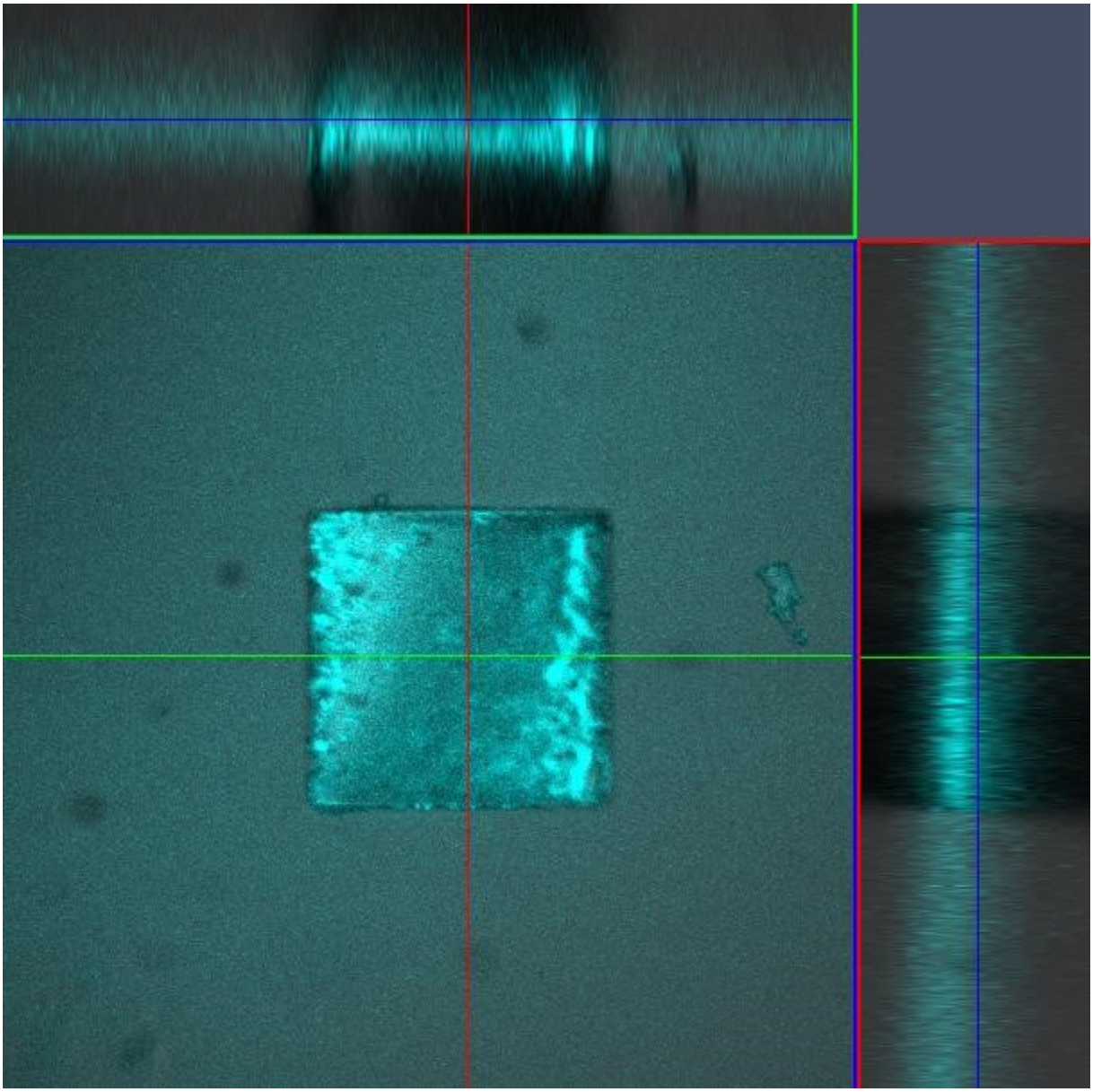

Figure A3.5. Written areas of the dry azosilk film (blue square) show increased fluorescence compared to the unwritten areas. The darkening shown in the writing planes is an artifact of the software. Vertical and horizontal projections of three-dimensional photolithography image are shown on the sides and demonstrate the absence of a microbubble compared to **Figure 4.1**.

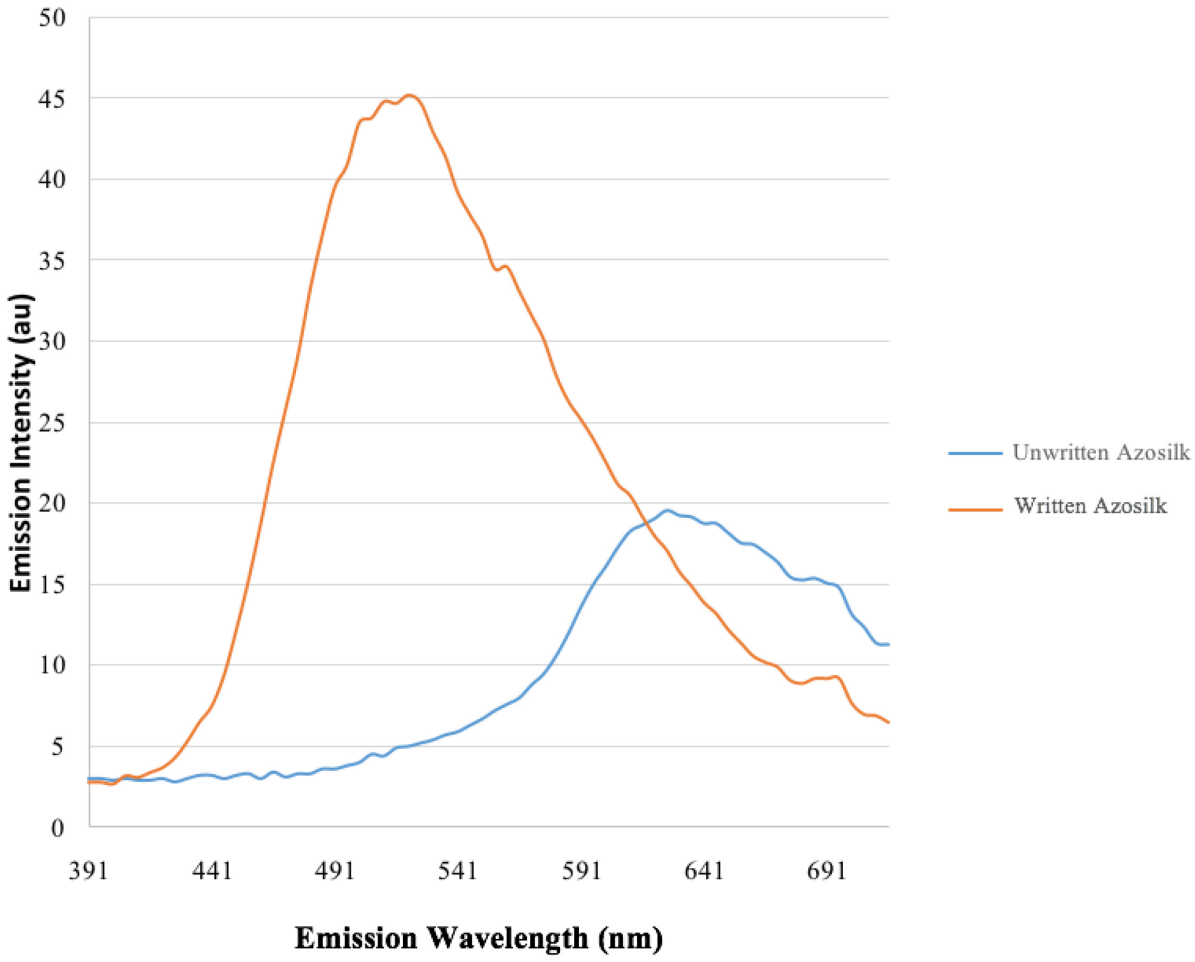

Figure A3.6. Emission spectra of written azosilk, unwritten azosilk in the dry conditions and taken from the image depicted in **Figure A4.5**. These spectra are achieved by following the same parameters used in creation of **Figure 4.1 (d)**; however, under dry conditions.

References

1. Rockwood, D. N.; Preda, R. C.; Yucel, T.; Wang, X. Q.; Lovett, M. L.; Kaplan, D. L. Materials fabrication from Bombyx mori silk fibroin. *Nat. Protoc.* **2011**, *6* (10), 1612–1631.

2. Lu, Q.; Hu, X.; Wang, X. Q.; Kluge, J. A.; Lu, S. Z.; Cebe, P.; Kaplan, D. L., Water-insoluble silk films with silk I structure. *Acta Biomater*. **2010**, *6* (4), 1380–1387.

3. Culver, J. C.; Hoffmann, J. C.; Poche, R. A.; Slater, J. H.; West, J.; Dickinson, M. E., Three-Dimensional Biomimetic Patterning in Hydrogels to Guide Cellular Organization. *Adv. Mater*., **2012**, *24* (17), 2344–2348.

Rationale for Chapter 5: Micropatterning azobenzene-modified silk surfaces for optical control of cell guidance and growth

In Chapter 4, we prepared bulk films of azosilk materials, and explored their surfaces using a confocal microscope. Direct photoexcitation of our azosilk films prompted the formation of well-defined fluorescent patterns that were confined within the irradiated region. Upon irradiating with higher intensities (>100 μJ/μm^2, 800 nm), raised blisters formed. These blisters were fluid filled and were found to contain fragments of amino acids and water. By studying these blisters using AFM indentations, we discovered that the microblistered regions (0.6 kPa) were significantly softer than their surrounding material (12 kPa). The ability to pattern a surface with both topological features and photosoftened regions have applications in guided cell growth, as tissues and cells have been demonstrated to be surprisingly sensitive to modulus and the topology of the surface they are cultured on. We thus extend the knowledge gathered in Chapter 4 towards applications in optically guiding cells. Chapter 5 explores this potential application, by plating cells onto patterned surfaces that were created using methodologies developed in Chapter 4. We plated CHO cells onto a patterned surface and tracked their motion over 8 hours. Specific regions on the patterned films elicit an accelerated cell migration when compared to non-patterned surfaces. The prepared manuscript 'Micropatterning azobenzene-modified silk surfaces for optical control of cell guidance and growth' was co-authored by Michael J. Landry, Anaïs Robert, Constantinos Noutsios, Firas Mubaid, Prof. Claire Brown, and Prof. Christopher J. Barrett, and provides a proof of principle that azosilk materials can be used to create topological features that affect cell migration using light, and this discovery provides the essential knowledge to explore the optically guided migration of other cell types.

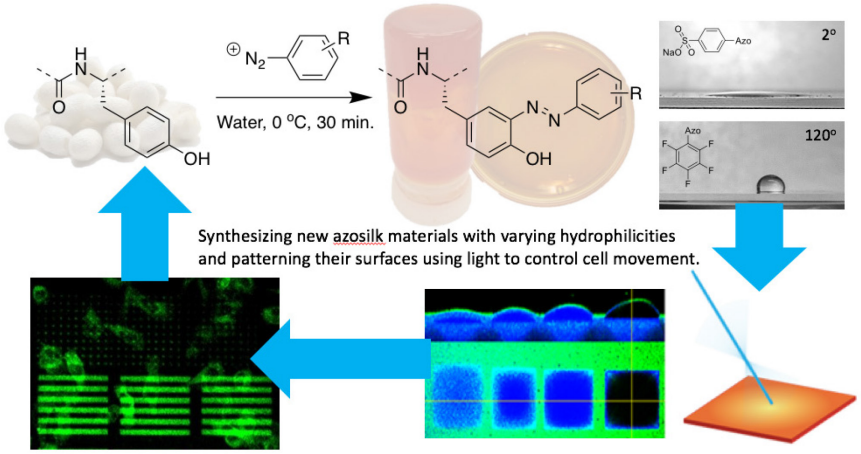

Chapter 5: Micropatterning azobenzene-modified silk surfaces for optical control of cell guidance and growth

Chapter 5 is based on a manuscript entitled 'Micropatterning azobenzene-modified silk surfaces for optical control of cell guidance and growth', and was co-authored by: Michael J. Landry, Anaïs Robert, Constantinos Noutsios, Firas Mubaid, Prof. Claire Brown, and Prof. Christopher J. Barrett.

5.1 Abstract

Directed cell motion is a critical field of study and plays a dominant role in a range of biological processes. Physical guidance cues, such as the mechanical properties of the surrounding tissues or extracellular matrices, have been found to be key in controlling cell movement. The development of tools to study the exact mechanical properties which elicit controlled cell migration, such as the creation of patterned surfaces, is costly, difficult to reproduce, or requires lengthy processing steps. Azosilk is a photo-responsive biomaterial which exhibits a 10-fold decrease in modulus upon irradiation with 800 nm light. Localized irradiation creates raised blisters which are confined to the irradiation region (>100μJ/μm^2). The topology and modulus of a growth surface have been shown to influence cell migration, thus we explored the use of patterned azosilk surfaces for optically guiding Chinese hamster ovary (CHO) cells. We assayed a family of 10 chemically distinct azosilk polymers for cell viability, and then patterned the highest performing surface with an array of dots and lines. CHO cells were cultured onto the patterned surfaces and were tracked over a period of 8 hours. CHO cells which adhered in a position between the dot and line patterns were found to migrate significantly faster than the cells within the non-irradiated regions (115 μm/hr, n = 10, $P < 0.05$), and formed localized focal adhesions towards each pattern during the migration. The development of tools to specifically pattern azosilk surfaces using an external stimulus offers a method to fabricate cheaper and more robust cell control surfaces for studying controlled cell migration.

5.2 Introduction

Cell migration and growth is an important yet complex field of study, owing to a complicated cascade of interactions between proteins (such as integrin, rho and rac GTPases), biochemical and biophysical aspects within each distinct cell line. Typically, there is an

orchestrated interaction between the cell tissue surface, dissolved chemical cues and membrane-bound proteins, which may guide cell movement or growth through a complicated signaling pathway. More specifically, cell locomotion can be summarized in 5 steps: (1) protrusion of a leading edge of a cell due to actin polymerization towards the direction of cell movement, followed by (2) sensing of the extracellular matrix (ECM) through integrin-ECM binding, that allows anchor points to be created between the cell cytoskeleton and the ECM surface.[1] If the cell is present in a three-dimensional ECM, (3) matrix metalloproteinases (matrixins) will degrade any ECM proteins present on the leading edge of the cell.[1] On the trailing end of the cell, (4) cell contraction occurs when active myosin II binds to actin filaments, creating so called actomyosin complexes, and generating a contractile force. This is followed by (5) detachment of the trailing edge due to the contractile force generated by actomyosin structures.[1] Both chemical and physical signals can interact with the proteins present during cell movement, such as rho and rac, and may influence the direction and speed of cell locomotion.

Gradients of biomolecules have been shown to dramatically affect how cells migrate across a surface or within a tissue.[2] These responses can either be attractive or repulsive (chemoattractant or chemorepellent, respectively), and may facilitate cells to migrate towards or away from a given chemical signal. These chemical signals are sensed by membrane-bound proteins, such as G-protein coupled receptors, which can aid in selection of the leading edge.[3] Research on cell guidance has heavily focused on chemical signals through chemotaxis pathways, but movement prompted by physical guidance cues, so called mechanotaxis, have garnered more attention recently.[4-5] Physical guidance cues can manifest either as a change in modulus or through topographical and morphological changes on a surface (i.e. scratches, bumps or bubbles). Mechanosensing of the surface is thought to occur through integrin binding to the ECM or through selective modulus detection by force-induced conformational changes in protein structure.[3] These conformational changes can alter the activity of ion channels or enzymes, and can expose cryptic binding domains and, as a result, trigger guided cell motion towards or away from the change in modulus.[3] As a result, cells have been demonstrated to be surprisingly sensitive to both surface structures present and the material moduli they are cultured on, and controlled movement can occur with just a small change in modulus (~10%).[6-7]

The creation of physical and chemical features onto a guidance surface can be achieved through microcontact printing[8] and through expensive clean room techniques that often involve harsh chemicals.[9] Clean room techniques can produce patterns down to a few 10s of nanometers in size.[9] Patterns on the order of a few microns have been shown to influence cell migration and motion, thus clean room techniques produce features of an adequate size to influence cells movement. However, each round of screening requires recreating patterns within the clean room and assessing their response separately, which can add a large amount of cost and time to a study. A variety of systems have been developed which overcome these issues, including light-responsive polymers which demonstrated photo-softening and photo-lithographic effects.[10]

Photo-responsive polymers have been developed in the early 1980's, and typically consisted of a photoswitchable molecule appended onto a side chain of a polymer.[11-12] Azobenzene is a photoswitchable molecule that exhibits both a thermally stable *trans*- and metastable *cis*-isomer. When the *trans*-isomer adsorbs light of the correct wavelength, it becomes photoexcited and isomerizes to the *cis*-isomer, which then can thermally relax back to the *trans*-isomer.[13] This strategy of appending photosensitive molecules onto polymers has evolved over the years into modern photo-responsive biomaterials, which have been employed to control biological processes such as growth, attachment and migration using light.[14-15] Photo-responsive polymers have been previously investigated for controlled drug delivery,[16] cell guidance,[17] and 'single cell switching' experiments.[18] A successful method to control attachment and growth of NIH 3T3 cells was demonstrated by Goulet-Hanssens and co-workers, where a well-known biomolecule (cyclic-RGD peptide) was appended to the end of a azobenzene polymer.[19-20] When this polymer was used to create cell growth surfaces, the cyclic-RGD peptide was found to be buried into the polymer surface. However, upon exposure to light, the azobenzene-cRGD molecules photoisomerized, which exposed the end of cRGD biomolecule to the surface, and prompted the attachment of the cultured NIH 3T3 cells to the cell surface.[19]

Silk-based photo-responsive materials have been making recent in-roads towards photo-controlled biological systems.[21-23] Particularly one system, azobenzene-modified silk (or so called 'azosilk'), has achieved photo-control over the topology of a surface.[24] Controlled irradiation of a surface using an 800 nm source allowed for the formation of microblisters that conformed to the region that was irradiated (**Figure 5.1**). These raised regions exhibited a significant fluorescent

signal (peaking at 470 nm, wide spectral bands) which was confined to the microblistered pattern, and additionally a notable 10x decrease in modulus (12 kPa to 0.6 kPa) was observed using AFM measurements.[24] This process was used to create objects on an azosilk surface that were 1-250 μm thick. This size regime is dictated by the focal length and quality of the lens used. Thus, dipping lens achieved the highest resolution objects, as they were found to minimize scattering effects. The size regime of the produced microblisters is on the proper order of magnitude to influence biological processes. Taking into consideration all the above advantages, azosilk was chosen as the ideal system for our study,[24-26] and we decided to assess the validity of using azosilk materials as a cell control surface for optically guiding cells. Thus, we explored the use of a series of azosilk patterns as a proof of principle for their ability to guide cells using the raised microblisters and photosoftened patterns in our films.

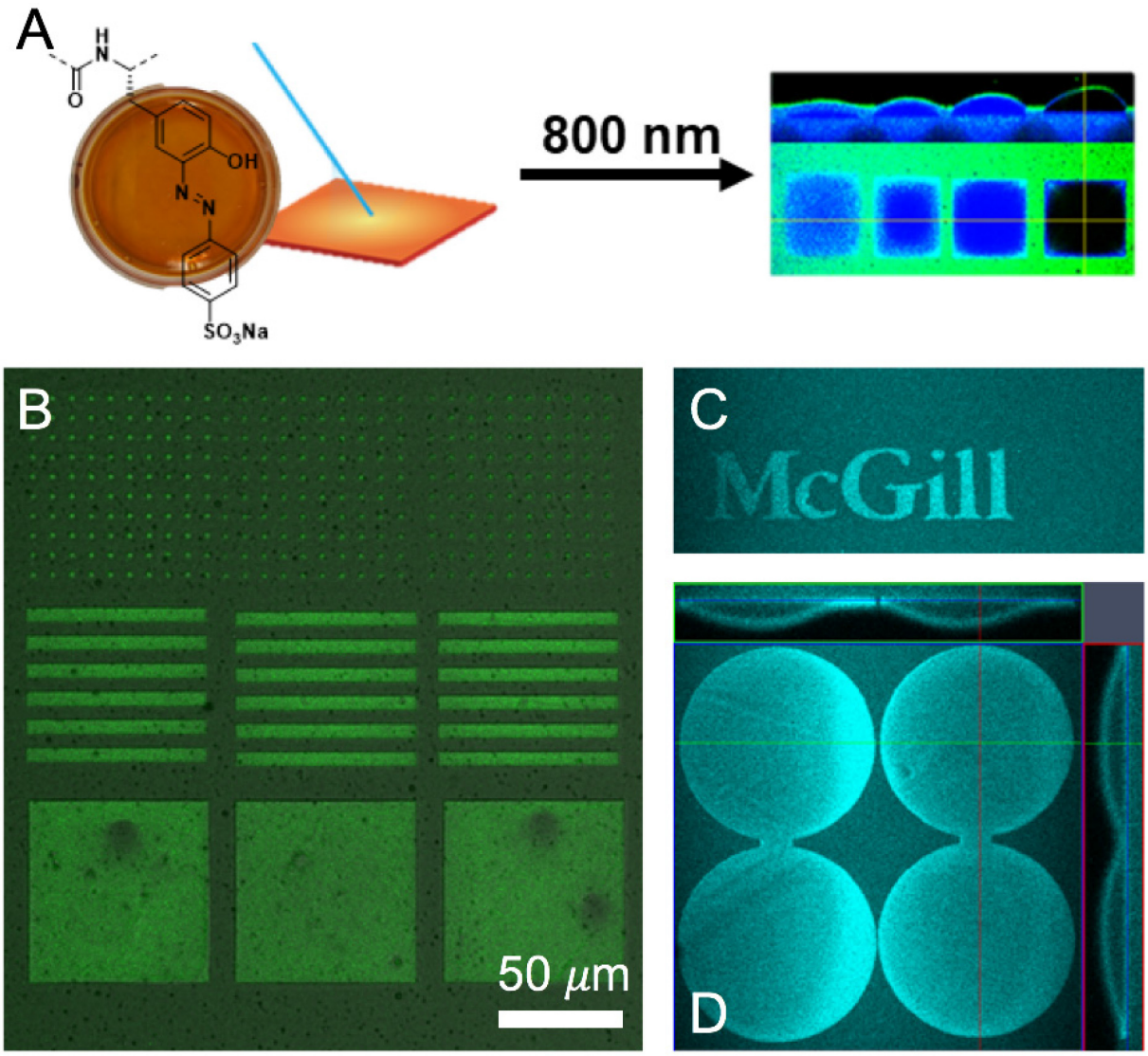

Figure 5.1. (A) A schematic representation of the process of writing onto an azobenzene surface, and the resulting topographic modification of the surface. Modulation of the surface topology is achieved by varying the depth at which features are inscribed. **(B)** A representative image showing a patterned surface with features on the cellular size regime. **(C)** An image depicting a McGill University logo, which demonstrates the effectiveness and resolution of the writing process. **(D)** A pseudo-three-dimensional reproduction of the three-dimensional nature of microblisters written into the surface of an azosilk film. Side panels above and to the right demonstrate the Z projection of the blisters out of the writing plan. Panels **(A)** and **(C)** were adapted from Landry *et al.*[24] with permission from The Royal Society of Chemistry, "Photo-induced structural modification of silk gels containing azobenzene side groups" Copyright 2017.

5.3 Materials and methods

5.3.1 Materials

All polymers, reagents, and salts used in the fabrication of the azosilk surfaces were purchased from Sigma-Aldrich, unless indicated. Silk fibroin was provided by Tajima Shoji LTD (Yokohama, Japan) and 8-well plates were purchased from Thermofisher (Waltham, USA).

5.3.2 Equipment, instrumentation and software

Distilled water was purified using a MilliQ Academic purification system (Millipore, Billerica, US) and use for the preparation of all aqueous solutions and for the dialysis of silk polymers. All images were acquired using a Zeiss multi-photon upright fluorescence microscope (Carl Zeiss Canada, Toronto, CA) equipped with a direct-coupled multiphoton laser (Coherent, Santa Clara, USA), and with multiple visible laser lines (458/488/514 nm argon laser, 543 nm, 594 nm, 633 nm). Images were further processed using Fiji and its various program extensions.[27] 6 or 12 well images were taken using an ImageXpressMicro (Molecular Devices, Sunnyvale, USA), using MetaMorph® microscopy automation software and processed using an image analysis software (MetaMorph®, Sunnyvale, USA). Two-photon imaging was performed on a Multi-Photon LSM: Zeiss Axioexaminer upright microscope using the 800 nm as the reading beam during the experiments.

5.3.3 Silk fibroin processing and azobenzene modification

Methods for the preparation of silk solutions from *Bombyx mori* silkworm cocoons were based on protocols from Rockwood *et al*.[28] To a vial, 1.25 mL of 0.2 M of an aniline derivative (in water or an appropriate solvent) was added along with 625 μL of 1.6 M toluenesulfonic acid solution in water. A stir bar was added, and the resulting clear solution was cooled to 4 °C in an ice bath. 625 μL of 0.2 M $NaNO_2$ in water was added dropwise to the cooled flask to produce the bright yellow diazonium salt solution. The solution was stirred for 25 minutes on ice. Separately, 0.25 mL of a boric acid/sodium borate buffer solution was added to 2 mL of the 5% w/v silk solution previously cooled at 4°C. The pH was adjusted to pH 9 before 0.5 mL of the diazonium salt was added dropwise over 2 minutes to produce a bright red solution that was allowed to stir for 30 minutes on ice. The red, azobenzene-modified silk was purified using standard desalinating columns NAP-25 (VWR International) with distilled water as the eluent.

5.3.4 **Processing azosilk solutions into films for biological testing and screening**

Each of the prepared azosilk solutions was initially fabricated into drop cast films into a 12 well plate for initial cell viability assays. This process involved taking 250 µL of the each azosilk solution and placing it into a well. The plate was covered with parafilm and 5 small airholes were made into each well. The plate was left to dry for 4-5 days in air. Once the dried films were obtained, they were placed into an oven at 45 °C, overnight, which produced water stable films. To determine if each film was successfully annealed, the well was submerged in 2 mL of 1 X PBS buffer and placed into an incubator overnight (37 °C).

5.3.5 **Patterning azosilk surfaces**

Once the films were processed in the 6 well plates, they were hydrated to a depth of about 10 mm by adding 5–10 mL of Milli-Q water and then mounted onto the microscope stage of the two-photon microscope. Either 10 or 63x water dipping lenses were used in conjunction with a mode-locked Ti-sapphire laser (Coherent Chameleon, 140 fs, 80 MHz repetition rate) tuned to 800 nm as a two-photon writing/reading beam. The laser powers measured before the objective lens used for writing and reading are typically 100 mW and 10 mW respectively, with pixel dwell times in the 6 to 8 microsecond range. Patterns were inspired from previously reported literature.[29] As in an effort to influence cells, the scale of the patterns was chosen to be roughly 10 times the cell radii across and the pattern to be tiled in order to adequately 'capture' enough cells. Patterns were made in Adobe Photoshop CS3 and scaled using a Matlab script provided by Culver *et al.*[30] in order to create the required regions of interest for selected irradiation. **Figure A4.1** shows an array of silk patterns achieved using the conditions.

5.3.6 **Cell work**

Fibronectin (Sigma, F-0895) coating of the azosilk growth substrates was conducted by placing 10 mL of a 2 µg/ml fibronectin/PBS solution onto the azosilk surfaces (6 well plate), and the plate was incubated for an hour at 37 °C. Azosilk substrates were then gently washed three times with PBS (1X) and used immediately. Chinese hamster ovary K1 (WT-CHO-K1) cells stably expressing paxillin-EGFP were used for all of the studies. Cells were grown in low glucose Dulbecco's Modified Eagle Medium (DMEM) (ThermoFisher Scientific, Grand Island, NY, 11885-084) supplemented with non-essential amino acids (ThermoFisher Scientific, 11140-

050), 1% penicillin-streptomyosin (ThermoFisher Scientific, 10378-016), 10% fetal bovine serum (ThermoFisher Scientific, 10082-147) and 25 mM 4-(2-hydroxyethyl)-1-piperazineethanesulfonic acid) (HEPES) (ThermoFisher Scientific, 15630-080). The media also contained 0.5 mg/mL of geneticin for maintenance of selection of paxillin-EGFP (ThermoFisher Scientific, 11811-031). After plating roughly 10-15 k (roughly 20% confluency) cells per each 35 mm dish, the CHO cells were allowed to incubate at 37 °C on a heated plate without any CO_2 atmosphere (due to HEPES buffer) for 1 hour prior to imaging.

5.3.7 **Live cell imaging**

Live cell videos were collected from a series of stills taken on the Mutli-Photon LSM: Zeiss Axioexaminer using a heated live cell chamber and HEPES buffer to maintain a correct pH during long periods of live cell imaging. Images were taken every 5-10 minutes (as indicated on the film) and were modified and made into movies using MetaXpress software. All analysis was conducted from these films using MetaXpress. Imaging was performed for 12 hours at a time, with fresh media being added every 4 hours.

5.4 **Results and discussion**

Azosilk materials can be chemically tailored through traditional diazonium coupling chemistry. These modified silks exhibit a wide range of hydrophobicity, which is dependent on the coupling partner of choice (**Figure 5.2** and **Figure A4.2.**). As an initial screen of the capability of each distinct azosilk material to culture CHO cells, a family of 10 azosilk materials were synthesized and plated onto a standard 12 well plate. In order to ensure that each film was water-stable, the plate was allowed to slowly dry over 5 days in air, which allowed for the β-sheets of the silk protein to self-assemble and achieve a Silk II structure, which has been previously found to be water-resistant.[31] To test that each material was water resistant, 1X PBS buffer was placed on top of each film, and the plate was placed into an incubator overnight at 37 °C. The next morning, the buffer was removed, the plate was sterilized (UV light, 30 min.) and CHO cells were cultured onto the films (see **Section 5.3.6**). A standard live/dead assay kit was used to determine viability of each azosilk polymer (calcein-AM/ethidium homodimer-1). Once the kit was applied, the cells were imaged over a period of 8 hours using a high throughput screening microscope. Using MetaXpress software, the CHO cell viability was tabulated for each azosilk substrate (**Table**

A4.1). The highest viability was achieved by a sodium sulfanilic-azobenzene derivative (96 ± 3%), while the lowest cell viability was recorded for the 4-(perfluorooctyl)aniline (40 ± 7%) and 2,3,4,5,6-pentafluoroaniline (49 ± 4%) derivatives of azosilk.

In parallel, films of each of the distinct azosilk polymers were created on piranha treated glass and processed similarly as the 12 well plates (5 days of slow drying followed by overnight in the oven at 45 °C). The hydrophobicity of each distinct azosilk film was measured by contact angle measurements (sessile drop, **Table A4.1**). An interesting, yet unexpected linear trend (R^2 = 0.9454, $P < 0.001$) emerges when plotting cell viability *vs* contact angle (**Figure 5.2 (A)**), where more hydrophilic azosilk films were found to achieve the highest viability, while the most hydrophobic polymers elicited a low survival. Attachment of cells is heavily dependent on integrin and other membrane-bound attachment factors, thus if the cell-expressed integrin is unable to bind to such hydrophobic surfaces, attachment does not occur, and thus the survival rate decreases.[32-33] Since each cell line expresses its own distinct integrin variants, attachment can be cell line and tissue specific, and can widely vary, if assemblage of basal proteins onto our azosilk surfaces is unable to proceed.[34] With the assay complete, we are able to select the highest performing azosilk material (sodium sulfanilic-azobenzene, **#3**) and proceed with blistering and cell guidance experiments.

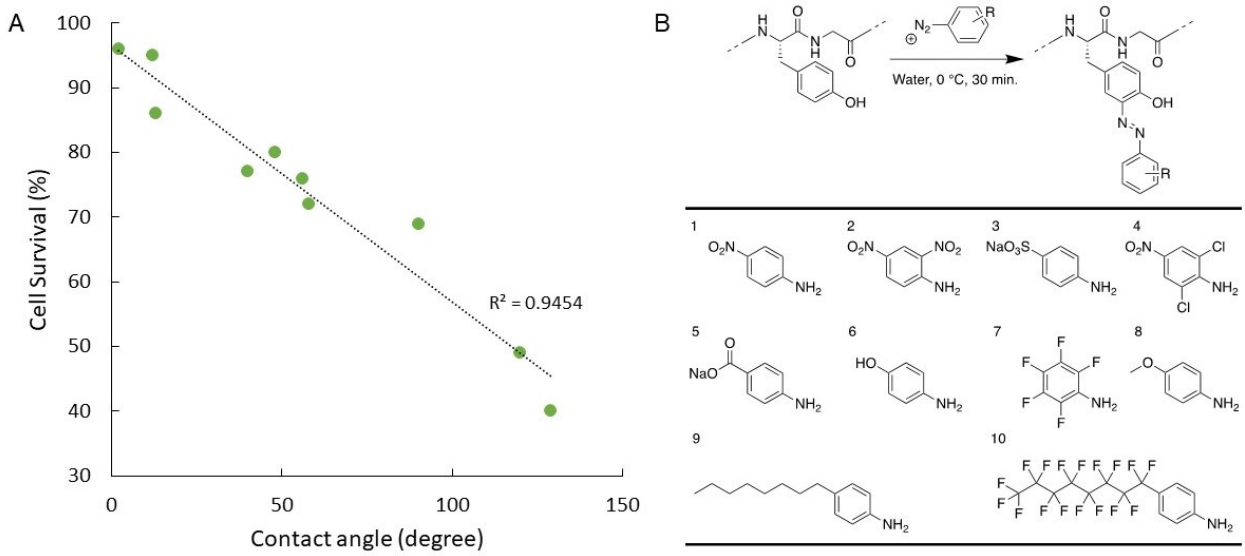

Figure 5.2. (A) CHO viability *vs* contact angle of the azosilk films which the CHO cells were plated on (line of best fit, $R^2 = 0.9454$, $P < 0.001$). **(B)** Schematic representation of the reaction scheme to create azosilk and the various 'head groups' used in this study.

With the optimal azosilk polymer selected (#**3**), the surface can now be blistered and inscribed with a specific pattern of choice. Micron sized dots have been demonstrated to affect cell migration, as they resemble nascent focal adhesions which are formed natively within tissue.[35] Lines also resemble native tissue and extracellular matrix components, and in fact, the idea of reproducing such features onto a surface is reminiscent of biomimicry, in a sense.[35] Such features have been shown to elicit an increased occurrence and stabilization of focal adhesions in the case of fibroblasts.[23,35] With this in mind, the patterns were designed as an array of 1 μm dots, 5 μm thick lines and large square irradiated regions, respectively (**Figure 5.3**). These features were inscribed into the film at a depth of 1 μm from the film surface. Previously, the writing depth has been shown to dramatically affect the size of the blisters formed on the surface.[24] Writing just below the surface of the film (~1 μm) maximized the observed photo-softening effect, going from 12 kPa on the non-written regions of the film to 0.6 on the blisters.[24] As previously shown, topological changes to a growth surface in conjunction with lower moduli are promising physical features to guide cells.[36] In the case of neurons, presynaptic assemblages occur on poly-L-lysine coated microbeads, as well as on arrays and gradients of modulus.[37-38] Coating flat surfaces with the same coating (PDL or PLL) elicited no additional presynaptic assemblages, thus the round topology of the bead was determined to be the key factor in the formation of these artificial

synapses. [37-38] This demonstrates the effectiveness of the topology of a growth surfaces to elicit specific responses from neurons, and the importance of creating controlled features on a surface with respect to the cell size cultured. [37-38] Unfortunately, both effects caused by inscription of azosilk films, namely photosoftening and the raised features, are unable to be disentangled; however, both effects have previously been shown to be beneficial to guiding cells.[39-40] Thus, to assess the inscribed patterned capacity to guide cells, CHO are plated onto the surface of the patterned azosilk material.

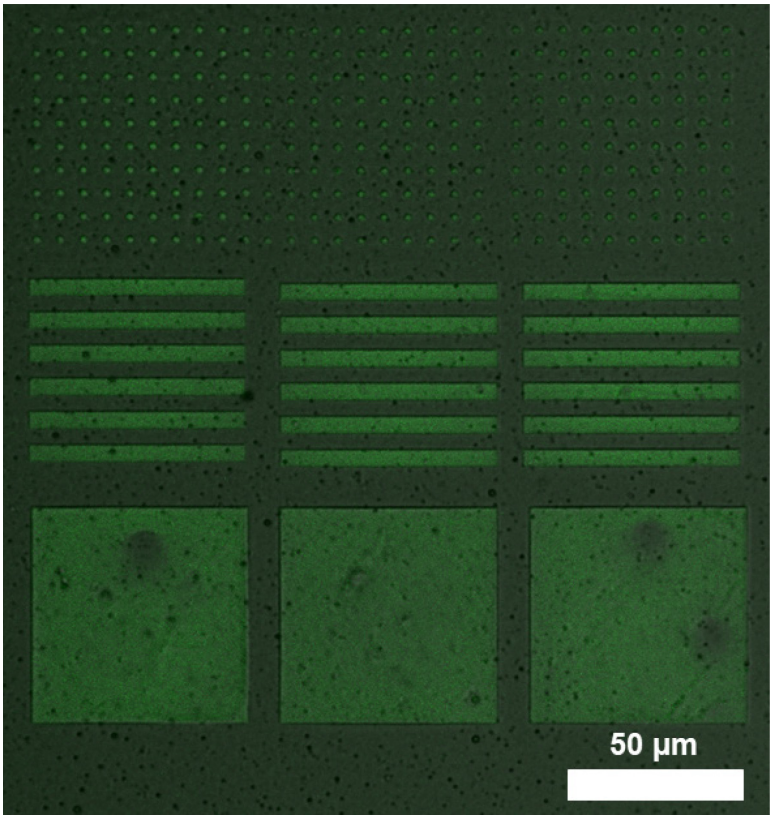

Figure 5.3. Fluorescence microscopy image of the patterned azosilk surface: (*top*) 1 µm radii dots that are separated by 5 µm in a grid pattern, (*middle*) 5 µm thin strips separated by 5 µm gaps, and (*bottom*) large squares completely irradiated. The pattern is excited using 800 nm and the fluorescence signal is taken from 400 – 750 nm.

The raised area proved difficult to enrich with enough cells, thus to populate the local environment of the patterns with additional CHO cells, a pipette loaded with the stock solution of cells was placed near the pattern and CHO cells are plated directly on top. 10-15 k cells were plated

onto each 6 well surface, roughly representing a 20% confluency. After allowing the cells to adhere to the surface for 4 hours, the plate was mounted onto a heated stage (37 °C) and images were taken every 10 minutes for 8 hours. From an initial qualitative assessment, the CHO cells were randomly dispersed over the pattern (**Figure A4.3**). After an additional hour, each CHO cell settled into a cobblestone shape, suggesting the surface was adequate for supporting their growth. This is additionally evident based on the presence of several dividing CHO cells. Since our CHO cell line was transfected with EGFP (WT-CHO-K1 cells stably expressing paxillin-EGFP), their cytoskeletal/focal adhesions proteins were visualized, and allowed for a facile method to track their position as well as their focal adhesions to the surface.

As an effort to determine the effect of our patterned substrates on cell adhesion, the number of focal adhesions were counted for both cells on the dots and lines patterns, and additionally on the non-irradiated area (**Figure 5.4(A)**). This was achieved by fixing the cells with paraformaldehyde, and then taking high resolution images of the cells on each pattern (**Figure 5.4(B) – (E)**). A simple methodology was employed by subtracting the background image (pattern) and isolating the increase in fluorescent signal associated with the focal adhesions.[41] To standardize these measurements, the total number of focal adhesions was divided by the total number of cells present, giving an average number of focal adhesions created per cell. While an additional square pattern is present in all images, due to the fluorescence intensity of the pattern, the number of focal adhesions was not possible to count specifically within that region. The highest number of focal adhesions per cell was elicited by the dot patterns (9.75 ± 1.7, **Figure 5.4 (B)** and **5.4 (C)**), however, this was not significantly different than the number of focal adhesions expressed by cells cultured on the non-irradiated area (8.25 ± 1.6, $P > 0.05$). CHO cells which formed focal adhesions to the dot pattern tended to form these anchors near the edge of the dot, rather than the center. Additionally, focal adhesions were found on the edge surface of each line (7.05 ± 1.5, **Figure 5.4 (D)** and **5.4 (E)**) and was not significantly different than the non-irradiated surface ($P > 0.05$). While the number of focal adhesions expressed per cell was not significantly different for each of the studied conditions, this can be rationalized by the difference in modulus values. While the raised patterns do show a 10x decrease in modulus (from 12 kPa to 0.6 kPa), this may be too abrupt of a change, as cells have been previously shown to respond to shallow gradients of moduli rather than a large steep change that was presented to them by the microblisters.[42]

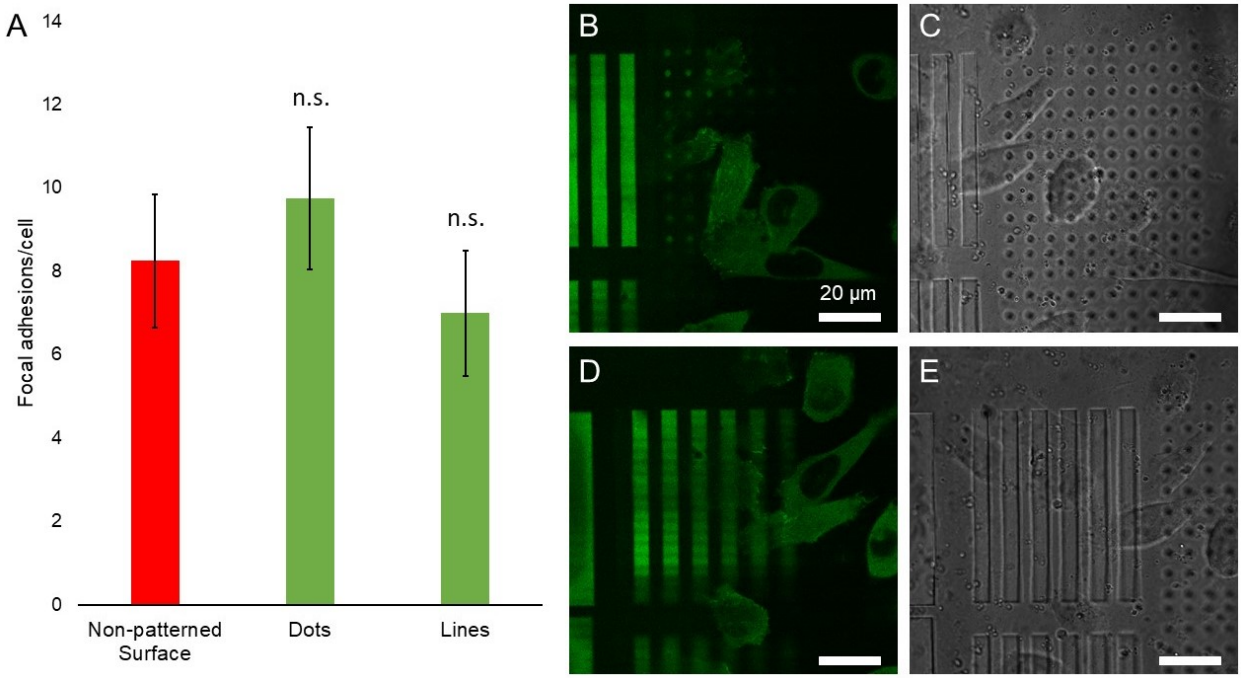

Figure 5.4. (A) Histogram illustrating the number of focal adhesions expressed per cell and grouped into three populations: cells on a dot pattern, on a line pattern or on the non-patterned surface (control, red). The number of focal adhesions per cell was found to be not significant as compared to the control (non-patterned surface) for both conditions ($P > 0.05$). **(B)** Fluorescence image of paxillin-EGFP CHO cells on a dot pattern, where higher fluorescence intensities indicated localized focal adhesions. **(C)** Corresponding brightfield image of **(B)**. **(D)** Fluorescence image of paxillin-EGFP CHO cells on a line pattern, where higher fluorescence intensities indicated localized focal adhesions. **(E)** Corresponding brightfield image of **(D)**.

Surface patterns, and modulus differences have been previously shown to influence the total area that a cell spreads.[43] Influence over cell area is a by-product of the binding strength of integrin or other extracellular matrix binding proteins to the cell growth surface.[43] The mechanical modulus of a substrate has also been previously shown to influence the spread size of cells onto surface as well. Softer substrates have been shown to elucidate a more ameboid shape (round) and movement of CHO cells, whereas harder substrates (glass or typical cell culture substrates) force the adoption of a more spread cell morphology (cobblestone).[44-45] Dots and lines have previously been investigated and have been shown to have an influence on the binding area of cell to a

surface.[29, 46] Influence over the general cell morphology occurs either through a change in modulus (mechanosensing through induced conformational changes to membrane proteins or integrin binding) or through a change in topography.[47]

To determine if our patterns had an influence over how spread the cultured CHO cells were, a series of CHO cell area measurements were taken: on dots, on lines and on the non-irradiated surface. Again, three populations of 25 cells from each condition were selected and their surface area was measured and quantified (**Figure 5.5 (A)**). During the initial cell adhesion, rounded cells landed onto the azosilk surface and, over the course of 4 hours, adopted their traditional cobblestone morphology. Other morphologies were not observed, except in the case of cell division, where the dividing cells formed a cleavage furrow and appeared rounder. While CHO cells which adhered to the dots did demonstrate a more elongated shape (**Figure 5.5 (B)** and **5.5 (C)**), their surface area did not statistically differ from both the cells adhered to the lines and the cells on the non-irradiated area ($P > 0.05$). CHO cells which were cultured on the dots patterned had a surface area of 430 ± 65 μm^2, whereas cells cultured on non-patterned areas were found to be slightly more spread (475 ± 66 μm^2). CHO cells cultured on line patterns (448 ± 45 μm^2) were also found to not differ significantly from the control ($P > 0.05$, non-patterned area). During this analysis, cells which were dividing or just divided were excluded, due to their immaturity. CHO cells on the surface of the squares were difficult to measure and were disregarded from this study, as the fluorescence emission of both written azosilk areas and the EGFP signals were difficult to separate and additional brightfield images were not clear in that area. While no significant difference was found between each of the populations of cells on each pattern, this behavior may be expected. While azosilk does exhibit a dramatic 10x decrease in modulus, perhaps this was not enough of a change to elucidate a morphological change to the CHO cells. Fibroblasts cells have been previously demonstrated to exhibit a dramatic 4-fold change in cell area (from 500 – 2000 μm^2) when cultured on surfaces that varied from 2-8 kPa.[48] This is a rather dramatic change; however, other cell types such as neurons do not show such a dramatic change in morphology or cell area, but do die when they are cultured on surfaces that are not in the correct range of modulus.[49] Perhaps, in our case, CHO cells were not a wise choice if we were trying to influence cell size with patterns of different modulus.

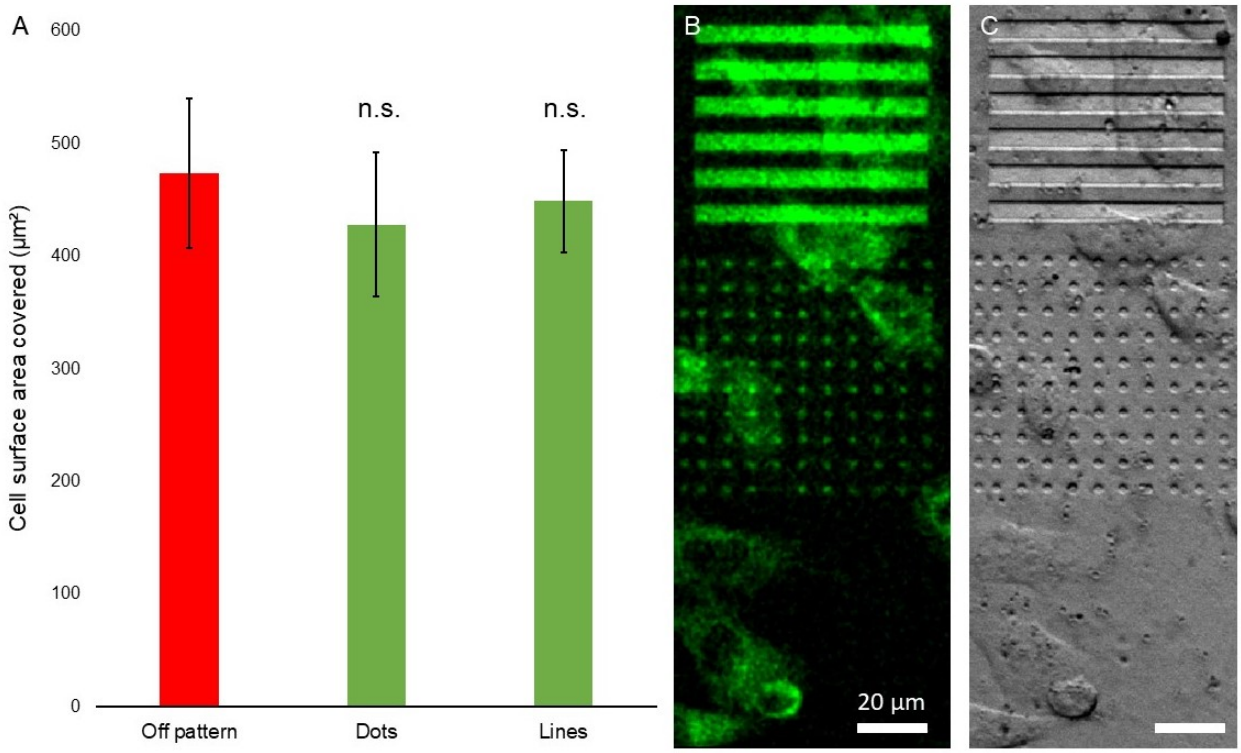

Figure 5.5. (A) A histogram depicting the average total area of a population of 75 cells (n = 3) that were adhered to regions off the pattern, on a dot pattern and on a line pattern. Off pattern was chosen as a control (red), and cells cultured on patterns consisting of dots and lines did not significantly differ in total surface area adhered from the control ($P > 0.05$). **(B)** Representative fluorescence images depicting the morphology of cells present on lines, dots and non-patterned areas. **(C)** Corresponding brightfield image to **(B)**.

As a final method to determine if CHO cells were influenced by our topological surface patterns, the cell migration speed was calculated for both cells on and off each of the patterns. This was achieved by separately tracking three populations of 25 cells each which were on patterns of: dots, lines or off the pattern. The exact position of each cell was marked in each frame of the time-lapse video, and the migration speed was calculated from the change in position with respect to time over the 8 hours of live cell imaging. **Figures A4.4**, **A4.5**, and **A4.6** are example plots of the position of each cell over the period of 8 hours of live cell imaging and each color represents a different cell. **Figure 5.6 (B)** is a representative image of CHO cells which were cultured on the raised dot pattern. The positional data is layered onto the fluorescence image and was represented using X's. **Figure 5.6 (C)** represents the positional data of CHO cells cultured on a line pattern.

These plots were generated using Metamorph imaging software and using the track objects function of the program. Cells which were present near the pattern, but not specifically on the pattern, were disregarded, as they were found to migrate back and forth between each of the patterns themselves. On average, EGFP-transfected CHO cells were found to migrate 25 ± 5 μm/hr on the dots, 29 ± 5 μm/hr on the lines and 29 ± 5 μm/hr on the non-irradiated region. **Figure 5.6 (A)** is a histogram of the average speed found from each group and demonstrates that there was no significant difference between cells cultured on dots or lines versus the control ($P > 0.05$). While a subset of 10 cells in total were found to have a higher cell velocity (dots maximum speed = 110 μm/hr and lines maximum speed = 134 μm/hr), these were found within an area which was situated between the lines and the dots. Their migration pattern was found to be semi-linear, forming focal adhesions to each of the dots or line patterns, yet not specifically choosing either pattern to further migrate onto. However, once these cells did migrate to either the patterned or the non-patterned area, their speed returned to normal (~25-29 μm/hr). Directionality of their motion was found to be random and conformed to the random-walk migration described by Harms and coworkers.[50] The speed was found to be consistent with the reported literature values as well.[50] While the speed was found to not differ significantly than the control, this present research does hold some promise for these patterns to function as a directed cell growth surface, as evident from the subset of 10 cells which migrated at a higher velocity than their control, which were found to be exclusively confined to a specific area within the pattern itself. Cells which were found to migrate between the dots and lines patterns were found to be significantly faster than cells off the pattern (115 μm/hr, $n = 10$, $P < 0.05$).

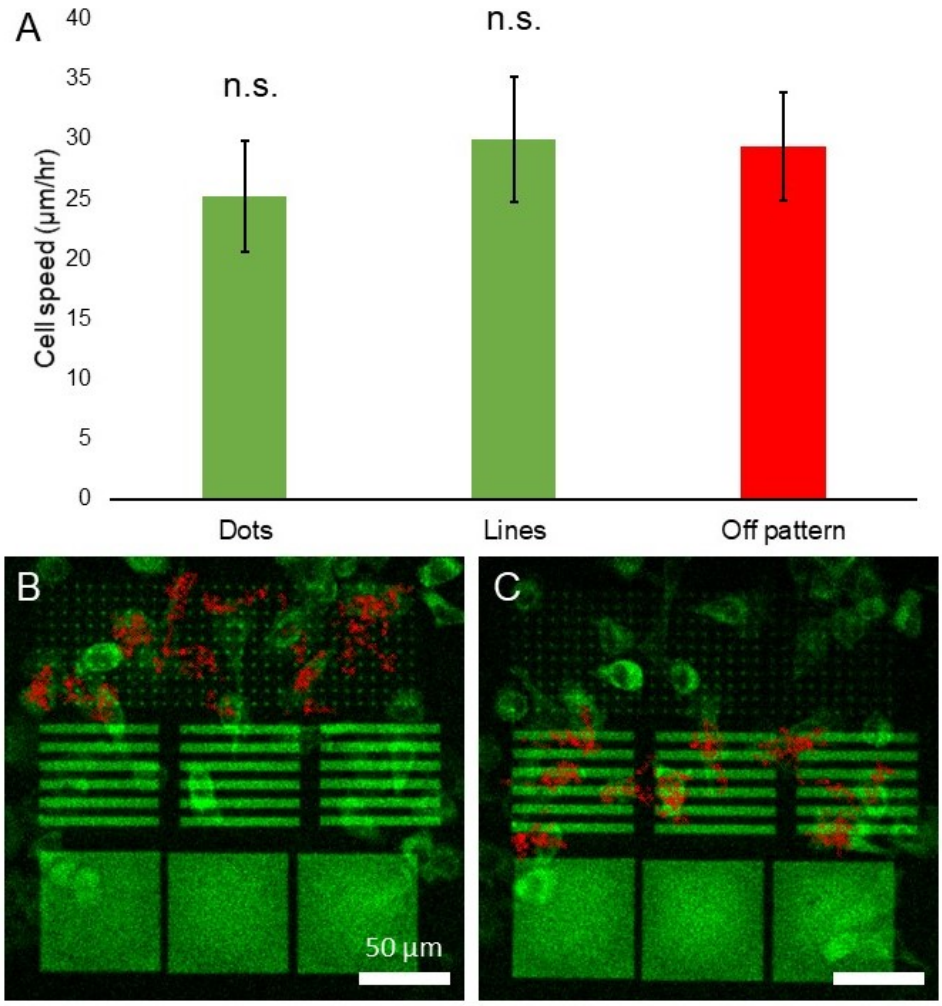

Figure 5.6. (A) A histogram depicting the average cell speed of cells cultured on a dot pattern, a line pattern and off a pattern. Comparing the migration speed of cells cultured on dots and lines to a non-patterned area shows that there is no significant difference ($P > 0.05$). **(B)** Cell position layered onto a fluorescence image of cells cultured on dots, and **(C)** lines.

Azosilk has been previously shown to be a flexible biomaterial for culturing a wide variety of cells. Azosilk has also been shown to be a photo-responsive material, which is evidently demonstrated by the dramatic photosoftening effect (10x) and by the production of microblisters which are confined to the irradiation area (800 nm, >100 $\mu J/\mu m^2$). By trying to merge these two areas together, azosilk has shown some promise as a photo-responsive biomaterial, which may have some influence over cell growth and migration. Evidently, azosilk does offer a platform which is more flexible than previous photo-lithography techniques and microcontact printing. This platform requires a standard confocal microscope and a freely available Matlab program[30] to create

a multitude of patterns. This platform offers a methodology to go from paper to pattern in a matter of a few hours, rather than the typical few days required to work in the clean room to produced new patterns in the case of microcontact printing. In our attempts to optically influence cellular motion, a subset of CHO cells which adhered between the dot and line patterns were found to migrate at a significantly faster velocity than the control (115 μm/hr, $n = 10$, $P < 0.05$), but once they migrate to either pattern, they slow back to the control's speed. While we did not explicitly find any significant differences between our control and the patterns for focal adhesions and cell adhesion area, we believe that this study may be used as a tool to study more moduli sensitive cells. The developed tools maybe more appropriately used for guiding neural cells or fibroblasts, both cell types which have been demonstrated to be very sensitive to modulus changes. In addition, neural cells have been shown to be sensitive to topological changes as well, thus this system maybe more applicable to the culture of motoneurons or oligodendrocytes.

5.5 **Conclusion**

Azosilk materials show promise as a flexible, facile and low-cost option to create topological features onto a film and holds promise as a platform for guiding cells. While tools exist to create discreet patterns onto a material, the described azosilk lithographic method allows for the creation of patterns onto a biomaterial film within a matter of hours rather than days, and additionally demonstrates a tunable hydrophobicity and modulus. We were able to select the most optimal azosilk derivative to maximize cell survival by tuning the hydrophobicity of the polymer with chemical modifications. While the work presented does not show any significant effect for enhancing adhesion (focal adhesions) or affecting the growth (surface area), we did find a significant speed change for cells which were found between the two patterns. This preliminary work for guiding the migration (cell speed) of CHO cells may be expanded to include more modulus or topologically sensitive cells, such as oligodendrocytes. Indeed, we believe that the development of these tools, including the lithographic process for azosilk, are useful and azosilk may serve as a next generation material for studying cell migration due to its flexibility and ease of creating patterns on-the-fly using localized laser light irradiation.

5.6 Acknowledgements

The project was support by a Collaborative Health Research Program (CHRP) grant from the Canadian Institutes of Health Research (CIHR 357055) and the Natural Sciences and Engineering Research Council (NSERC 493633-16, 261938-13).

5.7 References

1. Ridley, A. J.; Schwartz, M. A.; Burridge, K.; Firtel, R. A.; Ginsberg, M. H.; Borisy, G.; Parsons, J. T.; Horwitz, A. R., Cell migration: Integrating signals from front to back. *Science* **2003**, *302* (5651), 1704–1709.

2. Tweedy, L.; Knecht, D.A.; Mackay, G.M.; Insall, R.H., Self-generated chemoattractant gradients: Attractant depletion extends the range and robustness of chemotaxis. *PLoS Biol.* **2016**, *14* (3), e1002404.

3. Roca-Cusachs, P.; Sunyer, R.; Trepat, X., Mechanical guidance of cell migration: Lessons from chemotaxis. *Curr. Opin. Cell Biol.* **2013**, *25* (5), 543–549.

4. Recknor, J. B.; Recknor, J. C.; Sakaguchi, D. S.; Mallapragada, S. K., Oriented astroglial cell growth on micropatterned polystyrene substrates. *Biomaterials* **2004**, *25* (14), 2753–2767.

5. Whittlesey, K. J.; Shea, L. D., Nerve growth factor expression by PLG-mediated lipofection. *Biomaterials* **2006**, *27* (11), 2477–2486.

6. Clark, P.; Connolly, P.; Curtis, A. S.; Dow, J. A.; Wilkinson, C. D., Cell guidance by ultrafine topography *in vitro*. *J. Cell Sci.* **1991**, *99* (1), 73–77.

7. Patel, S.; Kurpinski, K.; Quigley, R.; Gao, H.; Hsiao, B. S.; Poo, M.-M.; Li, S., Bioactive nanofibers: Synergistic effects of nanotopography and chemical signaling on cell guidance. *Nano Lett.* **2007**, *7* (7), 2122–2128.

8. Bernard, A.; Renault, J.P.; Michel, B.; Bosshard, H.R.; Delamarche, E., Microcontact printing of proteins. *Adv. Mater.* **2000**, *12* (14), 1067–1070.

9. Craighead, H. G.; James, C. D.; Turner, A. M. P., Chemical and topographical patterning for directed cell attachment. *Curr. Opin. Solid State Mater. Sci.* **2001**, *5* (2), 177–184.

10. Schmaljohann, D., Thermo- and pH-responsive polymers in drug delivery. *Adv. Drug Deliv. Rev.* **2006**, *58* (15), 1655–1670.

11. de las Heras Alarcón, C.; Pennadam, S.; Alexander, C., Stimuli responsive polymers for biomedical applications. *Chem. Soc. Rev.* **2005**, *34* (3), 276–285.

12. Irie, M., *New Polymer Materials*: Springer: Berlin, Heidelberg, 1990.

13. Sailer, M.; Fernandez, R.; Lu, X.; Barrett, C. J., High levels of molecular orientation of surface azo chromophores can be optically induced even in a wet biological environment. *Phys. Chem. Chem. Phys.* **2013**, *15* (46), 19985–19989.

14. Hou, J.; Chen, R.; Liu, J.; Wang, H.; Shi, Q.; Xin, Z.; Wong, S.-C.; Yin, J., Multiple microarrays of non-adherent cells on a single 3D stimuli-responsive binary polymer-brush pattern. *J. Mater. Chem. B* **2018**, *6,* 4792–4798.

15. Landry, M. J.; Rollet, F.-G.; Kennedy, T. E.; Barrett, C. J., Layers and multilayers of self-assembled polymers: Tunable engineered extracellular matrix coatings for neural cell growth. *Langmuir* **2018**, *34* (30), 8709–8730.

16. Qiuning, L.; Chunyan, B.; Yunlong, Y.; Qiannan, L.; Dasheng, Z.; Shuiyu, C.; Linyong, Z., Highly Discriminating photorelease of anticancer drugs based on hypoxia activatable phototrigger conjugated chitosan nanoparticles. *Adv. Mater.* **2013**, *25* (14), 1981–1986.

17. Welle, A.; Horn, S.; Schimmelpfeng, J.; Kalka, D., Photo-chemically patterned polymer surfaces for controlled PC-12 adhesion and neurite guidance. *J. Neurosci. Methods* **2005,** *142* (2), 243–250.

18. Lugo, K.; Miao, X.; Rieke, F.; Lin, L. Y., Remote switching of cellular activity and cell signaling using light in conjunction with quantum dots. *Biomed. Opt. Express* **2012**, *3* (3), 447–454.

19. Goulet-Hanssens, A.; Barrett, C. J., Photo-control of biological systems with azobenzene polymers. *J. Polym. Sci. A Polym. Chem.* **2013**, *51* (14), 3058–3070.

20. Goulet-Hanssens, A.; Lai Wing Sun, K.; Kennedy, T. E.; Barrett, C. J., Photoreversible surfaces to regulate cell adhesion. *Biomacromolecules* **2012**, *13* (9), 2958–2963.

21. Amsden, J. J.; Domachuk, P.; Gopinath, A.; White, R. D.; Negro, L. D.; Kaplan, D. L.; Omenetto, F. G., Rapid nanoimprinting of silk fibroin films for biophotonic applications. *Adv. Mater.* **2010**, *22* (15), 1746–1749.

22. Applegate, M. B.; Coburn, J.; Partlow, B. P.; Moreau, J. E.; Mondia, J. P.; Marelli, B.; Kaplan, D. L.; Omenetto, F. G., Laser-based three-dimensional multiscale micropatterning of biocompatible hydrogels for customized tissue engineering scaffolds. *Proc. Natl. Acad. Sci. U. S. A.* **2015**, *112* (39), 12052–12057.

23. Applegate, M. B.; Perotto, G.; Kaplan, D. L.; Omenetto, F. G., Biocompatible silk step-index optical waveguides. *Biomed. Opt. Express* **2015**, *6* (11), 4221–4227.

24. Landry, M. J.; Applegate, M. B.; Bushuyev, O. S.; Omenetto, F. G.; Kaplan, D. L.; Cronin-Golomb, M.; Barrett, C. J., Photo-induced structural modification of silk gels containing azobenzene side groups. *Soft Matter* **2017**, *13* (16), 2903–2906.

25. Shen, Y.; Qian, Y.; Zhang, H.; Zuo, B.; Lu, Z.; Fan, Z.; Zhang, P.; Zhang, F.; Zhou, C., Guidance of olfactory ensheathing cell growth and migration on electrospun silk fibroin scaffolds. *Cell Transplant* **2010**, *19* (2), 147–157.

26. Yang, Y.; Ding, F.; Wu, J.; Hu, W.; Liu, W.; Liu, J.; Gu, X., Development and evaluation of silk fibroin-based nerve grafts used for peripheral nerve regeneration. *Biomaterials* **2007**, *28* (36), 5526–5535.

27. Schindelin, J.; Arganda-Carreras, I.; Frise, E.; Kaynig, V.; Longair, M.; Pietzsch, T.; Preibisch, S.; Rueden, C.; Saalfeld, S.; Schmid, B.; Tinevez, J.-Y.; White, D. J.; Hartenstein, V.; Eliceiri, K.; Tomancak, P.; Cardona, A., Fiji: an open-source platform for biological-image analysis. *Nat. Methods* **2012**, *9*, 676–682.

28. Rockwood, D. N.; Preda, R. C.; Yucel, T.; Wang, X.; Lovett, M. L.; Kaplan, D. L., Materials fabrication from *Bombyx mori* silk fibroin. *Nat. Protoc.* **2011**, *6* (10), 1612–1631.

29. Doyle, A. D.; Yamada, K. M., Mechanosensing *via* cell-matrix adhesions in 3D microenvironments. *Exp. Cell Res.* **2016**, *343* (1), 60-66.

30. Culver, J. C.; Hoffmann, J. C.; Poche, R. A.; Slater, J. H.; West, J. L.; Dickinson, M. E., Three-dimensional biomimetic patterning in hydrogels to guide cellular organization. *Adv. Mater.* **2012,** *24* (17), 2344–2348.

31. Lu, Q.; Hu, X.; Wang, X.; Kluge, J. A.; Lu, S.; Cebe, P.; Kaplan, D. L., Water-insoluble silk films with silk I structure. *Acta Biomater.* **2010**, *6* (4), 1380–1387.

32. Haas, T. A.; Plow, E. F., Integrin-ligarid interactions: a year in review. *Curr. Opin. Cell Biol.* **1994**, *6* (5), 656–662.

33. Hynes, R. O., Integrins: a family of cell surface receptors. *Cell* **1987**, *48* (4), 549–554.

34. Horbett, T.A.; Waldburger, J.J.; Ratner, B.D.; Hoffman, A.S., Cell adhesion to a series of hydrophili–hydrophobic copolymers studies with a spinning disc apparatus. *J. Biomed. Mater. Res.* **1988**, *22* (5), 383–404.

35. Curtis, A.; Wilkinson, C., Topographical control of cells. *Biomaterials* **1997**, *18* (24), 1573–1583.

36. Lim, J. Y.; Donahue, H. J., Cell sensing and response to micro- and nanostructured surfaces produced by chemical and topographic patterning. *Tissue Eng. A* **2007**, *13* (8), 1879–1891.

37. Lucido, A. L.; Suarez Sanchez, F.; Thostrup, P.; Kwiatkowski, A. V.; Leal-Ortiz, S.; Gopalakrishnan, G.; Liazoghli, D.; Belkaid, W.; Lennox, R. B.; Grutter, P.; Garner, C. C.; Colman, D. R., Rapid assembly of functional presynaptic boutons triggered by adhesive contacts. *J. Neurosci.* **2009**, *29* (40), 12449–12466.

38. Banerjee, A.; Arha, M.; Choudhary, S.; Ashton, R. S.; Bhatia, S. R.; Schaffer, D. V.; Kane, R. S., The influence of hydrogel modulus on the proliferation and differentiation of encapsulated neural stem cells. *Biomaterials* **2009**, *30* (27), 4695–4699.

39. Pimpon, U.; Toworfe, G. K.; Dietrich, F.; Lelkes, P. I.; Composto, R. J., Topographic guidance of endothelial cells on silicone surfaces with micro- to nanogrooves: Orientation of actin filaments and focal adhesions. *J. Biomed. Mater. Res. A* **2005**, *75A* (3), 668–680.

40. Nikkhah, M.; Edalat, F.; Manoucheri, S.; Khademhosseini, A., Engineering microscale topographies to control the cell–substrate interface. *Biomaterials* **2012,** *33* (21), 5230–5246.

41. Horzum, U.; Ozdil, B.; Pesen-Okvur, D., Step-by-step quantitative analysis of focal adhesions. *MethodsX* **2014**, *1*, 56–59.

42. Zaari, N.; Rajagopalan, P.; Kim, S. K.; Engler, A. J.; Wong, J. Y., Photopolymerization in microfluidic gradient generators: Microscale control of substrate compliance to manipulate cell response. *Adv. Mater.* **2004**, *16* (23-24), 2133–2137.

43. Lecuit, T.; Lenne, P.-F., Cell surface mechanics and the control of cell shape, tissue patterns and morphogenesis. *Nat. Rev. Mol. Cell Biol.* **2007**, *8*, 633–644.

44. Kim, J.; Kim, I. S.; Cho, T. H.; Lee, K. B.; Hwang, S. J.; Tae, G.; Noh, I.; Lee, S. H.; Park, Y.; Sun, K., Bone regeneration using hyaluronic acid-based hydrogel with bone morphogenic protein-2 and human mesenchymal stem cells. *Biomaterials* **2007**, *28* (10), 1830–1837.

45. Mei, Y.; Saha, K.; Bogatyrev, S. R.; Yang, J.; Hook, A. L.; Kalcioglu, Z. I.; Cho, S.-W.; Mitalipova, M.; Pyzocha, N.; Rojas, F.; Van Vliet, K. J.; Davies, M. C.; Alexander, M. R.; Langer, R.; Jaenisch, R.; Anderson, D. G., Combinatorial development of biomaterials for clonal growth of human pluripotent stem cells. *Nat. Mater.* **2010**, *9*, 768–778.

46. Ito, Y., Surface micropatterning to regulate cell functions. *Biomaterials* **1999**, *20* (23), 2333–2342.

47. Cukierman, E.; Pankov, R.; Stevens, D. R.; Yamada, K. M., Taking cell-matrix adhesions to the third dimension. *Science* **2001**, *294* (5547), 1708–1712.

48. Solon, J.; Levental, I.; Sengupta, K.; Georges, P. C.; Janmey, P. A., Fibroblast adaptation and stiffness matching to soft elastic substrates. *Biophys. J.* **2007**, *93* (12), 4453–4461.

49. Levental, I.; Georges, P. C.; Janmey, P. A., Soft biological materials and their impact on cell function. *Soft Matter* **2007**, *3* (3), 299–306.

50. Harms, G. S.; Pauls, S. W.; Hedstrom, J. F.; Johnson, C. K., Fluorescence and rotational dynamics of dityrosine. *J. Fluoresc.* **1997**, *7* (4), 283–292.

Appendix 4: Supplemental information for Chapter 5

Extra figures

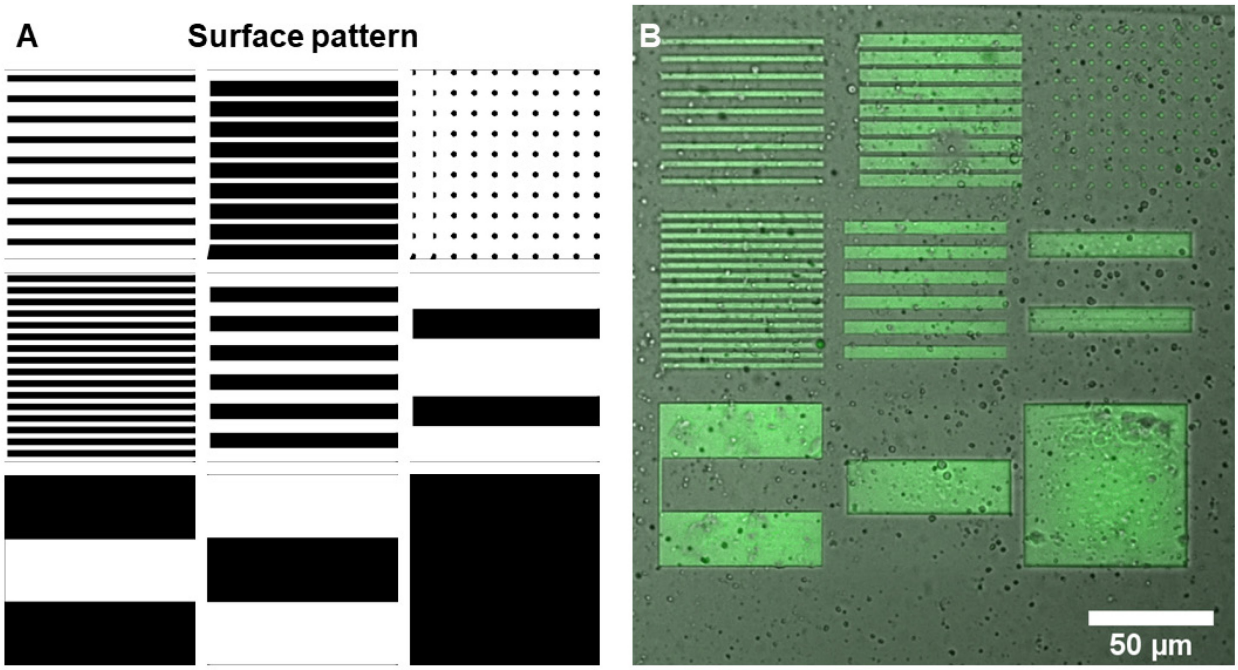

Figure A4.1. Pictographic representation of **(A)** the intended pattern to be inscribed onto the surface of the azosilk gel. Black represents areas where the laser will write and write represents areas where the laser will be turned off during the raster-scanning of the surface. **(B)** The resulting fluorescent image generated by inscribing the surface pattern via 'region of interest' irradiation.

Table A4.1. Table of each headgroup of group appended to silk to create azosilk, and the resulting contact angle and cell survival. The structures are arranged in ascending contact angle and cell survival.

Azosilk headgroup	Contact angle (deg)	Cell Survival (%)
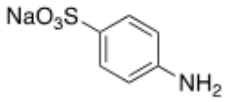	2 ± 2	96 ± 3
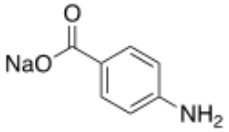	12 ± 8	95 ± 1
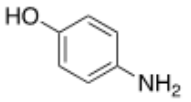	13 ± 9	86 ± 4
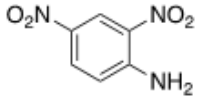	40 ± 6	77 ± 5
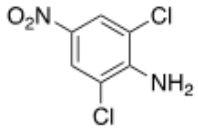	48 ± 2	80 ± 6
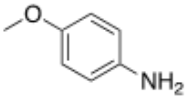	56 ± 1	76 ± 5
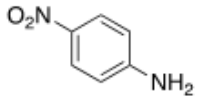	58 ± 4	72 ± 5
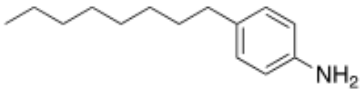	90 ± 4	69 ± 5
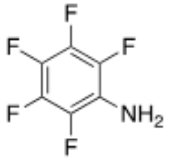	120 ± 3	49 ± 4
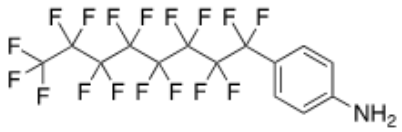	129 ± 2	40 ± 7

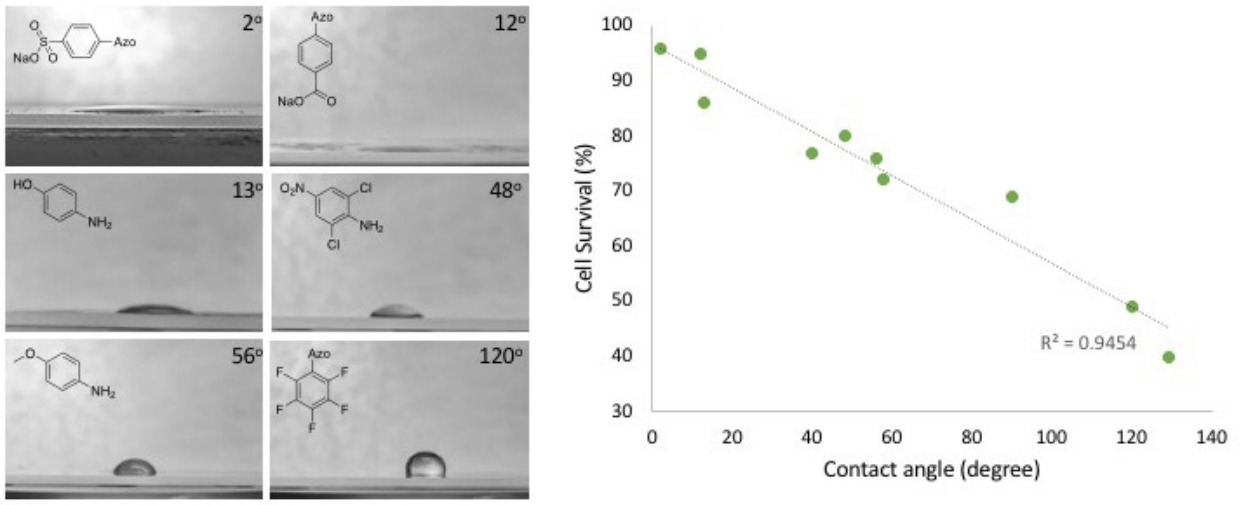

Figure A4.2. (*left*) Representative images of the contact angle measurements, demonstrating the wide range of contact angles that were achieved using different azobenzene headgroups. (*right*) CHO viability as determined by a Live/Dead assay kit (calcein-AM/ethidium homodimer-1) *vs* contact angle of the azosilk films the CHO cells were plated on (line of best fit, $R^2 = 0.9454$, $P < 0.001$).

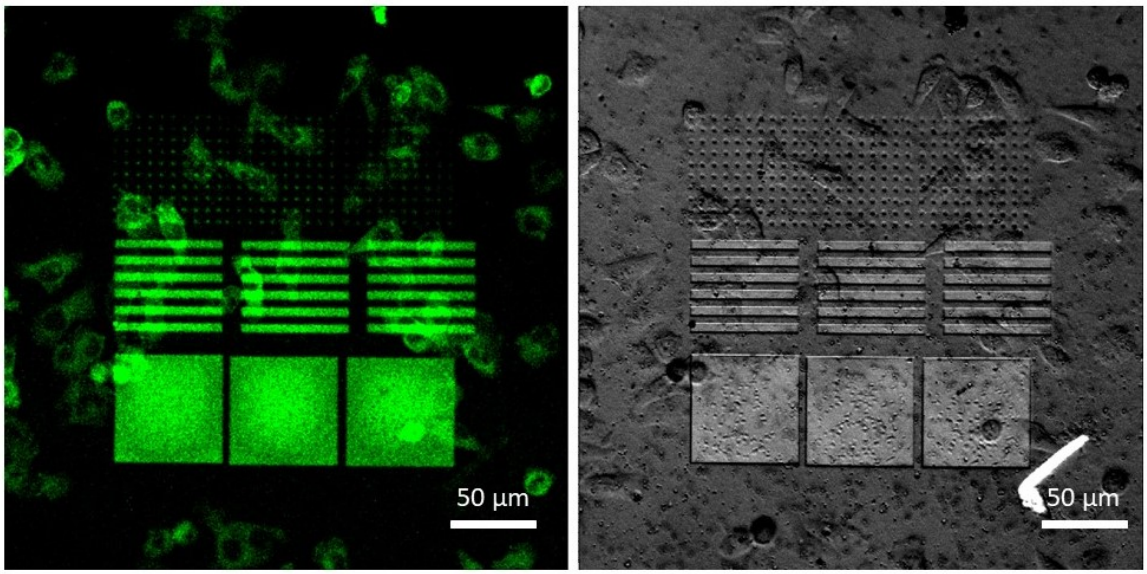

Figure A4.3. Images of CHO cells onto the surface of the inscribed azosilk film. (*Left*) Florescence image excited at 488 nm of the surface pattern and the paxillin-EGFP labelled CHO cells. The excitation of the written regions within the azosilk film also occur at 488 nm, as well as a broad adsorption throughout most of the visible spectrum, thus we see both the EGFP-labeled cell and the pattern. (*Right*) Bright field image of the cells and the raised pattern.

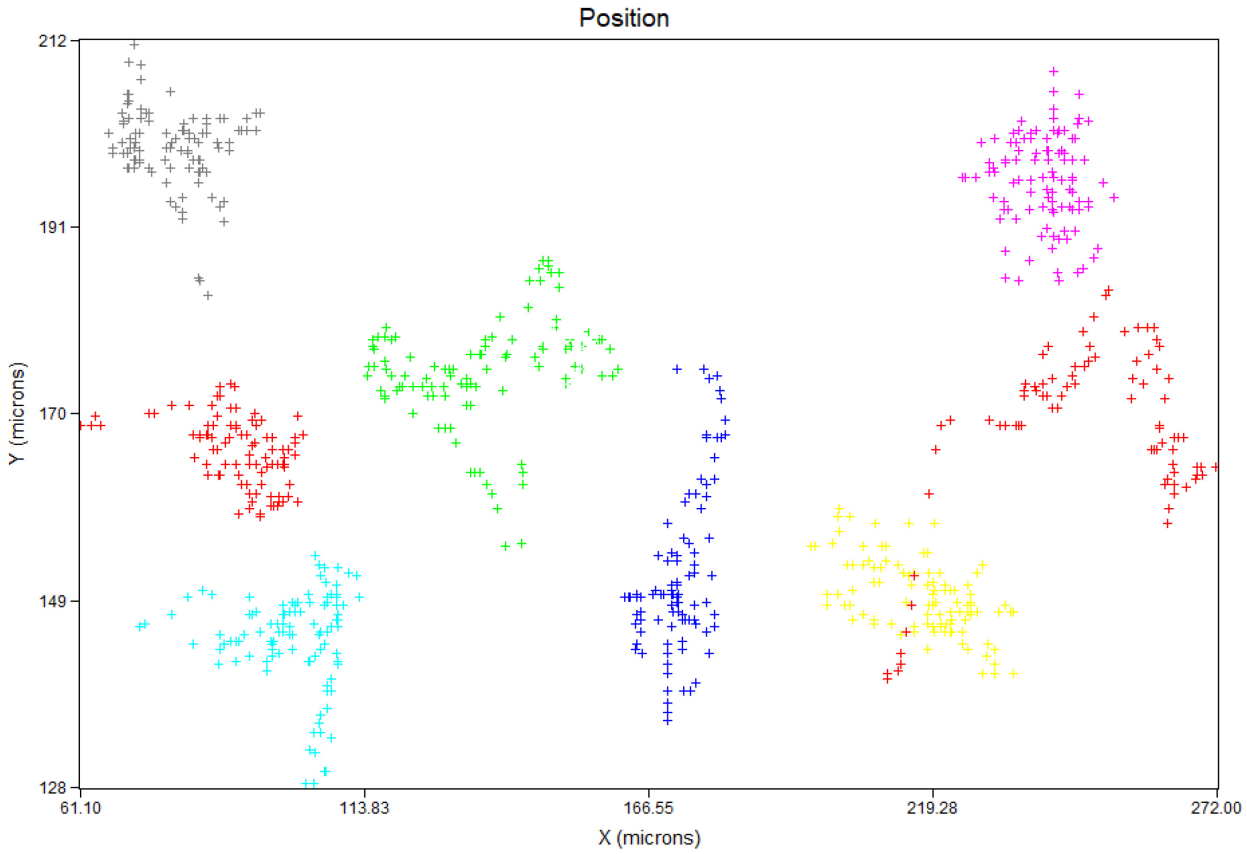

Figure A4.4. Plot of each trajectory of CHO cells which are present on the 5 μm thick lines. Only cells which were present within a range of 20 μm from the line pattern were tracked. The duration of the run is 10 hours and each mark is the position of the cell after 10 minutes. Each cross marks the position of the center of the cell (nucleus) and each color represents a separate cell. This is a representative image of the data set from 3 cell cultures.

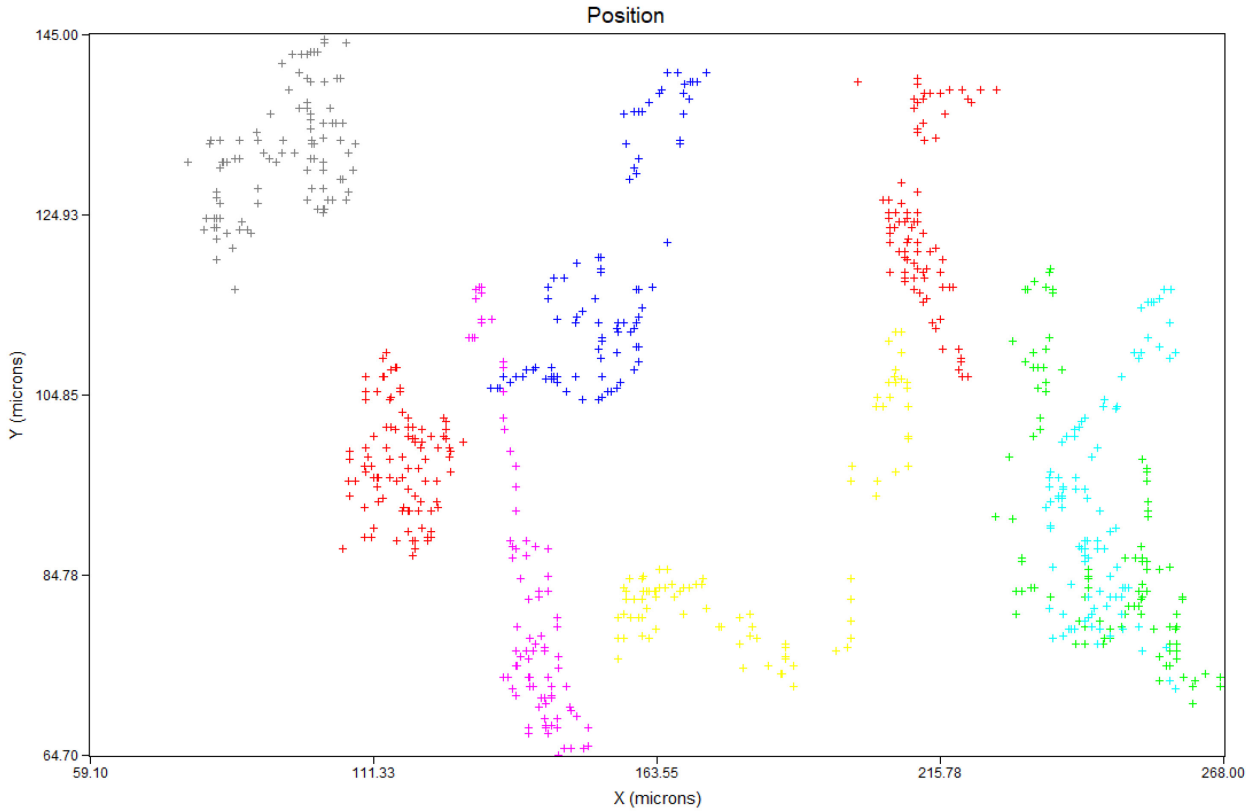

Figure A4.5. Plot of each trajectory of CHO cells which are present on the 1 μm radius dots. Only cells which were present within a range of 20 μm from the dot pattern were tracked. The duration of the run is 10 hours and each mark is the position of the cell after 10 minutes. Each cross marks the position of the center of the cell (nucleus) and each color represents a separate cell. This is a representative image of the data set from 3 cell cultures.

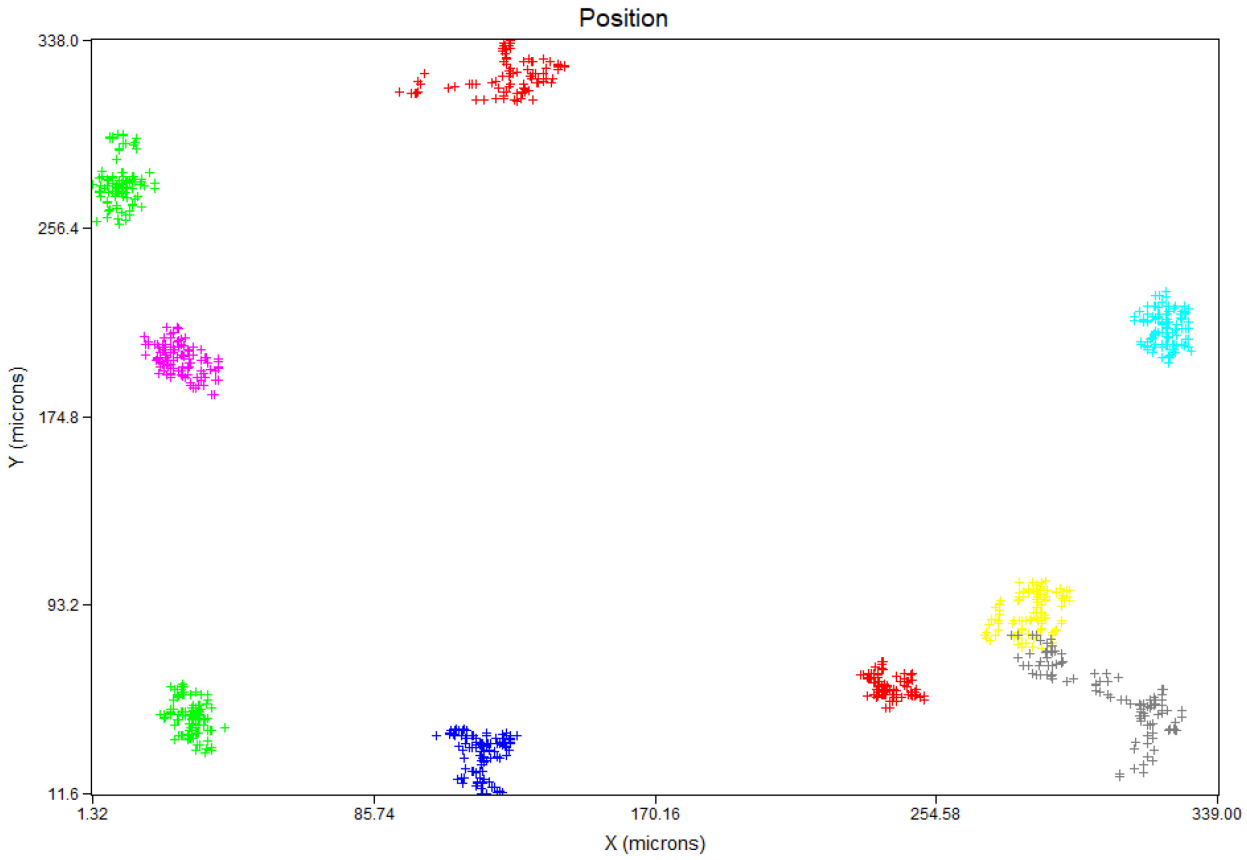

Figure A4.6. Plot of each trajectory of CHO cells which are present off the pattern. The duration of the run is 10 hours and each mark is the position of the cell after 10 minutes. Each cross marks the position of the center of the cell (nucleus) and each color represents a separate cell. This is a representative image of the data set from 3 cell cultures.

Chapter 6: Conclusions and Outlook

6.1 Summary and contributions to original knowledge

This thesis describes the creation and optimization of a photo-responsive biomaterial and demonstrates the use of the newly developed material in a variety of applications, including guided cell growth, augmented cell growth coatings, and artificial vascular tissue support materials. Chapter 2 explores the duality of synthetically created and biologically derived polyelectrolytes for the creation of wet, soft and biocompatible supportive coatings for cultivating neurons. The concepts presented in Chapter 1, in addition to the experimental results shown in Chapter 2 reiterate a well-known finding: bioinspired polymers perform more optimally for supporting tissue culture than traditionally synthesized plastics and provides an environment that is conducive to a real tissue matrix. Chapter 3 continues this bioinspired message, with the synthesis of azobenzene-modified polymers for electrospinning into suitable vascular graft materials. Chapter 4 builds on the three-dimensional material created within Chapter 3 by elucidating a method for tuning the topology and morphology of an azosilk surface using light. Finally, Chapter 5 explores the use of the patterned surfaces created in Chapter 4 for optically guiding CHO cell migration and growth.

A few key conclusions that arise from the presented chapters are worth further discussion. Chapter 2 demonstrated a quick and efficient method to characterize a surface's capacity to perform as an effective coating to support neural cells. By characterizing the surface coverage of a film, only materials which prompt the creation of extended neural networks are highlighted. Traditionally, Hoescht staining provided a quick and efficient method for assessing survival; however, the success of a neural coating relies on both high connectivity and process extension. Process extension can only be characterized using a stain which highlights the entire cell body, especially neuron cell processes themselves. Chapter 2 also demonstrates for the first time a silk-based polymer which outperforms PDL, the industry standard, as a coating. This answers one specific question that was posed within the context of this thesis: silk materials can replace existing technologies and can create solutions to existing problems. One such problem being the stability of PDL surfaces in long-term storage and in cultures. Silk materials have been demonstrated to resist degradation, as described in Chapter 2, and preliminary results demonstrate that surfaces created from silk-based PEMs last for up to 6 months in ambient storage conditions. This is longer than the few days that PDL surfaces are considered to be stable. Silk-based PEMs provide a platform to create a long lasting, cheap and tailored coating that is able to compete and outperform

PDL. Moreover, by employing a layer-by-layer approach, these coatings are not confined to the traditionally flat environment of cell culture dishes and can be applicable towards coating three-dimensional neural probes.

Chapter 3 extends the work on silk-based PEMs by synthesizing a family of azobenzene-modified silks, each possessing varying and distinct properties such as hydrophilicity and absorptivity. The members of this azosilk family were assayed for their viability by employing a standard live/dead staining assay on HAAECs. By plotting the hydrophobicity of each polymer versus their survival rate, a linear trend was found. Contrary to previous literature studies on hydrophobicity, we found that the ability for azosilk polymers to support HAAECs in culture depended highly on hydrophobicity: more hydrophobic azosilk polymers depressed survival while more hydrophilic polymers enhanced it. A remarkable feat of this contribution is the dramatic range of contact angles (1 – 120 degrees) achieved by transforming only 5 wt% of the total tyrosine residues of the silk polymer. Electrospinning with such hydrophobic polymers requires a balancing act of maintaining polymer cohesivity while allowing for evaporation of the solvent during the jump from the Taylor cone to the biased plate. Typically, the processing of silk-based materials required harsh solvents, such as hexafluoro-2-propanol, to solubilize and allow for the creation of monodisperse nanofibers. However, we chose to use only aqueous solutions with small fractions of additives, as solvents which were previously used to create silk fibers are very cytotoxic, and the added steps to remove these solvents add significant impurities. By using a mixture of water, DMF and a few drops of surfactant, nanometer scale fibers were achieved which possessed a superior compliance match to the native tissue while maintaining suitable tensile and elastic moduli. This contribution provides new methodologies to create optically responsive azosilk fiber mats, which were demonstrated to be supportive for growing HAAECs cells.

The results described in Chapter 4 demonstrate the power of combining a biocompatible polymer with a high performing chromophore. We describe a methodology to create discrete patterns within azosilk films by careful irradiation using an 800 nm light source. By employing a Matlab code which divides an image up into numerous regions of interest, we are able to achieve a quick workflow, from picture to pattern within minutes. Not only are we able to create fluorescent patterns, but upon exposure to higher intensity light, we can achieve fluid filled blisters with potential applications in cell guidance and microfluidics. Again, this effect was possible by

functionalizing silk with less than 5 wt% azobenzene. When comparing this lithographic methodology to existing technological innovations, such as photolithography, we can see how azosilk materials shine. For standard photolithographic techniques, masks and lengthy processing times are required for the creation of the etched silicon masters used in microcontact printing. This can take anywhere from a few days to months to create. From initial design of a pattern to the final result, the azosilk inscription process can take place in one single day. Patterning of a single 250 x 250 μm area of azosilk takes approximately 60 seconds, and only requires access to a standard two-photon confocal microscope, present within most biology departments, and the vector pattern, which is created using a mathematical program such as Matlab. This method provides access to surface modifications on the order of cell size, with of course the limitation of using only azosilk materials. However, if a different surface coating is desired, azosilk patterned surfaces can also be coated using a layer-by-layer approach or through surface absorption of the polymer or molecule of choice. In such a method, azosilk films would be created, their surface coated with a different polymer of choice, and then the polymer assemblage would be subjected to 800 nm light to be patterned. In this case, azosilk would act as a command surface, dictating the modulus and topology while the adherent polymer provides a different surface chemistry.

Finally, Chapter 5 explored the feasibility of using patterned azosilk surfaces, which were generated in Chapter 4, as cell guidance surfaces. This project proved to be a difficult challenge, as a multitude of different factors played into the controlled migration of cells and tissues. Previously, neurons and fibroblasts have been cultured on surfaces and their growth was monitored. The most influential structures that directed their growth were raised features on the same size regime as cells, and modulus gradients. We plated CHO cells onto the surface, and tracked their motion on the patterned surface over the course of 8 hours. While it may be true that CHO cells are not known to be sensitive to these physical guidance cues, we found a subset of cells that responded significantly to the pattern. This illustrated proof of principle may be used to explore more moduli sensitive cells, such as fibroblasts. Chapter 5 provided some proof that our lithographic process to create these tailored surfaces holds promise, and we can validate our claims that these materials are useful for guiding cells; claims which were made in Chapter 4.

One specific possibility that remains to be explored is *in vitro* patterning during the course of live cell imaging. One might imagine culturing cells and patterning the surface underneath or

beside a single adherent cell. While the notion of these experiments has been previously explored, they were conducted using UV light to pattern the surface, and thus the cells were found to exhibit adverse responses, such as cell death. One specific feature of the described patterning procedure is that it requires near-IR light, which has been demonstrated to not adversely affect cell cultures. This process seems exciting when used in the context of neural cell cultures, where presenting a microblister may prompt the growth cone to either form a presynaptic attachment or extend further processes along the newly formed blister. This may be the first demonstrated use of silk for optically influencing cell growth, which is important with the advent of many biotech companies exploring the possibility of implanting silk coated materials for interfacing with biological tissues.

6.2 **Outlook**

The work conducted within Chapters 2-5 should continue. The significance of the development of an externally addressable biomaterial is important, and may allow for single cell experiments, cell guidance and the development of truly biocompatible microfluidics chambers. The work within Chapters 2-5 is more fundamental in nature and may serve as a platform for the creation of real world devices. The work within Chapter 4 represents more of a fundamental study of the photo-responsive properties of azosilk and the remaining chapters focus on more applications towards biomedical devices. Azosilk should be explored fully within the biomedical device community, as it represents a well-tolerated, cheap and flexible platform of materials which may be exploited in many new biomedical devices.

Work within Chapter 2 may serve as a guide for the next generation of coatings for neural probes and implantable devices such as those at the brain-machine interface. Silk PEMs are stable, slowly biodegradable and low cost, thus possessing optimal properties to create a new generation of ‘ready-to-plate’ cell culture dishes for neurons. The fundamental work presented in Chapter 2 is complete, and thus these newly developed coatings may be explored for further applications in biomedical research. One potential application may lay in tissue engineering. Coating microbeads with silk-based polyelectrolyte multilayers may prompt the formation of three-dimensional cultures of neural cell networks. This is due to the previously understood relationship between spherical microbeads and the formation of artificial synapses on their surface. By packing a scaffold with such PEM-coated microbeads, artificial nerves may be created. Additionally, these coatings were found to be resistant to degradation, and may prompt an exploration of long lasting

neural probe coatings.

Neural probes have several limitations, and inserted probes tend to elicit the formation of glial scars around the inserted object, due to elastic modulus and compliance mismatches. Glial scars have been shown to be the main issue with neural probe rejection, as the scar material is electrically insulating, thus signals diminish over time. However, our materials present a soft, wet and 'ECM-like' surface, all properties which have been demonstrated to slow or even arrest the formation of glial scars. In addition, silk materials of a specific modulus range have been shown to prevent the migration of microglia and oligodendrocytes, effectively stopping the process of gliosis. At the same time, post-implant cell guidance may be possible due to work conducted in Chapter 4. 800 nm light penetrates highly into skin and may allow for post-operative tuning of implanted devices with patterns. One may imagine patterning a neural probe in order to guide growing axons towards reading pads. The penetration depth of IR laser light into any tissue has been previously explored. For such tissues as skin, a maximum transparency has been demonstrated to be 850+ nm. This penetration depth is a distracted by the tissues that the light is penetrating into, and can be affected by two-photon absorption profiles of blood, cytoplasm and other proteins. While the azosilk we explored for two-photon modification had its writing peak at 800 nm, other members of this azosilk family have been found possess a tunable writing absorption, and such derivatives may prove useful as implant materials for post-tuning *via* IR light.

Azosilk polymers can also be manufactured into electrospun mats for a variety of conduits, which are important for bioengineering, such as those used in nerve repair or as artificial blood vessels. The research presented in Chapter 3 may allow for the formation of new conduits for tissue engineering which are externally addressable. One might imagine creating an electrospun mat, impregnating the mat with cells, and guiding their position and growth externally using the photo-mechanical tuning procedures presented in Chapter 4. Stem cells can be induced into different cell lineages using modulus, or surface chemistry, thus one might imagine a methodology to create three-dimensional arrangements of induced stem cells using an external stimulus to tune the modulus of its surrounding matrix. This may have applications into artificial organs or tissues, especially since silk can be degraded with matrix proteases that are present during cell migration and growth. This allows for the creation of a tissue onto a scaffold and degradation of such a scaffold as the tissue forms. Additionally, since the surface can be tuned using different

headgroups, electrospun azosilk materials may have applications in optically controlled drug release. One might imagine loading a specific drug into an azosilk scaffold and optically releasing the drug over time to an applied region. This is especially plausible as 800 nm light, used to induce blisters and photo-actuation in azosilk polymers, is able to highly penetrate skin.

The work presented within Chapter 5 can be further explored. Physical guidance cues may be useful in eliciting some cell guidance, as demonstrated within Chapter 5, but using a combination of physical and chemical guidance cues may provide an even stronger response as a cooperative effect may be exploited. By loading growth factors into the confines of an azosilk surface, either through hydrogen bonding or through physical mixing, optical release of growth factors may be possible. One might imagine an experiment where nerve growth factors are loaded into an azosilk coating, and neural cells are guided using the optical release of growth factors in addition to the physical bumps on the surface. The action of patterning may be used to release the adherent nerve growth factor, thus combining chemical and physical guidance cues. This cooperative approach may prove to be a powerful tool, as it could be explored to further develop cell guidance materials, and expand the understanding of cellular guidance and migration.

Finally, the work presented within Chapter 4 on the photo-modification of azosilk surfaces maybe useful for creating microfluidic devices without the use of clean room techniques. By writing into the surface and creating microblisters, a channel can be effectively formed just under the surface. These microblisters could be drained, and inflated with a liquid of choice, such as water, and then operated as a typical microfluidics device. Chapter 4 presented this idea within the body of the text, but it is not fully explored. This idea should be fleshed out and explored further, as the proposed microfluidics chamber would be made from a biomaterial and could be used to culture and house cells within the confines of such a chamber. Culturing cells within a microfluidics chamber is an important concept, as such cells could be exposed to gradients of drugs or growth cues, and exposed cells could be observed for their responses. Additionally, since the surface of such a microfluidics chamber is created from more azosilk, a method to create and extend the pattern to additional chambers maybe implemented on-the-fly, as well as photo-actuated gates within the confines of the chamber, to control flow.

Indeed, light has a promising future not just in biomaterials, but towards biomedical devices

as well. With the development and exploration of azosilk as an optically addressable biomaterial is just beginning, the possibilities for its applications in the realm of biomedical devices seems almost never ending. We hope that the work presented within this thesis will inspire the formation of the next generation biomaterials, with a never-ending list of potential applications. The world of photomechanically mediated biomaterials continues to become more developed every day, but what is certain is the world of light-material interactions has a bright future.

Rationale for Appendix 5: Surface-plasmon-mediated hydrogenation of carbonyls catalyzed by silver nanocubes under visible light

Within Chapters 4 and 5, we explored the photoexcitation of our azosilk films to create well-defined fluorescent patterns which were confined within the irradiated region. Upon high intensity irradiation (>100 $\mu J/\mu m^2$, 800 nm), raised blisters formed, which were confined to the irradiation region and exhibited a dramatic 10-fold photosoftening effect. We also explored the applications of these raised blisters in optically guiding cell migration, with some promising preliminary data showing the potential of patterned surfaces to influence cell speed. Using a photomechanical effect to optically control a biological process was the ultimate goal for our project. However, light has also been demonstrated to perform photochemical work as well, and this is evident based on the formation of photoradicals during the photolithographic process of patterning azosilk.

Light-material interactions rely heavily on controlling the absorption of light, transferring energy within a system and eventually using this energy to achieve meaningful work, such as performing chemical reactions. Light can be used to drive photochemical reactions, such as Diels Alder, photoalkylation, [2+2] cycloadditions and the creation of photo-radicals in the case of radical polymerization. In general, the broad category of photochemistry is defined by any reaction which is mediated or prompted by a photon of light. Inspired by the work performed within Chapters 4 and 5, we desired to pursue the use of light to impact a photochemical transformation. The context of this thesis is on the preparation of an externally addressable biomaterial and thus work based on the creation of a new photocatalyst is orthogonal to the scope of this thesis, and thus was not presented as a chapter within the main body of the manuscript. We decided to include this contribution as an appendix to demonstrate the breadth of work which is achievable with light, and the extend of work completed.

We decided to study the effect of photoexcited nanoparticles used in reduction chemistry. Nanoparticles of the correct shape, size and composition exhibit a phenomenon called the surface plasmon. This effect is due to the coupling of electron density confined within the particle with electromagnetic radiation. Silver metal provides an attractive platform to explore these photochemical reactions as they have been previously demonstrated to possess a plasmon band which is accessible for photoactivation of both hydrogen and oxygen at its surface. Within

Appendix 5, we synthesized a silver nanocube catalyst which exhibited a large plasmon band and explored its use in the photo-reduction and photo-oxidation of carbonyl-containing compounds. The activation of reagent gas (either oxygen or hydrogen) on the surface of the catalyst was achieved through the excitation of the plasmon band of the silver nanocubes at 405 nm. Our study proposed a potential reaction mechanism involving plasmon-activated hot electrons. A large selection of primary and secondary alcohols can be accessed from ketones and aldehydes using milder conditions than previous silver-based catalysts. The contribution 'Surface-plasmon-mediated hydrogenation of carbonyls catalyzed by silver nanocubes under visible light' published in *ACS Catalysis* was co-authored by Michael J. Landry, Alexandra Gellé, Beryl Y. Meng, Prof. Christopher J. Barrett, and Prof. Audrey Moores, and provides a selective and mild route to primary and secondary alcohols and α,β-unsaturated alcohols.

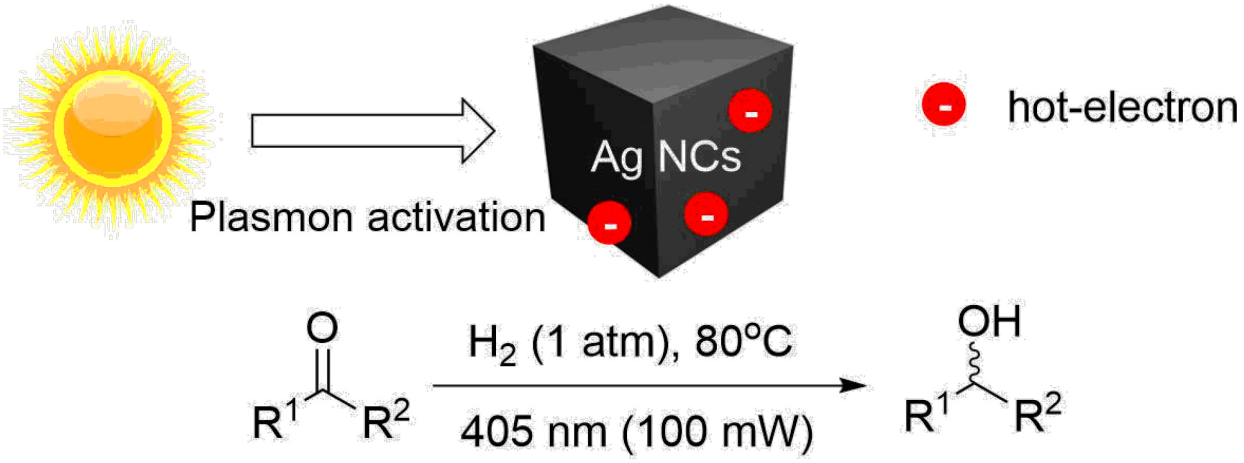

Appendix 5: Surface-plasmon-mediated hydrogenation of carbonyls catalyzed by silver nanocubes under visible light

Appendix 5 is based on a manuscript entitled 'Surface-plasmon-mediated hydrogenation of carbonyls catalyzed by silver nanocubes under visible light', was published in *ACS Catalysis* (Copyright 2017, American Chemical Society) and was co-authored by: Michael J. Landry, Alexandra Gellé, Beryl Y. Meng, Prof. Christopher J. Barrett, and Prof. Audrey Moores.

A5.1 Abstract

Plasmonic nanoparticles are exciting and promising candidates for light-activated catalysis. We report herein the use of plasmonic nanocubes for the activation of molecular hydrogen and the hydrogenation of ketones and aldehydes via visible light irradiation at 405 nm, corresponding to the position of the plasmon band of the nanocubes, at 80 °C. Only 1 atm of molecular hydrogen is required to access, using catalytic amounts of silver, primary, and secondary alcohols, with complete chemoselectivty for C═O over C═C reduction. The resulting catalytic system was studied over a scope of 12 compounds. Exposure to other wavelengths, or absence of light failed to provide activity, thus proving a direct positive impact of the plasmonic excitation to the catalytic activity. By varying the irradiation intensity, we studied the relationship between plasmon band excitation and catalytic activity and propose a potential reaction mechanism involving plasmon-activated hot electrons. This study expands the scope of reactions catalyzed by free-standing plasmonic particles and sheds light on H_2 activation by silver surfaces.

A5.2 Introduction

Energy consumption by the chemical industry is a significant source of pollution via generation of greenhouse gases.[1-3] Photochemical reactions have been investigated for over a century, with the end-goal of harvesting light as a renewable energy source and converting it directly into chemical energy.[4] Photochemistry can also open routes to products which are not accessible via thermal routes.[5] Energy transfer is a key step in being able to use light to do meaningful chemical work, and to this end, several light-harvesting systems have been developed, including solar cell materials,[6] photocatalysts,[7-9] and photoactivated materials,[10] relying on materials such as TiO_2,[11,12] porphyrin dyes,[13,14] ruthenium polypyridine complexes,[15-17] or organic dyes.[18,19] Light-activated catalytic reactions have seen wide use in organic chemistry[8] and also in remediation and depollution of organic dyes and conjugated organic systems.[20] Recent efforts have

allowed the development of such photocatalysts with a focus on activation with visible light.[21]

Nanomaterials of Cu, Ag, and Au possess an optical and electronic property called surface plasmon resonance (SPR), which confers to them powerful absorptive properties in the visible region. Conducting electrons in these materials oscillate in resonance with the incoming light field,[22-24] causing three effects.[1] SPR causes strong light absorption and scattering translating into exciting optical properties.[25,26,2] Strong field enhancement at the surface vicinity of these materials allows them to enhance signals, and was exploited to develop surface enhanced Raman spectroscopy (SERS) used for detection with molecular sensitivity.[27-32,3] Field enhancement also causes local heat generation and this has been used in the development of nanomedicines.[27, 33, 34] In the last 10 years, researchers have studied light-mediated catalysis using SPR-active nanoparticles (SPRANP), including for water splitting, CO_2 reduction, and organic pollutant degradation.[21,23,35-39] SPRANP operate according to three major schemes: their plasmon is enabled by visible light and they either activate a metal oxide support, another metal, or act as a catalyst on their own (**Figure A5.1**). For instance, Au nanoparticles (NPs) supported on oxides have been shown to catalyze the oxidation of formaldehyde,[38] alcohols,[40-43] and amines to imines,[44-46] C–C and amine–alkyne–aldehyde couplings,[46,47] hydroamination of alkynes,[46] oxidative degradation of phenol,[48] oxidative aldehyde-amine condensation to amide,[49] and hydroxylation of benzene.[50-52] In supported SPRANP, oxidative reactions are mediated by excited hot electrons from SPRANP which are transferred to the support where catalysis takes place (**Figure A5.1**).[21,38]

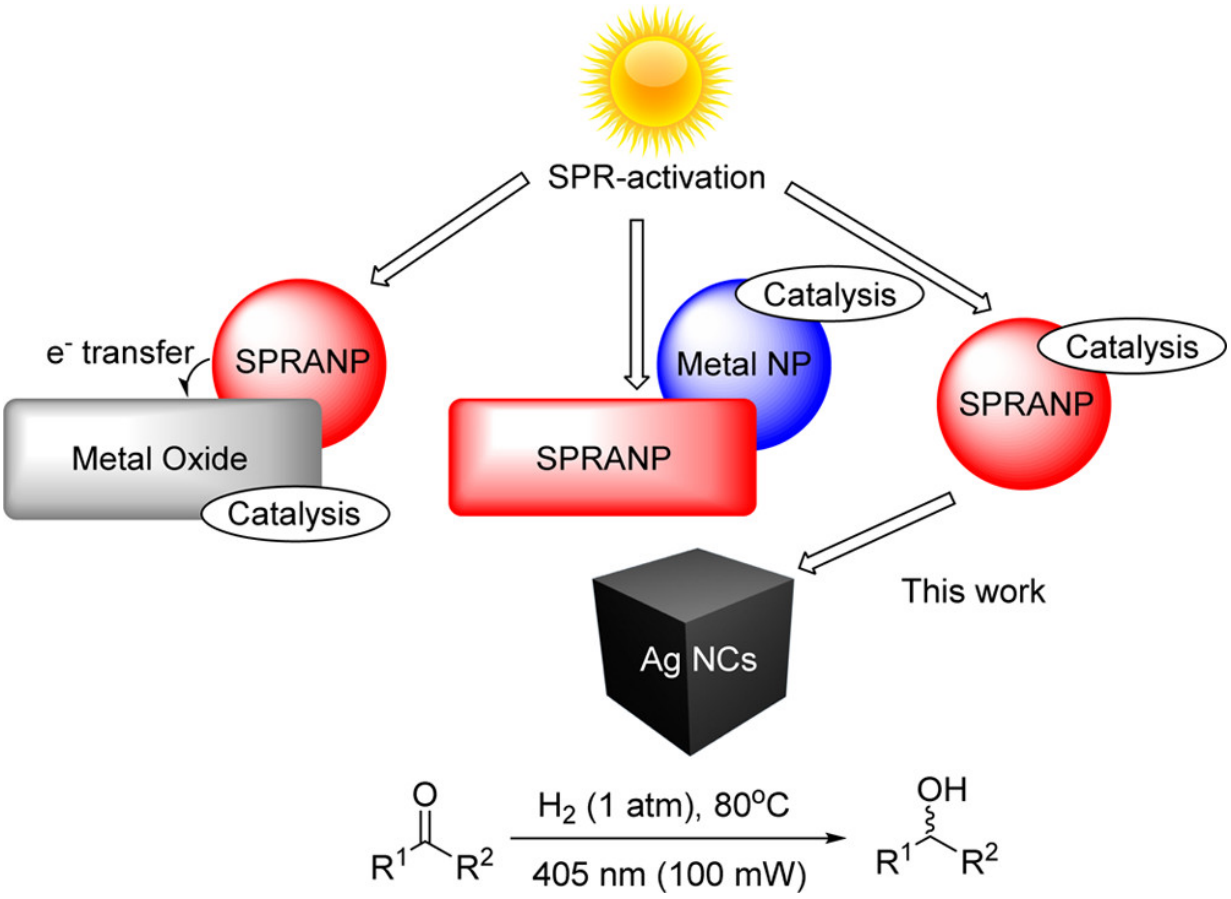

Figure A5.1. General categories of plasmonic photocatalysts relying on SPRANP.

Researchers have looked into combining the catalytic activity of non-plasmon active transition metals, such as Pt or Pd with optical properties of SPRANP. For instance, alloys of plasmon and nonplasmon metals were investigated.[46,53,54] Besides this, Halas and co-workers unraveled the potential of a less-explored plasmonic metal: aluminum.[55,56] Core–shell Al/Al_2O_3 nanocrystals were used as supports for Pd NPs, for the selective hydrogenation of acetylene to ethylene under white-light illumination.[56] Typical reactions such as ethanol dehydrogenation can be enhanced with such core–shell particles.[57] On the other end, free-standing, pure SPRANP can also perform plasmonic photocatalysis, for instance in oxidative couplings,[58,59] activations of reagent gases,[60] and reductive couplings.[61] The Scaiano group showed the reduction of alcohol with hydrogen peroxide with unsupported Au NPs.[62] The group of Linic looked at Cu NPs as SPR-activated propylene oxidation catalysts.[63] The same group explored silver nanocubes (Ag NCs) harvesting light via SPR to directly afford hot electrons and catalyze the epoxidation of ethylene.[53] In an effort to explore more the scope of catalytic processes available from pure silver as a

plasmonic metal, we wanted to look at their reductive chemistry in organic solvents. Hydrogenation is a reaction of high industrial relevance,[64] for which silver is typically a less active metal requiring high hydrogen pressure; its limited ability to activate H_2 compared to other metals is well-documented.[65] Still it affords heterogeneous catalysts with excellent chemoselectivity for the reduction of C═O over C═C bonds.[65-69] Au NPs, both in the free and supported versions, are known to enable the activation of molecular hydrogen via SPR,[70,71] but a similar effect had not been shown yet for silver. Activating silver toward H_2 splitting can help reduce the high temperature and pressure requirements for this reaction.

Herein, we report that plasmonic Ag NCs are able to drive catalytic reduction reactions and direct activation of H_2 through the absorption of visible light, at ambient pressure. This expands the use of catalytic plasmonic nanoparticles to reductive organic chemical transformations, where it has been less explored.

A5.3 **Results and discussion**

A5.3.1 **Synthesis and characterization of Ag NCs**

For this work, Ag NCs were selected for their enhanced SPR properties arising from their sharp vertices.[72,73] These sharp vertices are well-known to create "hot spots" where SPR is greatly enhanced.[23,35] We synthesized Ag NCs following the procedure already reported, using $AgNO_3$ as a precursor, polyvinylpyrrolidone (PVP) as a stabilizer, and HCl as an etchant.[53] Transmission electron microscopy (TEM) and scanning electron microscopy (SEM) (**Figure A5.2** and **Figures A5.9–A5.11**) revealed that most of the synthesized nanoparticles featured a cubic morphology, with occasionally a few rod- or prism-shaped particles observed. These cubes are monodisperse with an average edge length of 126 ± 12 nm (counted over 120 cubes in TEM images). In STEM, the shell of protective PVP polymer was clearly visible (**Figure A5.11**). Dynamic light scattering (DLS) experiments were also performed and results are consistent with SEM and TEM data (see **Section A5.7**). Energy-dispersive X-ray spectroscopy (EDS) measurements were obtained on Ag NCs imaged by STEM to probe their purity (**Figure A5.12**). Ag NCs were found to contain only Ag, Cl, C, and O. Importantly no other noble metals (Pt, Pd, or Ru), which could also lead to the expected reduction chemistry, was detected. An EDS linescan was also performed across a couple of AgNCs observed by high resolution STEM (**Figure A5.13**). Carbon and oxygen were

preeminent along the edges of the cubes, revealing the surface coverage of the PVP polymer. The presence of chlorine revealed by EDS was consistent with the Ag NC synthesis, which relies on chloride anions in order to direct the selective facet growth of the cubes. X-ray photoelectron spectroscopy (XPS) confirmed the presence of Ag, Cl, C, O, and N in the sample. Cl content could be quantified against Ag and Cl and accounts for 8% of the inorganic material (**Figure A5.14**). The $3d_{5/2}$ band of silver, centered at 368.3 eV is consistent with Ag(0). X-ray diffraction (XRD) featured (111) and (200) peaks distinctive of a pure Ag(0) phase (**Figure A5.16**).[74] The surface plasmon band (SPB) was measured using UV–vis spectroscopy and was determined to lie centered at 410 nm (**Figure A5.3**).

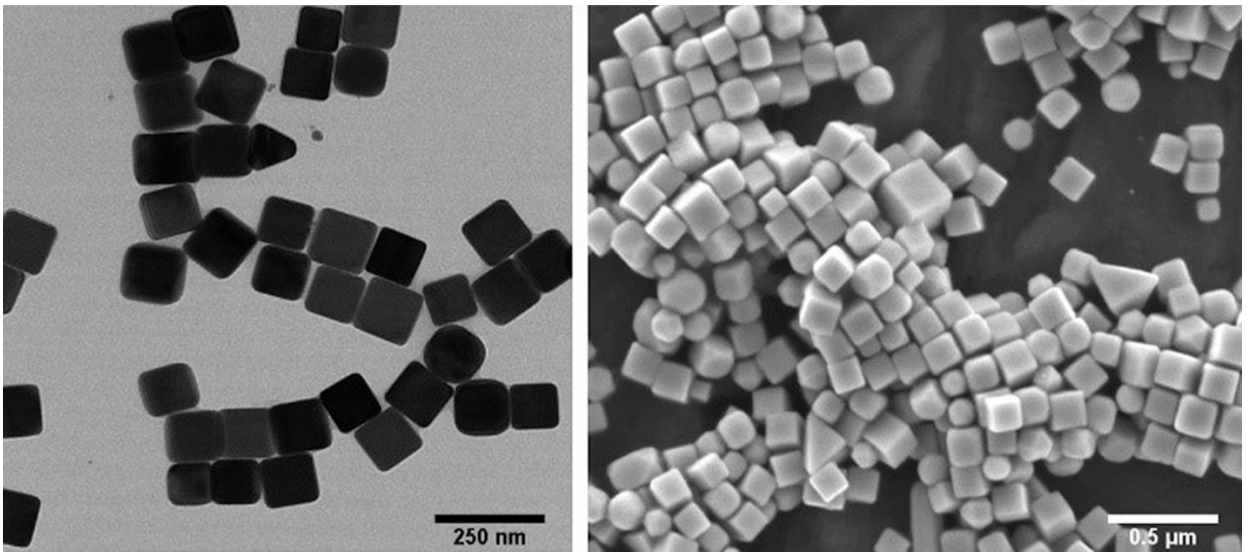

Figure A5.2. TEM (left) and SEM (right) images of Ag NCs.

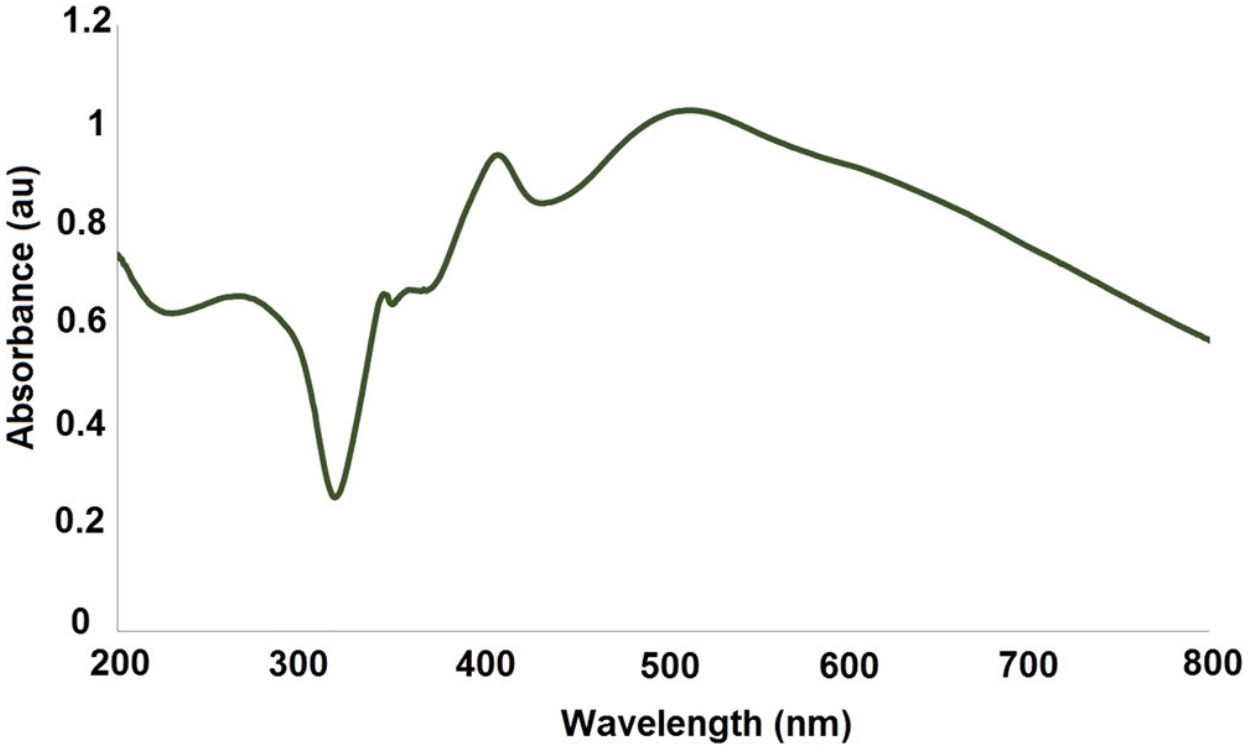

Figure A5.3. UV–vis spectrum of Ag NCs that demonstrates the surface plasmon band ranging from 400–420 nm.

A5.3.2 **Establishing catalytic activity**

To establish catalytic activity, the Ag NCs were first tested for the hydrogenation of

camphor to the diastereotopic mixture of borneol and isoborneol, using a hydrogen pressure of 1 atm for 24 h (**Figure A5.4**). Camphor was selected as model substrate for this reaction because, in the presence of light, it does not form photoradicals as other arylketones are known to do. When this reaction was performed under 1 atm of H_2 in the dark, at 40 or 60 °C, no conversion was measured after 24 h. Further heating at 80 or 100 °C afforded only trace or 6% conversions respectively under the same conditions (**Figure A5.4**). This is consistent with past accounts, as typically much higher pressures of molecular hydrogen (i.e., 40 bar) are required to trigger hydrogenation with silver nanoparticles.[66,75] However, when light from a 60 W lightbulb was introduced during the reaction, a promising increase in yield of 17% was measured at 40 °C. Upon raising the temperature, the yields improved further and reached 57% at 100 °C. In order to further ascribe this activity enhancement to the Ag NCs SPR properties, we employed a laser diode emitting light precisely at 405 nm, a wavelength within their plasmon band. The typical experimental setup for this reaction is illustrated in **Figure A5.8**. A dramatic improvement of yield was observed using the 405 nm laser, enhancing the yield to 87%, an increase of 45 points compared to the wide-spectrum light bulb of similar intensity (**Figure A5.4**). A series of control tests established that absence of H_2, absence of particles or exposure to 532 or 633 nm laser light failed to afford meaningful conversions, under the temperature spectrum explored herein (**Table A5.2**).

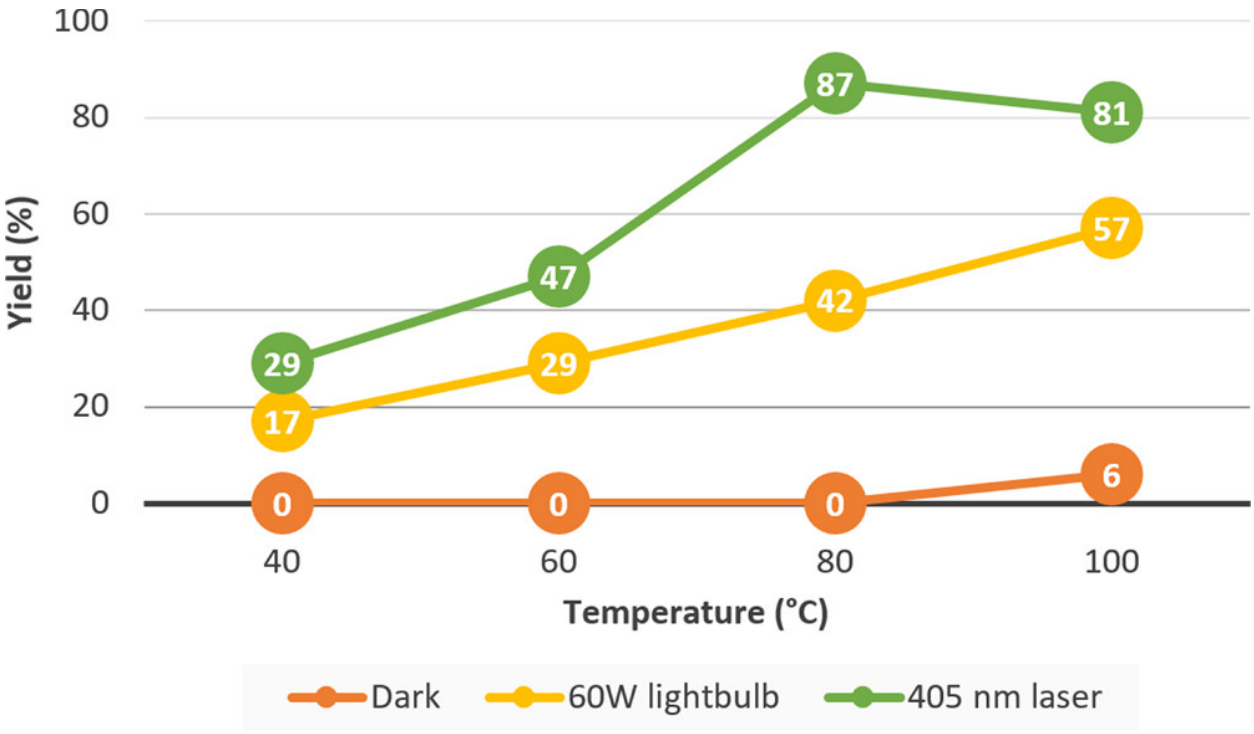

Figure A5.4. Yields observed for the hydrogenation of camphor with Ag NCs as catalyst. Reaction conditions: 1 mg of Ag NCs, 1 mmol of camphor and 5 mL of dioxane, H_2 pressure of 1 atm, 24 h.

Now that a link between light and catalytic activity was established, a solvent screening was performed to understand the impact of the polarity on the reaction. Dioxane, water, ethanol, hexane, ethyl acetate, and dichloromethane were assessed under the newly optimized conditions (H_2 pressure of 1 atm, 24 h) at their boiling point, or at 40 °C. We correlated the resulting yields (**Table A5.3**) with the solvent dielectric constant, ε, a classic parameter used to measure polarity and boiling temperature. Interestingly, a clear trend was observed, where the more polar the solvent, the better the activity (**Figures A5.17** and **A5.18**). Dioxane and water performed the best, achieving similar yields of near 80% at 100 °C. The case of dioxane is interesting: while this molecule has a dielectric constant of zero because of its high symmetry, it possesses polar bonds, which have a local polarizing effect on the medium. Similar results have been reported by others, where dioxane performed very well and similarly to polar solvents for C═O hydrogenation.[76] Ethanol only provided 30% conversion at 78 °C, a temperature at which dioxane afforded the excellent yield of 87%. All other solvents, all apolar, gave poor yields.

A5.3.3 **Mechanistic studies**

To probe further into the photocatalytic nature of this reaction, a light intensity versus yield experiment was conducted. Under optimized reaction conditions (H_2 pressure of 1 atm, 24 h, 80 °C), the 405 nm laser was expanded to the size of the reaction vessel and used at its full intensity of 204 mW/cm^2, then also under reduced intensities stepwise by employing various increasing optical density (OD) neutral density filters. As shown in **Figure A5.5**, below 60 mW/cm^2 the yield increased almost linearly as a function of light intensity, while after this value, a saturation was rapidly established. This saturation can be explained potentially by diffusion limitations in a solution-based catalytic process, when yields exceed 50%. A kinetic study was also carried out using camphor as the model reaction under hydrogen conditions. A mostly linear loss of camphor was observed, without induction period (**Figure A5.19**).

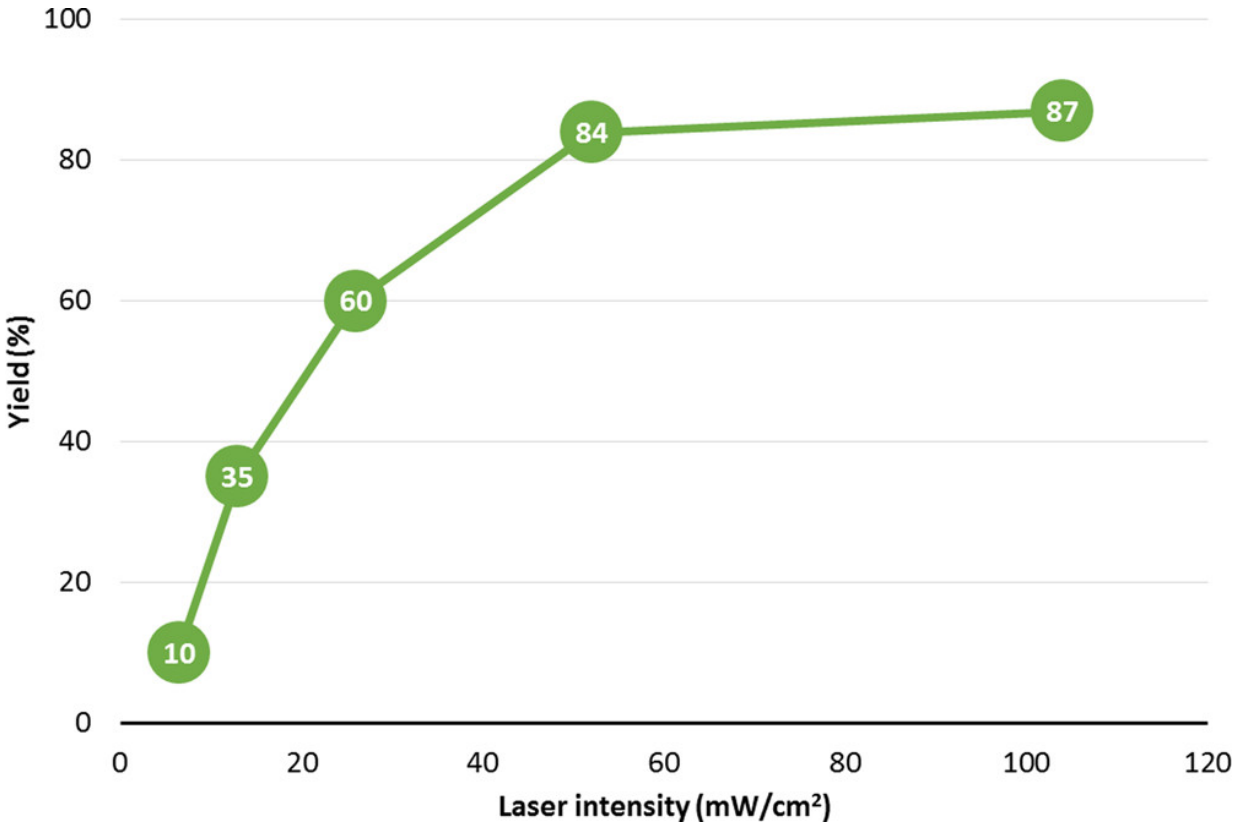

Figure A5.5. Yield (%) vs laser intensity (mW/cm^2) for the hydrogenation of camphor with Ag NCs as catalyst in dioxane, with H_2 pressure of 1 atm, 80 °C and for 24 h.

Unsupported SPRANP have been described to enable plasmonically enhanced catalysis via three main mechanisms:[23,24] (i) the formation of hot electron–hole pairs at the surface of the nanoparticle, followed by transfer of charge carriers to an adsorbed substrate, (ii) the photo-induced increase of the nanoparticle temperature and its thermal effects on the reaction rate, (iii) the photo-induced local field enhancement and its effect on other photo-activated processes. The reaction of hydrogenation with silver does not proceed *via* photo excitation of an organic molecule involved, so a field enhancement effect (iii) is unlikely. Also, since reaction with Ag NCs in the dark was negligible across the range of temperatures accessible in the liquid phase of dioxane, a potential thermal effect of the SPR (ii) should not lead to activity enhancement. Thermal effects are also typically encountered with nanoparticles much smaller than the ones we used.[35] The dependence of the yield on the light intensity before saturation is also in agreement with a linear relationship, consistent with a "hot-electron" process for low intensity photoactivation.[77] Recently, the group of Halas demonstrated the activation of H_2 by gold nanoparticles under plasmonic activation, and they proposed that hot electrons are directly responsible for the splitting of the H_2 molecule.[71] Thus, we propose a similar mechanism in **Figure A5.6**. When light is absorbed by the Ag NCs, a transient electron/hole pair is formed at its surface and the resulting hot electron is transferred to an adsorbed H_2 molecule. The rest of the proposed mechanism follows a Polanyi-Horuiti scheme.[78] Interestingly, it has been suggested by theoretical investigations that hydrides on silver surfaces may be directly photo-activated by SPR, which could participate as well in the process.[79]

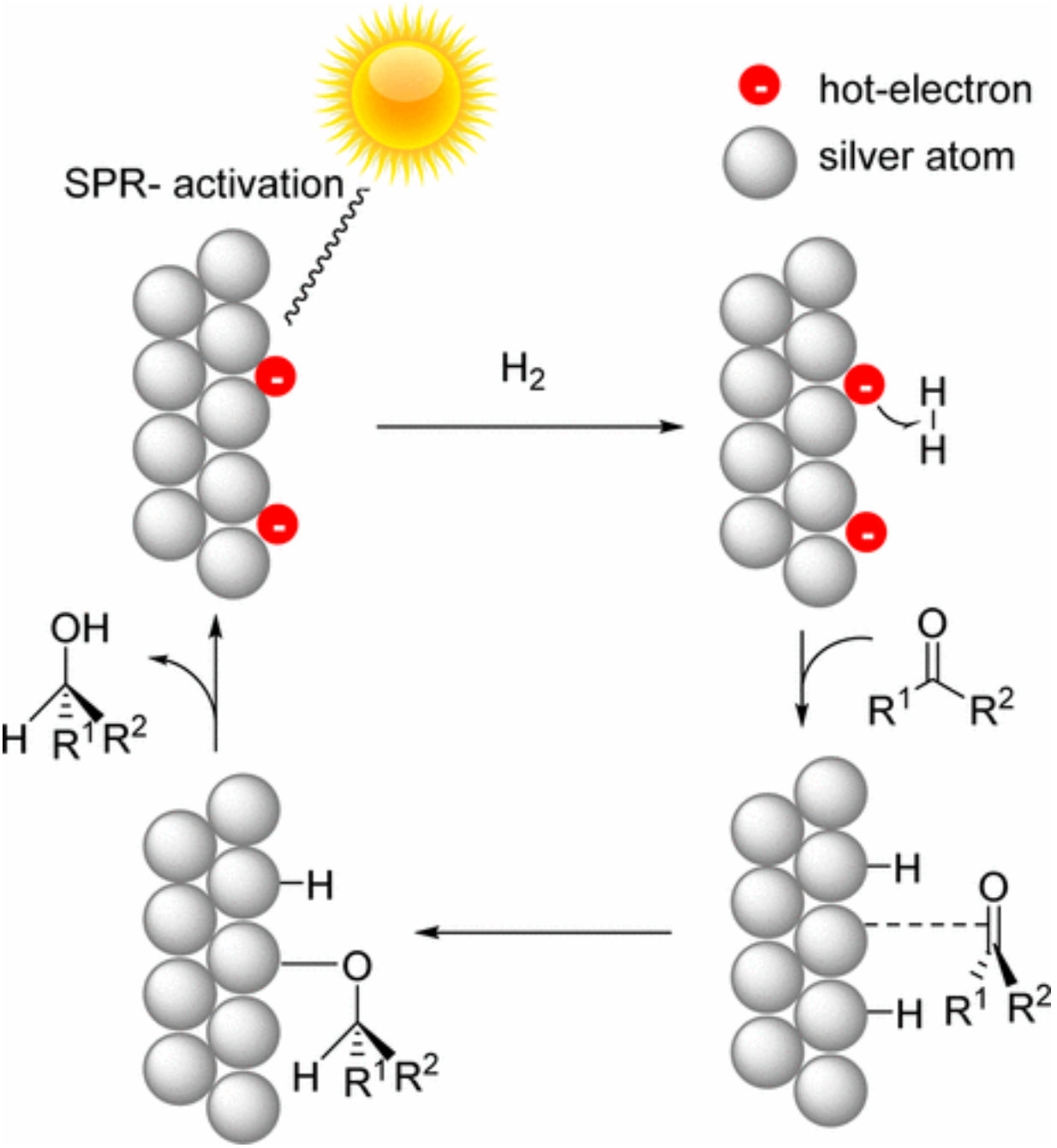

Figure A5.6. Proposed Mechanism for the Hydrogenation of Carbonyl Compounds with H_2 Catalyzed by Ag NCs.

Moreover, AgCl and Ag@AgCl NCs have been reported by others to be active photocatalysts in polymerization and oxidation reactions and it was important to rule out the presence of any AgCl phase in as-synthesized nanocatalysts.[80-82] XRD did not show any sign of

crystalline AgCl phase, and no typical AgCl UV signature was seen between 200 and 300 nm (**Figure A5.3**).

A5.3.4 **Scope of reaction**

With these results in hand, the scope of this reaction was explored with other ketones and aldehydes (**Figure A5.7**), setting the temperature to 80 °C and using the 405 nm laser as the irradiation source. Camphor **(1)**, for which we optimized the reaction gives a yield of 87%. Other aliphatic ketones gave the corresponding alcohol **(2–3)** in moderate yields, with percentages in the 30s and 50s of %. Aliphatic aldehydes afforded contrasted results with yields between 33% and 76% for **(4)** to **(6)**. Moving to conjugated carbonyl molecules, we observed better yields, consistent with their known enhanced reactivity toward hydrogenation. Benzophenone gives **(7)** with the best yields of the series (92%) and good yields around 75% are seen for benzyl-alcohol **(8)** and its p-chloro counterpart **(9)**. Perfect selectivity for **(9)** shows the tolerance of the procedure for chloroarene functionality. The di-m-t-butyl benzyl-alcohol **(10)** affords a low yield of 32% likely because of steric bulk which can hinder access to the metal nanoparticle surface. In the example of α,β-unsaturated aldehydes, we observe an interesting selectivity for the C═O bond reduction over the C═C bond, consistent with past accounts using Ag NPs for hydrogenation.[75] Citral is thus cleanly converted to geraniol **(11)** at 79% yield. With cinnamaldehyde, 80% yield of cinnamyl alcohol **(12)** was produced, along with 5% of hydrocinnamyl alcohol.

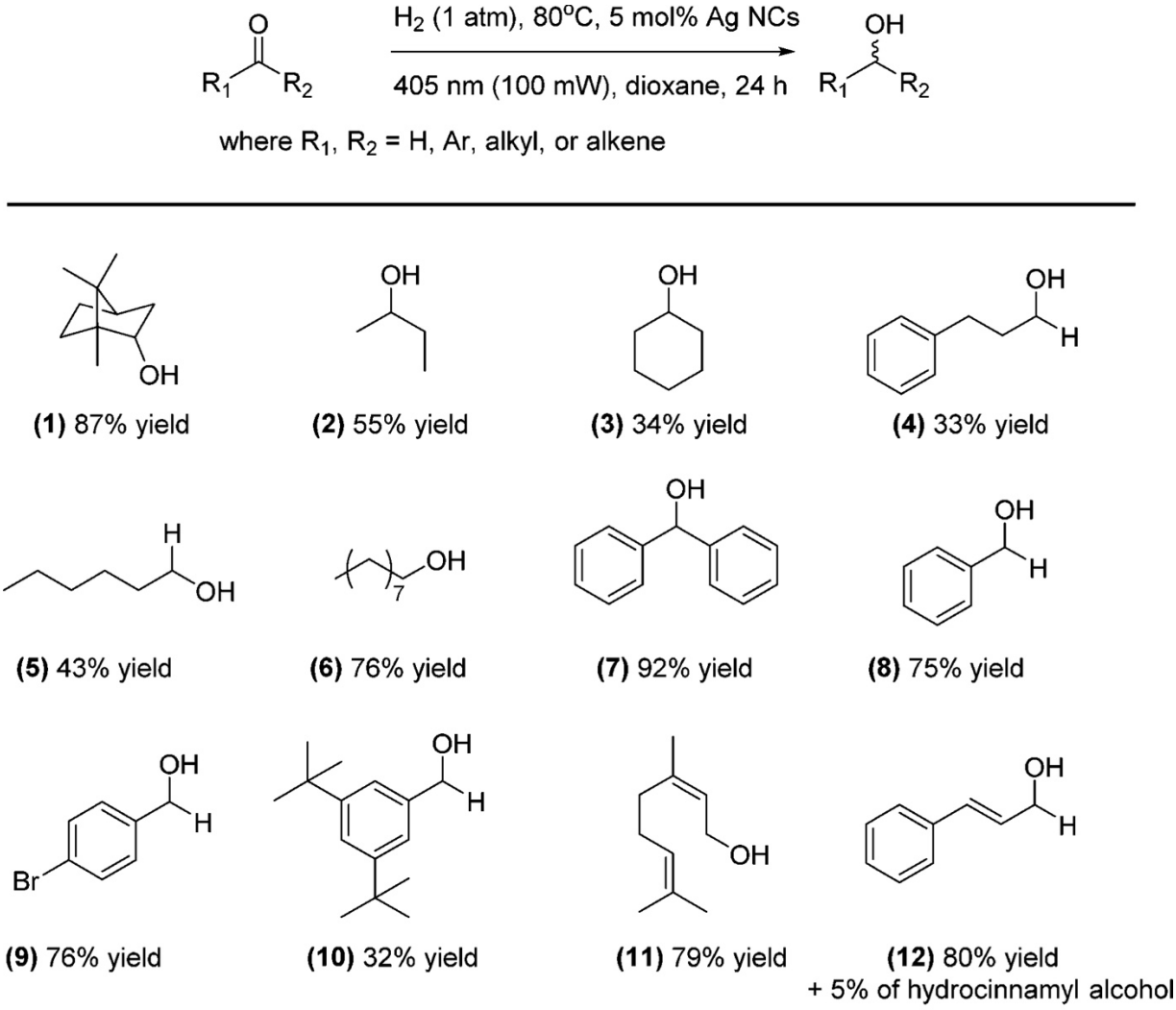

Figure A5.7. Scope of Products Obtained from SPR-Enhanced Hydrogenation of Ketones with Ag NCs.

To elucidate the potential leaching of soluble Ag species during the reaction, ICP-MS measurements were performed on the filtrate of the optimized hydrogenation reactions of camphor, after Ag NC removal. 0.57 ppm of Ag was measured in the product, which constitutes a negligible contamination (see **Section A5.7**). In an effort to determine if such leached soluble Ag species were responsible for catalytic reactivity, we performed two distinct experiments: a hot filtration and a blank test using $AgNO_3$ as catalyst. For the hot filtration, an optimized catalytic run was performed at 80 °C, with laser excitation. After 2 h, the Ag NCs were filtered off the reaction medium, and the run was further monitored for activity, under the same conditions for 6 additional

hours. Before the separation, a yield of 21% conversion to borneol was measured. At the end of the run, a similar yield of 23% was obtained. We also performed a reaction using $AgNO_3$ as catalyst, added to the reaction at a concentration of 0.57 ppm. This blank test afforded only trace conversion over the 24 h along with the appearance of a silver mirror on the side of the flask, characteristic of Ag(0). Homogenous Ag species have been reported recently to be active for hydrogenation, but require much higher loadings, H_2 pressures, and electron-accepting ligands.[69] These tests established that soluble species can not account for the reactivity described in this study.

A5.3.5 **Oxidation reactions**

In an effort to explore organic reactions catalyzed by SPR-activated Ag NCs, we also investigated the oxidation of aldehydes and alcohols to carboxylic acids. Ag NCs are known to activate O_2 with SPR and enable gas-phase epoxidation of alkenes.[53] For this study, we explored the oxidation of p-hydroxybenzaldehyde under air at atmospheric pressure for 18 h at 60 °C. Under these conditions, the corresponding carboxylic acid is produced at 95% under 405 nm laser irradiation, or using a light bulb, while in the dark this value falls to 34%. A scope of six molecules was explored and found yield values between 65% and 97% (**Figure A5.20**). Similar conditions were also tested for the direct oxidation of alcohols to carboxylic acids. Under the conditions we tested, we did observe a small activity, but we could not secure yields beyond 11% (**Figure A5.21**).

A5.4 **Conclusions**

These results demonstrate that SPR can be harnessed to activate silver toward hydrogenation of carbonyl compounds. SPR-activated silver-catalyzed hydrogenation proceeded smoothly at 1 atm of H_2 and 80 °C, conditions much milder than what is known for purely thermal silver-catalyzed processes. This reaction is the first example of SPR-activated reductive catalysis performed using pure, unmodified plasmonic nanoparticles. This catalyst has been shown to tolerate a wide variety of substrate scopes with moderate to high yields, with complete selectivity for C═O vs C═C double bond reduction. Kinetic studies, dose/response curves, solvent dependence, and complete Ag NCs characterization were combined to propose a mechanism via light-induced hot electron formation. This work is a proof-of-concept of the use of plasmon-active nanocatalysts for important organic transformations.

A5.5 **Acknowledgements**

We are grateful to Dr. David Liu for the help with TEM and SEM images, to Ms. Mary Bateman for the help with ICP, to Mr. Nicolas Brodusch for BFSTEM imaging and EDS analysis, to Mr. Louis Do for his help with the XRD measurements and to Dr. Madhu Kaushik for the help with GCMS. We thank the Natural Science and Engineering Research Council of Canada (NSERC) Discovery Grant program, the Canada Foundation for Innovation (CFI), the Canada Research Chairs (CRC), the Centre for Green Chemistry and Catalysis (CGCC), NSERC-Collaborative Research and Training Experience (CREATE) in Green Chemistry, and McGill University for their financial support.

A5.6 **References**

1. Burnham, A.; Han, J.; Clark, C. E.; Wang, M.; Dunn, J. B.; Palou-Rivera, I., Life-cycle greenhouse gas emissions of shale gas, natural gas, coal, and petroleum. *Environ. Sci. Technol.* **2012**, *46* (2), 619–627.

2. Searchinger, T.; Heimlich, R.; Houghton, R. A.; Dong, F.; Elobeid, A.; Fabiosa, J.; Tokgoz, S.; Hayes, D.; Yu, T. H., Use of U.S. croplands for biofuels increases greenhouse gases through emissions from land-use change. *Science* **2008**, *319* (5867), 1238–1240.

3. Franzén, R.; Xu, Y., Review on green chemistry: Suzuki cross coupling in aqueous media. *Canadian Journal of Chemistry* **2005**, *83* (3), 266–272.

4. Ciamician, G., The Photochemistry of the Future. *Science* **1912**, *36* (926), 385-394.

5. Svoboda, J.; Konig, B., Templated photochemistry: toward catalysts enhancing the efficiency and selectivity of photoreactions in homogeneous solutions. *Chem. Rev.* **2006**, *106* (12), 5413–5430.

6. Ding, G.; Jin, Q.; Chen, Q.; Hu, Z.; Liu, J., The fabrication of ordered bulk heterojunction solar cell by nanoimprinting lithography method using patterned silk fibroin mold at room temperature. *Nanoscale Res. Lett.* **2015**, *10* (1), 491.

7. Yoon, T. P.; Ischay, M. A.; Du, J., Visible light photocatalysis as a greener approach to photochemical synthesis. *Nat. Chem.* **2010**, *2*, 527–532.

8. Lin, S.; Ischay, M. A.; Fry, C. G.; Yoon, T. P., Radical cation Diels-Alder cycloadditions by visible light photocatalysis. *J. Am. Chem. Soc.* **2011**, *133* (48), 19350–19353.

9. Luo, J.; Zhang, J., Donor–acceptor fluorophores for visible-light-promoted organic synthesis: Photoredox/Ni dual catalytic $C(sp^3)$–$C(sp^2)$ cross-coupling. *ACS Catal.* **2016**, *6* (2), 873–877.

10. Ye, X.; Kuzyk, M. G., Photomechanical response of disperse red 1 azobenzene dye-doped PMMA polymer fiber. *Opt. Commun.* **2014**, *312*, 210–215.

11. Fujishima, A.; Rao, T. N.; Tryk, D. A., Titanium dioxide photocatalysis. *J. Photochem. Photobiol. C, Photochem. Rev.* **2000**, *1* (1), 1–21.

12. Sakthivel, S.; Kisch, H., Daylight photocatalysis by carbon-modified titanium dioxide. *Angew. Chem. Int. Ed. Engl.* **2003**, *42* (40), 4908–4911.

13. Wang, Z.; Medforth, C. J.; Shelnutt, J. A., Self-metallization of photocatalytic porphyrin nanotubes. *J. Am. Chem. Soc.* **2004**, *126* (51), 16720–16721.

14. Minoura, N.; Tsukada, M.; Nagura, M., Physico-chemical properties of silk fibroin membrane as a biomaterial. *Biomaterials* **1990**, *11* (6), 430–434.

15. Wang, P.; Zakeeruddin, S. M.; Moser, J. E.; Nazeeruddin, M. K.; Sekiguchi, T.; Gratzel, M., A stable quasi-solid-state dye-sensitized solar cell with an amphiphilic ruthenium sensitizer and polymer gel electrolyte. *Nat. Mater.* **2003**, *2* (6), 402–407.

16. Windle, C. D.; Perutz, R. N., Advances in molecular photocatalytic and electrocatalytic CO2 reduction. *Coord. Chem. Rev.* **2012**, *256* (21-22), 2562–2570.

17. Narayanam, J. M.; Stephenson, C. R., Visible light photoredox catalysis: applications in organic synthesis. *Chem. Soc. Rev.* **2011**, *40* (1), 102–113.

18. Neumann, M.; Fuldner, S.; Konig, B.; Zeitler, K., Metal-free, cooperative asymmetric organophotoredox catalysis with visible light. *Angew. Chem. Int. Ed. Engl.* **2011**, *50* (4), 951–954.

19. Hari, D. P.; Konig, B., Synthetic applications of eosin Y in photoredox catalysis. *Chem. Commun.* **2014**, *50* (51), 6688–6699.

20. Pelaez, M.; Nolan, N. T.; Pillai, S. C.; Seery, M. K.; Falaras, P.; Kontos, A. G.; Dunlop, P. S. M.; Hamilton, J. W. J.; Byrne, J. A.; O'Shea, K.; Entezari, M. H.; Dionysiou, D. D., A review on the visible light active titanium dioxide photocatalysts for environmental applications. *Appl. Catal. B* **2012**, *125*, 331–349.

21. Lang, X.; Chen, X.; Zhao, J., Heterogeneous visible light photocatalysis for selective organic transformations. *Chem. Soc. Rev.* **2014**, *43* (1), 473–486.

22. Moores, A.; Goettmann, F., The plasmon band in noble metal nanoparticles: an introduction to theory and applications. *New J. Chem.* **2006**, *30* (8), 1121–1132.

23. Long, R.; Li, Y.; Song, L.; Xiong, Y., Coupling solar energy into reactions: Materials design for surface plasmon-mediated catalysis. *Small* **2015**, *11* (32), 3873–3889.

24. Baffou, G.; Quidant, R., Nanoplasmonics for chemistry. *Chem. Soc. Rev.* **2014**, *43* (11), 3898–3907.

25. Hwang, Y. T.; Chung, W. H.; Jang, Y. R.; Kim, H. S., Intensive plasmonic flash light sintering of copper nanoinks using a band-pass light filter for highly electrically conductive electrodes in printed electronics. *ACS Appl. Mater. Interfaces* **2016**, *8* (13), 8591–8599.

26. Dong, S.; Zhang, K.; Yu, Z.; Fan, J. A., Electrochemically programmable plasmonic antennas. *ACS Nano.* **2016**, *10* (7), 6716–6724.

27. Jain, P. K.; Huang, X.; El-Sayed, I. H.; El-Sayed, M. A., Review of some interesting surface plasmon resonance-enhanced properties of noble metal nanoparticles and their applications to biosystems. *Plasmonics* **2007**, *2* (3), 107–118.

28. He, L.; Musick, M. D.; Nicewarner, S. R.; Salinas, F. G.; Benkovic, S. J.; Natan, M. J.; Keating, C. D., Colloidal Au-enhanced surface plasmon resonance for ultrasensitive detection of DNA hybridization. *J. Am. Chem. Soc.* **2000**, *122* (38), 9071–9077.

29. Homola, J.; Yee, S. S.; Gauglitz, G., Surface plasmon resonance sensors: review. *Sens. Actuators B, Chem.* **1999**, *54* (1-2), 3–15.

30. Barnes, W. L.; Dereux, A.; Ebbesen, T. W., Surface plasmon subwavelength optics. *Nature* **2003**, *424* (6950), 824–830.

31. Zhang, Y.; Manjavacas, A.; Hogan, N. J.; Zhou, L.; Ayala-Orozco, C.; Dong, L.; Day, J. K.; Nordlander, P.; Halas, N. J., Toward surface plasmon-enhanced optical parametric amplification (SPOPA) with engineered nanoparticles: A nanoscale tunable infrared source. *Nano Lett.* **2016**, *16* (5), 3373–3378.

32. Sharma, B.; Frontiera, R. R.; Henry, A.-I.; Ringe, E.; Van Duyne, R. P., SERS: Materials, applications, and the future. *Mater. Today* **2012**, *15* (1-2), 16–25.

33. Fitch, M. T.; Silver, J., CNS injury, glial scars, and inflammation: Inhibitory extracellular matrices and regeneration failure. *Exp. Neurol.* **2008**, *209* (2), 294–301.

34. Guidelli, E. J.; Ramos, A. P.; Baffa, O., Silver nanoparticle films for metal enhanced luminescence: Toward development of plasmonic radiation detectors for medical applications. *Sens. Actuators B* **2016,** *224*, 248–255.

35. Linic, S.; Aslam, U.; Boerigter, C.; Morabito, M., Photochemical transformations on plasmonic metal nanoparticles. *Nat. Mater.* **2015**, *14* (6), 567–576.

36. Hou, W.; Cronin, S. B., A Review of surface plasmon resonance-enhanced photocatalysis. *Adv. Funct. Mater.* **2013,** *23* (13), 1612–1619.

37. Awazu, K.; Fujimaki, M.; Rockstuhl, C.; Tominaga, J.; Murakami, H.; Ohki, Y.; Yoshida, N.; Watanabe, T., A plasmonic photocatalyst consisting of silver nanoparticles embedded in titanium dioxide. *J. Am. Chem. Soc.* **2008**, *130* (5), 1676–1680.

38. Chen, X.; Zhu, H. Y.; Zhao, J. C.; Zheng, Z. F.; Gao, X. P., Visible-light-driven oxidation of organic contaminants in air with gold nanoparticle catalysts on oxide supports. *Angew. Chem. Int. Ed. Engl.* **2008**, *47* (29), 5353–5356.

39. Wang, P.; Huang, B.; Qin, X.; Zhang, X.; Dai, Y.; Wei, J.; Whangbo, M. H., Ag@AgCl: a highly efficient and stable photocatalyst active under visible light. *Angew. Chem. Int. Ed. Engl.* **2008**, *47* (41), 7931–7933.

40. Tsukamoto, D.; Shiraishi, Y.; Sugano, Y.; Ichikawa, S.; Tanaka, S.; Hirai, T., Gold nanoparticles located at the interface of anatase/rutile TiO_2 particles as active plasmonic photocatalysts for aerobic oxidation. *J. Am. Chem. Soc.* **2012**, *134* (14), 6309–6315.

41. Naya, S.; Inoue, A.; Tada, H., Self-assembled heterosupramolecular visible light photocatalyst consisting of gold nanoparticle-loaded titanium(IV) dioxide and surfactant. *J. Am. Chem. Soc.* **2010**, *132* (18), 6292–6293.

42. Tanaka, A.; Hashimoto, K.; Kominami, H., Selective photocatalytic oxidation of aromatic alcohols to aldehydes in an aqueous suspension of gold nanoparticles supported on cerium(IV) oxide under irradiation of green light. *Chem. Commun.* **2011**, *47* (37), 10446–10448.

43. Tan, T. H.; Scott, J.; Ng, Y. H.; Taylor, R. A.; Aguey-Zinsou, K.-F.; Amal, R., Understanding plasmon and band gap photoexcitation effects on the thermal-catalytic oxidation of ethanol by TiO_2-supported gold. *ACS Catal.* **2016**, *6* (3), 1870–1879.

44. Naya, S.-i.; Kimura, K.; Tada, H., One-step selective aerobic oxidation of amines to imines by gold nanoparticle-loaded rutile titanium(IV) oxide plasmon photocatalyst. *ACS Catal.* **2013**, *3* (1), 10–13.

45. Sugano, Y.; Shiraishi, Y.; Tsukamoto, D.; Ichikawa, S.; Tanaka, S.; Hirai, T., Supported Au-Cu bimetallic alloy nanoparticles: an aerobic oxidation catalyst with regenerable activity by visible-light irradiation. *Angew. Chem. Int. Ed. Engl.* **2013**, *52* (20), 5295–5299.

46. Sarina, S.; Zhu, H.; Jaatinen, E.; Xiao, Q.; Liu, H.; Jia, J.; Chen, C.; Zhao, J., Enhancing catalytic performance of palladium in gold and palladium alloy nanoparticles for organic synthesis reactions through visible light irradiation at ambient temperatures. *J. Am. Chem. Soc.* **2013**, *135* (15), 5793–5801.

47. Gonzalez-Bejar, M.; Peters, K.; Hallett-Tapley, G. L.; Grenier, M.; Scaiano, J. C., Rapid one-pot propargylamine synthesis by plasmon mediated catalysis with gold nanoparticles on ZnO under ambient conditions. *Chem. Commun.* **2013**, *49* (17), 1732–1734.

48. Naya, S.-i.; Nikawa, T.; Kimura, K.; Tada, H., Rapid and complete removal of nonylphenol by gold nanoparticle/rutile titanium(IV) oxide plasmon photocatalyst. *ACS Catal.* **2013**, *3* (5), 903–907.

49. Pineda, A.; Gomez, L.; Balu, A. M.; Sebastian, V.; Ojeda, M.; Arruebo, M.; Romero, A. A.; Santamaria, J.; Luque, R., Laser-driven heterogeneous catalysis: efficient amide formation catalysed by Au/SiO_2 systems. *Green Chem.* **2013**, *15* (8), 2043–2049.

50. Zheng, Z.; Huang, B.; Qin, X.; Zhang, X.; Dai, Y.; Whangbo, M.-H., Facile *in situ* synthesis of visible-light plasmonic photocatalysts M@TiO_2 (M = Au, Pt, Ag) and evaluation of their photocatalytic oxidation of benzene to phenol. *J. Mater. Chem.* **2011**, *21* (25), 9079–9087.

51. Ide, Y.; Matsuoka, M.; Ogawa, M., Efficient visible-light-induced photocatalytic activity on gold-nanoparticle-supported layered titanate. *J. Am. Chem. Soc.* **2010**, *132* (47), 16762–16764.

52. Ide, Y.; Nakamura, N.; Hattori, H.; Ogino, R.; Ogawa, M.; Sadakane, M.; Sano, T., Sunlight-induced efficient and selective photocatalytic benzene oxidation on TiO_2-supported gold nanoparticles under CO_2 atmosphere. *Chem. Commun.* **2011,** *47* (41), 11531–11533.

53. Christopher, P.; Xin, H.; Linic, S., Visible-light-enhanced catalytic oxidation reactions on plasmonic silver nanostructures. *Nat. Chem.* **2011**, *3* (6), 467–472.

54. Wang, F.; Li, C.; Chen, H.; Jiang, R.; Sun, L. D.; Li, Q.; Wang, J.; Yu, J. C.; Yan, C. H., Plasmonic harvesting of light energy for Suzuki coupling reactions. *J. Am. Chem. Soc.* **2013**, *135* (15), 5588–5601.

55. McClain, M. J.; Schlather, A. E.; Ringe, E.; King, N. S.; Liu, L.; Manjavacas, A.; Knight, M. W.; Kumar, I.; Whitmire, K. H.; Everitt, H. O.; Nordlander, P.; Halas, N. J., Aluminum nanocrystals. *Nano Lett.* **2015**, *15* (4), 2751–2755.

56. Swearer, D. F.; Zhao, H.; Zhou, L.; Zhang, C.; Robatjazi, H.; Martirez, J. M.; Krauter, C. M.; Yazdi, S.; McClain, M. J.; Ringe, E.; Carter, E. A.; Nordlander, P.; Halas, N. J., Heterometallic antenna-reactor complexes for photocatalysis. *Proc. Natl. Acad. Sci. U. S. A.* **2016**, *113* (32), 8916–8920.

57. Kim, C.; Suh, B. L.; Yun, H.; Kim, J.; Lee, H., Surface plasmon aided ethanol dehydrogenation using Ag–Ni binary nanoparticles. *ACS Catal.* **2017**, *7* (4), 2294–2302.

58. da Silva, A. G.; Rodrigues, T. S.; Correia, V. G.; Alves, T. V.; Alves, R. S.; Ando, R. A.; Ornellas, F. R.; Wang, J.; Andrade, L. H.; Camargo, P. H., Plasmonic nanorattles as next-generation catalysts for surface plasmon resonance-mediated oxidations promoted by activated oxygen. *Angew. Chem. Int. Ed. Engl.* **2016**, *55* (25), 7111–7115.

59. Zhao, L.-B.; Liu, X.-X.; Zhang, M.; Liu, Z.-F.; Wu, D.-Y.; Tian, Z.-Q., Surface plasmon catalytic aerobic oxidation of aromatic amines in metal/molecule/metal junctions. *J. Phys. Chem. C* **2016**, *120* (2), 944–955.

60. Martirez, J. M.; Carter, E. A., Thermodynamic constraints in using AuM (M = Fe, Co, Ni, and Mo) alloys as N(2) dissociation catalysts: Functionalizing a plasmon-active metal. *ACS Nano.* **2016**, *10* (2), 2940–2949.

61. van Schrojenstein Lantman, E. M.; Deckert-Gaudig, T.; Mank, A. J.; Deckert, V.; Weckhuysen, B. M., Catalytic processes monitored at the nanoscale with tip-enhanced Raman spectroscopy. *Nat. Nanotechnol.* **2012**, *7* (9), 583–586.

62. Hallett-Tapley, G. L.; Silvero, M. J. n.; González-Béjar, M. a.; Grenier, M.; Netto-Ferreira, J. C.; Scaiano, J. C., Plasmon-mediated catalytic oxidation of sec-phenethyl and benzyl alcohols. *J. Phys. Chem. C* **2011**, *115* (21), 10784–10790.

63. Marimuthu, A.; Zhang, J.; Linic, S., Tuning selectivity in propylene epoxidation by plasmon mediated photo-switching of Cu oxidation state. *Science* **2013**, *339* (6127), 1590-1593.

64. Vries, J. G. d.; Elsevier, C. J., *The handbook of homogeneous hydrogenation*. Wiley-VCH: Weinheim, 2007; pp 1–30.

65. Claus, P., Selective hydrogenation of α,β-unsaturated aldehydes and other C=O and C=C bonds containing compounds. *Top. Catal.* **1998**, *5* (1/4), 51–62.

66. Mäki-Arvela, P.; Hájek, J.; Salmi, T.; Murzin, D. Y., Chemoselective hydrogenation of carbonyl compounds over heterogeneous catalysts. *Appl. Catal. A* **2005**, *292*, 1–49.

67. Zheng, J.; Duan, X.; Lin, H.; Gu, Z.; Fang, H.; Li, J.; Yuan, Y., Silver nanoparticles confined in carbon nanotubes: on the understanding of the confinement effect and promotional catalysis for the selective hydrogenation of dimethyl oxalate. *Nanoscale* **2016**, *8* (11), 5959–5967.

68. Yang, L.; Xing, L.; Cheng, C.; Xia, L.; Liu, H., Highly efficient and selective hydrogenation of chloronitrobenzenes to chloroanilines by H_2 over confined silver nanoparticles. *RSC Adv.* **2016,** *6* (38), 31871–31875.

69. Jia, Z.; Zhou, F.; Liu, M.; Li, X.; Chan, A. S.; Li, C. J., Silver-catalyzed hydrogenation of aldehydes in water. *Angew. Chem. Int. Ed. Engl.* **2013**, *52* (45), 11871–11874.

70. Mukherjee, S.; Libisch, F.; Large, N.; Neumann, O.; Brown, L. V.; Cheng, J.; Lassiter, J. B.; Carter, E. A.; Nordlander, P.; Halas, N. J., Hot electrons do the impossible: Plasmon-induced dissociation of H_2 on Au. *Nano Lett.* **2013**, *13* (1), 240–247.

71. Mukherjee, S.; Zhou, L.; Goodman, A. M.; Large, N.; Ayala-Orozco, C.; Zhang, Y.; Nordlander, P.; Halas, N. J., Hot-electron-induced dissociation of H_2 on gold nanoparticles supported on SiO_2. *J. Am. Chem. Soc.* **2014**, *136* (1), 64–67.

72. Wiley, B. J.; Im, S. H.; Li, Z. Y.; McLellan, J.; Siekkinen, A.; Xia, Y., Maneuvering the surface plasmon resonance of silver nanostructures through shape-controlled synthesis. *J. Phys. Chem. B* **2006**, *110* (32), 15666–15675.

73. Lachheb, H.; Puzenat, E.; Houas, A.; Ksibi, M.; Elaloui, E.; Guillard, C.; Herrmann, J.-M., Photocatalytic degradation of various types of dyes (Alizarin S, Crocein Orange G, Methyl Red, Congo Red, Methylene Blue) in water by UV-irradiated titania. *Appl. Catal. B* **2002**, *39* (1), 75–90.

74. Benjamin, W.; Yugang, S.; Brian, M.; Younan, X., Shape-controlled synthesis of metal nanostructures: The case of silver. *Chem. – Eur. J.* **2005**, *11* (2), 454–463.

75. Li, A. Y.; Kaushik, M.; Li, C.-J.; Moores, A., Microwave-assisted synthesis of magnetic carboxymethyl cellulose-embedded Ag–Fe_3O_4nanocatalysts for selective carbonyl hydrogenation. *ACS Sustainable Chem. Eng.* **2016**, *4* (3), 965–973.

76. Mukherjee, S.; Vannice, M., Solvent effects in liquid-phase reactions. Activity and selectivity during citral hydrogenation on Pt/SiO_2 and evaluation of mass transfer effects. *J. Catal.* **2006**, *243* (1), 108–130.

77. Christopher, P.; Xin, H.; Marimuthu, A.; Linic, S., Singular characteristics and unique chemical bond activation mechanisms of photocatalytic reactions on plasmonic nanostructures. *Nat. Mater.* **2012**, *11* (12), 1044–1050.

78. Horiuti, I.; Polanyi, M., Exchange reactions of hydrogen on metallic catalysts. *Trans. Faraday Soc.* **1934**, *30* (663), 1164–1172.

79. Yan, J.; Jacobsen, K. W.; Thygesen, K. S., First-principles study of surface plasmons on Ag(111) and H/Ag(111). *Phys. Rev. B* **2011**, *84* (23), 235430.

80. Yang, Y.; Zhao, Y.; Yan, Y.; Wang, Y.; Guo, C.; Zhang, J., Preparation of AgCl nanocubes and their application as efficient photoinitiators in the polymerization of N-Isopropylacrylamide. *J. Phys. Chem. B* **2015**, *119* (46), 14807–14813.

81. Wang, P.; Huang, B.; Qin, X.; Zhang, X.; Dai, Y.; Wei, J.; Whangbo, M. H., Ag@AgCl: a highly efficient and stable photocatalyst active under visible light. *Angew. Chem. Int. Ed. Engl.* **2008**, *47* (41), 7931–7933.

82. Han, L.; Wang, P.; Zhu, C.; Zhai, Y.; Dong, S., Facile solvothermal synthesis of cube-like Ag@AgCl: a highly efficient visible light photocatalyst. *Nanoscale* **2011**, *3* (7), 2931–2935.

A5.7 Supplemental information for Appendix 5

Experimental
General

All chemicals used in this work were purchased from Sigma-Aldrich. All ketones or aldehydes used for the reactions were purified using standard purification techniques[1] found in "Purification of Laboratory Chemicals, 5th edition" and NMR was used to confirm that these were pure before use in catalytic reactions. Hydrogen gas used was purchased from Air Liquide Canada and used without further purification or drying. Standard Schlenk line techniques were used during the synthesis of the nanoparticles and for manipulations during catalytic tests. All glassware used for the catalytic reactions was dried for 24 hours at 140°C in a glass drying oven. Fresh microwave vials were used for scope reactions to ensure that no other metal residue was found within the glass used in the reactions or cleaned using nitric acid and a base bath. The light sources used during the reactions were either a standard 60 W incandescent lightbulb or a 405 nm LED laser using a diverging lens to expand the laser source to desired irradiation area.

Equipment

Nuclear magnetic resonance (NMR) spectra were acquired with a 400 MHz Varian Mercury spectrometer. Gas Chromatography-Mass Spectrometry (GCMS) measurements were collected with a Thermo Polaris Q-Ion Trap gas chromatography/mass-spectrometer equipped with an auto-sampler. For UV-vis measurements, a Varian Cary 300 Bio UV-vis spectrophotometer was used; a solution of 1 mg Ag NCs was suspended in 10 mL ethanol *via* sonication, with 10 mL of ethanol as reference. The same solution was used for dynamic light scattering (DLS) characterization with a Brookhaven 90plus DLS instrument. The data were fitted using the algorithm provided with the assumption of an effective diameter of a perfect sphere. Scanning electron microscopy was performed on a FEI Inspect F-50 FE-SEM instrument; the sample was prepared by suspending in ethanol and drop-casted onto the metallic post**.** Energy-dispersive X-ray spectroscopy and bright-field scanning transmission electron microscopy were performed on a Hitachi SU-9000 coldfield emission instrument and transmission electron microscopy on a Philips CM200 200 kV. Cu/ lacey carbon grids were used, on which a drop of the prepared solution was dropped and dried *in vacuo*. A Thermo Scientific K-Alpha instrument was used for X-ray photoelectron spectroscopy after deposition of the Ag NCs on copper tape with a

FEI Inspect F-50 FE-SEM instrument. Powder sample crystallinity was tested using a Bruker D2 PHASER X-Ray Diffractometer equipped with a Cu-Kα (λ = 1.54 Å) source, LinxEye detector and a Ni filter.

Synthesis of Ag NCs

The synthesis of the nanoparticle catalyst was reproduced from a previous literature procedure with some modifications.[2] 100 mL of ethylene glycol that was used for multiple experiments was purified by shaking large amounts of $CaSO_4$ and filtered into a pre-flushed argon round bottom flask. Additional $CaSO_4$ was added to the flask and stirred overnight. A fractional distillation apparatus was added to the round bottom flask and the ethylene glycol was distilled under vacuum. A similar procedure was used to dry acetone which was used as a solvent for washing the particles. Each of these solvents was kept under argon in a polymerization Schlenk flask for long-term storage. A new dried 100 mL Schlenk flask equipped with a stir bar was evacuated and refilled with argon three times. 5 mL of the distilled ethylene glycol was transferred *via* cannula and this flask and was heated with an oil bath to 140-145°C. While ethylene glycol was heated, three solutions were prepared: 0.1 M $AgNO_3$, 0.15 M polyvinylpyrrolidone (PVP in terms of monomer, 55 k M.W.), and a 30 mM HCl. All solutions were prepared using the dried ethylene glycol as the solvent and were shaken into solution using sonication or a shaker table. During the shaking, all solutions were kept covered under aluminum foil. The HCl solution was prepared using concentrated HCl. After 1.5 hours of heating, 100 µL of the 30 mM HCl solution was transferred to the heated Schleck flask and the stirring was regulated to 600 RPM. This solution was stirred for 10 minutes before proceeding. During this waiting period, a syringe pump was primed with 3 mL of the $AgNO_3$ and PVP solutions in separate syringes. Once 10 minutes had passed, the syringe pump was turned on and the solutions were delivered at a rate of 0.74 mL/min. The solution changed from a clear, colorless solution to a deep, opaque purple color. Within 2 minutes, the color shifted to beige. After 21 hours, the reaction was cooled to room temperature and a centrifuge tube was prepared by flushing with argon for 10 minutes. The contents of the Schlenk flask were sonicated to suspend any particles on the side of the flask and transferred to the centrifuge tube *via* cannula or under a high flow of argon in glove bag. 10 mL of dried acetone was added, and the cubes were sonicated in the tube once again. The cubes were isolated by centrifugation at 9000 RPM for 20 minutes at room temperature and the supernatant

was removed using a syringe. This procedure was repeated 5 times and the final solution of cubes were suspended in anhydrous ethanol with sonication. At this point, samples were taken for all characterization and the remaining material was transferred to a small vial and dried *in vacuo* with the aid of a high-vacuum line. This grey powder was stored under argon at -20°C in a freezer.

Hydrogenation catalytic tests reactions

A pre-dried 2-8 mL microwave vial from ChemGlass was equipped with 1-10 mmol of aldehyde or ketone, 5 mL of solvent, 1 mg of Ag NCs and a stirring bar. The reaction vessel was capped with a septum and Ar gas was bubbled through the reaction mixture for 20 minutes to ensure complete de-gassing. This procedure was performed in complete darkness. Then the septum was removed quickly and replaced with a microwave crimp top with a septum middle. The vial was evacuated *via* a needle attached to the Schlenk line, and a balloon of hydrogen was attached and injected. The reaction was then heated to a temperature of 40, 60, 80 or 100°C (depending on the entry) using an oil bath for 24 hours (**Table A5.2**). Depending on the entry, the vial was carefully left in the dark, or exposed for the whole duration of the test with the lightbulb or the laser. The setup is illustrated in **Figure A5.8**. After the reaction was completed, the vial was cooled to room temperature and then sonicated for 20 minutes to ensure any product absorbed on Ag NCs was desorbed. The reaction mixture was then transferred to a centrifuge tube and centrifuged at 9000 rpm for 10 minutes. The supernatant was transferred to a pre-weighed round bottom flask and solvent was removed *in vacuo*. The procedure was performed in triplicate. All reported yields were isolated yields, except for camphor where GCMS measurements using a standard curve were employed.

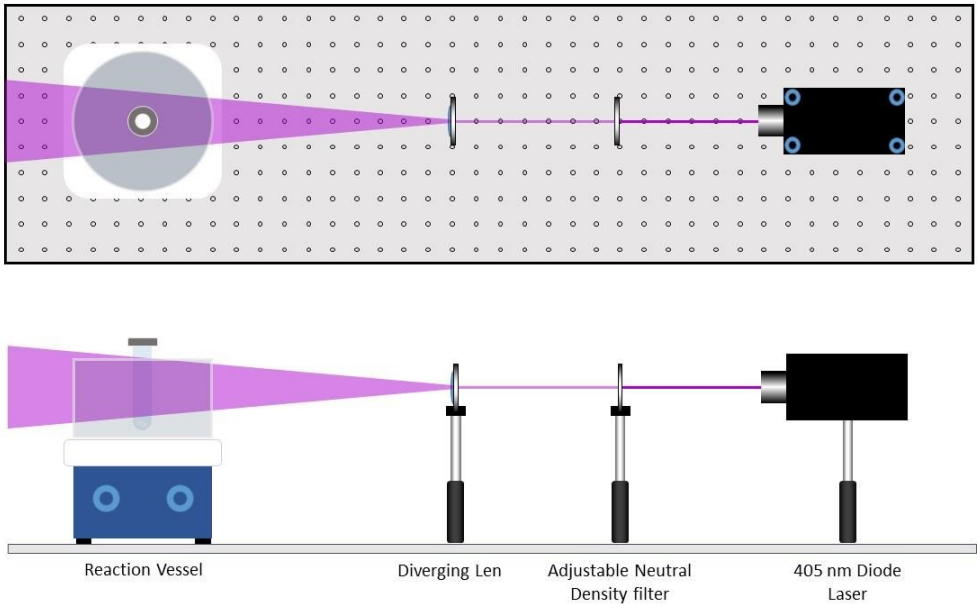

Figure A5.8. Overall schematic representation of the reaction setup showing positions of all components. The setup has three optical parts: the laser, adjustable neutral density filter and a diverging lens. For variable intensity *vs* yield experiments, light intensity was measured in the same position and distance from the laser as the flask position by first removing it, placing a light meter where the flask was, then replacing the flask for the experiment.

Oxidation catalytic tests

To a pre-dried 2-8 mL microwave vial from ChemGlass, 5 mmol of p-hydroxybenzaldehyde was added and dissolved in 5 mL of p-dioxane. 5 mg of silver nanocubes was added to the reaction vessel and a stirring bar was added along with a crimp cap with a septum. A double balloon of air was attached and added to the top. The reaction was then heated in an oil bath to 80°C and exposed to 405 nm light for 18 hours. After the reaction was completed, the vial was cooled to room temperature and then sonicated for 20 minutes to ensure any absorbed product was removed from the surface of the particles. The reaction mixture was transferred to a centrifuge tube and was centrifuged at 9000 rpm for 10 minutes. The supernatant as transferred to a pre-weighed round bottom flask. This procedure is preformed two times more and the resulting solution is rotary evaporated to dryness.

ICP analysis

Silver nanocubes were analyzed before and after preforming the standard camphor reduction reaction and the silver content in the product checked using ICP-MS. The sample preparation was completed by digesting 1.5 mg of fresh Ag NCs into 0.35 mL nitric acid, 1.65 mL of 30% hydrogen peroxide and 1 mL of water and was heated gently to produce a standard solution. Samples of the final worked up reaction product (35 mg) were taken and digested into nitric acid, 0.35 mL of nitric acid, 1.65 mL of 30% hydrogen peroxide, and 1 mL of water and heated as above. The solutions were each diluted to 12 mL with water from a MilliQ purification system. The amount of silver in the Ag NCs was checked to compare to what was transferred into products. A blank was run and subtracted from the resulting silver found. During the course of three reactions, 0.57 ppm of silver was transferred into the product from an average of 3 trials of each reaction.

Electron microscopy

Scanning electron microscopy (SEM)

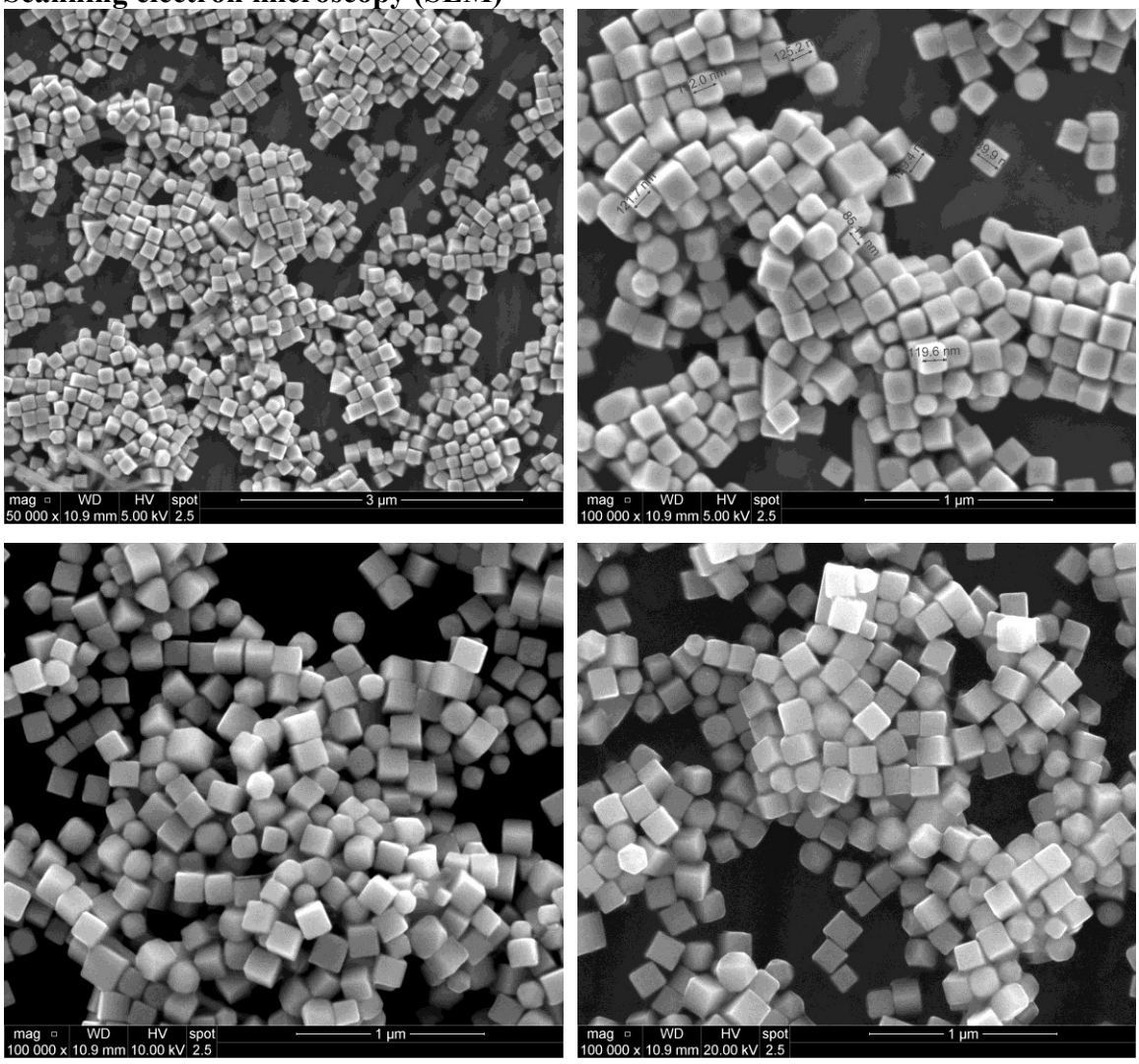

Figure A5.9. SEM images of Ag NCs.

Transmission electron microscopy (TEM)

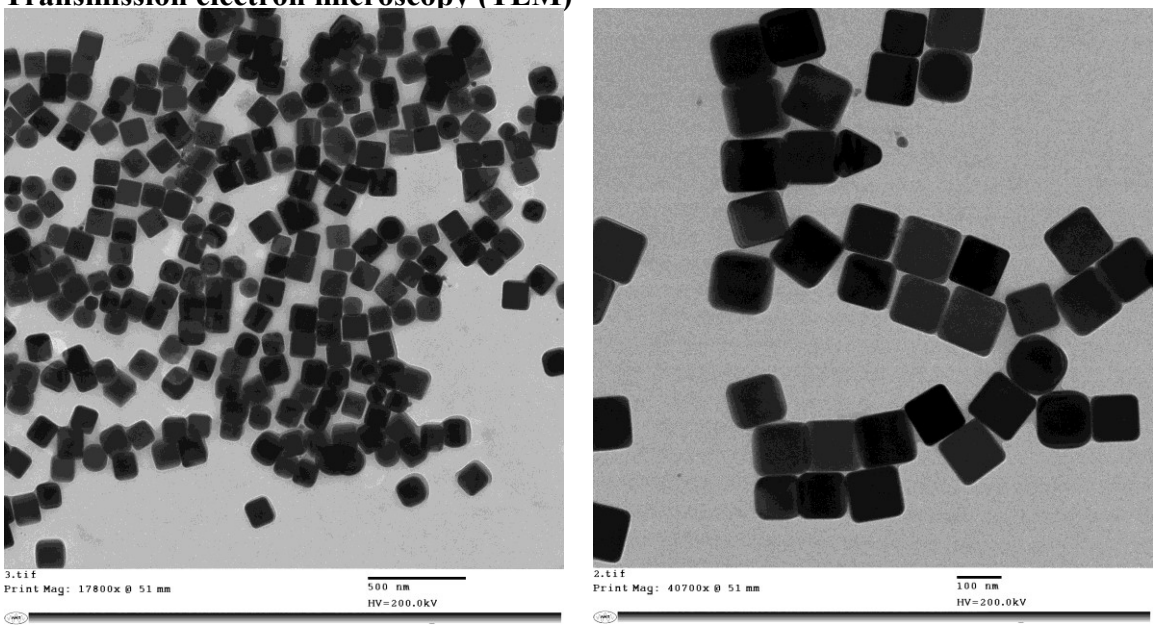

Figure A5.10. TEM images of Ag NCs.

Bright-field scanning transmission electron microscopy (BFSTEM)

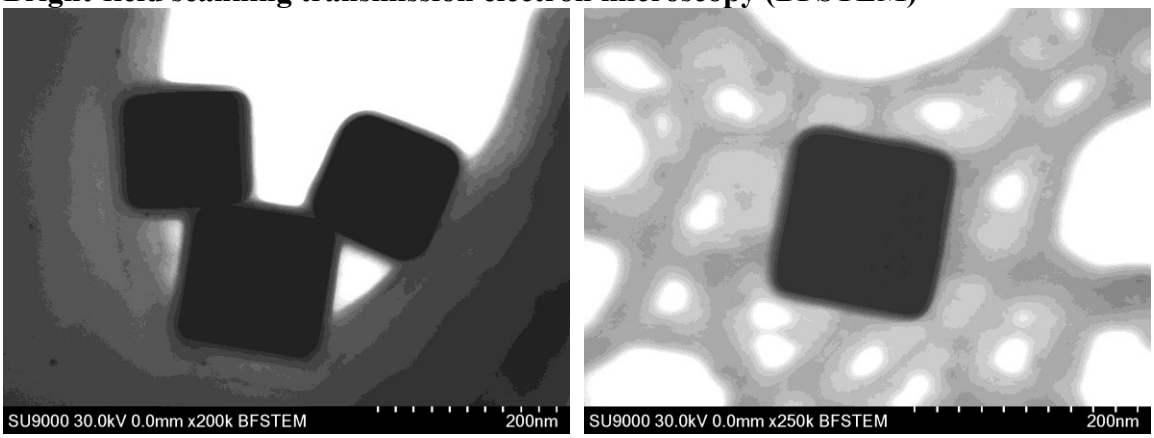

Figure A5.11. BFSTEM images of Ag NCs on Cu/ lacey carbon grids.

EDS analysis

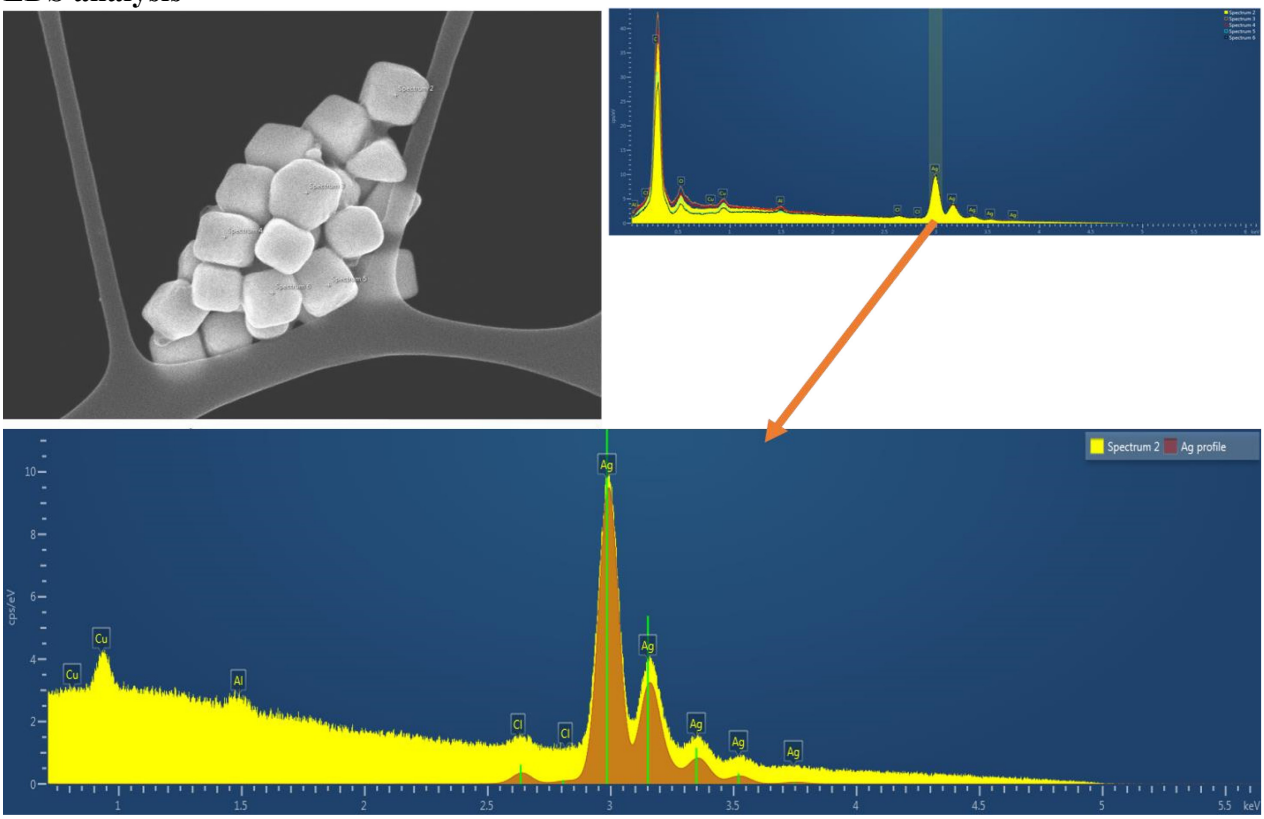

Figure A5.12. STEM micrograph (top left) and EDS spectra (top right and bottom) of Ag NCs. The bottom view focuses on the silver region, where the silver contribution is provided in orange over the total count in yellow.[3]

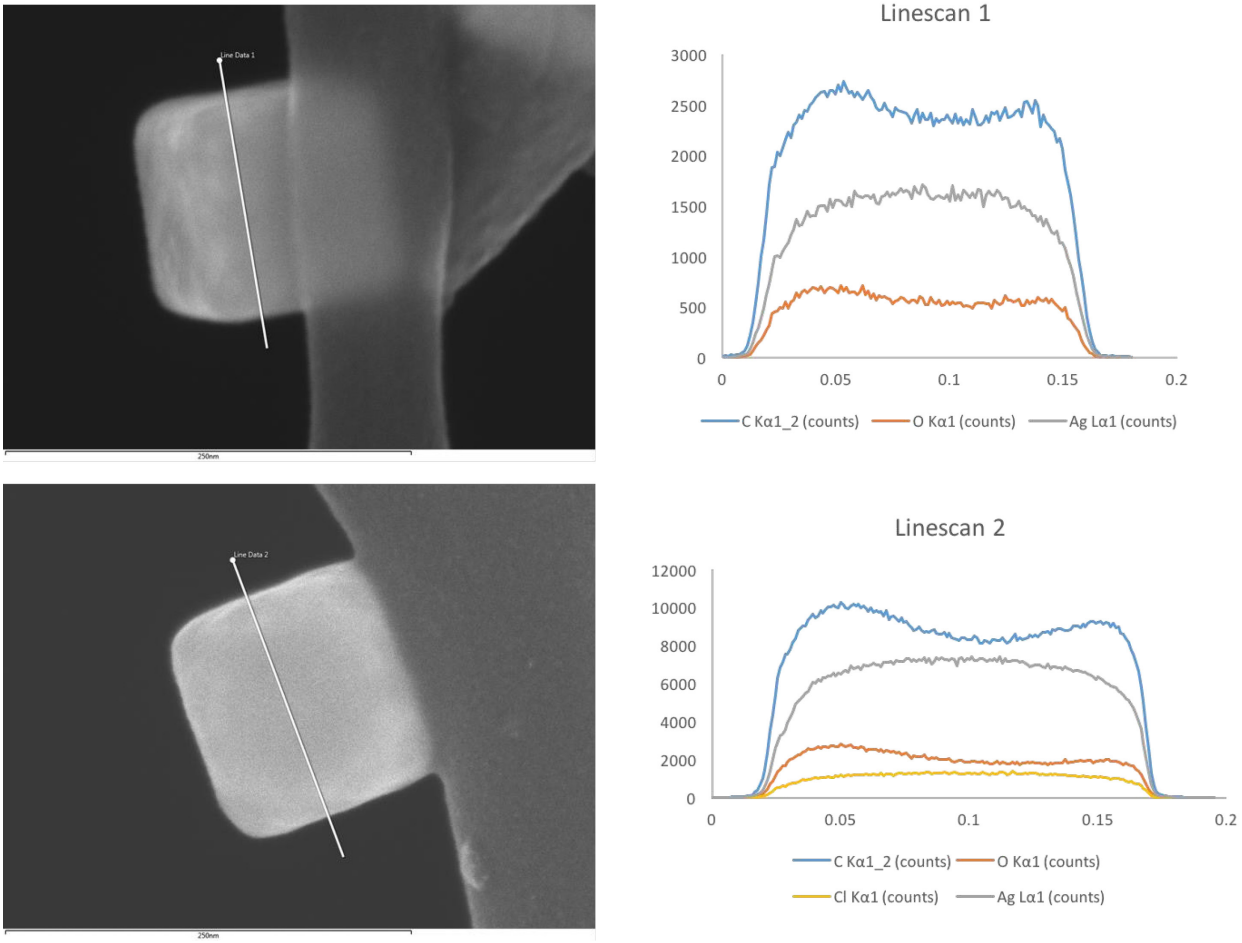

Figure A5.13. STEM images (left) and corresponding EDS 'linescan' elemental profile (right) of Ag NCs.

X-ray photoelectron spectroscopy

Samples of the Ag NCs were taken from a batch after suspended in ethanol and dried overnight in a vacuum oven at 80°C. After the sample seemed dry, the tubes containing the sample were loaded into a Schlenk flask and dried overnight under high vacuum to remove and residual water. Once fully dried, the samples were crushed into a powder and placed onto copper tape and analyzed using a Thermo Scientific K-Alpha instrument.

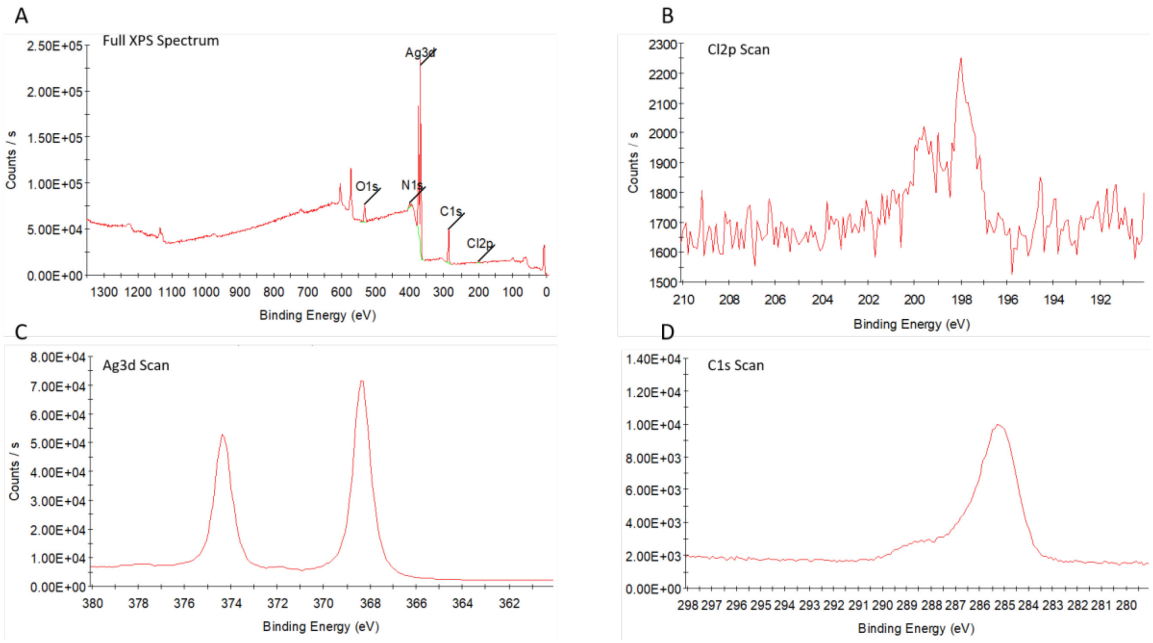

Figure A5.14. XPS full scan **(A)** and closeup on Cl2p scan **(B)**, Ag3d scan **(C)** and C1s **(D)** of Ag NCs.

Table A5.1. Elemental identification and quantification of Ag NCs by XPS.

Name	Peak BE	Height CPS	FWHM eV	Area (P) CPE eV	Atomic %	Q
Ag3d	368.92	181182.98	2.62	941706.57	20.90	1
C1s	286.05	37003.85	3.68	154975.37	59.77	1
O1s	532.80	18975.27	4.26	87931.07	13.29	1
Cl2p	198.78	2016.10	4.76	11153.52	1.81	1
N1s	401.13	5092.16	3.11	18589.85	4.23	1

Dynamic light scattering

A solution of 0.1 mg/mL of Ag NCs in anhydrous ethanol was filtered using a 0.2 µm PTFE syringe filter and analyzed using a Brookhaven 90plus DLS instrument, using a model which assumed a perfect sphere. A count rate of 1361.0 kcps was achieved during the measurement using

a dust filter and taking an average of 5 scans together and collecting at the detector 90° to the 35 mW solid state laser.

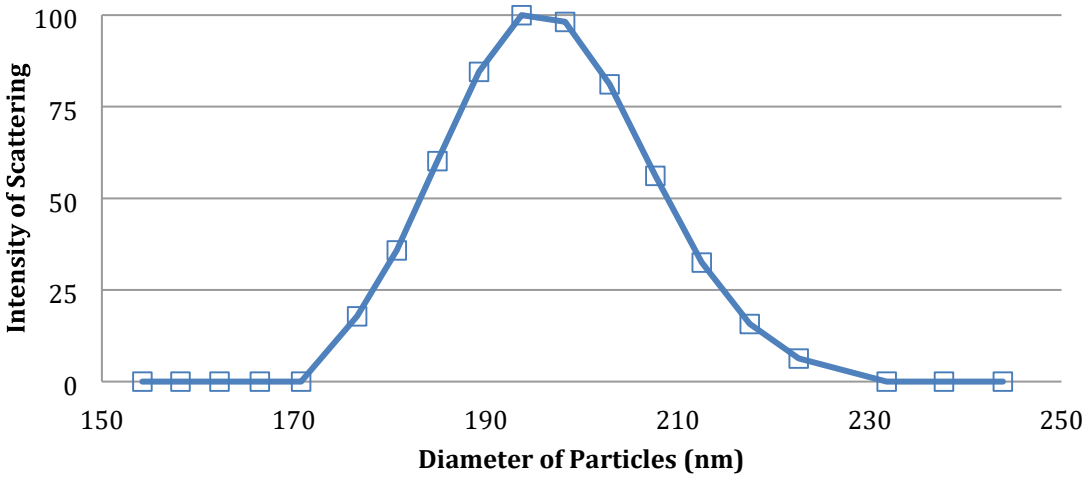

Figure A5.15. Fitted DLS data showing the hydrodynamic diameter of Ag NCs *vs* intensity of scattering from a solution of Ag NCs (0.1 mg/mL) in ethanol to determine polydispersity of particles.

Polydispersity was calculated using equation:

$$D = \frac{\mu}{\Gamma^2}$$

where D is the polydispersity, μ is the calculated standard deviation within the raw data distribution and Γ is the average of the standard deviation plus the average of the data.[4]

X-Ray diffraction

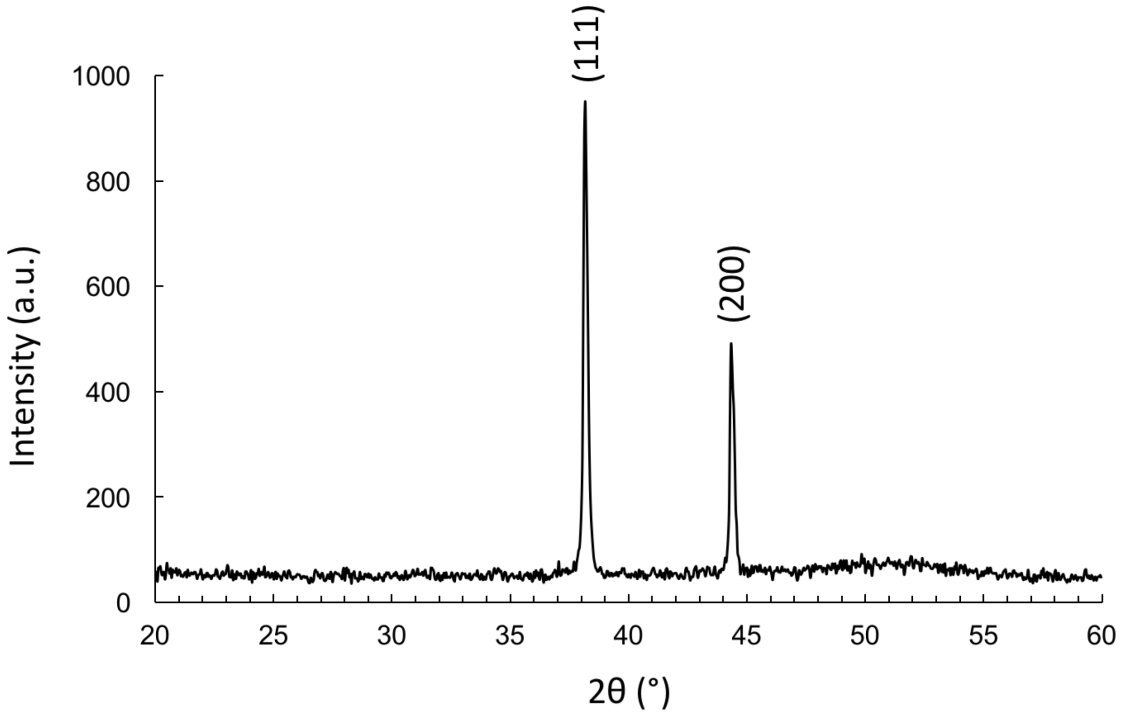

Figure A5.16. PXRD spectra of silver nanocubes taken from a 2θ range of 20° to 60°.

Catalytic test optimization

Table A5.2. Results for the hydrogenation of camphor with Ag NCs as catalyst as a function of temperature, H_2 pressure, and light exposure. Reaction conditions: 500 μL of 0.04 mg/mL Ag NCs solution in ethanol, 1 mmol of camphor and 1 mL of dioxane, 24 hours. Control experiments presented here involve using off-plasmon excitation, using argon as a reagent gas and performing these reactions in the dark.

Temperature (°C)	**Hydrogen Pressure (atm)**	**Light source**	**GCMS (% yield of product)**
40	1	405 nm laser	29%
40	1	None	N/R
40	1	Light bulb	17%
60	1	405 nm laser	47%
60	1	None	Trace
60	1	Light bulb	29%
80	1	405 nm laser	87%
80	1	None	Trace
80	1	Light bulb	42%
100	1	405 nm laser	81%
100	1	None	6%
100	1	Light bulb	57%
80	Argon	405 nm laser	N/R
100	1	405 nm laser	N/R without cubes.
100	1	532 nm laser	5%
100	1	633 nm laser	N/R

Table A5.3. Isolated yields for a series of solvents used in the hydrogenation of camphor with Ag NCs as catalyst as a function of temperature, H_2 pressure and 405 nm laser exposure. Reaction conditions: 500 µL of 0.04 mg/mL Ag NCs solution in ethanol, 1 mmol of camphor and 1 mL of solvent, 1 bar of H_2, 24 hours.

Solvent	**Boiling Point (°C)**	**Dielectric constant, ε**	**Yield at boiling point**	**Yield at 40°C**
Dioxane	101	2.25	81%	29%
Water	100	80.1	80%	24%
Ethanol	78	24.5	30%	11%
Hexane	68	1.88	5%	<1%
Ethyl Acetate	77	6.2	3%	<1%
Dichloromethane	39	8.93	<1%	<1%

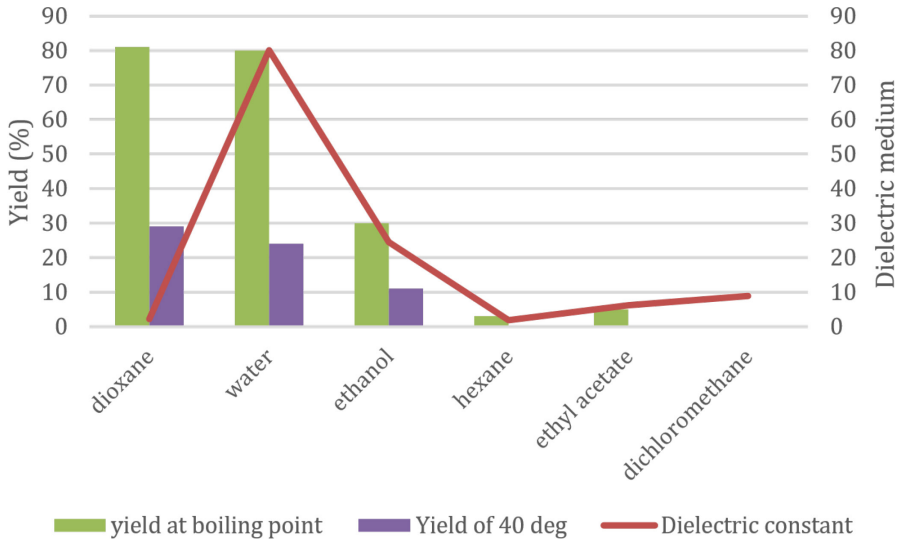

Figure A5.17. Correlation between yield for camphor hydrogenation at boiling point or 40°C (solid bars) with dielectric medium for each solvent (line). Excellent correlation was observed, except for dioxane, which is known to behave like a polar solvent in hydrogenation, despite small ε.[5]

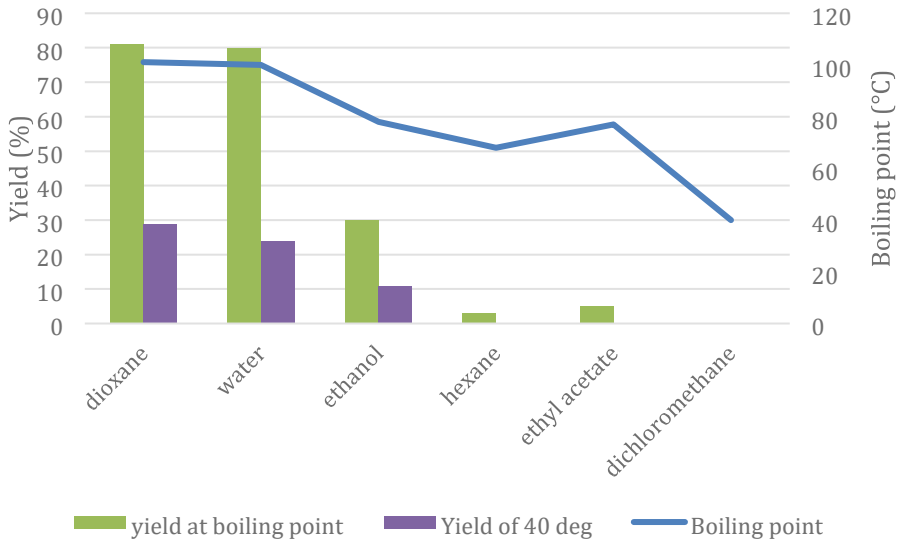

Figure A5.18. Correlation between yield for camphor hydrogenation at boiling point or 40°C (solid bars) with boiling point for each solvent (line).

Kinetic experiments

NMR experiments for kinetic runs were performed using a J. Young tube, sealed under 1 atmosphere of hydrogen. 1.1 mg of catalyst was added to the tube as a semi-suspension in 1 mL

of toluene-d_8. 50 mg of camphor was added along with an equimolar amount of dioxane, and the tube was evacuated and refilled with argon gas three times. The tube was evacuated one last time, closed, and a septum was fitted over the entrance. A balloon full of hydrogen was added and the tube was opened, allowing the hydrogen to flow into the tube. The tube was closed and heated to 80 °C and exposed to the 405 nm laser light. The consumption of camphor was monitored by NMR and is shown in **Figure A5.19**.

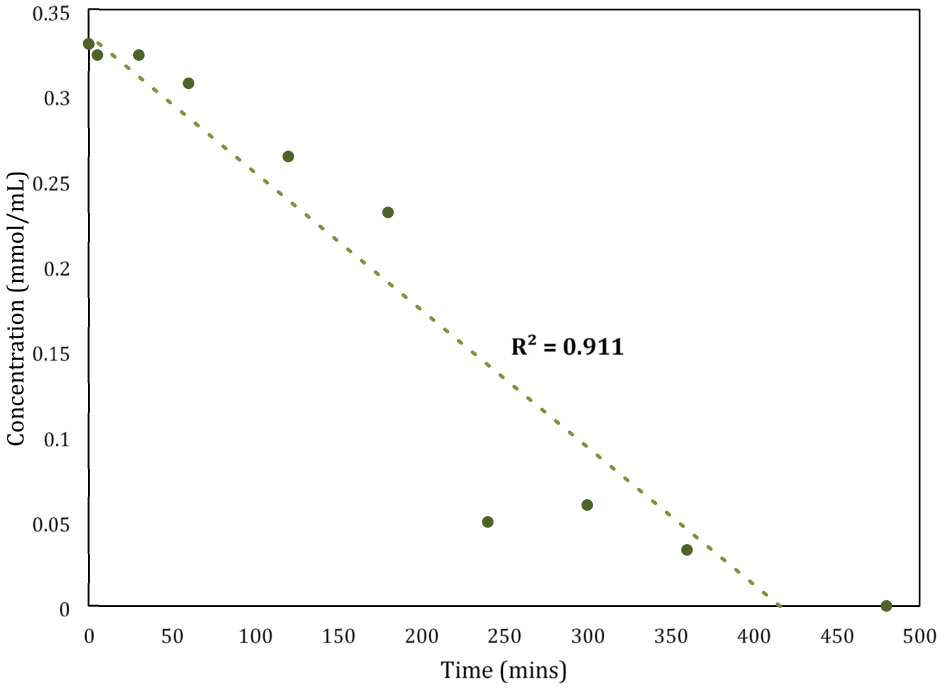

Figure A5.19. Kinetic analysis of the reaction showing the consumption of camphor along the reaction time. By linear regression, an R^2 value of 0.911 is found. A linear trend in the reaction rate is consistent with the uncertainty arising from the method used to probe the reaction progress (NMR, ∽5% uncertainty).

Hot filtration experiment

To determine the exact role of any leeched species that occurred throughout the catalytic transformation, a hot filtration experiment was conducted. A standard hydrogenation reaction was performed for 2 hours before an 1 mL aliquot was taken, spun down at 9000 k RPM and the supernatant was removed and dried *in vacuo* to yield a semisolid white product. While that procedure was occurring, a separate three-necked Schlenk flask was flushed with argon for 20 minutes and equipped with a magnetic stirbar. Just as the 2 hour mark for the standard reaction

was reached, a fritted filter was attached to the flask and another round bottom flask was placed on top and the entire newly setup apparatus was put under vacuum and refilled with argon. The fritted part of the filter was heated with a heat gun for 2 minutes, the top round bottom flask was removed and the standard hydrogenation reaction solution was transferred to the top of the frit with a syringe and a septum was attached. The solution was filtered, leaving a clear, slightly yellow solution. A fresh balloon of hydrogen was placed on top and the reaction was continued for an additional 5 hours. At the end, an aliquot was removed and worked up by removing solvents and NMR spectroscopy was performed on both samples. At the two hour mark, the yield was found to be 21% and after 6 hours of reaction after the cubes were removed the yield was measured to be 23%, well within the NMR error.

Light intensity *vs* yield experiments

To probe the nature of the photo-plasmonic effect observed during this reaction, a light intensity *vs* yield dependence set of experiments of the standard reaction was performed. The typical conditions shown in the 'Hydrogenation catalytic test reaction' section was employed using camphor as a substrate and the laser intensity was varied. This was achieved by reducing the intensity of the beam stepwise, by rotating a variable OD neutral density filter wheel to desired specific irradiation levels of light striking the reaction flask.

Scope of reaction

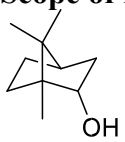

Isoborneol **(1)**: white solid. ^{1}H NMR (400 MHz, $CDCl_3$): δ=0.81 (s, 3 H), 0.91 (s, 3H), 1.03 (s, 3H), 1.50 (m, 1H), 1.59-1.82 (m, 6H), 3.66 (1H, m). 87% yield.

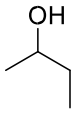

2-butanol **(2)**: slightly yellow liquid. ^{1}H NMR (400 MHz, $CDCl_3$): δ=3.62 (m, 1H), 1.42 (m, 2H), 1.12 (m, 3H), 0.88 (m, 3H). 55% yield.

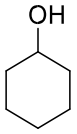

Cyclohexanol **(3)**: clear liquid. ^{1}H NMR (400 MHz, $CDCl_3$): δ=3.55 (m, 1H), 2.97 (s, br, 1H), 1.62-1.70 (m, 2H), 1.32-1.64 (m, 8H). 34% yield.

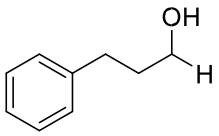

3-Phenyl-1-propanol **(4)** – clear oil. ^{1}H NMR (400 MHz, $CDCl_3$): δ=7.24-7.19 (m, 2H), 7.157.11 (m, 3H), 3.62(t, J=6.3 Hz, 2H), 2.64 (t, J=7.8 Hz, 2H), 1.89-1.80 (m, 2H), 1.50 (s, 1H). 33% yield.

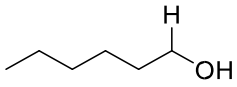

1-hexanol **(5):** clear liquid. ^{1}H NMR (400 MHz, $CDCl_3$): δ=3.65 (t, J=4.5 Hz, 2H), 1.59 (m, 2H), 1.45-1.35 (m, 6H), 0.89 (m, 3H). 43% yield.

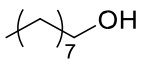

1-Nonanol **(6)**: clear liquid. ^{1}H NMR (400 MHz, $CDCl_3$): δ=3.60 (t, J= 4.3 Hz, 2H), 1.59 (m, 2H), 1.44 (m, 2H), 1.24-1.32 (m, 10H), 0.88 (m, 3H). 76% yield.

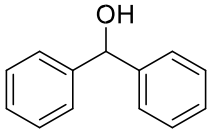

Diphenylmethanol **(7)**: clear crystalline solid. ^{1}H NMR (400 MHz, $CDCl_3$): δ=2.20 (d, J = 4.1 Hz, 1H), 5.88 (s, br, 1H), 7.19-7.27 (m, 2H), 7.30-7.35 (m, 4H), 7.35-7.39 (m, 4H). 92% yield.

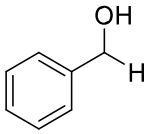

Phenylmethanol **(8)**: Colourless oil. ^{1}H NMR (400 MHz, $CDCl_3$): δ=7.25-7.5 (m, 5H), 4.50 (s, 2H), 2.66 (br s, 1H). 75% yield.

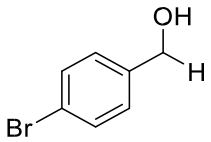

(4-bromophenyl)methanol **(9)**: slightly yellow oil. ^{1}H NMR (400 MHz, $CDCl_3$): δ=7.55 (d, J=8.3 Hz, 2H), 7.30 (d, J=8.3 Hz, 2H), 4.72 (s, 2H), 1.75 (s, br, 1H). 76% yield.

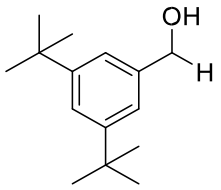

(3,5-di-tert-butylphenyl)methanol **(10)**: slightly yellow oil. ^{1}H NMR (400 MHz, $CDCl_3$): δ=1.35 (s, 18H), 4.73 (s, 2H), 7.22 (d, J=1.8 Hz, 2H), 7.36 (t, J= 1.8 Hz, 1H). 32% yield.

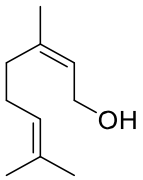

(Z)-3,7-dimethyloct-2,6-diene-1-ol **(11)**: slightly yellow oil. ^{1}H NMR (400 MHz, $CDCl_3$): δ=1.50 (s, 1H), 1.59 (s, 3H), 1.68 (s, 3H), 1.70 (s, 3H), 2.0-2.1 (m, 4H), 4.14 (d, J = 6.9 Hz, 2H), 5.09 (m, 1H), 5.40 (m, 1H). 79% yield.

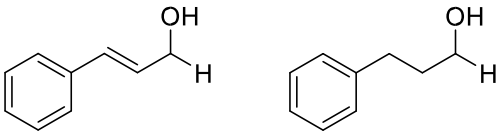

(E)-3-phenylprop-2-en-1-ol (Cinnamyl alcohol) **(12)**: yellow oil. ^{1}H NMR (400 MHz, $CDCl_3$): δ=7.40 (m, 5H), 6.65 (d, J=15.6 Hz, 1H), 6.40 (m, 1H), 4.30 (m, 1H), 1.95 (s, 1H). 80% yield + 5% of the fully hydrogenated product. Products are separated *via* column chromatography. 1:4 ethyl acetate: hexane. NMR spectrum for the fully hydrogenated product matches that of the **(4)**.

Photocatalytic oxidation reaction

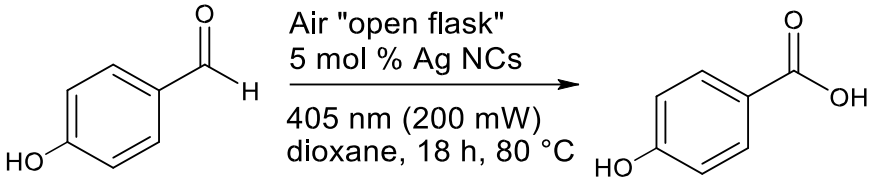

Temperature scope of oxidation reaction

The above standard oxidative reaction conditions were used, but varying the temperature. As temperature rises, yield increases and thermal saturation was observed to occur at around 80 °C.

Table A5.4. Table comparing optimization conditions for the standard photo-oxidation reaction. Control experiments showed no reactivity when the catalyst was not present, or when the reagent gas was not air.

Temperature (°C)	Reagent Gas	Catalyst Load (mg)	Light source	NMR yield
60	Air (1 atm)	5	Light bulb	95%
60	Air (1 atm)	5	Dark	34%
60	Air (1 atm)	5	405 nm laser	95%
80	Air (1 atm)	5	Light bulb	96%
80	Air (1 atm)	5	Dark	46%
80	Air (1 atm)	5	405 nm laser	97%
80	Argon	5	405 nm laser	N/R
80	Air (1 atm)	0	405 nm laser	N/R

Oxidation of aldehyde

When aldehydes are used with standard reaction conditions, the oxidative reaction occurs selectively and with high yields even using bulkier, bromo-substituted substrates, and alkyl and aryl substrates.

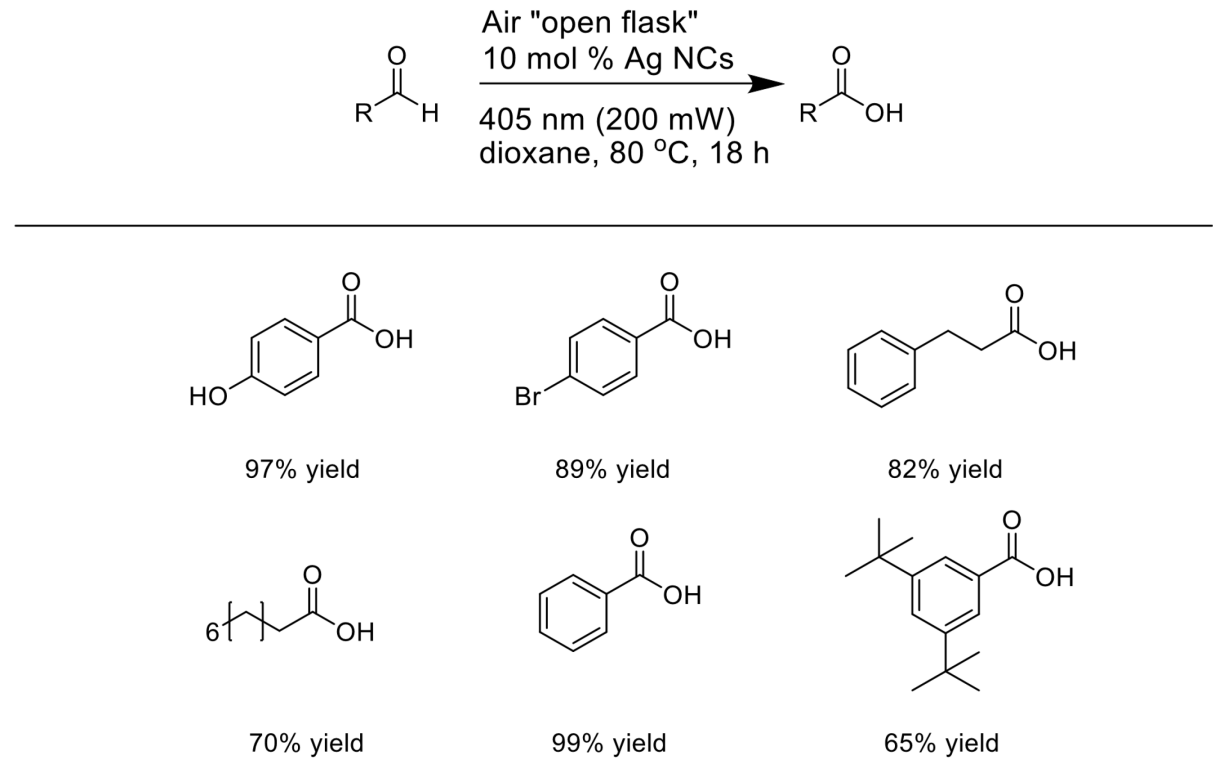

Figure A5.20. Scope of the reaction, showing yields of the optimized reaction conditions on various aldehydes for the oxidation reaction.

Oxidation from alcohol

To investigate the oxidative potential of this reaction, oxidation from the alcohol was tried, yet with little success. Typical yields were low, and no side-products were found. If the substrate's functional group was an aldehyde instead, typically high conversions/yields were found with only starting material found in the end.

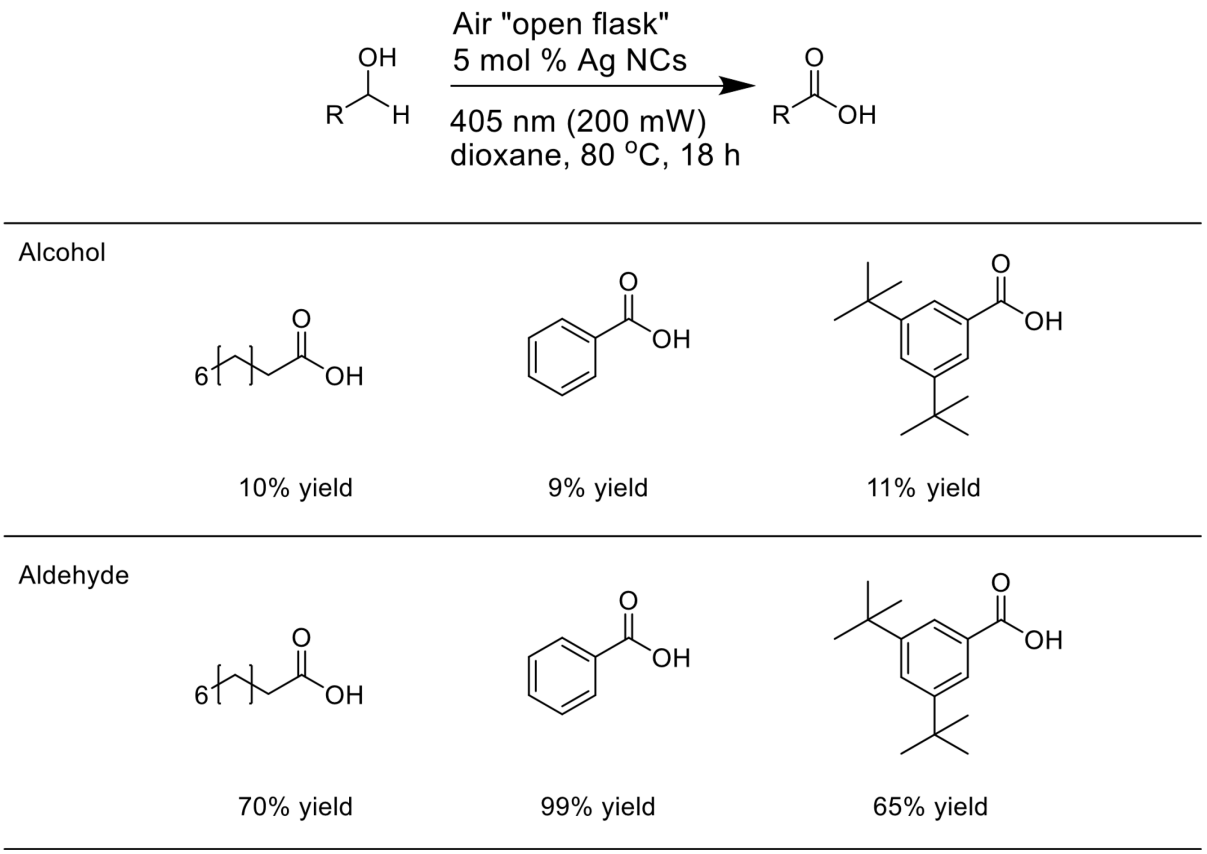

Figure A5.21. Comparing reactivity between aldehydes and alcohols for the photo-oxidative reaction. Yields are higher using aldehydes over alcohols. For the oxidation from alcohol to aldehyde and then directly to carboxylic acids, no aldehydes were found suggesting that the oxidative rate for aldehydes is higher due to higher reactivity.

References

1. Armarego, W. L. F.; Chai, C. L. L., *Purification of laboratory chemicals*. Butterworth-Heinemann: 2003; p 609-609.

2. Christopher, P.; Xin, H.; Linic, S., Visible-light-enhanced catalytic oxidation reactions on plasmonic silver nanostructures. *Nat Chem* **2011,** *3* (6), 467-72.

3. Sansonetti, J. E.; Martin, W. C., Handbook of Basic Atomic Spectroscopic Data. *Journal of Physical and Chemical Reference Data* **2005,** *34* (4), 1559-2259.

4. Hassan, P. A.; Kulshreshtha, S. K., Modification to the cumulant analysis of polydispersity in quasielastic light scattering data. *J Colloid Interface Sci* **2006,** *300* (2), 744-8.

5. Mukherjee, S.; Vannice, M., Solvent effects in liquid-phase reactionsI. Activity and selectivity during citral hydrogenation on Pt/SiO2 and evaluation of mass transfer effects. *Journal of Catalysis* **2006,** *243* (1), 108-130.